

KINETIC MODELS FOR THE PREDICTION OF WEATHERING OF COMPLEX  
MIXTURES ON NATURAL WATERS

By

John McIlroy

A DISSERTATION

Submitted to  
Michigan State University  
in partial fulfillment of the requirements  
for the degree of

Chemistry—Doctor of Philosophy

2014

## ABSTRACT

### KINETIC MODELS FOR THE PREDICTION OF WEATHERING OF COMPLEX MIXTURES ON NATURAL WATERS

By

John McIlroy

Models play a vital role in predicting environmental fates of pollutants, which is critical for effective remediation. However, many fate and transport models for complex mixtures, *e.g.* petroleum products, do not incorporate the individual compounds, which are responsible for toxicity and environmental persistence. In this research, a diesel/water microcosm mimicked an environmental fuel spill with simulated weathering by evaporation and irradiation. Temporal changes in composition were assessed by gas chromatography-mass spectrometry (GC-MS) and time of flight mass spectrometry (ToF-MS) with atmospheric pressure chemical ionization (APCI).

During evaporation, first-order kinetic rate constants were calculated for selected compounds and employed to develop predictive models, based on GC retention indices. Models were initially developed for compounds from individual classes (normal alkane, branched alkane, alkyl benzene, and polycyclic hydrocarbon) and later expanded to include compounds from all classes (comprehensive model). Using the comprehensive model, the rate constants were predicted with an average error of 10%, whereas the class specific models resulted in less error (4 – 8%). A model was also developed that incorporated varying temperature (5 to 35 °C), allowing for the prediction of the rate constants over environmentally relevant temperatures (16 % error). Using the rate constant, the fraction remaining of individual compounds was determined. The fraction

remaining of individual compounds was used to calculate the fraction remaining of the total fuel ( $\pm 6\%$ ), and was in good agreement with currently available evaporation models. The variable-temperature model successfully applied to predict the fraction remaining of other petroleum products, demonstrating applicability beyond diesel fuel. The variable-temperature model was also used to predict chromatographic profiles of a fuel after evaporation, estimated the length of time a fuel has been evaporated using the predicted chromatogram, and estimate the time to reach a specific percent evaporated for an individual compound or for the entire fuel.

First-order kinetic rate constants were also determined for diesel fuel irradiated with simulated sunlight for 10 hours by GC-MS and APCI-ToF-MS. The decay of hydrocarbons and formation of oxygenated compounds began within the first hour of irradiation. Using GC-MS, a two-fold increase in the rate constant was observed during irradiation ( $0.004 - 1.211 \text{ h}^{-1}$ ) than predicted from the variable-temperature evaporation model ( $0.000 - 0.379 \text{ h}^{-1}$ ). Compounds unlikely to evaporate also decayed, indicating they were precursors to photooxidation. In the APCI-ToF-MS, rate constants were determined for decay of hydrocarbons ( $0.003 - 0.210 \text{ h}^{-1}$ ) and formation of oxygenated compounds ( $0.002 - 1.173 \text{ h}^{-1}$ ). The kinetic rate constants developed in this work provided valuable information about changes in individual compounds during the weathering of petroleum products. Predicting changes in individual compounds provides additional information not available in most current models impact assessment and guide remediation of petroleum releases.

## ACKNOWLEDGEMENTS

I would like to thank everyone that has helped me throughout my time at Michigan State. I appreciate my advisors, Vicki McGuffin and Dan Jones, for all of their help, support, and weekly discussions while completing my Ph.D. and Master's research. I would also like to thank Ruth Smith for serving as my Master's advisor, providing help and guidance throughout my research, and for serving on my committee. Also, thank you to John McCracken and Ned Jackson for serving on my committee and providing helpful comments and suggestions in the formulation of this project.

I could not have done this without the support of all of the MSU Chemistry Department and the current and former members of the McGuffin, Jones, and Forensic Chemistry research groups. I would like to specifically thank Kathy Severin for help with instrumentation and Steven Halpin for assistance in writing Matlab algorithms. I have also been fortunate to receive financial support through the U.S Environmental Protection Agency's STAR Fellowship, the J. Edgar Hoover Scientific Scholarship, and Pfizer.

Last, I would like to thank all my friends and family for all of their help and support throughout the process. In particular I want to thank my wife Katie for everything she did to help me throughout graduate school.

This document was developed under STAR Fellowship Assistance Agreement no. FP917295 awarded by the U.S. Environmental Protection Agency (EPA). This work has not been formally reviewed by EPA. The views expressed in this publication are solely those of the authors, and EPA does not endorse any products or commercial services mentioned in this publication.

# TABLE OF CONTENTS

<b>LIST OF TABLES</b> .....	<b>viii</b>
<b>LIST OF FIGURES</b> .....	<b>xiii</b>
<b>1. Introduction</b> .....	<b>1</b>
<b>1.1 Petroleum Release into the Environment</b> .....	<b>1</b>
<b>1.2 Petroleum Composition</b> .....	<b>2</b>
1.2.1 <i>Composition of Crude Oil</i> .....	2
1.2.2 <i>Refined Petroleum Products</i> .....	7
1.2.3 <i>Composition of Diesel Fuel</i> .....	8
<b>1.3 Oil Spill Weathering</b> .....	<b>11</b>
1.3.1 <i>Physical Weathering Processes</i> .....	12
1.3.1.1 <i>Evaporation</i> .....	12
1.3.1.2 <i>Spreading</i> .....	14
1.3.1.3 <i>Dissolution</i> .....	14
1.3.1.4 <i>Emulsification</i> .....	15
1.3.1.5 <i>Natural Dispersion</i> .....	15
1.3.1.6 <i>Sedimentation</i> .....	15
1.3.2 <i>Chemical Weathering: Photooxidation</i> .....	16
1.3.3 <i>Biological Weathering: Biodegradation</i> .....	16
<b>1.4 Analytical Strategies for Characterization of Crude Oil and Petroleum Products</b> .....	<b>17</b>
1.4.1 <i>Gas Chromatography</i> .....	18
1.4.2 <i>Liquid Chromatography</i> .....	18
1.4.3 <i>Mass Spectrometry</i> .....	19
1.4.4 <i>Strategies for Analysis of Diesel Fuel</i> .....	21
<b>1.5 Basis of Predictive Models</b> .....	<b>23</b>
1.5.1 <i>Physical Properties</i> .....	23
1.5.2 <i>Chromatographic Retention Index</i> .....	24
1.5.3 <i>Kendrick Mass Defect</i> .....	25
<b>1.6 Oil Spill Modeling</b> .....	<b>26</b>
1.6.1 <i>Fate and Transport Modeling of Oil Spills</i> .....	26
1.6.2 <i>Evaporation of Petroleum Constituents</i> .....	27
1.6.2.1 <i>Theory</i> .....	27
1.6.2.2 <i>Empirical Models</i> .....	29
1.6.2.3 <i>Analytical Model</i> .....	32
1.6.2.4 <i>Pseudo-component Model</i> .....	38
1.6.2.5 <i>Kinetic Models</i> .....	42
1.6.3 <i>Photodegradation of Petroleum Products</i> .....	45
1.6.3.1 <i>Direct photolysis</i> .....	46
1.6.3.2 <i>Indirect Photolysis</i> .....	47
1.6.3.3 <i>Photooxidation Studies</i> .....	49

1.7 Objectives and Aims .....	52
REFERENCES.....	55
<b>2. Gas Chromatographic Retention Index as a Basis for Predicting Evaporation Rates of Complex Mixtures .....</b>	<b>67</b>
2.1 Introduction .....	67
2.2 Materials and Methods.....	69
2.2.1 Sample Collection.....	69
2.2.2 Evaporation Chamber.....	70
2.2.3 Evaporation of Diesel Fuel .....	72
2.2.4 Gas Chromatography-Mass Spectrometry Analysis.....	72
2.2.5 Identification and Quantification of Selected Compounds .....	74
2.3 Results and Discussion.....	93
2.3.1 Determination of Kinetic Rate Constants.....	93
2.3.2 Predicting Kinetic Rate Constant Based on Boiling Point.....	105
2.3.3 Predicting Kinetic Rate Constant Based on Retention Index.....	106
2.3.4 Correction of Retention Indices using McReynolds Constants .....	115
2.3.5 Model Validation.....	120
2.4 Applications of the Models.....	120
2.5 Conclusions.....	132
REFERENCES.....	134
<b>3. Variable-Temperature Model for Predicting Environmental Evaporation Rates of Petroleum Products using Gas Chromatographic Retention Indices .....</b>	<b>139</b>
3.1 Introduction .....	139
3.2 Materials and Methods.....	140
3.2.1 Sample Collection.....	140
3.2.2 Evaporation of Fuel Samples .....	140
3.2.3 Gas Chromatography-Mass Spectrometry Analysis.....	141
3.2.4 Data Analysis .....	142
3.3 Results .....	154
3.3.1 Arrhenius Plots.....	202
3.3.2 Fixed-temperature Models.....	208
3.3.3 Variable-Temperature Model.....	214
3.3.4 Applications of Model .....	215
3.3.4.1 Calculation of Fraction Remaining with Fluctuating Temperatures .....	215
3.3.4.2 Compound Distribution .....	221
3.3.4.3 Evaporation Rates of Other Complex Mixtures .....	224
3.3.4.4 Evaporation Time .....	230
3.3.4.5 Time to Specific Fraction Remaining .....	231
3.3.4.6 Comparison to Other Evaporation Models.....	235
3.4 Discussion and Conclusions .....	236
REFERENCES.....	240

<b>4. Determination of Kinetic Rate Constants during Solar-Simulated Irradiation of Diesel Fuel by Gas Chromatography-Mass Spectrometry and High Resolution Mass Spectrometry .....</b>	<b>243</b>
<b>4.1 Introduction .....</b>	<b>243</b>
<b>4.2 Materials and Methods.....</b>	<b>244</b>
4.2.1 <i>Collection of Diesel Fuel.....</i>	244
4.2.2 <i>Irradiation of Diesel Fuel.....</i>	244
4.2.3 <i>Sample Extraction .....</i>	252
4.2.4 <i>Selection of an Internal Standard .....</i>	253
4.2.5 <i>Gas Chromatography-Mass Spectrometry .....</i>	254
4.2.6 <i>Time of Flight-Mass Spectrometry.....</i>	255
<b>4.3 Results .....</b>	<b>255</b>
4.3.1 <i>Visual Observations and Mass Change of Diesel Residue.....</i>	255
4.3.2 <i>Gas Chromatography-Mass Spectrometry of Diesel Residue .....</i>	256
4.3.3 <i>Determination of Elemental Formulas by High Resolution Mass Spectrometry .....</i>	266
4.3.4 <i>Kendrick Mass Defect.....</i>	267
4.3.5 <i>Principal Component Analysis.....</i>	271
4.3.6 <i>Determination of Photooxidation Rate Constants.....</i>	274
4.3.6.1 <i>Kinetic Rate Constants Determined from Gas Chromatography-Mass Spectrometry .....</i>	277
4.3.6.2 <i>Kinetic Rate Constants Determined from High Resolution Mass Spectrometry .....</i>	279
4.3.7 <i>Analysis of Precipitate formed during Irradiation of Diesel Fuel .....</i>	298
<b>4.4 Discussion and Conclusions .....</b>	<b>303</b>
<b>REFERENCES.....</b>	<b>308</b>
<b>5. Conclusions and Future Works .....</b>	<b>312</b>
<b>5.1 Evaporation .....</b>	<b>312</b>
5.1.1 <i>Conclusions.....</i>	312
5.1.2 <i>Limitations .....</i>	314
5.1.3 <i>Future Directions .....</i>	315
<b>5.2 Photooxidation.....</b>	<b>317</b>
5.2.1 <i>Conclusions.....</i>	317
5.2.2 <i>Limitations .....</i>	318
5.2.3 <i>Future Directions .....</i>	320
<b>REFERENCES.....</b>	<b>322</b>

## LIST OF TABLES

Table 1-1. Common defined compound classes found in crude oil. For each class, several example compounds are listed. The example structure is of the bolded example compound. ....	4
Table 1-2. Selected properties of petroleum and petroleum products. ....	5
Table 1-3. Distillation temperature and carbon range for typical petroleum products [10, 11].	10
Table 2-1. The injection parameters optimized using the precision in peak area of a mixture of five normal alkanes. ....	75
Table 2-2. Selected compounds monitored during evaporation of diesel fuel to develop the model. The following information is listed for each compound: compound class, peak number (#) (corresponding to peaks labeled in Figure 2-3 – Figure 2-8), mass-to-charge ratio ( $m/z$ ) of extracted ion chromatogram used for quantification, retention time ( $t^T_R$ ), boiling point ( $T_B$ ), retention index ( $I^T$ ), rate constant ( $k$ ), characteristic lifetime ( $\tau$ ), and number of $\tau$ in 300 hours. For the compound class the follow abbreviations were used: normal alkane (Norm), branched alkane (Bran), alkyl aromatic (Arom), polycyclic hydrocarbon (Poly). ....	77
Table 2-3. Selected compounds monitored during evaporation of diesel fuel to validate the model. The following information is listed for each unidentified compound: compound class, mass-to-charge ratio ( $m/z$ ) of extracted ion chromatogram used for quantification, retention time ( $t^T_R$ ), retention index ( $I^T$ ), rate constant ( $k$ ), characteristic lifetime ( $\tau$ ), and number of $\tau$ in 300 hours. The absolute percent error (APE) between the experimental and predicted rate constant is also shown. ....	91
Table 2-4. Compounds utilized to confirm linearity of calibration curves. For each compound, the retention time ( $t^T_R$ ), concentration range, slope ( $m$ ), intercept ( $b$ ), and coefficient of determination ( $R^2$ ) are shown. ....	94
Table 2-5. Class-specific models developed to predict the rate constant, based on the <i>uncorrected</i> retention index. For each model, the number of compounds used to create the model ( $n$ ) as well as the slope ( $m$ ), intercept ( $b$ ), and coefficient of determination ( $R^2$ ) for Equation 2-3 are shown. In addition, the mean absolute percent error (MAPE) for predicting compounds in each class is shown. For the compound class the follow abbreviations were used: normal alkane (Norm), branched alkane (Bran), alkyl aromatic (Arom), polycyclic hydrocarbon (Poly). ....	110
Table 2-6. Class-specific models developed to predict the rate constant, based on the <i>corrected</i> retention index. For each model, the number of compounds used to create the model ( $n$ ) as well as the slope ( $m$ ), intercept ( $b$ ), and coefficient of determination	

( $R^2$ ) for Equation 2-3 are shown. In addition, the mean absolute percent error (MAPE) for predicting compounds in each class is shown. For the compound class the following abbreviations were used: normal alkane (Norm), branched alkane (Bran), alkyl aromatic (Arom), polycyclic hydrocarbon (Poly)..... 119

Table 2-7. Fraction remaining ( $F_{IT}$ ) for selected compounds in evaporated diesel fuel (20 °C, 100 h), experimental and predicted using the comprehensive model with retention index ( $I^T$ ) correction. The absolute percent error (APE) is also shown..... 124

Table 3-1. Selected compounds monitored during evaporation of diesel fuel for development of fixed-temperature and variable-temperature models. The following information is listed for each compound: Peak number in Table 3-3 – Table 3-12 (Peak #), the identity of the compound, the class to which the compound was assigned, the mass-to-charge ( $m/z$ ) ratio of the extracted ion chromatogram (EIC) used to quantify the compound, the retention time ( $t^T_R$ ), the boiling point ( $T_b$ ), and retention index ( $I^T$ ) before and after correction. .... 143

Table 3-2. Selected compounds monitored during evaporation of diesel fuel for validation of fixed-temperature and variable-temperature models. The following information is listed for each compound: Peak number in Table 3-3 – Table 3-12 (Peak #), the class to which the compound was assigned, the mass-to-charge ( $m/z$ ) ratio of the extracted ion chromatogram (EIC) used to quantify the compound, the retention time ( $t^T_R$ ), and retention index ( $I^T$ ) before and after correction. .... 151

Table 3-3. For model development, the experimental rate constant ( $k_{exp}$ ), characteristic lifetime ( $\tau$ ), and the number of  $\tau$  in 300 h for selected compounds monitored during the evaporation of diesel fuel at 5 °C. The predicted rate constant ( $k_{pred}$ ) and absolute percent error (APE) was calculated using the fixed-temperature (fixed T) and variable-temperature (variable T) models. Compounds with  $\tau > 0.5$  in 300 h were excluded from the table (peaks 16 – 37, 43 – 45, 72 – 77). Several compounds had retention indices less than 800 (peaks 1, 38, 46) and were also excluded, as the retention index could not be accurately extrapolated. .... 156

Table 3-4. For model validation, the experimental rate constant ( $k_{exp}$ ), characteristic lifetime ( $\tau$ ), and the number of  $\tau$  in 300 h for selected compounds in diesel fuel evaporated at 5 °C. The predicted rate constant ( $k_{pred}$ ) and absolute percent error (APE) was calculated using the fixed-temperature (fixed T) and variable-temperature (variable T) models. Compounds with  $\tau > 0.5$  in 300 h were excluded from the table (peaks 80, 84, 85, 105, 106). .... 162

Table 3-5. For model development, the experimental rate constant ( $k_{exp}$ ), characteristic lifetime ( $\tau$ ), and the number of  $\tau$  in 300 h for selected compounds monitored during the evaporation of diesel fuel at 10 °C. The predicted rate constant ( $k_{pred}$ ) and absolute percent error (APE) was calculated using the fixed-temperature (fixed T) and variable-temperature (variable T) models. Compounds with  $\tau > 0.5$  in 300 h were excluded from the table (peaks 19 – 37, 43 – 45, 73 – 77). Several compounds had retention indices

lower than 800 (peaks 1, 38, 46) and were also excluded, as the retention index could not be accurately extrapolated. .... 165

Table 3-6. For model validation, the experimental rate constant ( $k_{exp}$ ), characteristic lifetime ( $\tau$ ), and the number of  $\tau$  in 300 h for selected compounds in diesel fuel evaporated at 10 °C. The predicted rate constant ( $k_{pred}$ ) and absolute percent error (APE) was calculated using the fixed-temperature (fixed T) and variable-temperature (variable T) models. Compounds with  $\tau > 0.5$  in 300 h were excluded from the table (peaks 80, 84, 85, 105, 106). .... 171

Table 3-7. For model development, the experimental rate constant ( $k_{exp}$ ), characteristic lifetime ( $\tau$ ), and the number of  $\tau$  in 300 h for selected compounds monitored during the evaporation of diesel fuel at 20 °C. The predicted rate constant ( $k_{pred}$ ) and absolute percent error (APE) was calculated using the fixed-temperature (fixed T) and variable-temperature (variable T) models. Compounds with  $\tau > 0.5$  in 300 h were excluded from the table (peaks 23-37, 44, 45, 57). Several compounds had retention indices lower than 800 (peaks 1, 38, 46) and were also excluded, as the retention index could not be accurately extrapolated. .... 174

Table 3-8. For model validation, the experimental rate constant ( $k_{exp}$ ), characteristic lifetime ( $\tau$ ), and the number of  $\tau$  in 300 h for selected compounds in diesel fuel evaporated at 20 °C. The predicted rate constant ( $k_{pred}$ ) and absolute percent error (APE) was calculated using the fixed-temperature (fixed T) and variable-temperature (variable T) models. Compounds with  $\tau > 0.5$  in 300 h were excluded from the table (peaks 80, 85, 105, 106). .... 180

Table 3-9. For model development, the experimental rate constant ( $k_{exp}$ ), characteristic lifetime ( $\tau$ ), and the number of  $\tau$  in 300 h for selected compounds monitored during the evaporation of diesel fuel at 30 °C. The predicted rate constant ( $k_{pred}$ ) and absolute percent error (APE) was calculated using the fixed-temperature (fixed T) and variable-temperature (variable T) models. Compounds with  $\tau > 0.5$  in 300 h were excluded from the table (peaks 24 – 37, 45, 77). Several compounds had retention indices lower than 800 (peaks 1, 38, 46) and were also excluded, as the retention index could not be accurately extrapolated. .... 183

Table 3-10. For model validation, the experimental rate constant ( $k_{exp}$ ), characteristic lifetime ( $\tau$ ), and the number of  $\tau$  in 300 h for selected compounds in diesel fuel evaporated at 30 °C. The predicted rate constant ( $k_{pred}$ ) and absolute percent error (APE) was calculated using the fixed-temperature (fixed T) and variable-temperature (variable T) models. Compounds with  $\tau > 0.5$  in 300 h were excluded from the table. 189

Table 3-11. For model development, the experimental rate constant ( $k_{exp}$ ), characteristic lifetime ( $\tau$ ), and the number of  $\tau$  in 300 h for selected compounds monitored during the evaporation of diesel fuel at 35 °C. The predicted rate constant ( $k_{pred}$ ) and absolute percent error (APE) was calculated using the fixed-temperature (fixed T) and variable-temperature (variable T) models. Compounds with  $\tau > 0.5$  in 300

h were excluded from the table (peaks 26 – 37, 45). Several compounds had retention indices lower than 800 (peaks 1, 38, 46) and were also excluded, as the retention index could not be accurately extrapolated..... 192

Table 3-12. For model validation, the experimental rate constant ( $k_{exp}$ ), characteristic lifetime ( $\tau$ ), and the number of  $\tau$  in 300 h for selected compounds in diesel fuel evaporated at 35 °C. The predicted rate constant ( $k_{pred}$ ) and absolute percent error (APE) was calculated using the fixed-temperature (fixed T) and variable-temperature (variable T) models. Compounds with  $\tau > 0.5$  in 300 h were excluded from the table.199

Table 3-13. The activation energy ( $E_A$ ), pre-exponential factor ( $A$ ), coefficient of determination ( $R^2$ ) determined from the Arrhenius plot of using all temperatures (5, 10, 20, 30, 35 °C). ..... 204

Table 3-14. The activation energy ( $E_A$ ), pre-exponential factor ( $A$ ), coefficient of determination ( $R^2$ ) determined from the Arrhenius plot of using the three highest temperatures (20, 30, 35 °C). The enthalpy of vaporization ( $H_{vap}$ ) from the literature and the enthalpy of activation ( $H_A$ ) determined from the Arrhenius plot and Equation 3-3 as well as the difference between the two values ( $H_{vap} - H_A$ ) are also shown. .... 206

Table 3-15. The fixed temperature models developed for each temperature, including the number of compounds ( $n$ ), the slope ( $m$ ), intercept ( $b$ ), and coefficient of determination ( $R^2$ ) for linear regression with Equation 3-4 are shown. Also shown is the mean absolute percent error (MAPE) in the prediction of the rate constant for each temperature using the fixed temperature models as well as the variable temperature model (Equation 3-6). ..... 210

Table 3-16. The rate constant ( $k$ ) at each temperature for decalin ( $RI = 1045$ ), which was not included in the original model. The observed rate constant ( $k_{obs}$ ) as well as the experimentally predicted ( $k_{exp}$ ) rate constant using the fixed temperature and variable model is also shown. The absolute percent error (APE) between the experimental and predicted rate constants are shown for each model. .... 213

Table 3-17. The mean absolute percent error (MAPE) for 29 compounds using the corresponding fixed temperature model (Table 3-15) and the variable temperature model (Equation 3-6). ..... 216

Table 3-18. The fraction of fuel remaining predicted using the variable-temperature model with temperature data collected every two minutes, every five hours, every twelve hours, and the running average temperature (Figure 3-3). The experimental fraction of fuel remaining ( $F_T$ ) based on the average change in mass was 0.83. The percent error between the experimental and predicted values using the model is also shown. In addition, the percent error between the models using the 2-min temperature interval compared to the longer intervals is shown. .... 219

Table 4-1. A list of compounds monitored by the GC-MS experiment. For each compound the mass-to-charge ( $m/z$ ) ratio for the extracted ion chromatogram, the

retention time ( $t_R$ ), retention index ( $I^T$ ), the observed rate constant ( $k_{obs}$ ), and a predicted rate constant ( $k_{pre}$ ) for evaporation available from Chapter 3. .... 259

Table 4-2. The exact mass, the number of carbon atoms (C), the number of hydrogen atoms (H), the number of oxygen atoms (O), the double bond equivalence (DBE), the Kendrick mass defect (KMD), the rate constant for decay ( $k_d$ ), and the uncertainty in the rate constant for compounds identified using mass spectrometry. .... 281

Table 4-3. The exact mass, the number of carbon atoms (C), the number of hydrogen atoms (H), the number of oxygen atoms (O), the double bond equivalence (DBE), the Kendrick mass defect (KMD), the first ( $1^{st}$ ) and zeroth ( $0^{th}$ ) rate constant for formation ( $k_f$ ), and the uncertainty in the rate constant for compounds identified using mass spectrometry. .... 291

## LIST OF FIGURES

Figure 1-1. Sample distillation curve of Alaska North Slope oil (southern pipeline). Distillation data from National Oceanic and Atmospheric Administration's ADIOS 2 modelling program [18].	9
Figure 1-2. Different weathering processes effecting a petroleum release in the environment. The thickness of the line indicates the contribution of weathering process. Figure adapted from National Oceanic and Atmospheric Administration and the American Petroleum Institute [6, 22].	13
Figure 1-3. A compound in oil ( $C$ ) becoming oxidized ( $C_{ox}$ ) via indirect photolysis. A sensitizer ( $S$ ) absorbs sunlight and enters an excited singlet state ( $^1S^*$ ). The sensitizer can react with oxygen to form reactive oxygen species (ROS), which can then oxidize $C$ . Through intersystem crossing, the $^1S^*$ can enter the triplet state ( $^3S^*$ ), which can directly oxidize $C$ or can react with oxygen, to form singlet oxygen ( $^1O_2$ ). Singlet oxygen can then oxidize $C$ . Figure adapted from Schwarzenbach <i>et al.</i> [87].	48
Figure 2-1. Schematic diagram of the evaporation chamber in temperature-controlled incubator. See Section 2.2.2 for detailed description.	71
Figure 2-2. Total ion chromatogram for diesel fuel. The bottom trace is an expanded portion of the chromatogram, showing the region where more volatile compounds are observed.	83
Figure 2-3. Extracted ion chromatogram of $m/z$ 57 for diesel fuel. The bottom trace is an expanded portion of the chromatogram, showing the region where more volatile compounds are observed. The peak numbers correspond to the compounds listed in Table 2-2.	84
Figure 2-4. Extracted ion chromatogram of $m/z$ 83 for diesel fuel. The bottom trace is an expanded portion of the chromatogram, showing the region where more volatile compounds are observed. The peak numbers correspond to the compounds listed in Table 2-2.	85
Figure 2-5. Extracted ion chromatogram of $m/z$ 91 for diesel fuel. The bottom trace is an expanded portion of the chromatogram, showing the region where more volatile compounds are observed. The peak numbers correspond to the compounds listed in Table 2-2.	86
Figure 2-6. Extracted ion chromatogram of $m/z$ 105 for diesel fuel. The bottom trace is an expanded portion of the chromatogram, showing the region where more volatile compounds are observed. The peak numbers correspond to the compounds listed in Table 2-2.	87

Figure 2-7. Extracted ion chromatogram of  $m/z$  117 for diesel fuel. The bottom trace is an expanded portion of the chromatogram, showing the region where more volatile compounds are observed. The peak numbers correspond to the compounds listed in Table 2-2. .... 88

Figure 2-8. Extracted ion chromatogram of  $m/z$  128 for diesel fuel. The bottom trace is an expanded portion of the chromatogram, showing the region where more volatile compounds are observed. The peak number corresponds to the compound listed in Table 2-2. .... 89

Figure 2-9. Total ion chromatograms of diesel fuel evaporated at 20 °C for 0 – 300 h. For reference, selected  $n$ -alkanes are labeled by carbon number.  $n$ -Heneicosane ( $C_{21}$ ) was used for normalization (\*). .... 96

Figure 2-10. Residual abundances of  $n$ -octane (a),  $n$ -decane (b),  $n$ -dodecane (c), and  $n$ -tetradecane (d) as a function of evaporation time normalized to the peak height of  $n$ -heneicosane in the EIC at  $m/z$  57. Linear regression equations:  $n$ -octane:  $C_t = 0.448 * \exp(-2.26 * 10^{-1} * t)$ ,  $R^2 = 0.980$ ,  $F = 3882$ ;  $n$ -decane:  $C_t = 5.926 * \exp(-2.01 * 10^{-2} * t)$ ,  $R^2 = 0.982$ ,  $F = 4359$ ;  $n$ -dodecane:  $C_t = 10.475 * \exp(-2.20 * 10^{-3} * t)$ ,  $R^2 = 0.807$ ,  $F = 330$ ;  $n$ -tetradecane:  $C_t = 9.276 * \exp(-0.00 * 10^0 * t)$ ,  $R^2 = 0.000$ ,  $F = 0$ . The rate constant,  $k$ , is underlined in each equation. .... 97

Figure 2-11. A chromatogram of unevaporated diesel fuel showing the compounds with decay curves corresponding to  $>5 \tau$  (blue),  $5 - 1 \tau$  (yellow),  $1 - 0.5 \tau$  (red), and  $<0.5 \tau$  (green). 101

Figure 2-12. The coefficient of determination (a) F-statistic (b), and relative standard deviation for each compound *versus* the number of tau ( $\tau$ ) in the decay curve. The inset in a shows an expanded region, from 0 –  $5\tau$ . .... 103

Figure 2-13. Natural logarithm of evaporation rate constant ( $\ln(k)$ ) *versus* boiling point for normal alkanes (a). Linear regression equation:  $y = -5.09 * 10^{-2} * x + 18.83$ ,  $R^2 = 0.999$ ,  $n = 5$ . Natural logarithm of evaporation rate constant ( $\ln(k)$ ) *versus* boiling point for all selected compound classes (b): normal alkanes (■), branched alkanes (●), alkyl benzenes (◆), and polycyclic hydrocarbons (▲). Linear regression equation:  $y = -4.51 * 10^{-2} * x + 16.71$ ,  $R^2 = 0.961$ ,  $n = 23$ . Compound with the \* indicates naphthalene, which sublimates and likely contains large error in the boiling point. Boiling point *versus* chromatographic retention index on HP-1MS stationary phase (c). Linear regression equation:  $y = 2.33 * 10^{-1} * x + 213.2$ ,  $R^2 = 0.991$ ,  $n = 23$ . .... 107

Figure 2-14. Natural logarithm of evaporation rate constant ( $\ln(k)$ ) *versus* chromatographic retention index on HP-1MS stationary phase for all selected compound classes: normal alkanes (■), branched alkanes (●), alkyl benzenes (◆), and polycyclic hydrocarbons (▲). The linear regression of each model is shown: normal alkanes (green), branched alkanes (blue), alkyl benzenes (red), polycyclic hydrocarbons (purple), and comprehensive (black). The regression equations are shown in Table 2-5.

Figure 2-15. Natural logarithm of evaporation rate constant ( $\ln(k)$ ) *versus* chromatographic retention index on HP-1MS stationary phase for all compound classes: normal alkanes (■), branched alkanes (●), alkyl benzenes (◆), and polycyclic hydrocarbons (▲). Linear regression equation:  $y = -1.04 * 10^{-2} * x + 6.70$ ,  $R^2 = 0.981$ ,  $n = 51$ . 113

Figure 2-16. Natural logarithm of evaporation rate constant ( $\ln(k)$ ) *versus* corrected chromatographic retention index on HP-1MS stationary phase for all selected compound classes: normal alkanes (■), branched alkanes (●), alkyl benzenes (◆), and polycyclic hydrocarbons (▲). The linear regression of each model is shown: normal alkanes (green), branched alkanes (blue), alkyl benzenes (red), polycyclic hydrocarbons (purple), and comprehensive (black). 117

Figure 2-17. Natural logarithm of evaporation rate constant ( $\ln(k)$ ) *versus* corrected chromatographic retention index on HP-1MS stationary phase for all compound classes: normal alkanes (■), branched alkanes (●), alkyl benzenes (◆), and polycyclic hydrocarbons (▲). Linear regression equation:  $y = -1.05 * 10^{-2} * x + 6.71$ ,  $R^2 = 0.990$ ,  $n = 51$ . 118

Figure 2-18. Total ion chromatogram of diesel fuel with the fraction remaining at each retention index (red dashed line) for evaporation at 20 °C for 100 h. 122

Figure 2-19. Total ion chromatogram for kerosene (a) and marine fuel stabilizer (b). The peak numbers correspond to the compounds listed in Table 2-2. 131

Figure 3-1. Representative total ion chromatograms of diesel samples prior to evaporation and after evaporation for 300 h at 5 – 35 °C. Even-numbered normal alkanes are labeled for reference. 155

Figure 3-2. Natural logarithm of evaporation rate constant ( $\ln(k)$ ) *versus* retention index for selected compounds. Linear regression equations: 5 °C (×)  $y = -1.12 * 10^{-2} * x + 6.78$ ,  $R^2 = 0.987$ ,  $n = 42$ ; 10 °C (■),  $y = -1.05 * 10^{-2} * x + 6.17$ ,  $R^2 = 0.982$ ,  $n = 46$ ; 20 °C (▲),  $y = -1.05 * 10^{-2} * x + 6.71$ ,  $R^2 = 0.990$ ,  $n = 51$ ; 30 °C (◆),  $y = -1.02 * 10^{-2} * x + 7.35$ ,  $R^2 = 0.995$ ,  $n = 58$ ; 35 °C (●),  $y = -1.00 * 10^{-2} * x + 7.62$ ,  $R^2 = 0.993$ ,  $n = 61$ . 209

Figure 3-3. The temperature profile (a) of the fluctuating evaporation experiment with the temperature recorded every two minutes (solid line) and as a running average temperature (dashed line). The temperatures at 5-h intervals (circles) and 12-h intervals (stars) are also shown. The fraction of fuel remaining (b) calculated using the variable temperature model using the temperature at 2 min intervals (solid line) 5-h intervals (circles), 12-h intervals (stars), and running average temperature (dashed line). The percent fuel remaining is shown in Table 3-18. 218

Figure 3-4. The fraction remaining curve (a) predicted using the variable temperature model, using the average temperature (17.1 °C) during the fluctuating temperature experiment (100 h). Also shown are chromatograms of diesel fuel (normalized to heneicosane), unevaporated (b), predicted by multiplying the unevaporated

chromatogram (b) by the fraction remaining curve (a), and the actual chromatogram of diesel fuel after the fluctuating temperature experiment (d). ..... 222

Figure 3-5. A chromatogram of diesel fuel prior to evaporation (a) and after 100 h evaporation at 20 °C (b). In part b, the solid black chromatogram represents the experimentally evaporated fuel, while the red dashed line represents the predicted distribution of compounds, using the variable temperature model. The numbers correspond to peak numbers given in Table 3-1. .... 226

Figure 3-6. A chromatogram of kerosene prior to evaporation (a) and after 100 h evaporation at 20 °C (b). In part b, the solid black chromatogram represents the experimentally evaporated fuel, while the red dashed line represents the predicted distribution of compounds, using the variable temperature model. The numbers correspond to peak numbers given in Table 3-1. .... 227

Figure 3-7. A chromatogram of marine fuel stabilizer prior to evaporation (a) and after 100 h evaporation at 20 °C (b). In part b, the solid black chromatogram represents the experimentally evaporated fuel, while the red dashed line represents the predicted distribution of compounds, using the variable temperature model. The numbers correspond to peak numbers given in Table 3-1. .... 228

Figure 3-8. The Pearson product-moment correlation (PPMC) coefficients between a chromatogram of diesel fuel evaporated on water for 100 h at 20 °C and the predicted evaporation chromatogram, based on the variable-temperature model for 0 – 1000 h tested at 1-h intervals. The PPMC coefficient maximized at 117 h (0.9986), with values greater than 0.998 from 89 – 151 h. .... 233

Figure 3-9. The predicted fraction remaining, using the variable-temperature model (Equation 10), over 10,000 h (approximately 1 year) at an average temperature of 20 °C. 234

Figure 4-1. A diagram depicted the solar simulator used for irradiation. A commercially available xenon light source was utilized along with several plano-convex lens to homogenize the beam. A beam turner redirected the beam from the source to the sample. The sample was placed on an aluminum block, connected to a circulating water bath to maintain constant temperature. The sample and block were housed inside a Plexiglas box with a hole in the top to allow light to pass. Two filters (KG2) were placed over the hole to reduce the infrared light reaching the sample. A ray tracing is shown as the red dashed line. .... 246

Figure 4-2. A diagram showing how uniformity was measured. The irradiated sample was contained in a petri dish (dashed line, diameter ~5.5 cm). Intensity measurements were taken at the points where the grid lines intersect. .... 248

Figure 4-3. A spectrum of the sun [7] (black dotted line) compared to the spectrum of a xenon light source (dashed blue line) and the xenon light source with 2 KG2 filters (solid red line) (a). The same spectra are shown in b, but all were collected using the same spectrometer. The spectra were normalized to the average intensity between 500 – 550

nm. The spectral irradiance of the sun and the xenon source with the 2 KG2 filters is shown in part c. .... 250

Figure 4-4. Total ion chromatograms (a) and extracted ion chromatograms (b) of  $m/z$  216 of diesel fuel irradiated for 0 – 10 h as well as a 10 h dark control. In the total ion chromatogram the even numbered normal alkanes are labeled for reference. The peaks at 34.39 min and 34.77 min correspond to methyl pyrenes. .... 258

Figure 4-5. The output from mass spectrometry analysis of diesel fuel. An example TIC chromatogram (a) is representative of all chromatograms indicating the region over which the spectra were averaged (red line). The mass spectrum prior to irradiation (b) and after irradiation for 10 h (c) and the 10 hour dark control (d) are also shown. Quinoline-d7 (\*) was used at the lock mass. The formulas for each mass is in Table 4-2 and Table 4-3. .... 264

Figure 4-6. The Kendrick mass defect *versus* the nominal mass for an unirradiated diesel sample (a). Compounds in a horizontal row have the same double bond equivalence (DBE) and differ by 14 Da, indicating a difference in one methylene group. Compounds in a diagonal line, indicate the same number of carbon atoms, and differ by 2 Da, indicating a difference in 2 hydrogen atoms. The Kendrick mass defect *versus* the nominal mass for the unirradiated diesel fuel (large red circles) overlaid with the 10 hour dark control (small black circles) (b), and the 10 hour irradiated sample (small black diamonds) (c). .... 269

Figure 4-7. The PCA scores plot (a) and loadings plot (b) for samples irradiated for 0 h (●), 1 h (■), 2 h (◆), 4 h (▲), 6 h (+), 8 (▼), and 10 h (◆). .... 272

Figure 4-8. Decay and formation curves for various compounds. The regression equation is shown and the first order rate constant is underlined. From the GC-MS analysis: methyl pyrene (a) (retention time 34.77 min,  $y = 0.033 * \exp(-0.243 * t)$ ). From the HR-MS analysis: C<sub>16</sub>H<sub>19</sub> (b) ( $m/z$ : 211.15,  $y = 1.840 * \exp(-0.205 * t)$ ), C<sub>13</sub>H<sub>17</sub>O<sub>1</sub> (c) ( $m/z$ : 189.13,  $y = 6.291 * \exp(-0.0165 * t)$ ), C<sub>18</sub>H<sub>21</sub>O<sub>2</sub> (d) ( $m/z$ : 269.15,  $y = 0.097 * \exp(-0.045 * t)$ ). .... 275

Figure 4-9. The rate constant for decay (a) and formation (b) of selected compounds *versus* the mass of the compound. Compounds are classified based on the number of double bond equivalences (4: red, 5: orange, 6: yellow, 7: light green, 8: dark green, 9: light blue, 10: dark blue, 11: purple) and number of oxygens (0: ●, 1: ▲, 2: ■). .... 296

Figure 4-10. An infrared spectrum of the precipitate formed from diesel after 10 hours of irradiation. Several peaks are labeled for reference. .... 299

Figure 4-11. The mass spectrum of the precipitate formed from diesel fuel after 10 h of irradiation. The peak marked with “x” at 391.28 is from a phthalate and is present in the blank. It was used as a lock mass in this analysis. .... 300

# 1. Introduction

## 1.1 Petroleum Release into the Environment

Petroleum and petroleum products have become a major part of everyday life, with over 18.5 million barrels of oil used each day in the United States [1]. Due to this widespread use of petroleum, there are unintentional releases of petroleum and petroleum products into the environment. Each year, an estimated 380,000,000 gallons of petroleum and petroleum products are released into the environment by natural seeps and through man-made activities [2]. The release by natural seeps accounts for approximately 45% of the oil released worldwide, but these releases are slow and distributed over a wide range of locations. As a result, contamination levels at most locations are low, which allows local environments to adapt in part through physical and chemical processes that disperse and degrade petroleum constituents [2-4]. The remaining oil released into the environment (over 200,000,000 gallons) results from human activities, and many of which are accidental spills. These spills can occur at various points during distribution, including the extracting, transporting, and consuming phases [2]. Oil spilled during extraction accounts for approximately 5% of oil spills worldwide, while transport accounts for approximately 25%. Activities related to consumption of oil and oil products account for the remaining 70% of the oil released into the environment worldwide [2].

These releases can have a devastating effect on the surrounding environment for years after the release [2, 5, 6]. Many of the components in oil are toxic to plant and animal life, and exposure can result in acute and chronic problems [2, 5]. In addition to

ecological impacts, oil spills often have a devastating impact on the local economy [5, 7], particularly when commercial fishing or agricultural production is reduced. These activities usually do not resume until the risks of exposure have dwindled to acceptable levels, but there is great uncertainty in predicting when it is safe to resume these activities. Environmental modeling of oil spills provides an important tool to help assess potential health and economic impacts. Modeling the fate and transport of petroleum products can be used to determine exposure risks, direct remediation, and mitigate disruption to commercial activities [5]. More about modeling the fate of petroleum products will be discussed in Section 1.6

## **1.2 Petroleum Composition**

Crude oil was formed from the incomplete decay of organic material, primarily algae, archaea, bacteria, and zooplankton that inhabited aquatic environments. These dead organisms settled and were covered by sediment, which compressed and trapped it. When elevated pressures were accompanied by elevated temperatures for millions of years, crude oil was formed from chemical transformations and physical migration through rock [8-10]. Each deposit of oil experienced different temperatures and starting material, therefore each oil has specific properties including viscosity, specific gravity, and vapor pressure which generated specific markers that can be used to identify the source and influence the fate of the oil after a spill [5, 9, 11].

### *1.2.1 Composition of Crude Oil*

Crude oil consists mostly of hydrocarbons, but also has oxygen-, sulfur-, and nitrogen-containing compounds, as well as trace amounts of metals [8, 9]. Using gas

chromatography-mass spectrometry (GC-MS), more than 300 different compounds were identified in crude oil [12, 13]. Using high-resolution mass spectrometry, elemental formulas for over 17,000 unique petroleum constituents have been assigned [14].

There are four major classes of compounds found in crude oil: alkanes, aromatic hydrocarbons, resins, and asphaltenes (Table 1-1). The alkane class contains hydrocarbons that are bonded through covalent  $\sigma$  bonds. This class comprises 25 – 90 percent of the composition of most crude oils (Table 1-2) and this group can be further sorted into sub-classifications as normal alkanes, branched alkanes, and cyclic alkanes. The normal alkanes are defined as those hydrocarbons with straight saturated alkyl chains. In crude oils, the chain lengths of normal alkanes typically range from *n*-pentane (*n*-C<sub>5</sub>) to *n*-tetracontane (*n*-C<sub>40</sub>). Branched alkanes are structural isomers of the normal alkanes, consisting of the same chemical formula, but with branching rather than a linear arrangement of carbons. The branched alkanes reflect different biosynthetic origins than the linear alkanes. Cyclic alkanes are characterized by the presence of a ring. Crude oils typically contain five- or six-membered aliphatic rings with 1 – 14 alkyl substitutions [9, 11]. Terpanes and steranes usually have three six-membered rings with either an additional six-membered (terpanes) or a five-membered (steranes) ring. Alkenes and alkynes, which are related to alkanes, are rarely found in petroleum.

Table 1-1. Common defined compound classes found in crude oil. For each class, several example compounds are listed. The example structure is of the bolded example compound.

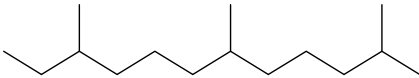
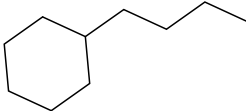
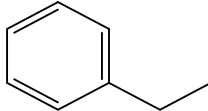
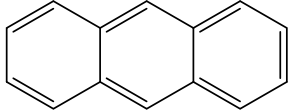
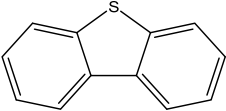
Class	Example Compounds	Example Structure
<b>Alkane</b>		
Normal	<b>Decane (C<sub>10</sub>H<sub>22</sub>)</b>	
	Pentadecane (C <sub>15</sub> H <sub>32</sub> )	
	Eicosane (C <sub>20</sub> H <sub>42</sub> )	
Branched	<b>2,6,10-Trimethyldodecane (C<sub>15</sub>H<sub>32</sub>)</b>	
	Phytane (C <sub>20</sub> H <sub>42</sub> )	
Cyclic	<b>Butylcyclohexane (C<sub>10</sub>H<sub>20</sub>)</b>	
	Cyclopentane (C <sub>5</sub> H <sub>10</sub> )	
<b>Aromatic</b>		
BTEX	<b>Ethylbenzene (C<sub>8</sub>H<sub>10</sub>)</b>	
	1,3,5-trimethylbenzene (C <sub>9</sub> H <sub>12</sub> )	
PAH	<b>Anthracene (C<sub>14</sub>H<sub>10</sub>)</b>	
	Tetralin (C <sub>10</sub> H <sub>12</sub> )	
	Pyrene (C <sub>16</sub> H <sub>10</sub> )	
<b>Polar Compounds</b>		
Resins	<b>Dibenzothiophene (C<sub>12</sub>H<sub>8</sub>S)</b>	
	Carbazole (C <sub>12</sub> H <sub>9</sub> N)	
	Dibenzofuran (C <sub>12</sub> H <sub>8</sub> O)	
Asphaltenes	No defined formula	Varies: contains heteroatoms, aromatic and alkane portions

Table 1-2. Selected properties of petroleum and petroleum products.

	Crude Oil		Refined Product			
	Light Crude	Heavy Crude	Gasoline	Diesel	Intermediate Fuel oil	Bunker Oil
% Composition <sup>1</sup>						
Alkane	55 – 90	25 – 80	50 – 60	65 – 95	25 – 35	20 – 30
Aromatic	10 – 35	15 – 40	25 – 40	5 – 25	40 – 60	30 – 50
Polar	1 – 15	5 – 40	0	0 – 2	15 – 25	10 – 30
% Distilled <sup>2</sup>						
100 °C	2 – 15	1 – 10	70	1	-	-
200 °C	15 – 40	2 – 25	100	30	2 – 5	2 – 5
300 °C	30 – 60	15 – 45	-	85	15 – 25	5 – 15
400 °C	45 – 85	25 – 75	-	100	30 – 40	15 – 25
Residual	15 – 55	25 – 75	-	-	60 – 70	75 – 85
°API Gravity	30 – 50	10 – 30	65	35	10 – 20	5 – 15
Density (g/mL @ 15 °C)	0.78 – 0.88	0.88 – 1.00	0.72	0.84	0.94 – 0.99	0.96 – 0.104
Viscosity (cSt)	5 – 50	50 – 50000	0.5	2	1000 – 15000	10000 – 50000

1. Adapted from Fingas [11].

2. Adapted from Wang *et al.* [9].

Aromatic compounds contain at least one benzene ring, which is a six-membered ring with three delocalized  $\pi$  bonds (Table 1-1). This class comprises 10 – 40 percent of the composition of crude oils (Table 1-2) and can be further classified as benzene, toluene, ethylbenzene, and xylene (BTEX) or polycyclic aromatic hydrocarbons (PAHs). BTEX compounds contain a single benzene ring with alkyl substitutions. In crude oils, PAHs typically contain between 2 – 6 rings and contain multiple alkyl substitutions [5, 9]. BTEX and PAHs are of great concern when released into the environment owing to their toxicity and carcinogenic potential [9]. BTEX compounds are more volatile and pose a greater risk to first responders. PAHs pose a greater long-term risk, because they are more carcinogenic and less volatile, and therefore more persistent in the environment [2].

Resins are a large group of polar molecules containing a heteroatom, such as nitrogen, oxygen, or sulfur (Table 1-1). These polar compounds are responsible for the adhesion observed in crude oil [11]. Resins make up a relatively small amount of crude oils, often ranging from 2 – 20 % (Table 1-2) [9]. Sulfur-containing resins account for 0.1 – 6% of crude oil, while the oxygen- and nitrogen-containing resins account for 0.1 – 3% [9]. Another group of polar molecules is defined as asphaltenes, which are compounds with minimal solubility in hydrocarbon solvents. These compounds are not dissolved in the crude oil, rather exist as colloidal suspensions in the oil. The exact formulas and compositions of asphaltene constituents are largely unknown, but are estimated to have masses ranging from several hundred to over 5000 g/mol when they are aggregated together.

Crude oil is typically classified as either light or heavy crude. Heavy crude oil is defined as having an American Petroleum Institute gravity ( $^{\circ}$ API) above 30 $^{\circ}$ . The API

gravity is calculated based on the relative density (*RD*) of the oil compared to water at 60 °F.

$$^{\circ}API = \frac{141.5}{RD} - 131.5 \quad \text{Equation 1-1}$$

The °API gravity scale for oils typically ranges from 10 – 70° and varies inversely with the density of the oil. Heavy crude oil, which typically is found in oil sands, has a higher abundance of resins and asphaltenes, resulting in the oil being more viscous (Table 1-2) and requiring additional refining before use as transportation fuels [9]. The °API gravity is often readily available for each crude oil and is, therefore, commonly used in environmental models as a predictor of physical properties.

### 1.2.2 Refined Petroleum Products

Crude oil is refined into a number of more useful petroleum products for distribution and consumption, with a wide range of physical properties, depending on the use. Fractional distillation is used to separate crude oil into five to seven fractions, based on boiling point. A sample distillation curve, showing the volume of petroleum distilled at each temperature, is shown in Figure 1-1. Distillation curves are often utilized to predict physical properties for modeling the fate and transport of the oil during an environmental release. However, distillation curves are far less widely available than °API gravity. When available, distillation data provides more accurate prediction of properties for environmental models [15].

After distillation, some fractions are used as is, while other fractions undergo additional distillation or chemical conversion. Chemical conversion breaks down large

molecules or rearranges molecules to produce compounds with a desired set of properties including volatility and speed of ignition. Catalytic cracking is one of the most common chemical conversions, which, with the help of a catalyst, breaks apart large molecules, increasing their volatility [8]. The chemical composition of the refined product can vary greatly based on the starting material, differences in the refining process, and blending of the fuels [16, 17]. Common refined petroleum products include gasoline, kerosene, diesel fuel, and heating oils. Common distillation temperature ranges (Table 1-3) and physical properties (Table 1-2) are shown for selected petroleum products [9, 11]. Fractions distilled at lower temperatures are more volatile (e.g. gasoline), and less dense and less viscous. These fractions tend to evaporate very quickly and will pose little environmental hazard. Fractions distilled at higher temperature are less volatile and will be more persistent in the environment (e.g. diesel fuel). Fractions distilled at the highest temperatures (e.g. bunker oil) are viscous and dense, which can cause the fuel to sink in water. These fractions are persistent in the environment and can pose a challenge during remediation [2].

### *1.2.3 Composition of Diesel Fuel*

Diesel fuel, which was the primary sample used in the research described in subsequent chapters, consists mostly of alkanes (65 – 95 %), but also contains up to 25% aromatic compounds and up to 2% resins (Table 1-2). The compounds in diesel fuel also have a wide range of boiling points (~100 – 400 °C), encompassing volatile and nonvolatile compounds. Depending on the starting material, diesel fuel is produced

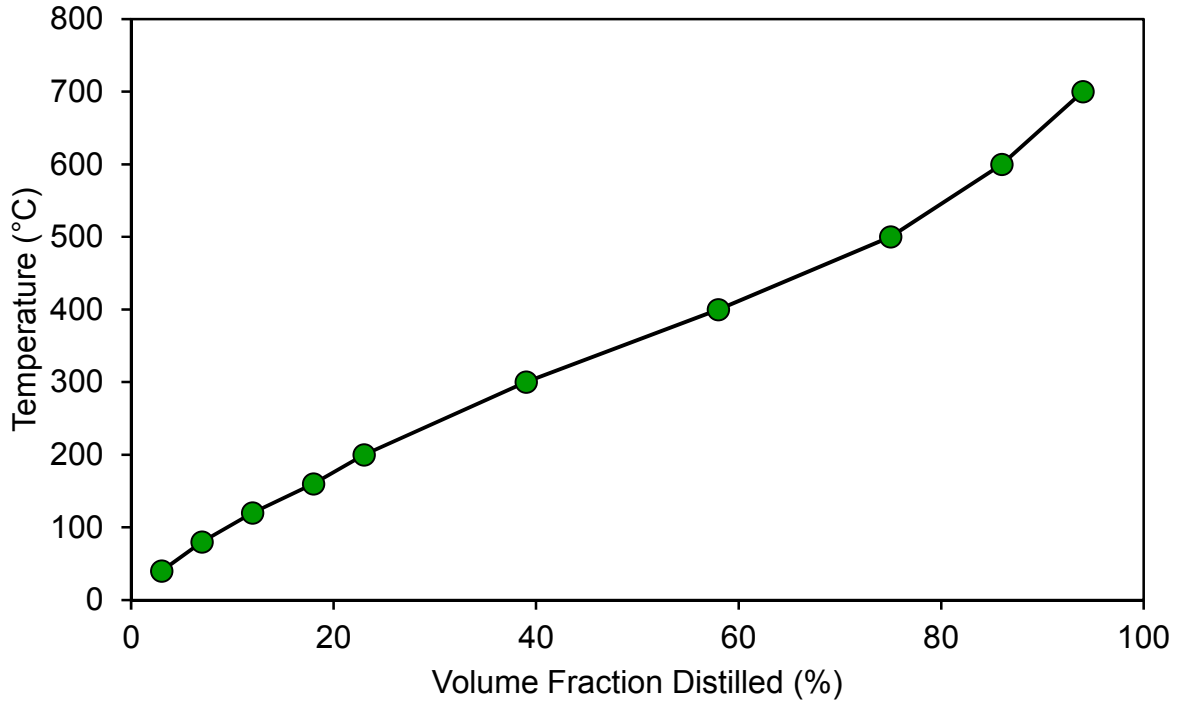


Figure 1-1. Sample distillation curve of Alaska North Slope oil (southern pipeline). Distillation data from National Oceanic and Atmospheric and Administration's ADIOS 2 modelling program [18].

Table 1-3. Distillation temperature and carbon range for typical petroleum products [10, 11].

Petroleum Product	Distillation Temperature (°C)	Carbon Range
Liquefied Petroleum Gas	< 30	1 – 4
Petroleum ether	20 – 60	5 – 6
Ligroin	60 – 100	6 – 7
Gasoline	40 – 205	5 – 10
Jet Fuel	105 – 265	8 – 14
Kerosene	175 – 315	10 – 16
Diesel fuel	170 – 400	9 – 24
Gas Oil	>275	12 – 70
Bunker Oil	>365	20 – 70
Lubricating Oil	Nonvolatile (liquid)	variable
Asphalt / coke	Nonvolatile (solid)	variable

directly after fractional distillation or may be blended with other products after chemical conversion. For example, diesel fuel is often blended with more volatile fractions, such as kerosene or jet fuel, to lower the gel point for use in cold weather. This is typically referred to as winter diesel. Diesels that are not blended with a more volatile fraction are summer diesels [17]. Before distribution, diesel fuel is treated to remove sulfur, in order to comply with ultra-low sulfur regulations (<15 ppm) [17]. Other compounds containing heteroatoms are removed in this process and are generally present at low ppm levels [19]. While the starting material and refining can result in a variable chemical composition for diesel fuel, diesel specifications are tightly regulated [20]. Diesel fuel is often blended with additives such as antioxidants (e.g. 2,4-dimethyl-1-6-t-butyl phenol) and ignition improvers (e.g. isopropyl nitrate) that could be present during an analysis [17].

### **1.3 Oil Spill Weathering**

After an environmental release of a petroleum product, the oil begins undergoing physical, chemical, and biological weathering almost immediately. The physical properties of the fuel as well as the extent of weathering play important roles in predictions of the environmental fate and impact of an oil spill [5, 21]. As the oil is weathered, the density and viscosity change. In some cases, the viscosity of an oil can increase by an order of magnitude in the first twenty-four hours and an increase in density can result in the residual oil sinking in water [6]. Weathering also plays an important role in remediation. Chemical dispersants, for example, are typically most effective for oils with low viscosities, so they should be applied before the oil becomes too viscous. The weathering processes that occur are dependent on the type of oil that has been spilled,

the location of the spill (on land, in fresh water, in salt water), the temperature, and many other environmental factors [21, 22].

The most common weathering processes are shown in Figure 1-2. Most weathering processes described in the figure are physical weathering processes with the exception of photooxidation, which is a chemical weathering process, and biodegradation, which is a biochemical weathering process. Each of these weathering processes will be discussed in more detail in the following sections.

### *1.3.1 Physical Weathering Processes*

#### 1.3.1.1 Evaporation

Evaporation is the process of the volatile components at the surface of the oil escaping and entering the vapor phase, leaving behind the heavier, less-volatile components [5, 23, 24]. Evaporation is typically the most dominant weathering process; it begins immediately after a spill and can continue throughout the oil spill cleanup [6, 15, 25]. Most material losses due to evaporation occur within the first few days [2, 22]. Evaporation can account for 100% of the mass lost in refined fuels, such as gasoline, to as little as 5% of the mass lost in the heavier Bunker C oil [2, 15]. For typical crude oil, the mass lost due to evaporation ranges from 40 – 75% [2, 22]. The rate of evaporative mass loss is dependent on temperature (including air and water temperature, as well as solar heating) and the composition of the fuel [6, 22]. Some debate still exists whether evaporation is dependent on surface area and wind speed [2, 26]. This will be discussed

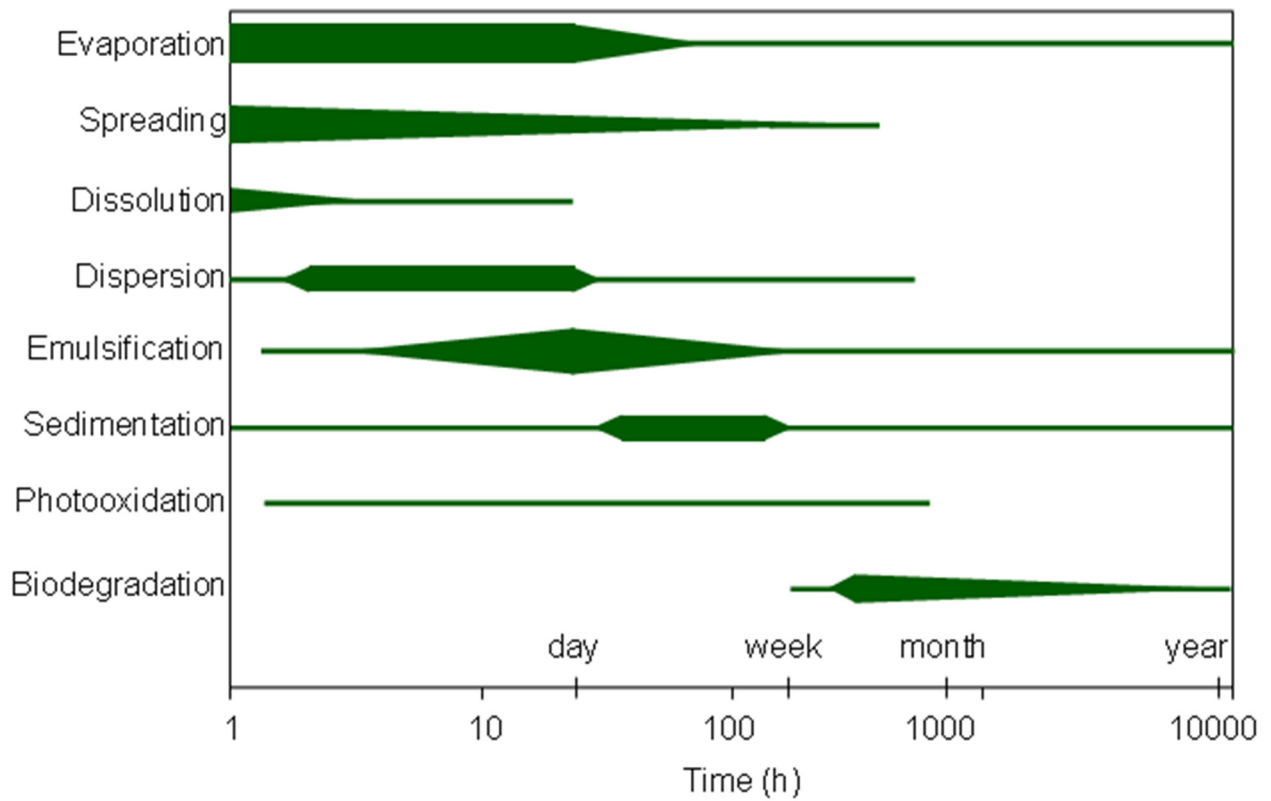


Figure 1-2. Different weathering processes effecting a petroleum release in the environment. The thickness of the line indicates the contribution of weathering process. Figure adapted from National Oceanic and Atmospheric Administration and the American Petroleum Institute [6, 22].

in more detail in Section 1.6.2. Evaporation has the greatest effect on many physical properties of fuels, including density and viscosity. By the removal of the small, volatile component, the remaining fuel is more dense and viscous [5, 6]. Evaporation can also affect the toxicity of the fuel. Many of the compounds considered to be the most toxic to aquatic life, typically the BTEX and naphthalene compounds, are removed by evaporation [22] and may undergo photodegradation in the atmosphere. PAHs are more toxic, but are less water soluble and have lower bioavailabilities than BTEX compounds, resulting in a decreased acute toxicity for PAHs in the aquatic environment [27].

#### 1.3.1.2 Spreading

Spreading is the horizontal movement of the oil on water, due to gravity, currents, and wind, producing the characteristic oil slick [21, 22]. The spreading is slowed by increasing viscosity of the oil [26]. Oils with low viscosity form thin layers on water (~0.01 mm), while more viscous oils have greater thicknesses (~1 mm) [15, 22, 28]. After forming, these slicks can move with the wind and currents [21]. Wave action can break slicks into multiple smaller slicks over time [29]. The spreading of the oil begins immediately after a spill and can continue throughout the course of the spill [22].

#### 1.3.1.3 Dissolution

Dissolution describes the dissolving of water-soluble components of oil into the water layer, creating an underwater oil slick [15]. The BTEX compounds are the most water-soluble and, due to their toxicity, the most dangerous to aquatic life [6]. These compounds also are volatile and, therefore, may quickly evaporate from the spill zone [27]. As a result, dissolution accounts for only a small amount (0 – 5 %) of mass loss

from an oil spill [15, 22]. The rates of mass loss caused by dissolution depends on the temperature, chemical composition of the spill, the solubilities of the compounds in water, and the surface area [22, 27].

#### 1.3.1.4 Emulsification

Emulsification describes the process of a liquid being dispersed within another immiscible liquid, forming small droplets. These droplets are typically formed through wave action in the ocean [5]. Formation of emulsions increases the density and viscosity of the oil, slows most other weathering processes, and increases the total volume of the spill [2, 22], which hampers remediation [5]. The major factor that affects emulsification is the wave energy, which causes the oil and water emulsions to form [22].

#### 1.3.1.5 Natural Dispersion

Dispersion describes the formation and transport of suspended oil droplets in water [2, 6, 22]. These droplets are formed through wave action and can then be spread both vertically and horizontally in the water column [2, 22, 29]. Dispersion is a significant weathering process accounting for 10 – 60% of the mass loss of a spill [22]. Rates of dispersion depend on the wave action, as well as the properties of the oil and rates of other weathering processes [26]. Dispersed oil will often dissolve into the water and biodegrade more rapidly than emulsions or surface slicks due to the high surface area-to-volume ratio in the small droplets [6].

#### 1.3.1.6 Sedimentation

Sedimentation occurs when oil droplets adhere to sediments in the seawater or from the shore and become denser than water and sink. Oil droplets can also be ingested

by aquatic organisms, which excrete the oil in fecal matter [6, 22]. Sedimentation typically occurs with resins and asphaltenes and can make up 10% of the mass lost during a spill. The oil sediment can be harmful to aquatic organisms and can remain in the environment for decades [15].

### *1.3.2 Chemical Weathering: Photooxidation*

Photooxidation describes the oxidation of compounds in oil by sunlight. Chromophores in the oil and seawater absorb ultraviolet and visible radiation from the sun, and react to form oxidized products including alcohols, ketones, and carboxylic acids [2]. These oxidized products are more polar and water-soluble than their precursors, which can lead to increased dispersion after photooxidation [30]. Photooxidation alters the physical properties of the fuel and results in the formation of more toxic compounds [2, 22]. Photooxidation is not believed to account for much of the mass lost during weathering, but the formation of toxic compounds makes photooxidation an important weathering process. In addition, photooxidation can convert larger molecules, which resist evaporation, dissolution, and biodegradation, into molecules that are more readily degraded [31]. For remediation, photo-catalysts such as titanium dioxide are added to the oil to encourage photo-degradation [31]. The extent of photooxidation depends on levels of exposure to sunlight and the presence of chromophores and quenchers in the environment. There will be more discussion of photooxidation in Section 1.6.3.

### *1.3.3 Biological Weathering: Biodegradation*

Biodegradation is the degradation of oil by organisms, mostly bacteria and fungi, breaking the compounds in oil into oxidized products or carbon dioxide and water if the

process proceeds to completion [22]. There are multiple enzymatic pathways for biodegradation, and complete degradation of complex compounds, such as PAHs, likely requires several different organisms [2, 32]. Normal alkanes have been shown to be the most readily degraded, while PAHs and resins typically take much longer [32]. Biodegradation is considered to be a major source of the mass loss during weathering, however it is a slow process [15, 22]. Many factors affect rates of microbial degradation including the organisms that are present, temperature, oxygen availability, nutrients in the seawater, and the properties of the oil [2, 22].

#### **1.4 Analytical Strategies for Characterization of Crude Oil and Petroleum Products**

Many analytical techniques have been applied to the analysis of crude oil and petroleum products [33]. However, no single technique has yet to provide a complete analysis of oil, due to its complexity, and complementary techniques are necessary to investigate the wide range of compounds. The number of compounds estimated to be present in crude oil is 10,000 – 100,000, with a large range in mass and heteroatom containing compounds [34]. Some techniques, such as infrared and ultraviolet spectroscopy are not sufficiently specific for individual compound identification, but are useful in screening for certain classes of compounds or functional groups. Other methods, such as mass spectrometry, are more specific and allow for the identification of individual compounds [9]. Several of the most common instrumental techniques for petroleum analysis are highlighted, which will provide insight into the need for complementary techniques for the comprehensive analysis of petroleum.

### 1.4.1 Gas Chromatography

Gas chromatography (GC) has been the most common method for analysis of petroleum. The GC is often coupled with a flame ionization detector (FID) or mass spectrometer (MS) detector [9, 12, 13, 16, 35, 36]. Chromatography is used to separate compounds in the complex mixture so they do not all arrive at the detector at the same time. When GC is coupled to MS (GC-MS), the chromatographic separation provides high separation efficiency, after which the analytes are ionized in the mass spectrometer. This process may yield both molecular and fragment ions, and the masses of these ions are helpful for analyte identification based on the mass-to-charge ( $m/z$ ) ratios of the ions [9, 37]. In order to improve separation peak capacity, two-dimensional GC x GC methods have also been utilized [37-40]. These methods resolve peaks that co-elute in the first GC separation by performing a second, very fast separation using a stationary phase with a different polarity than the first [40]. GC methods offer great advantages, because the separation is fast and simple and can easily be coupled with a mass spectrometer. However, GC analysis is limited to analytes that can partition into the gas phase, so the analyte must be volatile. This corresponds to nonpolar compounds with boiling points up to  $\sim 425$  °C or molar masses up to  $\sim 1200$  Da [41]. In particular, refined petroleum products are well suited for GC-MS analysis, given the boiling point range and the nonpolar nature of hydrocarbons [37, 40].

### 1.4.2 Liquid Chromatography

Another common method for analyzing petroleum is liquid chromatography (LC) [9, 33, 42, 43]. In many cases, the LC system is also coupled to a mass spectrometer, although other detection methods are available [42-44] LC is capable of separating small

and large molecules (over 100,000 Da), but can be complicated by method development, including selection of the mobile phase to achieve selective retention, choice of stationary phase (packing material, particle size, and pore size), and detector [44, 45]. LC is not limited by volatility, making it useful for the analysis of high molecular weight PAHs, resins and asphaltenes [33, 35]. LC is typically useful in analyzing alkanes with greater than 16 carbons and PAHs with 2 – 6 rings.

### *1.4.3 Mass Spectrometry*

Mass spectrometry methods can be coupled to GC, LC, or samples can be directly injected into the MS using flow injection analysis (FIA) [46]. Using mass spectrometry allows for the determination of the molecular or fragment ion masses, which in turn can be used to determine elemental formulas of each if sufficient mass measurement accuracy is available. Additional stages of mass spectrometry ( $MS^n$ ) can be utilized to further fragment the ions, to help elucidate their structures. The single quadrupole mass spectrometer often coupled with GC typically provides low mass resolution ( $m/\Delta m = 2000$ ), yielding only nominal masses (masses accurate to integer values). Assignments of exact elemental formulas require higher mass resolution and mass measurement accuracy. High-resolution mass spectrometers ( $m/\Delta m > 10,000$ ), such as time-of-flight (ToF) and Fourier-transform ion cyclotron resonance mass spectrometry (FT-ICR MS), have allowed for the visualization of previously unresolved masses and the assignments of elemental formulas for a large number of detected analytes [46]. In recent years, these high-resolution mass analyzers have been widely applied to analysis of crude oils, eliciting tens of thousands of unique elemental formulas. This has resulted in the emergence of a sub-discipline known as petroleomics, which applies analytical technique

in efforts to determine comprehensive chemical composition as well as establish physical properties and reactivities of all petroleum constituents [14, 34].

An important consideration that affects the MS analysis is the selection of ionization method [46]. Mass spectrometers measure mass-to-charge ( $m/z$ ) ratios by accelerating ions by application of an electric field. Uncharged molecules do not experience such acceleration, therefore, ionization determines which compounds can be detected [47]. Typically, electron ionization (EI) is used for GC-MS analysis, and it provides universal ionization of all molecules that elute from the GC column. Moreover, using electron ionization facilitates identification because the fragmentation of a compound can be compared to mass spectrum libraries [16, 37, 48]. For less volatile compounds not amenable to GC, electrospray ionization (ESI), atmospheric pressure photoionization (APPI), and atmospheric pressure chemical ionization (APCI) [14, 33, 34, 49-51]. ESI is typically used for compounds with high molecular weights or compounds that have polar (acidic or basic) functional groups. In ESI, compounds are ionized by creating a charged droplet, containing solvent and the compound to be ionized. The solvent is evaporated and the charge is transferred onto the compound. The analyte must have a higher proton affinity than the solvent. Methanol has a proton affinity of approximately 760 kJ/mol. APPI and APCI are preferred for smaller (~1000 Da) and less-polar compounds, and have been less widely applied in the analysis of petroleum than ESI [46, 47]. In APCI, the sample in solution is introduced into the ion source where it is vaporized and a corona discharge is used to ionize the reagent gas. The reagent gas can then transfer the charge to the analyte. At atmospheric pressure there is excess reagent gas, resulting in efficient ionization. In APPI, compounds are ionized using photons.

Polar compounds have higher ionization potentials and are not as well ionized as nonpolar compounds.

The complexity of petroleum requires the use of a range of complementary analytical techniques if comprehensive information is to be generated. While nonpolar, volatile compounds including alkanes and small aromatics are effectively analyzed by GC, larger aromatic compounds as well as the polar and resin fractions lack the volatility needed for GC separation. LC or FIA coupled to MS allows for the analysis of more polar compounds, however most LC-compatible ionization methods will not ionize alkanes. The most polar compounds are more efficiently ionized using ESI, while moderately polar compounds including aromatic hydrocarbons are more effectively ionized using APCI or APPI.

#### *1.4.4 Strategies for Analysis of Diesel Fuel*

In the analysis of diesel fuel, GC-MS is by far the most common instrumental approach because most of the compounds are volatile and have been distilled [37, 52]. However, chromatographic separation by GC cannot resolve all compounds in a mixture as complex as diesel, therefore, many low abundance compounds are obscured by more abundant compounds. In GC-MS analysis, approximately 100 separate peaks have been reported in analyses of diesel fuels [40]. Two-dimensional gas chromatography (GC x GC) has been applied to achieve additional separation [40, 53]. In GC x GC, a mixture is first separated on a column with a nonpolar stationary phase, where the separation is based on boiling point. The eluent is transferred to a second column with a more polar stationary phase, where compounds are separated based on molecular interactions with

the stationary phase. This increases the peak capacity of the analysis, resulting in the observation of over 1000 resolved compounds [40].

While high-resolution instrumentation has been widely applied to crude oils [54, 55], surprisingly, few studies have used these high-resolution instruments with diesel fuel, even though diesel contains polar compounds, which would not be observed by GC. Hughey *et al.* used ESI-FT-ICR-MS to compare the heteroatomic hydrocarbon content during different stages of the refining process of diesel fuel [19]. ESI allowed for efficient ionization of heterocyclic constituents, however, hydrocarbons without a heteroatom were not observed [19]. Rostad and Hostettler utilized ESI in negative ion mode with a quadrupole mass analyzer to identify polar acidic compounds in refined fuels [56], but only heteroatom-containing compounds were observed and therefore, pure hydrocarbons were not included [56].

Diesel fuel has been analyzed using Penning ionization with FT-ICR-MS, resulting in ionization of PAHs and heteroatom-containing compounds [57]. APCI has also been shown to ionize more moderately polar molecules, such as PAHs, in addition to heteroatom-containing constituents [58, 59]. This ionization of PAHs was enhanced by the use of an aprotic solvent to transport the fuel into the mass spectrometer ion source [58]. This makes APCI a useful ionization method for diesel fuel, which contains both PAHs and heteroatomic hydrocarbons. However, there are no literature reports of using APCI for the analysis of diesel fuel.

## 1.5 Basis of Predictive Models

In most environmental models, an easily obtained property is typically the basis of the model and is used to predict the hard to obtain values. For example, the vapor pressure of compound can be used to predict that compounds rate of evaporation. Physical properties (*e.g.* vapor pressure, boiling point *etc.*) are often used at the basis for models because they are easy to obtain. However, for complex mixture, such as petroleum, obtaining physical properties can be challenging and therefore, other methodologies, such as analytical measurement, are needed.

### 1.5.1 Physical Properties

Many of the predictive models for weathering of oil spills rely on using the known physical properties of a compound or oil, such as the vapor pressure and boiling point. Such properties are often used as the basis for predictive modeling [29, 60]. The vapor pressures, boiling points, and other physical properties for some compounds are available in the literature [61-63]. However, many compounds abundant in petroleum are not included in these references. Moreover, identification of a specific compound in a complex petroleum mixture is challenging, given the large number of isomers and structurally-related compounds that yield similar mass spectra. Physical properties of many fuels are typically not available, requiring the properties to be estimated from the distillation curve or °API gravity. As a fuel is weathered, these estimates become unreliable, leading to increased uncertainty in the predictive model.

### 1.5.2 Chromatographic Retention Index

The physical properties of a compound can be estimated using analytical measurements as a surrogate. One common example is the retention of a compound during a chromatographic separation. Quantitative structure-retention relationships (QSRRs) have been applied to predict physical and chemical properties based on linear free-energy relationships [62, 64]. QSRRs were first observed as a log-linear relationship between retention time and carbon number. Kováts expanded on this relationship and demonstrated a correlation between retention on a nonpolar stationary phase and boiling point [65]. This led to the generation of Kováts retention indices. Retention indices provide broadly applicable retention scale relative to the normal alkanes, resulting in a retention index value, independent from many GC parameters including stationary phase, column dimensions, and temperature. For temperature-programmed GC, retention indices ( $I^T$ ) are calculated for a compound of interest based on the retention time of that compound ( $t_{R,i}^T$ ) and the retention time of the normal alkanes of carbon number  $z$  that elute before ( $t_{R,z}^T$ ) and after ( $t_{R,z+1}^T$ ) [66, 67].

$$I^T = 100 \left[ \frac{t_{R,i}^T - t_{R,z}^T}{t_{R,z+1}^T - t_{R,z}^T} + z \right] \quad \text{Equation 1-2}$$

QSRRs have been applied to predict physical properties such as solubility, vapor pressure, reactivity, octanol-water partition coefficient, and many other physical and structural properties [62, 68]. Retention indices as a predictor for physical properties in a complex mixture are advantageous because the compound does not require definitive identification and can be determined from a GC experiment. Previous predicative models, which required known physical properties, would become more broadly applicable by

applying an analytically-derived surrogate in place of the physical property. Moreover, retention indices are available in the literature for many compounds [69], therefore, if the identity compound is known, no GC experiment is necessary to obtain the retention index.

### 1.5.3 Kendrick Mass Defect

Another analytical measurement that has been useful in grouping petroleum constituents with similar structural features is the Kendrick mass defect. High-resolution mass spectrometers measure ion masses with accuracies within a few parts-per-million (ppm), which can be used to calculate a short list of molecular formulas that are within experimental error for each ion [51]. Accurate masses have been useful in petroleomics, resulting in the assignments of thousands of unique formulas to ions generated from crude oil [34, 55]. In the mass spectra of petroleum samples, series of peaks are observed separated by approximately 2 mass units or 14 mass units, corresponding to a difference of two hydrogen atoms (relating to a double bond or ring) or a methylene (CH<sub>2</sub>) group, respectively [51]. The repeating pattern of methylene groups can be used to group compounds using the Kendrick mass defect, which groups compounds together if they differ only by the number of methylene groups. For example, the Kendrick mass defect would be common for all alkanes, as they are a homologous series differing by the number of methylene groups. The Kendrick mass scale ( $m_K$ ) makes the exact mass ( $m_E$ ), of CH<sub>2</sub> equal to exactly 14, instead of <sup>12</sup>C equal to 12 (or mass of methylene being 14.01565 Da).

$$m_K = m_E \left( \frac{14.00000}{14.01565} \right) \quad \text{Equation 1-3}$$

The Kendrick mass defect (KMD) can then be calculated as the difference between the Kendrick mass and the nominal mass ( $m_N$ ).

$$KMD = m_K - m_N \quad \text{Equation 1-4}$$

This conversion results in the mass defect for compounds that differ by the number of methylene groups, but have the same heteroatoms and double bond equivalences (DBE), which can be calculated based on the number of carbon, hydrogen and nitrogen atoms.

$$DBE = C - \frac{H}{2} + \frac{N}{2} + 1 \quad \text{Equation 1-5}$$

The Kendrick mass defect allows for rapid grouping of compounds based on differences in the number of rings or double bonds, as these are not differences of only the number of methylene groups.

## 1.6 Oil Spill Modeling

The ultimate goal of most oil spill modeling is to predict the movement of the oil in the environment in order to direct remediation and assess potential impacts. The movement of the oil in the environment is closely tied to the weathering, therefore most comprehensive predictive models also include a weathering component [15]. These weathering models were developed using empirical measurements of oil spills in the environment using the analytical instrumentation discussed above.

### 1.6.1 Fate and Transport Modeling of Oil Spills

There are many types of predictive models used in impact assessment after oil spills. Many focus on modeling the three-dimensional transport and fate of the oil in the environment, and are typically developed by government agencies or companies. The

National Oceanic and Atmospheric Administration (NOAA) utilizes two modeling software packages, General NOAA Operational Modeling Environment (GNOME) and Automated Data Inquiry for Oil Spills version 2 (ADIOS2) [29, 70]. GNOME is used for trajectory modeling while ADIOS2 models the weathering [18, 71]. The OILTRANS model was developed for the Atlantic Regions' Coastal Pollution Response (ARCOPOL) in Europe [72, 73]. SIMAP is an example of commercially available oil spill modeling software [2, 27, 74]. Other sophisticated three-dimensional oil modeling programs include: COZOIL [75], SINTEF OSCAR [76, 77], OILMAP [78], GULFSPILL [79], MOHAD [80], POSEISON OSM [81], OD3D [82], MEDSLIK [83-85], and BioCast [86].

Each fate and transport model consists of many smaller models used to predict the transport and weathering processes during an oil spill [2]. The overall fate and trajectory is determined by combining the outcome of each of the individual processes. The performance of one algorithm within the comprehensive model can greatly affect the results and accuracy of the other algorithms [26, 60]. Comprehensive models are continually being refined to incorporate more accurate individual models and estimations to provide a comprehensive and accurate prediction. In this work, new methods, based on kinetic rate constants, were developed as predictive models for evaporation and photooxidation.

### *1.6.2 Evaporation of Petroleum Constituents*

#### 1.6.2.1 Theory

Evaporation is the movement of a molecule from the liquid phase into the gaseous phase. In order to move into the gas phase, the molecule must have more energy than

the intermolecular forces that keep it in the liquid. At a given temperature, molecules have a range of kinetic energies, which allows some of those molecules to break the intermolecular forces and reach the gas phase. The pressure of the molecules in the gas phase above the liquid is the vapor pressure [87]. In pure liquids, the rate of evaporation is constant over time, however, that is not the case in a mixture [88, 89]. In a mixture, the vapor pressure of a compound can be expressed in terms of Raoult's Law, which states that the vapor pressure of a liquid is proportional to the mole fraction of the liquid in a mixture [90]. As the mixture evaporates, the composition and, therefore, the equilibrium vapor pressure changes, which make predicting the rate of evaporation as a function of time challenging. In addition, evaporation of a mixture results in an increase in viscosity and density, leading to increased diffusion coefficients.

The vapor pressure of a compound at equilibrium can be determined using the Clausius-Clapeyron equation.

$$\frac{\partial \ln(P)}{\partial T} = \frac{\Delta H_{\text{vap}}}{RT^2} \quad \text{Equation 1-6}$$

The equilibrium vapor pressure ( $P$ ) is related to enthalpy of vaporization ( $\Delta H_{\text{vap}}$ ) and the absolute temperature ( $T$ ) and the gas constant ( $R$ ) [90]. The enthalpy of vaporization is typically independent of temperature under most environmental conditions. However, phase changes and variation in mixture composition can lead to changes in the enthalpy of vaporization [90]. Many of the models commonly used to predict evaporative loss are based on the correlation between the vapor pressure and the evaporation rate [29, 60, 72, 91-96]. However, little is still understood about the physics and chemistry that occur during evaporation in a complex mixture released into the environment [2, 24, 97].

Comprehensive oil modeling software is typically a combination of many different fate and transport models. In a petroleum release, evaporation is a major weathering process and must be account for in environmental models. The evaporation model within comprehensive modeling software typically falls into one of three types of models: empirical [88, 98, 99], analytical [26, 100], and pseudo-component [26, 29, 60, 73, 101, 102]. Each type requires different inputs and makes different assumptions about how the rate of evaporation is affected over time. Some software only includes a single evaporation model, while other programs include several models from which the analyst can choose [2, 26, 72].

#### 1.6.2.2 Empirical Models

The empirical models use laboratory measurements of specific fuels to predict temporal changes in mass at various temperatures [99, 103, 104]. Much of the work to develop these predictive models has been conducted by Fingas, who used the temporal changes in mass of crude oils and refined fuels placed into petri dishes to determine the percent evaporated [15, 24, 88, 98, 103, 104]. A plot of the percent evaporated *versus* time was generated and fit to either a logarithmic or square root function using curve-fitting software [98]. This procedure was repeated for hundreds of different fuels at various temperatures [24]. These empirical models are easy to apply and have been used to predict the percent evaporated (by mass) based on the fuel source, the temperature ( $T$ ), and the time ( $t$ ) [60, 72, 98]. An example of an empirical model for southern diesel fuel (diesel fuel for use in the southern United States) evaporated for less than 5 days:

$$\%Evap = (-0.02 + 0.013 T) \sqrt{t} \quad \text{Equation 1-7}$$

The empirical models determined by Fingas for many crude oils and refined petroleum products are available in the literature [24].

Fingas also developed two general equations to predict the percent evaporated using the percent (by mass) distilled on a distillation curve for a specific fuel at 180 °C ( $D$ ) [25]. One model is for oils that evaporate in a logarithmic fashion with time, which Fingas concluded would encompass most crude oils and petroleum products [24].

$$\%Evap = (0.165 D + 0.045 (T - 15)) \ln(t) \quad \text{Equation 1-8}$$

A second empirical model was developed for oils that evaporate with the square root of time, which was diesel fuel and some crude oils [21, 24].

$$\%Evap = (0.0254 D + 0.01(T - 15)) \sqrt{t} \quad \text{Equation 1-9}$$

While these more general empirical models do not require that the source of the fuel be known or have an existing empirical model, they do require that the percent distilled at 180 °C be known. These data are often not readily available and would still require knowing the type and composition of fuel that was spilled. Typical percent distilled at 180 °C for diesel fuel is 5 – 20% [18]. In addition, as empirical models there is no direct relationship to thermodynamic principles. There is no fundamental explanation why some of the oils that were tested evaporated with a logarithmic or square root relationship with time. This makes further application of these models cumbersome.

Another interesting aspect of the empirical models is that they assume oil evaporation is not boundary layer-regulated, unlike the other evaporation models [88]. The boundary layer is the thin layer of air (typically less than 1 mm), just above the oil,

that the evaporated molecules enter [25, 105]. If the boundary layer becomes saturated over the course of the evaporation, the process is considered to be boundary layer-regulated. The result is that the air layer becomes saturated and evaporation slows [25]. This is true of compounds that evaporate quickly. Evaporation of water is also boundary layer-regulated. Fingas argues that this assumption is invalid for crude oil or petroleum product because many of the compounds evaporate slowly [25]. If evaporation is not boundary layer-regulated, then many factors, including the surface area of the spill or the wind speed, do not affect the rate of evaporation [25, 88, 97]. While this assumption is contrary to most oil spill modeling [26], the models proposed by Fingas are generally comparable to the other models [28, 60] and are included in some oil spill modeling software programs [72, 73].

By varying the surface area, wind speed, and volume of liquid, Fingas demonstrated that water demonstrated boundary layer regulation, while oil and petroleum products did not [88]. For water, Fingas observed a significant increase in the rate of evaporation with increasing wind speed, demonstrating boundary layer regulation. However, for oil, petroleum products and hydrocarbons greater than nonane, Fingas observed only a small increase in the rate of evaporation with increasing wind. In addition, Fingas also demonstrated that increasing the area of the spill does not affect the rate of evaporation, indicating a lack of boundary layer regulation [88].

The advantage of the empirical model is the simplicity and the ease of prediction. Moreover, these simplistic models correlate well with the more complex models discussed below. This allows for fast estimations of the percent evaporated without the need for complex computer programs. The major drawback of this method is that the type of oil

must be known and an empirical model must already have been developed. Even when utilizing the general models, the percent distilled at 180 °C and the temporal relationship (logarithmic or square root) with evaporation must be known.

### 1.6.2.3 Analytical Model

The analytical models use a fundamental thermodynamic approach combined with empirical measurements for the development. In order to develop this semi-empirical approach, many assumptions and empirical measurements were used [60, 97]. This approach assumes that the oil behaves as a single component, which has physical properties that change linearly over time as weathering progresses [29]. The derivation of the analytical model and

A generic, semi-empirical evaporation equation was proposed, demonstrating the major factors in rate of evaporation ( $E$ ), including the mass transfer coefficient ( $k_m$ ), the concentration ( $C_s$ ) of the liquid being evaporated, wind speed ( $U$ ), and diffusion at the boundary layer ( $S$ ) [25].

$$E = K C_s U S \quad \text{Equation 1-10}$$

Sutton proposed a model to predict the rate of evaporation of a pure liquid, specifically water, based on Equation 1-10, using empirical measurements [106].

$$E = K C_s U^{7/9} a^{-1/9} Sc^{-r} \quad \text{Equation 1-11}$$

This equation introduced the dependence of spill area ( $a$ ), and Schmidt number ( $Sc$ ) in the rate of evaporation. The Schmidt number is the ratio of the air's kinematic viscosity to the evaporating molecule's diffusion coefficient in air. The exponent ( $r$ ) relates to the

effect of diffusion, and typically ranges from 0 – 2/3 [25, 106]. The powers associated with each variable were empirically determined.

MackKay and Matsugu proposed an equation relating the rate of evaporation ( $E$ ) or change in concentration over time, based on vapor pressure ( $P$ ), temperature of the pool of liquid ( $T$ ), gas constant ( $R$ ), and mass transfer coefficient ( $k_m$ ) [107].

$$E = \frac{k_m P}{RT} \quad \text{Equation 1-12}$$

The equation for the mass transfer coefficient was based on the work by Sutton [106].

$$k_m = 0.0292 U^{7/9} a^{-1/9} Sc^{-2/3} \quad \text{Equation 1-13}$$

The coefficients for the equation were empirically determined using the evaporation of water, the aromatic hydrocarbon cumene, and gasoline from large evaporation pans [100, 106, 107]. They also investigated the effect of spill area and wind speed. The rate of evaporation was based on the volume change over time. MackKay and Matsugu found that Equation 1-12 worked well to predict the evaporation of a pure liquid, but did not work well for gasoline, which had a variable vapor pressure due to evaporation [107]. For this work, MackKay and Matsugu concluded that Equation 1-12 could describe evaporation when there is a constant vapor pressure.

Stiver and MackKay developed several experiments to determine the rate of evaporation for individual compounds in a complex mixture, using four crude oils and a “synthetic oil”, which was a mixture of  $n$ -alkanes [100]. Three different evaporation methods were applied, evaporation of a thin film from a tray, gas stripping, and distillation. Oil samples evaporated from a thin film allowed for monitoring temporal changes in mass,

and gas stripping allowed for monitoring temporal changes in both mass and volume. Distillation was performed to generate a distillation curve, monitoring volume distilled at various temperatures.

Stiver and Mackay adapted Equation 1-12 to predicting the evaporation rate for an individual compound ( $i$ ) from a thin film, within a complex mixture [100].

$$N_i = \frac{k_m a \chi_i \gamma_i P_i}{RT} \quad \text{Equation 1-14}$$

The vapor pressure of a compound in a mixture was determined using Raoult's law, based on the vapor pressure of the pure compound ( $P_i$ ), the mole fraction ( $\chi_i$ ), and the activity coefficient ( $\gamma_i$ ). Equation 1-14 can be expressed in terms of the change in the number of moles of an individual compound ( $n_i$ ) at time ( $t$ ).

$$\frac{\partial n_i}{\partial t} = \frac{k_m a \left( \frac{n_i}{n_t} \right) \gamma_i P_i}{RT} \quad \text{Equation 1-15}$$

The total moles ( $n_t$ ) present can be determined from the fraction evaporated ( $F_E$ ), the initial volume of oil ( $V_0$ ), and the initial oil molar volume ( $\nu_{c_0}$ ) [93].

$$n_t = \frac{(1 - F_E) V_0}{\nu_{c_0}} \quad \text{Equation 1-16}$$

Equation 1-16 can be substituted into Equation 1-15 and rearranged to form Equation 1-17.

$$\frac{\partial n_i}{n_i} = \frac{\nu_{c_0}}{(1 - F_E)} \frac{\gamma_i P_i}{RT} \frac{k_m a \partial t}{V_0} \quad \text{Equation 1-17}$$

The evaporative exposure ( $\theta$ ) incorporates the terms that are a function of the size of the spill.

$$\theta = \frac{k_m a t}{V_0} \quad \text{Equation 1-18}$$

The mean effective oil molar volume ( $v_c$ ) was used to account for the changes in the activity coefficient and oil molar volume due to evaporation.

$$v_c = \frac{v_{c_0} \gamma_i}{(1 - F_E)} \quad \text{Equation 1-19}$$

By substituting Equation 1-18 and Equation 1-19 into Equation 1-17 and rearranging, the fraction remaining can be predicted for an individual compound [93].

$$\frac{\partial n_i}{n_i} = \frac{v_c P_i}{RT} \partial \theta \quad \text{Equation 1-20}$$

Equation 1-20 is further simplified using the Henry's Law constant (H), which is the ratio of the compound in the gas phase ( $P/RT$ ) to the compound in the liquid phase ( $1/l$ ), at equilibrium [100].

$$H = \frac{v_c P_i}{RT} \quad \text{Equation 1-21}$$

Substituting Equation 1-21 into Equation 1-20, the fraction remaining ( $F_i$ ), or change in moles over the initial moles, for an individual compound can be calculated based on the Henry's Law constant and the evaporative exposure.

$$\partial F_i = H \partial \theta \quad \text{Equation 1-22}$$

If  $H$  is independent of  $F$ , Equation 1-22 can be integrated, to calculate the fraction remaining [93, 100].

$$F = H \theta \quad \text{Equation 1-23}$$

To this point, all calculations were for an individual compound. However, this can be extended to a complex mixture. However, physical properties, such as activity coefficients or vapor pressure, which were used to determine the fraction remaining for an individual compound now must be estimated for the bulk fuel. Also, in a complex mixture or at concentrations above infinite dilution,  $H$  is not independent of  $F$ , so an equivalence must be established. This can be achieved using a form of the Clausius-Clapeyron equation.

$$\ln\left(\frac{P_1}{P_2}\right) = \frac{\Delta H_{vap}}{R} \left(\frac{1}{T_2} - \frac{1}{T_1}\right) \quad \text{Equation 1-24}$$

The Clausius-Clapeyron equation can be rearranged, so that  $P_A$  is the atmospheric pressure at which the boiling point ( $T_b$ ) is recorded, and  $P$  is the vapor pressure at temperature  $T$ .

$$\ln\left(\frac{P}{P_A}\right) = B \left(1 - \frac{T_b}{T}\right) \quad \text{Equation 1-25}$$

The  $B$  term is dimensionless and equal to the heat of vaporization ( $\Delta H_{vap}$ ) over the gas constant ( $R$ ) and the boiling point.

$$B = \frac{\Delta H_{vap}}{RT_b} \quad \text{Equation 1-26}$$

Equation 1-21 can be rearranged based on Equation 1-25.

$$\ln(H) = \ln\left(\frac{P_A v_c}{RT}\right) + B - \frac{BT_b}{T} \quad \text{Equation 1-27}$$

Equation 1-27 can then be simplified.

$$\ln(H) = A - \frac{BT_b}{T} \quad \text{Equation 1-28}$$

A is a constant that can be determined for an oil, based on experimental distillation. Stiver and MacKay determined empirical values for A and B by linear regression of  $\ln(H)$  versus  $T_b$ . Empirically determined values using five crude oils were  $A = 6.3$  and  $B = 10.3$  [23, 100]. These oils are likely not representative of all possible petroleum products, so new fitting coefficients might be required.

As previously noted, the boiling point of a fuel is needed. A mixture does not have a true boiling point, but Stiver and MacKay proposed a simplified equation predict the boiling point, based on experimental distillations.

$$T_b = (T_0 + T_G)F \quad \text{Equation 1-29}$$

In this equation,  $T_0$  is the initial boiling point of the distillation, where the fraction evaporated is 0 and  $T_G$  is the temperature gradient of the distillation curve [100]. Combining Equation 1-22, Equation 1-28, and Equation 1-29 yields

$$\partial F = \exp\left(A - \frac{(T_0 + T_G)F}{T}\right) \partial \theta \quad \text{Equation 1-30}$$

When utilizing the analytical model, several temperatures ( $T_0$  and  $T_G$ ) must be estimated from the distillation curve. The distillation curves utilized to develop this model, were based on small-scale laboratory distillations, and these distillation data are not

available for most oils [60, 108]. In addition, the estimation for the  $A$  and  $B$  terms were determined from the distillation of only a few oils, and may not be representative of all oils. The analytical method also assumes a linear relationship between the fraction evaporated and the boiling point, making the analytical model better suited for oils with a linear distribution of distillation cuts [26, 108]. These estimates present significant sources of uncertainty in the predictive capacity of the model [28, 29, 100, 107].

#### 1.6.2.4 Pseudo-component Model

The most common method currently used for estimating extent of evaporation is the pseudo-component model. This model, which is based on the analytical model developed by Stiver and MacKay, approximates the composition of the complex fuel as several discrete and independent components, rather than as a single component, as is done with the analytical method. The total evaporation of the fuel is based on the sum of the evaporation of the pseudo-components. This allows for a more accurate determination of vapor pressure and molar volume, but requires additional assumptions and empirical data.

Payne *et al.* developed a method for predicting the rate of evaporation for oil based on several well-characterized pseudo-components, which were selected based on distillation [102]. The oil was distilled and each fraction became a pseudo-component. The temperature of the distillation, volume fraction distilled, and °API gravity (Equation 1-1) were then determined for each cut [102]. However, these data are not widely available for most oils, making broad applicability challenging [60]. Jones expanded on a pseudo-component model (discussed below) using standard distillation data [109] without requiring the °API gravity [60]. In order to accomplish this, Jones used empirical

relationships between boiling point and molar volume for the normal alkanes. In addition, Jones developed an empirical function relating the vapor pressure of pseudo-components to the boiling point using Antoine's equation rather than the Clausius-Clapeyron equation used in the analytical model [26, 60].

Like the analytical model, the pseudo-component model is based on the rate of evaporation (similar to Equation 1-14) proposed by Stiver and MacKay [100].

$$\frac{\partial V_i}{\partial t} = \frac{k_{m,i} a(t) P_i \bar{V}_i \chi_i(t)}{R T} \quad \text{Equation 1-31}$$

Equation 1-31 can be used to predict the volume ( $V_i$ ) of a pseudo-component ( $i$ ) at time ( $t$ ), based on the mass transfer coefficient ( $k_{m,i}$ ), vapor pressure ( $P_i$ ), relative molar volume ( $\bar{V}_i$ ), and mole fraction at  $t$  ( $\chi_i(t)$ ) for each pseudo-component as well as water temperature ( $T$ ), spill area at  $t$ , ( $a(t)$ ), and the gas constant ( $R$ ) [72, 73]. The mass transfer coefficient was calculated with slight modifications in the equation determined from Mackay and Matsugu (Equation 1-13), using the wind speed ( $U$ ), the length of the oil slick downwind of the source ( $X$ ), and the Schmidt number ( $Sc$ ) [107].

$$k_{m,i} = 0.0048 U^{7/9} a^{-1/9} Sc^{-2/3} \quad \text{Equation 1-32}$$

An approximation for the Schmidt number was used, based on the mole-weighted average of the oil ( $MW_{ave}$ ) [73].

$$Sc = 1.3676 \left( \frac{0.018}{MW_{ave}} \right)^{-1/2} \quad \text{Equation 1-33}$$

The mole-weighted average is calculated from the molecular weight ( $MW_i$ ), the initial molar volume ( $V_{i_0}$ ) and relative molar volume of each pseudo-component.

$$MW_{ave} = \frac{\sum \frac{MW_i * V_{i_0}}{\bar{V}_i}}{\sum \frac{V_{i_0}}{\bar{V}_i}} \quad \text{Equation 1-34}$$

Using the boiling point of each pseudo-component ( $T_{b,i}$ ), the molecular weight, and relative molar volume can be calculated, using a correction derived from the normal alkanes between propane ( $C_3$ ) and eicosane ( $C_{20}$ ) [18]. The boiling point for each pseudo-component is the average temperature between the beginning and end of the cuts on the distillation curve [102].

$$MW_i = 0.04132 - (1.985 * 10^{-4} T_{b,i}) + (9.494 * 10^{-7} T_{b,i}^2) \quad \text{Equation 1-35}$$

$$\bar{V}_i = 7.0 * 10^{-5} - (2.102 * 10^{-7} T_{b,i}) + (1.0 * 10^{-9} T_{b,i}^2) \quad \text{Equation 1-36}$$

The vapor pressure of each pseudo-component can be estimated using Antoine's equation, based on the atmospheric pressure ( $P_a$ ), water temperature, and boiling point,

$$\ln\left(\frac{P_i}{P_a}\right) = \frac{8.75 + 1.987 * \log(T_{b,i}) [T_{b,i} - C]^2}{RT_{b,i}} \left[ \frac{1}{T_{b,i} - C} - \frac{1}{T - C} \right] \quad \text{Equation 1-37}$$

where C is

$$C = 0.19(T_{b,i} - 18.0) \quad \text{Equation 1-38}$$

The mole fraction was calculated based on the molar volumes.

$$\chi_i(t) = \frac{\frac{V_i}{\bar{V}_i}}{\sum_{j=1}^{i_{max}} \frac{V_j}{\bar{V}_j}} \quad \text{Equation 1-39}$$

Equation 1-31 through Equation 1-39 can be combined to estimate the volume remaining of each pseudo-component.

$$\frac{\partial V_i}{\partial t} = \frac{0.0656 * U^{7/9} \left( \frac{0.018}{MW_{ave}} \right)^{1/3}}{X^{1/9}} \frac{a(t) P_i V_i}{R T \sum_{j=1}^{i_{max}} \frac{V_j}{V_j}} \quad \text{Equation 1-40}$$

To calculate the fraction evaporated (v/v) for each pseudo-component, Equation 1-40 is solved at each time step (which is typically about 1 hour). The total fraction evaporated (v/v) is the sum of the fraction evaporated of each of the pseudo-components, divided by the initial volume of oil spilled [73].

Jones compared theoretical evaporations of a light, medium, and heavy crude oil using the empirical, analytical, and pseudo-component models [60]. The fraction remaining over time was compared when the temperature, volume, thickness, and wind speed were individually varied for each oil. Overall, the models performed similarly, predicting fractions remaining within ~10% of each other, despite the large differences in how each model was developed. Jones reported that the models were only moderately sensitive ( $\pm 10\%$ ) to changes in temperatures, thicknesses, and wind speeds that would be commonly observed in the environment [60].

Variations of the pseudo-component model are currently the most widely utilized in comprehensive oil modeling software [18, 26, 28, 29, 72, 73]. In general, the empirical [88, 98], analytical [93, 100], and pseudo-component [60, 102] models result in similar percent of fuel remaining after evaporation [26, 28, 60]. However, the use of the Clausius-Clapeyron equation in the analytical model has been reported to result in vapor pressures

that are higher than actual values for the less volatile compounds [18]. The vapor pressure calculation based on Antoine's equation was shown to be more reliable [29]. Because the rate of evaporation is directly related to vapor pressure, this is a critical calculation in the model [91, 110]. However, in the pseudo component model, estimates are used to obtain the molar volume is based on the molar volumes of n-alkanes from 3 – 20 carbons. This estimates can result in wide errors, especially for fuels with large aromatic content.

#### 1.6.2.5 Kinetic Models

The models for evaporation discussed in Sections 1.6.2.2 to 1.6.2.4 all utilize empirically derived fitting coefficients for at least some of the estimates included in the model. The empirical models developed by Fingas have no thermodynamic basis, making extension of the model challenging. The analytical and pseudo-component models have a thermodynamic basis, however they require extensive estimations and assumptions. These models require empirical fitting coefficients to obtain physical properties of a fuel.

Another method proposed for estimating the rate of evaporation is using kinetic models. Evaporation can be thought of as process of a molecule moving from the liquid to the gas phase, with a rate constant of  $k$ . Kinetic equations allow for the determination of analyte concentration at a specific time, given the reaction order. Rate constants for evaporation from a complex mixture were found to be first-order decays [92].

$$C_t = C_0 * \exp(-k * t)$$

Equation 1-41

where  $C_t$  is the concentration at time  $t$  and  $C_0$  is the initial concentration [105, 111, 112]. As an alternative to the rate constant, the characteristic lifetime ( $\tau = 1/k$ ) or the half-life ( $t_{1/2}$ ), which is the time in which the concentration of analyte decreases by one-half, can be used.

Regnier and Scott experimentally determined the kinetic rate constant for normal alkanes in diesel fuel at four temperatures (5, 10, 20, and 30 °C) with constant wind (13 mi hr<sup>-1</sup>) [92]. Diesel fuel was evaporated in petri dishes and an aliquot was removed for GC-MS analysis. The normal alkanes in the diesel samples were quantified after various evaporation times and used to determine kinetic rate constants. Using the vapor pressure ( $P$ ) and rate constant ( $k$ ) of the normal alkane at each temperature, the rate constant could be predicted [92].

$$\log(P) = 1.25 \log(k) + 0.160 \quad \text{Equation 1-42}$$

This vapor pressure model was only applied to the normal alkanes, but the authors hypothesized that it could be applied to all compounds. One of the major drawbacks is that in order to utilize the model, the vapor pressure of the compound had to be known. Moreover, this model was only capable of predicting the evaporation of individual compounds, not the entire oil. However, this work demonstrated that the evaporation rate constant did correlate with the vapor pressure of a compound.

Another kinetic model was developed by Butler to predict the age of tar balls [113]. This model assumed that the fraction remaining of an individual compound is proportional to vapor pressure. The fraction remaining ( $x/x_0$ ) of an individual compound can be determined based on the based on the rate constant ( $k$ ), the vapor pressure ( $P$ ), the time ( $t$ ), and the initial amount ( $x_0$ ) [25, 113, 114].

$$\frac{x}{x_0} = \exp\left(-\frac{k P t}{x_0}\right) \quad \text{Equation 1-43}$$

The vapor pressure was determined as a function of carbon number ( $N$ ), using the normal alkanes [113].

$$P = \exp(10.94 - 1.06 N) \quad \text{Equation 1-44}$$

Equation 1-43 and Equation 1-44 can be combined to predict the fraction remaining for a compound, based on the carbon number [114].

$$\frac{x}{x_0} = \exp\left[-\left(\frac{k t}{x_0}\right) \exp(10.94 - 1.06N)\right] \quad \text{Equation 1-45}$$

However, this prediction required an estimation of the rate constant, which required experimental determination, based on the weathering of the oil [113]. While this model did not require identification of a compound, an assumption was made that the vapor pressure of a compound was related to the normal alkane with the same number of carbon atoms.

Kinetic models are useful in determining rate constants for evaporation of an individual compound. The fraction remaining of that compound can then be determined using the rate constant and Equation 1-41. The initial concentration of analyte is not required when determining the fraction remaining, it is only necessary to obtain an absolute concentration. Identification of the compound is also unnecessary, as long as the vapor pressure can be determined. Determination of the vapor pressure without identifying a compound can be challenging, but analytical properties such as retention index on a nonpolar stationary phase have been shown to predict the vapor pressure [40]. Existing kinetic models for evaporation have not been applied to an entire fuel, only to

individual compounds from a complex mixture. In order for kinetic models to be useful, they must be capable of predicting evaporation of a bulk fuel as well as individual compounds.

### *1.6.3 Photodegradation of Petroleum Products*

Most comprehensive oil spill modeling software programs do not include fate models due to photodegradation [2, 73, 115]. Many consider photodegradation to account for a very small amount of the mass loss for oil, making it insignificant compared to other weathering processes [21, 22, 116]. Photodegradation typically consists of oxidation of compounds, however, other degradation pathways, such as direct photolysis also occurs. Photooxidation typically results in increased toxicity and water solubility for a number of compounds [21, 70, 116]. Even if photodegradation does not account for significant mass loss, the formation of toxic products can have a significant environmental impact.

Many compounds in crude oil can absorb the UV and visible components of sunlight, resulting in the promotion of that compound to the excited state. The energy absorbed by the compound can be dissipated in several ways. The compound can return to the ground state, without resulting in a structural change. The energy can be released into the environment as heat, via internal conversion. A photon of light can also be released through fluorescence or phosphorescence. The energy can be transferred to another molecule (photosensitization), which can dissipate the energy or undergo a reaction. Last, the energy can directly break the bonds in the compound, forming fragments, peroxides, or radicals that can react with other compounds. [87, 117]. Reactions through photosensitization is thought to be the dominant pathway for

photodegradation. Many compounds found in the environment, such as dissolved organic matter in water, serve as photosensitizers [116, 118].

In general, the processes and mechanisms responsible for photodegradation of the components in oils are not well understood [118-120]. Photooxidation, the most common photodegradation method, has been shown to result from direct photolysis as well as through photosensitization, typically with singlet oxygen ( $^1\text{O}_2$ ) or electron transfer involving free radicals [31, 118, 120-126]. Previous work has focused on determining the mechanism and predicting the rate of photooxidation of individual compounds. For petroleum products released into the environment, there are many factors that influence the degradation including composition of the oil, presence of photosensitizers or quenchers in the environment, intensity of solar irradiation, temperature, and extent of weathering [30, 118, 119, 124, 126]. Moreover, in environmental studies, differentiating between the effects of photooxidation and biodegradation is challenging, because both result in oxidized products [115, 116, 122, 123, 127]. In laboratory studies, experimental conditions vary widely among researchers. Light sources have varied from mercury and xenon arc lamps to natural sunlight. The irradiance of the source (250 W/m<sup>2</sup> [30] – 1260 W/m<sup>2</sup> [119]) and irradiation times widely varied. These differences in experimental conditions, which could lead to different mechanisms, resulted in contradictory conclusions between investigations [122, 123, 128]. Most research supports that normal alkanes in oil are largely unaffected by photooxidation, while aromatic compounds are typically converted into polar compounds or resins through the addition of oxygen [33, 118, 119, 129].

#### 1.6.3.1 Direct photolysis

Direct photolysis is the absorption of light energy by a chromophore resulting in the breaking of bonds. While direct photolysis has been demonstrated for many compounds in petroleum products, photosensitized reactions are more likely in environmental spills due to the large number of sensitizers in the environment. Oil also has low photon energies relative to carbon-carbon or carbon-hydrogen bond energies [122-124, 130, 131]. For example, a photon of 315 nm, the short-wavelength end of the UVA range, deposits about 91 kcal/mol, which is slightly more than weak C-H and C-C bonds. Direct photolysis has been proposed to be the dominant mechanism in dilute solutions, owing to the short lifespan of reactive oxygen species [128].

#### 1.6.3.2 Indirect Photolysis

Photodegradation is believed to occur via indirect photolysis, due to the large number of sensitizers in the environment and in petroleum. Indirect photolysis requires a sensitizer (S) to absorb light, resulting in the sensitizer entering the excited singlet state ( $^1S^*$ ) (Figure 1-3) [87, 117, 131]. Once the energy is absorbed, it is transferred to another compound. The excited-state sensitizer ( $^1S^*$ ) can react with oxygen in the ground state ( $^3O_2$ ) to form reactive oxygen species (e.g.  $OH^\bullet$ ,  $O_2^{\bullet-}$ ,  $H_2O_2$ , etc.), which can oxidize a compound in oil. Some sensitizers ( $^1S^*$ ) can also undergo intersystem crossing, resulting

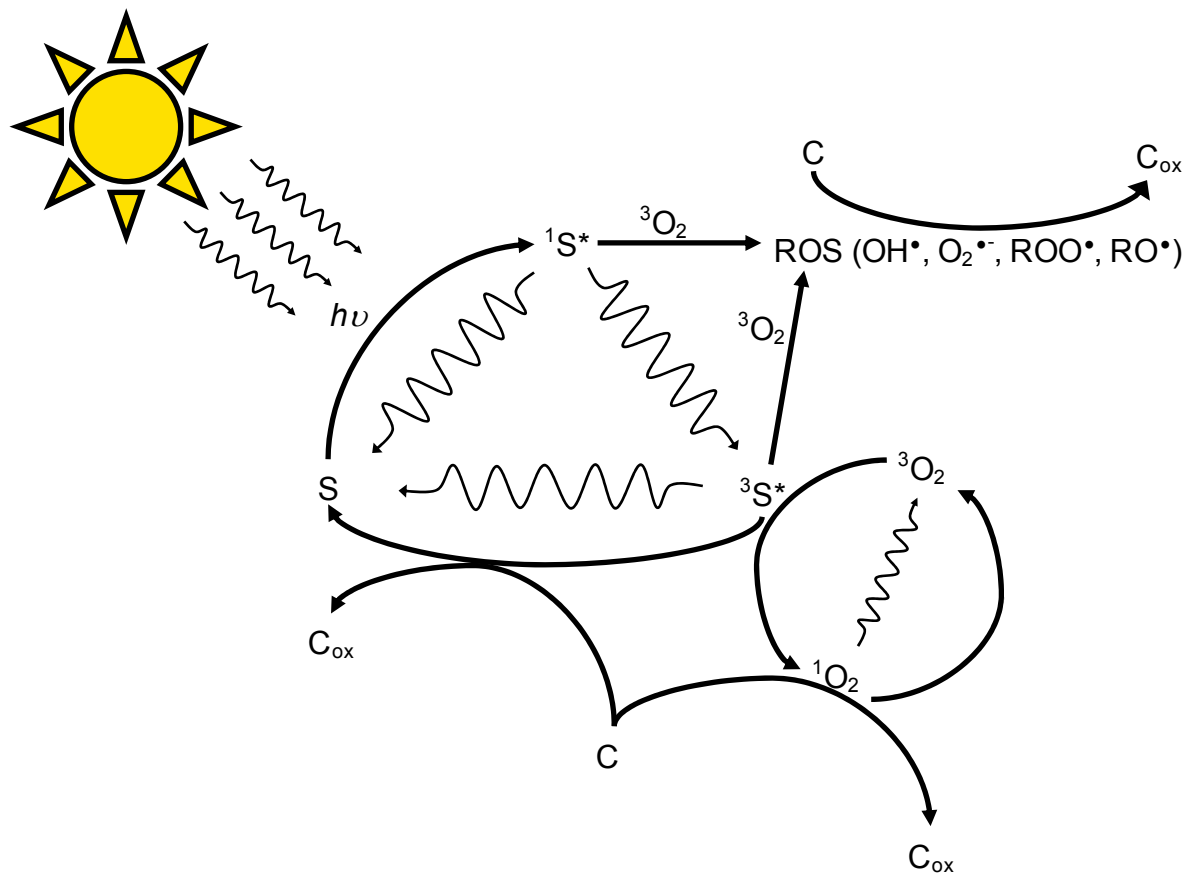


Figure 1-3. A compound in oil (C) becoming oxidized ( $C_{ox}$ ) via indirect photolysis. A sensitizer (S) absorbs sunlight and enters an excited singlet state ( $^1S^*$ ). The sensitizer can react with oxygen to form reactive oxygen species (ROS), which can then oxidize C. Through intersystem crossing, the  $^1S^*$  can enter the triplet state ( $^3S^*$ ), which can directly oxidize C or can react with oxygen, to form singlet oxygen ( $^1O_2$ ). Singlet oxygen can then oxidize C. Figure adapted from Schwarzenbach *et al.* [87].

in an excited sensitizer in the triplet excited state ( $^3S^*$ ) [87]. This sensitizer can react with triplet oxygen ( $^3O_2$ ), resulting in the formation of singlet oxygen ( $^1O_2$ ), which can oxidize the oil constituent. Last, the sensitizer ( $^3S^*$ ) can directly react with the oil compound, resulting in oxidation [87, 132].

### 1.6.3.3 Photooxidation Studies

Predicting the products and rates of photooxidation for some pure compounds is fairly well established. Much of the initial work was performed by Zepp and Schlotzhauer, who experimentally determined the half-life for the direct photolysis of 13 PAHs, which ranged from 0.034 h for naphthacene to 71 h for naphthalene [131, 133]. They then predicted the half-life for these PAHs at various depths in water, where light would be attenuated by absorption.

This led to the development of a model in which the first-order rate constant for direct photolysis of a pure compound ( $k_p$ ) is related to the rate constant for light absorption ( $k_a$ ) and the quantum yield ( $\Phi$ ) of the number of reactions per photon of absorbed light [87].

$$k_p = \Phi * k_a \quad \text{Equation 1-46}$$

The rate constant for light absorption is calculated from the irradiance of the light ( $W_\lambda$ ), the molar absorptivity ( $\epsilon_\lambda$ ), the attenuation of light ( $\alpha_\lambda$ ) through a layer of thickness ( $z$ ), where  $\lambda$  indicates the wavelength of light [128, 130, 134].

$$k_{a_\lambda} = \frac{W_\lambda * \epsilon_\lambda}{z * \alpha_\lambda} \quad \text{Equation 1-47}$$

Plata *et al.* compared rate constants for direct photolysis of pure PAHs found in the literature to actual rates for PAHs in No. 6 fuel oil coated on rocks after a spill [128]. The observed rate of photodegradation was substantially higher than those from the literature, indicating that other reactions must be occurring simultaneously, and direct photolysis cannot account completely for photooxidation [128].

The rate of indirect photolysis for a pure compound is more complicated to predict. Indirect photolysis depends on sensitizer as well as the reactant, resulting in pseudo-first-order or second-order kinetics [135, 136]. The overall reaction rate ( $R_{ox}$ ) is dependent on the compound of interest ( $C$ ), the concentration of each oxidant ( $Ox$ ), and the rate constant ( $k_{ox}$ ) for each oxidant [135].

$$R_{ox} = \frac{-d[C]}{dt} = \sum k_{ox} * [Ox] * [C] \quad \text{Equation 1-48}$$

The oxidants must be identified and their concentrations directly measured. In addition, the rate constant for these oxidants must be known and are wavelength and compound dependent as seen in Equation 1-47 [135]. These models have limited utility in estimation of photooxidation of petroleum products, because they were developed for systems with a single compound being oxidized by a few well-known sensitizers. In the photooxidation of petroleum, many compounds are simultaneously oxidized, with compounds in the petroleum as well as in the environment acting as sensitizers [121-123]. Therefore, the rate of photodegradation depends on the composition of the petroleum product as well as the environmental conditions including the dissolved organic and inorganic matter, the intensity of the sunlight and the temperature [30, 137].

Most recent studies have focused on using new analytical instrumentation to identify products formed by photooxidation during weathering of petroleum spills. In many previous studies, instrumental limitations made identifying oxidized products in crude oil challenging [116]. For example, most oxidized products could not be analyzed by GC-MS. In addition, GC-MS did not provide adequate separation compounds in crude oil. Recent experiments have utilized two dimensional gas chromatography and high-resolution mass spectrometry for the analysis of petroleum [34, 40, 116].

Islam *et al.* divided the fuel into fractions (saturate, aromatic, resin, and asphaltene) and analyzed each fraction after photooxidation using gravimetric analysis and Fourier transform ion cyclotron resonance mass spectrometry (FT-ICR MS) with atmospheric pressure photoionization (APPI) [33]. The gravimetric analysis of petroleum fractions is common for assessing weathering. Based on the gravimetric analysis, Islam *et al.* showed that after photooxidation there was no statistical difference in the saturate fraction, a significant increase in the resin fraction, and a significant decrease in the aromatic fraction, which is consistent with most previous work [33, 138]. However, using FT-ICR MS, substantial changes in the saturate fraction was observed. After photooxidation, there was a decrease in abundances of heteroatom-containing compounds, particularly those containing sulfur, in the saturate fraction. There was also an observed decrease in the number of compounds in the saturate fraction with high double-bond equivalences (DBE), indicating preferential degradation of these hydrocarbons [33]. This is contradictory to most work, which indicated that the saturate fraction is relatively unchanged by photooxidation.

Radovic *et al.* showed preferential degradation for certain compounds, using samples collected from the *Deepwater Horizon* platform blowout, treating them by irradiation with a xenon source [118]. Samples were fractionated using thin-layer chromatography followed by analysis using GC-MS and infrared spectroscopy. After irradiation, there was a decrease in abundances of the aromatic fraction, an increase in the resin fraction, and an increase in the oxygen content of the resin and asphaltenes. Radovic *et al.* also observed preferential photooxidation for compounds with increased alkyl substitution and additional aromatic rings [118]. In addition, Radovic *et al.* demonstrated that PAHs with the same number of rings but with a *peri*-condensed structure were preferentially degraded compared to those with a *cata*-condensed structure [118, 139]. A *peri*-condensed PAH is more compact, with at least one carbon atom shared between three aromatic rings. They also observed degradation of triaromatic steranes, which are typically thought of as unaltered by weathering and are often used to determine the origin of the oil [118]. These findings demonstrated many of the analytical challenges and conflicting conclusions still persistent in much published literature dealing with the weathering of petroleum.

## **1.7 Objectives and Aims**

Part of the challenge in assessing petroleum discharges arises from the complexity of the sample and the changes in the physical and chemical properties that occur due to weathering. Better understanding of the fundamentals of these weathering processes shows promise to improve impact assessments of discharges and to assess remediation effectiveness. Current evaporation models rely on physical properties not readily available for most fuels. This leads to estimations which can introduce additional error.

No model currently exists for predicting photodegradation in a complex mixture such as petroleum. There are still significant knowledge gaps concerning what compounds in the oil react, what products are formed, and by what mechanisms.

The objective of this research is to develop empirical rate constants for individual compounds undergoing relevant weathering processes that will provide a better understanding of the fundamental changes that occur during weathering. These rate constants serve as the foundation for predictive models of the fate of petroleum in the environment. In order to accomplish this objective, the following aims were outlined:

1. Generate rate constants capable of characterizing environmental weathering processes.
2. Associate physical properties of compounds with analytical measurements, as a basis for a model to predict the rate constant associated with the weathering processes.
3. Apply rate constants and subsequent models to weathering processes to elicit better understanding of the fundamental changes that occur.

In this work, diesel fuel was subjected to evaporation and photodegradation. GC-MS and ToF-MS were utilized to monitor the fuel during each weathering process. Kinetic rate constants for individual compounds in each weathering process were generated using the temporal change in abundance. The kinetic rate constants allowed for comparisons of individual compounds during weathering. From this work, models for predicting evaporation over environmentally relevant temperature were developed. Rate constants from photodegradation provided key insights into the decay and formation of compounds during irradiation. The models developed from this work will predict rates of

specific weathering processes, rather than the comprehensive fate and transport of the fuel. However, these models can be incorporated into more comprehensive models that encompass other fate and transport models. Moreover, this work will provide methodologies for developing predictive models based on analytical properties, which could be applied to other weathering processes such as dissolution or biodegradation.

## REFERENCES

## REFERENCES

- [1] U.S.E.I. Administration, U.S. Energy Information Administration, International Energy Statistics. <<http://www.eia.gov/cfapps/ipdbproject/>>. April 30, 2014.
- [2] National Research Council, Oil in the Sea III : Inputs, Fates, and Effects, National Academy Press, Washington, D.C., 2003.
- [3] D. Schmidt-Etkin, in: M. Fingas (Ed.), Oil Spill Science and Technology (Chapt. 2), Elsevier, Burlington, MA, 2011.
- [4] G. Shigenaka, in: M. Fingas (Ed.), Oil Spill Science and Technology (Chapt. 27), Elsevier, Burlington, MA, 2011.
- [5] U.S.E.P. Agency, US Environmental Protection Agency, Understanding Oil Spills and Oil Spill Response, 1999. <<http://www.epa.gov/oem/content/learning/pdfbook.htm>>. April 30, 2014.
- [6] M.O. Hayes, R. Hoff, J. Michel, D. Scholz, G. Shigenaka. An Introduction to Coastal Habitats and Biological Resources for Oil Spill Response. Hazardous Materials Response and Assessment Division, National Oceanic and Atmospheric Administration, HMRAD 92-4 Seattle, WA, 1992.
- [7] M.D. Garza-Gil, A. Prada-Blanco, M.X. Vázquez-Rodríguez, Ecological Economics, 58 (2006) 842.
- [8] E. Stauffer, J.A. Dolan, R. Newman, Fire Debris Analysis, Elsevier, Burlington, MA, 2008.
- [9] Z. Wang, M. Fingas, C. Yang, J. Christensen, in: R.D. Morrison, B.L. Murphy (Eds.), Environ. Forensics, Elsevier, Burlington, MA, 2006.
- [10] R.B. Gupta, A. Demirbas, Gasoline, Diesel, and Ethanol Biofuels from Grasses and Plants, Cambridge University Press, New York, NY, 2010.

- [11] M. Fingas, in: M. Fingas (Ed.), Oil Spill Science and Technology (Chapt. 3), Elsevier, Burlington, MA, 2011.
- [12] Z.D. Wang, M. Fingas, K. Li, J. Chromatogr. Sci., 32 (1994) 361.
- [13] Z.D. Wang, M. Fingas, K. Li, J. Chromatogr. Sci., 32 (1994) 367.
- [14] A.G. Marshall, R.P. Rodgers, Proc. Natl. Acad. Sci. U. S. A., 105 (2008) 18090.
- [15] M. Fingas, The Basics of Oil Spill Cleanup, CRC Press, Boca Raton, FL, 2013.
- [16] Z.D. Wang, M. Fingas, D.S. Page, J. Chromatogr. A, 843 (1999) 369.
- [17] C. Corporation, Chevron Corporation, Diesel Fuels Technical Review, 2007. <<http://www.chevronwithtechron.com/products/diesel.aspx>>. May 1, 2014.
- [18] N.O.a.A. Administration, National Oceanic and Atmospheric Administration, ADIOS. <<http://response.restoration.noaa.gov/adios/>>. May 6, 2014.
- [19] C.A. Hughey, C.L. Hendrickson, R.P. Rodgers, A.G. Marshall, Energy Fuels, 15 (2001) 1186.
- [20] ASTM Standard D975, 2007, Standard Specification for Diesel Fuel Oils, ASTM International, West Conshohocken, PA, 2007, <<http://www.astm.org/>>.
- [21] M. Fingas, in: M. Fingas (Ed.), Oil Spill Science and Technology (Chapt. 8), Elsevier, Burlington, MA, 2011.
- [22] A.P. Institute, Fate of Spilled Oil in Marine Waters, 1999
- [23] M. Nazir, F. Khan, P. Arnyotte, R. Sadiq, Process Saf. Environ. Protect., 86 (2008) 141.
- [24] M. Fingas, in: M. Fingas (Ed.), Oil Spill Science and Technology (Chapt. 9), Elsevier, Burlington, MA, 2011.

- [25] M. Fingas, *Journal of Petroleum Science Research*, 2 (2013) 104.
- [26] M. Reed, O. Johansen, P.J. Brandvik, P. Daling, A. Lewis, R. Fiocco, D. Mackay, R. Prentki, *Spill Sci. Technol. Bull.*, 5 (1999) 3.
- [27] D.F. McCay, *Mar. Pollut. Bull.*, 47 (2003) 341.
- [28] D.P. French-McCay, *Environ. Toxicol. Chem.*, 23 (2004) 2441.
- [29] W. Lehr, R. Jones, M. Evans, D. Simecek-Beatty, R. Overstreet, *Environ. Modell. Softw.*, 17 (2002) 191.
- [30] T. Saeed, L.N. Ali, A. Al-Bloushi, H. Al-Hashash, M. Al-Bahloul, A. Al-Khabbaz, A. Al-Khayat, *Mar. Environ. Res.*, 72 (2011) 143.
- [31] S.M. King, P.A. Leaf, A.C. Olson, P.Z. Ray, M.A. Tarr, *Chemosphere*, 95 (2014) 415.
- [32] R.C. Prince, R.M. Garrett, R.E. Bare, M.J. Grossman, T. Townsend, J.M. Suflita, K. Lee, E.H. Owens, G.A. Sergy, J.F. Braddock, J.E. Lindstrom, R.R. Lessard, *Spill Sci. Technol. Bull.*, 8 (2003) 145.
- [33] A. Islam, Y. Cho, U.H. Yim, W.J. Shim, Y.H. Kim, S. Kim, *J. Hazard. Mater.*, 263 (2013) 404.
- [34] A.G. Marshall, R.P. Rodgers, *Accounts Chem. Res.*, 37 (2004) 53.
- [35] C.S. Hsu, G.J. Dechert, D.J. Abbott, M.W. Genowitz, R. Barbour, in: C. Song, C.S. Hsu, I. Mochida (Eds.), *Chemistry of Diesel Fuels*, Taylor & Francis, New York, 2000.
- [36] A. Kabir, K.G. Furton, in: C.F. Poole (Ed.), *Gas Chromatography*, Elsevier, Waltham, MA, 2012.
- [37] R.B. Gaines, G.J. Hall, G.S. Frysinger, W.R. Gronlund, K.L. Juare, *Environ. Forensics*, 7 (2006) 77.
- [38] B.M. Zorzetti, J.J. Harynuk, *Anal. Bioanal. Chem.*, 401 (2011) 2423.

- [39] B.M. Zorzetti, J.M. Shaver, J.J. Harynuk, *Anal. Chim. Acta*, 694 (2011) 31.
- [40] J.S. Arey, R.K. Nelson, L. Xu, C.M. Reddy, *Anal. Chem.*, 77 (2005) 7172.
- [41] P.J. Marriott, in: E. Heftmann (Ed.), *Chromatography*, Elsevier, New York, NY, 2004.
- [42] J.V. Goodpaster, S.B. Howerton, V.L. McGuffin, *J. Forensic Sci.*, 46 (2001) 1358.
- [43] S.B. Howerton, J.V. Goodpaster, V.L. McGuffin, *Anal. Chim. Acta*, 459 (2002) 61.
- [44] R.M. Smith, in: E. Heftmann (Ed.), *Chromatography* Elsevier, New York, NY, 2004.
- [45] D.A. Skoog, F.J. Holler, S.R. Crouch, *Principles of Instrumental Analysis*, Thomson Brooks/Cole, Belmont, CA, 2007.
- [46] E. de Hoffmann, V. Stroobant, *Mass Spectrometry Principles and Applications*, John Wiley & Sons, Hoboken, NJ, 2007.
- [47] J.T. Watson, O.D. Sparkman, *Introduction to Mass Spectrometry*, John Wiley & Sons, Hoboken, NJ, 2007.
- [48] Z.D. Wang, M. Fingas, *J. Chromatogr. A*, 712 (1995) 321.
- [49] M. Commodo, I. Fabris, C.P.T. Groth, O.L. Gulder, *Energy Fuels*, 25 (2011) 2142.
- [50] D.J. Porter, P.M. Mayer, M. Fingas, *Energy Fuels*, 18 (2004) 987.
- [51] C.A. Hughey, C.L. Hendrickson, R.P. Rodgers, A.G. Marshall, K.N. Qian, *Anal. Chem.*, 73 (2001) 4676.
- [52] Z. Wang, J.H. Christensen, in: R.D. Morrison, B.L. Murphy (Eds.), *Environmental Forensics Contaminant Specific Guide*, Elsevier, Burlington, MA, 2006.
- [53] J.S. Arey, R.K. Nelson, C.M. Reddy, *Environ. Sci. Technol.*, 41 (2007) 5738.

- [54] Y.E. Corilo, D.C. Podgorski, A.M. McKenna, K.L. Lemkau, C.M. Reddy, A.G. Marshall, R.P. Rodgers, *Anal. Chem.*, 85 (2013) 9064.
- [55] C.A. Hughey, R.P. Rodgers, A.G. Marshall, *Anal. Chem.*, 74 (2002) 4145.
- [56] C.E. Rostad, F.D. Hostettler, *Environ. Forensics*, 8 (2007) 129.
- [57] C. Le Vot, C. Afonso, C. Beaugrand, J.C. Tabet, *Int. J. Mass Spectrom.*, 367 (2014) 35.
- [58] Y.H. Kim, S. Kim, *J. Am. Soc. Mass Spectrom.*, 21 (2010) 386.
- [59] C.H. Marvin, R.W. Smith, D.W. Bryant, B.E. McCarry, *J. Chromatogr. A*, 863 (1999) 13.
- [60] R.K. Jones, *Proceedings; Environmental Canada Twentieth Arctic and Marine Oilspill Program Technical Seminar*, 1 (1997) 43.
- [61] R.L. Brown, S.E. Stein, in: P.J. Linstrom, W.G. Mallard (Eds.), *NIST Chemistry Webbook, NIST Standard Reference Database Number 69*, National Institute of Standards and Technology, Gaithersburg, MD, 2011. <http://webbook.nist.gov>, (retrieved February 26, 2014).
- [62] D. Mackay, W.Y. Shiu, K.C. Ma, *Illustrated Handbook of Physical-Chemical Properties and Environmental Fate for Organic Chemicals* Lewis, Chelsea, MI, 1993.
- [63] W.M. Haynes (Ed.), *Crc Handbook of Chemistry and Physics*, CRC Press, Boca Raton, FL, 2011.
- [64] K. Heberger, in: C.F. Poole (Ed.), *Gas Chromatography*, Elsevier, Waltham, MA, 2012.
- [65] F. Sauracalixto, A. Garciaraso, P.M. Deya, *J. Chromatogr. Sci.*, 20 (1982) 7.
- [66] H. Vandendool, P.D. Kratz, *J. Chromatogr.*, 11 (1963) 463.

- [67] IUPAC, Compendium of Chemical Terminology (the "Gold Book"), Blackwell Scientific Publications, Oxford, 1997.
- [68] R. Kaliszan, Structure and Retention in Chromatography, Harwood Academic Publishers, Amsterdam, The Netherlands, 1997.
- [69] S.E. Stein, in: P.J. Linstrom, W.G. Mallard (Eds.), NIST Chemistry Webbook, NIST Standard Reference Database Number 69, National Institute of Standards and Technology, Mass Spec Data Center, Gaithersburg, MD, 2011. <http://webbook.nist.gov>, (retrieved February 26, 2014).
- [70] J. Beegle-Krause, International Oil Spill Conference Proceedings, 2001 (2001) 865.
- [71] National Oceanic and Atmospheric Administration, Gnome. <http://response.restoration.noaa.gov/oil-and-chemical-spills/oil-spills/response-tools/gnome.html>. May 6, 2014.
- [72] A. Berry, Development of OILTRANS Model Code, 2011. [http://www.arcopol.eu/arcopol/archivos/documentacion/102/Development\\_OILTRANS\\_model\\_code.pdf](http://www.arcopol.eu/arcopol/archivos/documentacion/102/Development_OILTRANS_model_code.pdf). 2/17/2014.
- [73] A. Berry, T. Dabrowski, K. Lyons, Mar. Pollut. Bull., 64 (2012) 2489.
- [74] ASA, ASA, SIMAP Integrated Oil Spill Impact Modeling System. <http://www.asascience.com/software/simap/>. May 7, 2014.
- [75] M. Reed, E. Gundlach, T. Kana, Oil and Chemical Pollution, 5 (1989) 411.
- [76] M. Reed, O.M. Aamo, P.S. Daling, Spill Sci. Technol. Bull., 2 (1995) 67.
- [77] M. Reed, N. Ekrol, H. Rye, L. Turner, Spill Sci. Technol. Bull., 5 (1999) 29.
- [78] M.L. Spaulding, V.S. Kolluru, E. Anderson, E. Howlett, Spill Sci. Technol. Bull., 1 (1994) 23.
- [79] A.H. Al-Rabeh, R.W. Lardner, N. Gunay, Environ. Modell. Softw., 15 (2000) 425.

- [80] P. Carracedo, S. Torres-López, M. Barreiro, P. Montero, C.F. Balseiro, E. Penabad, P.C. Leitao, V. Pérez-Muñuzuri, *Mar. Pollut. Bull.*, 53 (2006) 350.
- [81] P. Annika, T. George, P. George, N. Konstantinos, D. Costas, C. Koutitas, *Mar. Pollut. Bull.*, 43 (2001) 270.
- [82] B. Hackett, Ø. Breivik, C. Wettré, in: E. Chassignet, J. Verron (Eds.), *Ocean Weather Forecasting*, Springer Netherlands, 2006, p. 507.
- [83] M. De Dominicis, N. Pinardi, G. Zodiatis, R. Lardner, *Geosci. Model Dev.*, 6 (2013) 1851.
- [84] M. De Dominicis, N. Pinardi, G. Zodiatis, R. Archetti, *Geosci. Model Dev.*, 6 (2013) 1871.
- [85] M. De Dominicis, S. Falchetti, F. Trotta, N. Pinardi, L. Giacomelli, E. Napolitano, L. Fazioli, R. Sorgente, P. Haley Jr, P. J. Lermusiaux, F. Martins, M. Cocco, *Ocean Dynamics*, 64 (2014) 667.
- [86] J.K. Jolliff, T.A. Smith, S. Ladner, R.A. Arnone, *Ocean Model.*, 75 (2014) 84.
- [87] R.P. Schwarzenbach, P.M. Gschwend, D.M. Imboden, *Environmental Organic Chemistry*, John Wiley & Sons, Hoboken, NJ, 2003.
- [88] M.F. Fingas, *J. Hazard. Mater.*, 57 (1998) 41.
- [89] K. Okamoto, N. Watanabe, Y. Hagimoto, K. Miwa, H. Ohtani, *J. Loss Prev. Process Ind.*, 23 (2010) 89.
- [90] K.T. Valsaraj, *Elements of Environmental Engineering: Thermodynamics and Kinetics*, CRC Press, Boca Raton, FL, 1995.
- [91] K. Okamoto, N. Watanabe, Y. Hagimoto, K. Miwa, H. Ohtani, *Fire Saf. J.*, 44 (2009) 756.
- [92] Z.R. Regnier, B.F. Scott, *Environ. Sci. Technol.*, 9 (1975) 469.

- [93] W. Stiver, W.Y. Shiu, D. Mackay, *Environ. Sci. Technol.*, 23 (1989) 101.
- [94] G. Loncar, G.B. Paklar, I. Janekovic, *J. Appl. Math.* (2012) 20.
- [95] F. Heymes, L. Aprin, A. Bony, S. Forestier, S. Cirocchi, G. Dusserre, *Process Saf. Prog.*, 32 (2013) 193.
- [96] M.R. Riazi, G.A. Al-Enezi, *Chem. Eng. J.*, 73 (1999) 161.
- [97] M. Fingas. *Proceedings of the 1999 International Oil Spill Conference*, American Petroleum Institute, Washington, DC, (1999) 185.
- [98] M.F. Fingas, *J. Hazard. Mater.*, 56 (1997) 227.
- [99] M.F. Fingas (Ed.), *Oil Spill Science and Technology: Prevention, Response, and Cleanup*, Elsevier, Burlington, MA, 2011.
- [100] W. Stiver, D. Mackay, *Environ. Sci. Technol.*, 18 (1984) 834.
- [101] A.H. Alrabeh, H.M. Cekirge, N. Gunay, *Appl. Math. Model.*, 13 (1989) 322.
- [102] J.R. Payne, B.E. Kirstein, G.D. McNabb, J.L. Lambach, C. de Oliveira, R.E. Jordan, W. Hom, *International Oil Spill Conference Proceedings*, 1983 (1983) 423.
- [103] M.F. Fingas, *J. Hazard. Mater.*, 42 (1995) 157.
- [104] M.F. Fingas, *J. Hazard. Mater.*, 107 (2004) 27.
- [105] R.L. Smith, *Ann. Occup. Hyg.*, 45 (2001) 437.
- [106] O.G. Sutton, *Proceedings of the Royal Society of London. Series A, Containing Papers of a Mathematical and Physical Character*, 146 (1934) 701.
- [107] D. Mackay, R.S. Matsugu, *Can. J. Chem. Eng.*, 51 (1973) 434.

- [108] R. Jones, *Journal of Environmental Engineering*, 122 (1996) 761.
- [109] ASTM Standard D86-04b, 2004, Standard Test Method for Distillation of Petroleum Products at Atmospheric Pressure, ASTM International, West Conshohocken, PA, 2004, <<http://www.astm.org/>>.
- [110] M.R. Riazi, M. Edalat, *J. Pet. Sci. Eng.*, 16 (1996) 291.
- [111] W.C. Yang, H. Wang, *Water Res.*, 11 (1977) 879.
- [112] U.H. Yim, S.Y. Ha, J.G. An, J.H. Won, G.M. Han, S.H. Hong, M. Kim, J.H. Jung, W.J. Shim, *J. Hazard. Mater.*, 197 (2011) 60.
- [113] J.N. Butler, *Marine Chemistry*, 3 (1975) 9.
- [114] J.N. Butler, in: H.L. Windom, R.A. Duce (Eds.), *Marine Pollutant Transfer*, Lexington Books, Lexington, MA, 1976.
- [115] D.E. Nicodem, C.L.B. Guedes, R.J. Correa, *Marine Chemistry*, 63 (1998) 93.
- [116] C. Aeppli, C.A. Carmichael, R.K. Nelson, K.L. Lemkau, W.M. Graham, M.C. Redmond, D.L. Valentine, C.M. Reddy, *Environ. Sci. Technol.*, 46 (2012) 8799.
- [117] A. Gilbert, J. Baggott, *Essentials of Molecular Photochemistry*, CRC Press, Boca Raton, FL, 1991.
- [118] J.R. Radovic, C. Aeppli, R.K. Nelson, N. Jimenez, C.M. Reddy, J.M. Bayona, J. Albaiges, *Mar. Pollut. Bull.*, 79 (2014) 268.
- [119] M.T. Griffiths, R. Da Campo, P.B. O'Connor, M.P. Barrow, *Anal. Chem.*, 86 (2014) 527.
- [120] M.P. Fasnacht, N.V. Blough, *Aquat. Sci.*, 65 (2003) 352.
- [121] R.J. Correa, D. Severino, R.D. Souza, E.F. de Santana, L.L. Mauro, S.D.S. Alvarenga, D.E. Nicodem, *J. Photochem. Photobiol. A-Chem.*, 236 (2012) 9.

- [122] D.E. Nicodem, M.C.Z. Fernandes, C.L.B. Guedes, R.J. Correa, *Biogeochemistry*, 39 (1997) 121.
- [123] D.E. Nicodem, C.L.B. Guedes, M.C.Z. Fernandes, D. Severino, R.J. Correa, M.C. Coutinho, J. Silva, *Prog. React. Kinet. Mech.*, 26 (2001) 219.
- [124] F. ThomINETTE, J. Verdu, *Marine Chemistry*, 15 (1984) 91.
- [125] M.P. Fasnacht, N.V. Blough, *Environ. Sci. Technol.*, 37 (2003) 5767.
- [126] M.P. Fasnacht, N.V. Blough, *Environ. Sci. Technol.*, 36 (2002) 4364.
- [127] P.F. Pesarini, R.G.S. de Souza, R.J. Correa, D.E. Nicodem, N.C. de Lucas, J. *Photochem. Photobiol. A-Chem.*, 214 (2010) 48.
- [128] D.L. Plata, C.M. Sharpless, C.M. Reddy, *Environ. Sci. Technol.*, 42 (2008) 2432.
- [129] M. D'Auria, L. Emanuele, R. Racioppi, V. Velluzzi, *J. Hazard. Mater.*, 164 (2009) 32.
- [130] R.G. Zepp, D.M. Cline, *Environ. Sci. Technol.*, 11 (1977) 359.
- [131] J.R. Payne, C.R. Phillips, *Environ. Sci. Technol.*, 19 (1985) 569.
- [132] M.C. DeRosa, R.J. Crutchley, *Coord. Chem. Rev.*, 233 (2002) 351.
- [133] R.G. Zepp, P.F. Schlotzhauer, in: P.W. Jones, P. Leber (Eds.), *Polynuclear Aromatic Hydrocarbons Third International Symposium on Chemistry and Biology-Carcinogenesis and Mutagenesis*, Ann Arbor Science Publishers, Ann Arbor, MI, 1979.
- [134] A. Leifer, *The Kinetics of Environmental Aquatic Photochemistry: Theory and Practice*, American Chemical Society, Washington, DC, 1988.
- [135] T. Mill, *Chemosphere*, 38 (1999) 1379.

[136] R. Larson, L. Forney, L. Grady Jr., G.M. Klecka, S. Masunaga, W. Peijnenburg, L. Wolfe, in: G. Klecka, B. Beoethling, J. Franklin, L. Grady, D. Graham, P.H. Howard, K. Kannan, R.J. Larson, D. Mackay, D. Muir, D. van de Meent (Eds.), *Evaluation of Persistence and Long-Range Transport of Organic Chemicals in the Environment*, SETAC Press, Pensacola, FL, 2000.

[137] M. Gutierrez, M. Luiz, N.A. Garcia, *Scientia Marina*, 58 (1994) 207.

[138] R.M. Garrett, I.J. Pickering, C.E. Haith, R.C. Prince, *Environ. Sci. Technol.*, 32 (1998) 3719.

[139] C.S. Hsu, V.V. Lobodin, R.P. Rodgers, A.M. McKenna, A.G. Marshall, *Energy Fuels*, 25 (2011) 2174.

## **2. Gas Chromatographic Retention Index as a Basis for Predicting Evaporation Rates of Complex Mixtures**

### **2.1 Introduction**

The 2010 Deepwater Horizon oil spill in the Gulf of Mexico highlighted the environmental hazards of petroleum discharges and the knowledge gaps that hinder accurate impact assessment and remediation [1]. In particular, predicting the fate and transport of petroleum continues to be an ongoing challenge. Discharged petroleum constituents are distributed between air, water, and sediment on the basis of their physical and chemical properties. The composition of a spill is continuously altered by physical, chemical, and biological weathering processes that begin immediately after a release occurs [2]. Physical weathering processes, including evaporation, change pollutant distribution by transporting constituents away from the initial point of release [2]. Evaporation is the most prevalent contributor to losses of volatile petroleum constituents, often accounting for up to 75% of the mass loss, and is therefore a critical component to oil spill models [2-11]. The weathering processes continuously change the composition of the fuel, as well as altering physical properties such as viscosity and density, making comprehensive modeling very challenging [9, 12, 13]. Accurate predictive models are necessary to determine the presence and loss of compounds, time of release [14, 15], and source [16-18] of environmental spills.

The current models used to predict evaporation (Chapter 1) rely on estimations of physical properties which increases uncertainty in the model or empirical measurements which make extrapolation of the model challenging. Also, current models focus on

monitoring the evaporation of the bulk fuel, rather than the individual compounds within the fuel. In this work, empirical measurements were utilized to determine evaporation rate constants for individual compounds within the complex mixture. These rate constants were employed to build mathematical expressions to predict evaporation rates for each compound. This approach has been previously used to determine evaporation rate constants for normal alkanes in diesel fuel [19]. Regnier and Scott [19] demonstrated that evaporation rate constants for the normal alkanes between *n*-nonane and *n*-octadecane were first-order and could be predicted based on the vapor pressure of the normal alkane. In work by Smith [20], first-order evaporation rate constants were calculated for individual compounds in a simple mixture based on the vapor pressure and mass transfer coefficient of that compound, as well as the surface area, temperature, and total number of moles in the spill. These works have demonstrated that first-order rate constants can be utilized to determine the evaporation rate for individual compounds from a simulated petroleum spill. However, in these previous works, only major constituents were monitored, and no predictive model for all compounds was developed.

The use of physical properties, such as vapor pressure and boiling point, to predict evaporation rates is theoretically based and accurate. However, it is cumbersome for complex mixtures because of the large number of compounds. The use of physical properties requires that the individual compounds be identified and that the corresponding magnitude of the property be known. The prediction of physical properties by means of analytical measurements is well reported in the literature [21-23]. Arey *et al.* [24] showed that the retention index (*I*) in gas chromatography (GC) on a non-polar stationary phase can be used to estimate the vapor pressure and boiling point. In addition, the retention

index on a second, polar stationary phase (i.e., 2-dimensional GC, or GC x GC) can be used to estimate other physical properties such as water solubility and octanol–water partition coefficient. GC x GC can also provide better separation of compounds, which can assist in compound identification, especially when used with in conjunction with mass spectrometry [25, 26].

An empirically-derived surrogate measurement, such as GC retention index, has several distinct advantages. First, it will allow the development of a theoretically based and accurate model of evaporation, without the challenges associated with using physical properties. Moreover, it will obviate the need to identify the compounds present in a complex mixture in order to predict the evaporation rates. To demonstrate these concepts, models were developed in this study to predict the kinetic rate constant for evaporation of individual compounds, first based on boiling point, then based on GC retention index. From the predicted kinetic rate constants, the fraction remaining of each individual compound, as well as the fraction remaining of total fuel can be estimated.

## **2.2 Materials and Methods**

### *2.2.1 Sample Collection*

Diesel fuel was chosen as an illustrative complex mixture because of its wide range of compounds (aliphatic, substituted aromatics, and polycyclic aromatic hydrocarbons) and boiling points (~ 100 – 400 °C). Diesel fuel is also well suited for analysis by gas chromatography-mass spectrometry (GC-MS). Diesel fuel was collected from a local service station in East Lansing, Michigan in July of 2010. The fuel was transferred to acid-washed amber bottles and stored at approximately 5 °C until use.

Several other petroleum fuels were used for the validation studies. Kerosene was purchased from a local service station in July of 2010 and stored in amber bottles at approximately 5 °C. Marine fuel stabilizer (Pennzoil, Houston, TX) was purchased and stored in its original container.

### *2.2.2 Evaporation Chamber*

An evaporation chamber was constructed to isolate external vibrations, maintain constant temperature and humidity, control air flow, and minimize explosion hazards (Figure 2-1). The chamber was fabricated from aluminum owing to its favorable thermal properties. A Plexiglas front panel allowed for viewing of the samples, while a door in the panel provided access to the interior of the chamber. A vibration-isolated shelf was constructed to minimize any external disturbance of the samples. To control temperature, the evaporation chamber was placed into an Ambi-Hi-Lo incubator (5 – 50 °C ± 0.5 °C, model 3550DT, Lab-Line, Melrose Park, IL). To control relative humidity (RH), trays of distilled water were placed inside the evaporation chamber. Temperature and humidity were monitored and recorded at two-minute intervals using a data logger (0 – 55 °C ± 0.3 °C , 10 – 95% RH ± 5% RH, model TR-74Ui, T & D Corporation, Nagano, Japan). A peristaltic pump (Masterflex L/S drive, model 7523-40, with L/S Easy-Load II pump head, model 77200-62, Cole-Parmer, Vernon Hills, IL) with Viton tubing (Cole-Parmer) circulated the air within the chamber (~ 80 mL min<sup>-1</sup>). A copper tube (12 in x 0.5 in OD x 0.37 in ID) filled with activated carbon (6 – 14 mesh, Fisher Scientific, Waltham, MA) was placed in-line to remove volatile compounds as they evaporated from the diesel fuel,

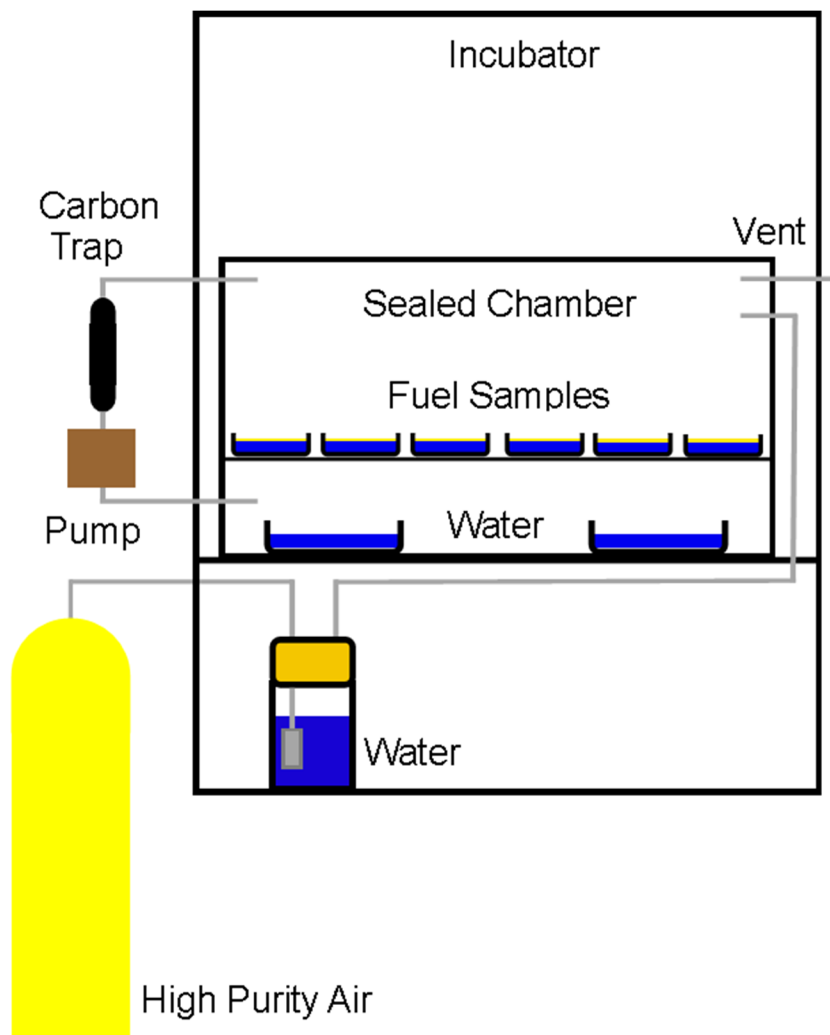


Figure 2-1. Schematic diagram of the evaporation chamber in temperature-controlled incubator. See Section 2.2.2 for detailed description.

thereby minimizing the explosion hazard. Additional dishes of activated carbon were placed in the evaporation chamber and Ambi-Hi-Lo Incubator. High purity air was also introduced to the chamber ( $\sim 30 \text{ mL min}^{-1}$ ) after being sparged through distilled water located in the temperature-controlled oven.

### *2.2.3 Evaporation of Diesel Fuel*

To develop the models, a thin film of diesel fuel (1.0 mL,  $\sim 0.5 \text{ mm}$ ) on distilled water (15 mL) was evaporated in glass petri dishes (60 mm ID x 15 mm). Diesel samples were evaporated at  $20 \text{ }^\circ\text{C}$  in triplicate for nine different lengths of time (0 – 300 h). For the validation studies, three different fuel samples, diesel, kerosene, and marine fuel stabilizer, were evaporated at  $20 \text{ }^\circ\text{C}$  for 100 h. For diesel fuel, three petri dishes were prepared with fuel and water as previously described. An additional three dishes were prepared with the fuel alone. These latter dishes were weighed before and after evaporation in order to determine the mass lost. For kerosene and marine fuel stabilizer, two petri dishes were prepared with fuel and water and another dish with the fuel alone.

### *2.2.4 Gas Chromatography-Mass Spectrometry Analysis*

After evaporation, the fuel residues were extracted from the petri dishes for GC-MS analysis. Approximately 1 mL of dichloromethane was added to each dish, then the diesel/water/dichloromethane mixture was quantitatively transferred to a separatory funnel. The petri dish was rinsed with additional 2 – 3 mL aliquots of dichloromethane, which were combined with the first in the separatory funnel. The organic layer was transferred to a 10.0 mL volumetric flask. The extracted diesel residue was further diluted

(1:50) in dichloromethane and transferred to a sealed autosampler vial for GC-MS analysis.

All analyses were performed using a gas chromatograph (model 7890N, Agilent Technologies, Santa Clara, CA) with an automatic liquid sampler (model 7693, Agilent Technologies) that was coupled to a mass spectrometer (model 5975, Agilent Technologies). The GC was equipped with a capillary column containing a 100% poly(dimethylsiloxane) stationary phase (HP-1MS, 30 m x 0.25 mm x 0.25  $\mu\text{m}$ , Agilent Technologies). Compounds generally elute from this nonpolar stationary phase based on boiling point owing to the weak interactions between the compound and stationary phase. Ultra-high-purity helium was used as the carrier gas (1 mL  $\text{min}^{-1}$ ). The diluted diesel extract (1  $\mu\text{L}$ ) was injected using a pulsed (15 psi for 0.25 min) split (50:1) injection at 280  $^{\circ}\text{C}$  (the injection optimization is discussed below). The GC temperature program began at 50  $^{\circ}\text{C}$  with a 5  $^{\circ}\text{C min}^{-1}$  ramp rate to 280  $^{\circ}\text{C}$  and a final hold time of 4 min. The transfer line was maintained at 300  $^{\circ}\text{C}$ . The mass spectrometer employed electron ionization (70 eV) with a quadrupole mass analyzer, which scanned mass-to-charge ratios ( $m/z$ ) 40 – 550 at a scan rate of 2.91 scans  $\text{s}^{-1}$ .

An optimization was performed to minimize variation from injection in the GC-MS analysis. Five normal alkanes ( $\text{C}_8$ ,  $\text{C}_{10}$ ,  $\text{C}_{12}$ ,  $\text{C}_{14}$ , and  $\text{C}_{16}$ ), spanning a large range of volatilities, were analyzed five times by GC-MS and the precision of the injection was monitored using percent relative standard deviation (RSD) in the peak area. The injection parameters that were tested included the pre- and post-injection dwell time, the pulsed injection pressure and time, and the gas saver on or off (Table 2-1). The injection dwell time is the length of time that the syringe is left in the injection port prior to or after injection.

A longer pre-injection dwell time helps the syringe to heat prior to injection, resulting in more efficient volatilization. A longer post-injection dwell time ensures all of the sample is delivered from the syringe. The pressure pulse prior to injection forces the sample onto the column more quickly and minimizes degradation of the sample. The gas saver reduces the flow rate from the split valve to minimize consumption of carrier gas. Optimization (Table 2-1) resulted in increased precision of injection, with the average RSD of the five normal alkanes decreasing from 8.5% prior to optimization to 2.9% after optimization.

#### *2.2.5 Identification and Quantification of Selected Compounds*

After GC-MS analysis of the diesel fuel, individual compounds were identified and quantified (Table 2-2). First, compound classes were assigned based on characteristic fragment ions: normal alkanes ( $m/z$  57), branched and cyclic alkanes ( $m/z$  57 and  $m/z$  83), alkyl aromatics ( $m/z$  91 and  $m/z$  105), and polycyclic hydrocarbons ( $m/z$  91,  $m/z$  117, and  $m/z$  128) [18, 27]. The  $m/z$  values of these fragments were used to generate extracted ion chromatograms (EICs) that were characteristic of each compound class [18]. By employing EICs, there was less interference from co-eluting compounds and an increased signal-to-noise ratio, which allowed for detection of low-abundance compounds. The total ion chromatogram (TIC) and example EICs for each compound class are shown in Figure 2-2 to Figure 2-8. The selected compounds that are numbered correspond to the peak numbers in Table 2-2.

Table 2-1. The injection parameters optimized using the precision in peak area of a mixture of five normal alkanes.

<b>Parameter</b>	<b>Range tested</b>	<b>Optimized Value</b>
Pre-injection dwell time	0 – 0.06 min	0.02 min
Post-injection dwell time	0 – 0.08 min	0.05 min
Pressure pules	No pulse – 40 psi	15 psi
Pulse duration	0.1 – 1 min	0.25 min
Gas saver	On/off	Off

Compounds were identified by searching against a database of mass spectra (NIST/EPA/NIH Mass Spectral Library 02, Version 2.0a, Agilent Technologies). To help identify some structural isomers, relative retention indices were compared to literature values [28]. In some cases, compounds could only be provisionally identified and were assigned to a compound class based on characteristic ions from their mass spectra. Seventy-eight selected compounds were monitored over the course of the evaporation experiments, of which forty-six were definitively identified. Selection of compounds to monitor was based on the ability to identify/classify the compound, the volatility of the compound, and the abundance being greater than ~20% of the maximum peak in the EIC.

To assist in identifying compounds and as part of the model development, the retention index under temperature-programmed conditions ( $I^T$ ) was calculated for each selected compound. The retention index is calculated based on the retention time of the compound of interest ( $t_{R,i}^T$ ) and the retention time of the normal alkanes of carbon number  $z$  that elute before ( $t_{R,z}^T$ ) and after ( $t_{R,z+1}^T$ ) [29, 30].

$$I^T = 100 \left[ \frac{t_{R,i}^T - t_{R,z}^T}{t_{R,z+1}^T - t_{R,z}^T} + z \right] \quad \text{Equation 2-1}$$

The index is independent of GC parameters such as column dimensions, stationary phase thickness, flow rate, and temperature program and, hence, is more broadly applicable than retention time or retention factor. The retention index is an advantageous surrogate over physical properties in the development of the model,

Table 2-2. Selected compounds monitored during evaporation of diesel fuel to develop the model. The following information is listed for each compound: compound class, peak number (#) (corresponding to peaks labeled in Figure 2-3 – Figure 2-8), mass-to-charge ratio ( $m/z$ ) of extracted ion chromatogram used for quantification, retention time ( $t_R^T$ ), boiling point ( $T_B$ ), retention index ( $I^T$ ), rate constant ( $k$ ), characteristic lifetime ( $\tau$ ), and number of  $\tau$  in 300 hours. For the compound class the follow abbreviations were used: normal alkane (Norm), branched alkane (Bran), alkyl aromatic (Arom), polycyclic hydrocarbon (Poly).

Compound	Class	#	$m/z$	$t_R^T$ (min)	$T_B$ (K)*	$I^T$	$k$ (h <sup>-1</sup> )	$\tau$ (h)	# $\tau$ in 300 h
2-Methyl heptane	Bran	1	57	3.398	391		0.308	3.24	92.52
Octane	Norm	2	57	3.748	399	800	0.226	4.43	67.69
4-Methyl octane	Bran	3	57	4.814	415	862	0.108	9.27	32.36
3-Methyl octane	Bran	4	57	4.948	417	869	0.097	10.29	29.15
Nonane	Norm	5	57	5.479	424	900	0.066	15.19	19.75
Dimethyl octane isomer	Bran	6	57	6.248		933	0.045	22.08	13.59
Ethyl methyl heptane isomer	Bran	7	57	6.411		940	0.044	22.76	13.18
Methyl nonane isomer	Bran	8	57	6.883		960	0.033	30.30	9.90
Unidentified	Bran	9	57	7.105		970	0.029	34.67	8.65
Decane	Norm	10	57	7.816	447	1000	0.020	49.75	6.03
4-Methyl decane	Bran	11	57	8.434	460	1024	0.016	61.08	4.91
5-Methyl decane	Bran	12	57	9.326		1058	0.012	84.53	3.55

Table 2-2 cont'd

Compound	Class	#	m/z	$t_R^T$ (min)	$T_B$ (K)*	$I^T$	$k$ (h <sup>-1</sup> )	$\tau$ (h)	# $\tau$ in 300 h
2-Methyl decane	Bran	13	57	9.506	462	1064	0.011	95.18	3.15
3-Methyl decane	Bran	14	57	9.670		1071	0.010	97.63	3.07
Undecane	Norm	15	57	10.439	468	1100	0.007	134.07	2.24
Unidentified	Bran	16	57	11.960		1155	0.005	219.07	1.37
Methyl undecane isomer	Bran	17	57	12.217		1165	0.004	255.54	1.17
Unidentified	Bran	18	57	12.392		1171	0.004	258.38	1.16
Dodecane	Norm	19	57	13.184	489	1200	0.002	453.77	0.66
2,6-Dimethyl undecane	Bran	20	57	13.616		1216	0.002	495.57	0.61
Unidentified	Bran	21	57	14.618		1254	0.001	771.87	0.39
Unidentified	Bran	22	57	15.213		1276	0.001	1182.54	0.25
Tridecane	Norm	23	57	15.848	507	1300	0.000	2041.5	0.15
Unidentified	Bran	24	57	17.527		1365	0.000	40719.8	0.01
2,6,10- Trimethyl decane	Bran	25	57	17.900		1379			
Tetradecane	Norm	26	57	18.430	523	1400			
Unidentified	Bran	27	57	20.027		1465			

Table 2-2 cont'd

Compound	Class	#	m/z	$t_R^T$ (min)	$T_B$ (K)*	$I^T$	$k$ (h <sup>-1</sup> )	$\tau$ (h)	# $\tau$ in 300 h
Pentadecane	Norm	28	57	20.890	540	1500			
Hexadecane	Norm	29	57	23.186	554	1600			
2,6,10- Trimethyl pentadecane	Bran	30	57	24.369		1654			
Heptadecane	Norm	31	57	25.395	575	1700			
Pristane	Bran	32	57	25.628		1711			
Octadecane	Norm	33	57	27.488	589	1800			
Phytane	Bran	34	57	27.791		1815			
Nonadecane	Norm	35	57	29.539		1900			
Eicosane	Norm	36	57	31.400	616	2000			
Heneicosane	Norm	37	57	33.276	635	2100			
Methyl cyclohexane	Bran	38	83	2.856	374		0.621	1.61	186.37
Ethyl cyclohexane	Bran	39	83	4.226	405	828	0.181	5.53	54.25
Propyl cyclohexane	Bran	40	83	6.067	429	925	0.059	17.06	17.59
Butyl cyclohexane	Bran	41	83	8.527	453	1027	0.018	54.77	5.48
Pentyl cyclohexane	Bran	42	83	11.272	477	1130	0.007	146.06	2.05

Table 2-2 cont'd

Compound	Class	#	m/z	$t^T_R$ (min)	$T_B$ (K)*	$I^T$	$k$ (h <sup>-1</sup> )	$\tau$ (h)	# $\tau$ in 300 h
Hexyl cyclohexane	Bran	43	83	14.288	498	1241	0.002	491.22	0.61
Heptyl cyclohexane	Bran	44	83	16.833	510	1338	0.000	2371.08	0.13
Octyl cyclohexane	Bran	45	83	19.462	528	1442			
Toluene	Arom	46	91	3.194	384		0.486	2.06	145.81
Ethyl benzene	Arom	47	91	4.511	409	844	0.170	5.89	50.95
<i>m/p</i> -Xylene	Arom	48	91	4.663	412	853	0.135	7.39	40.57
<i>o</i> -Xylene	Arom	49	91	5.071	417	876	0.111	9.03	33.24
Propyl benzene	Arom	50	91	6.365	432	938	0.055	18.05	16.62
Butyl benzene	Arom	51	91	8.871	456	1040	0.017	57.36	5.23
Unidentified	Arom	52	91	10.171		1090	0.011	94.32	3.18
1,2,3,4- Tetrahydro- naphthalene	Poly	53	91	11.465	480	1137	0.008	133.32	2.25
Pentyl benzene	Arom	54	91	11.576		1141	0.007	148.60	2.02
Methyl tetralin isomer	Poly	55	91	12.980		1193	0.004	227.41	1.32
Unidentified	Poly	56	91	17.066		1347	0.001	1980.24	0.15
Unidentified	Poly	57	91	19.660		1450			

Table 2-2 cont'd

Compound	Class	#	m/z	$t_R^T$ (min)	$T_B$ (K)*	$I^T$	$k$ (h <sup>-1</sup> )	$\tau$ (h)	# $\tau$ in 300 h
Ethyl methyl benzene isomer	Arom	58	105	6.534		945	0.047	21.50	13.96
1,3,5-Trimethyl benzene	Arom	59	105	6.720	438	953	0.037	26.99	11.11
Ethyl Methyl benzene isomer	Arom	60	105	6.930		962	0.040	25.02	11.99
1,2,4-Trimethyl benzene	Arom	61	105	7.291	442	978	0.032	31.40	9.56
Unidentified	Arom	62	105	7.734		996	0.028	35.28	8.50
1,2,3-Trimethyl benzene	Arom	63	105	7.950	449	1005	0.025	39.49	7.60
Methyl propyl benzene isomer	Arom	64	105	8.754		1036	0.018	56.47	5.31
Methyl propyl benzene isomer	Arom	65	105	8.854		1040	0.017	59.02	5.08
Methyl propyl benzene isomer	Arom	66	105	9.139		1050	0.016	62.08	4.83
Unidentified	Arom	67	105	10.113		1088	0.011	91.90	3.26
Indane	Poly	68	117	8.212	450	1015	0.027	37.16	8.07
Methyl indane isomer	Poly	69	117	9.565		1067	0.015	66.96	4.48

Table 2-2 cont'd

Compound	Class	#	m/z	$t^T_R$ (min)	$T_B$ (K)*	$I^T$	$k$ (h <sup>-1</sup> )	$\tau$ (h)	# $\tau$ in 300 h
Unidentified	Poly	70	117	10.958		1119	0.009	112.48	2.67
Unidentified	Poly	71	117	11.220		1128	0.008	118.47	2.53
Unidentified	Poly	72	117	13.516		1212	0.004	271.36	1.11
Methyl tetralin isomer	Poly	73	117	14.303		1242	0.003	379.08	0.79
Methyl tetralin isomer	Poly	74	117	14.974		1267	0.002	468.15	0.64
Methyl tetralin isomer	Poly	75	117	15.760		1297	0.001	787.51	0.38
Methyl tetralin isomer	Poly	76	117	16.349		1319	0.001	1110.96	0.27
Methyl tetralin isomer	Poly	77	117	17.591		1368	0.000	2785.81	0.11
Naphthalene	Poly	78	128	11.949	491	1155	0.008	127.33	2.36

\* Source reference [31]

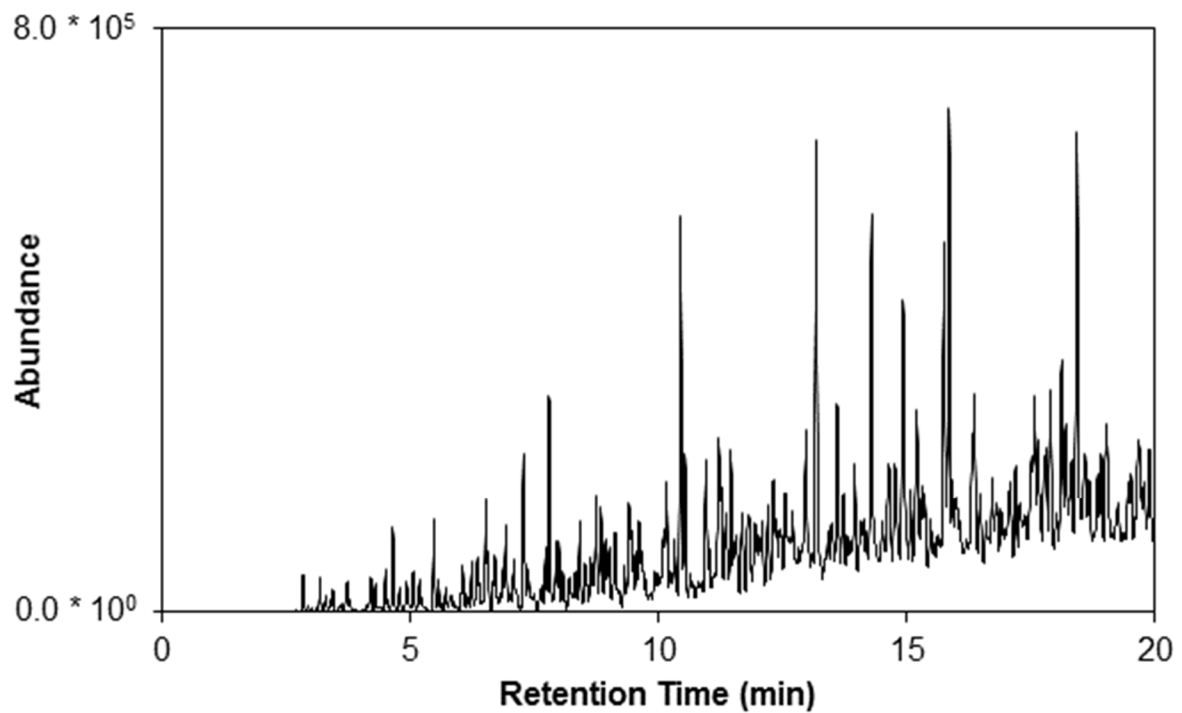
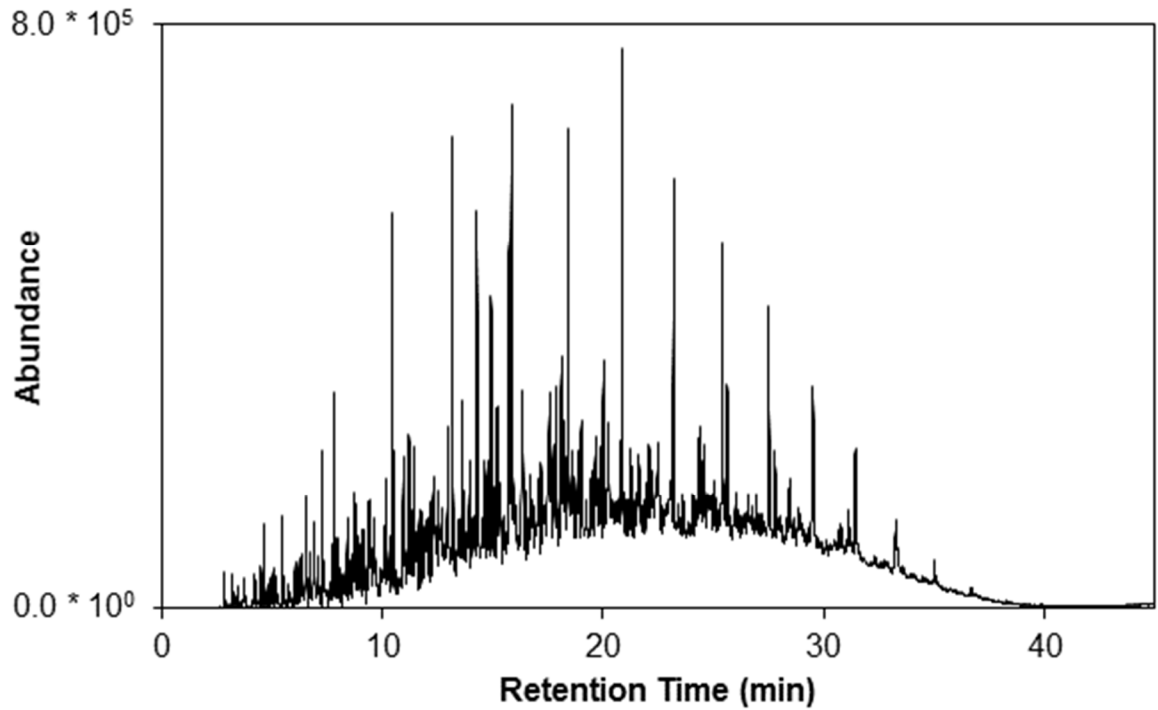


Figure 2-2. Total ion chromatogram for diesel fuel. The bottom trace is an expanded portion of the chromatogram, showing the region where more volatile compounds are observed.

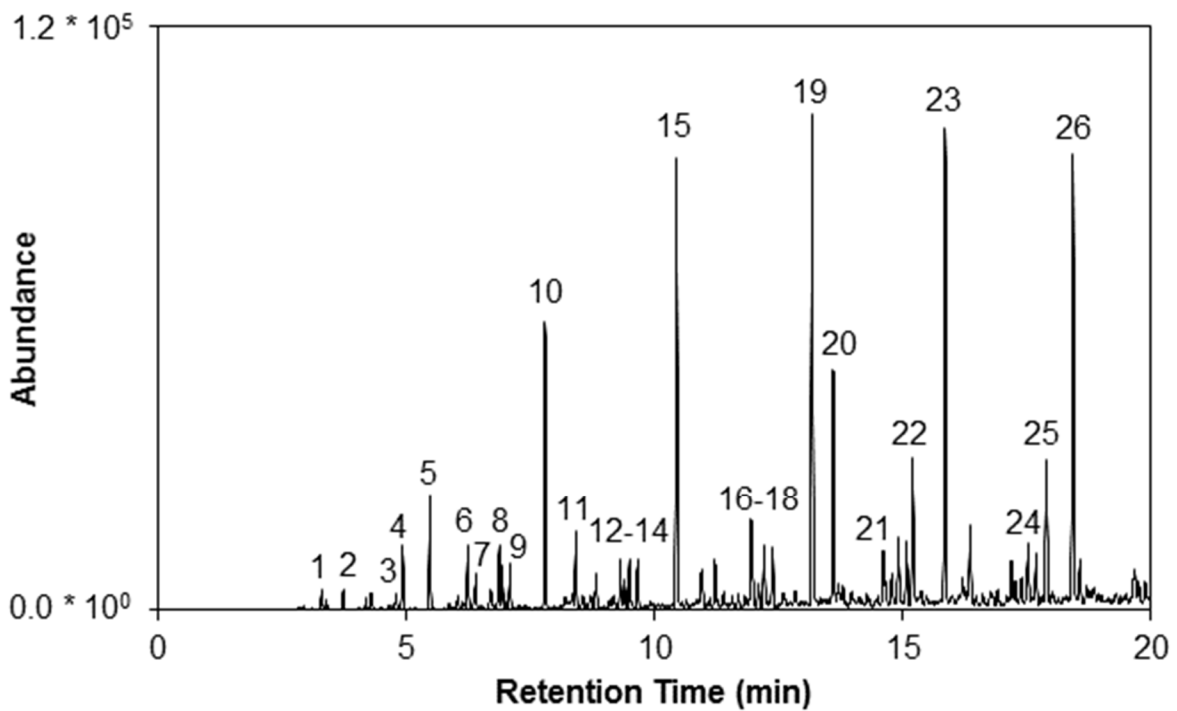
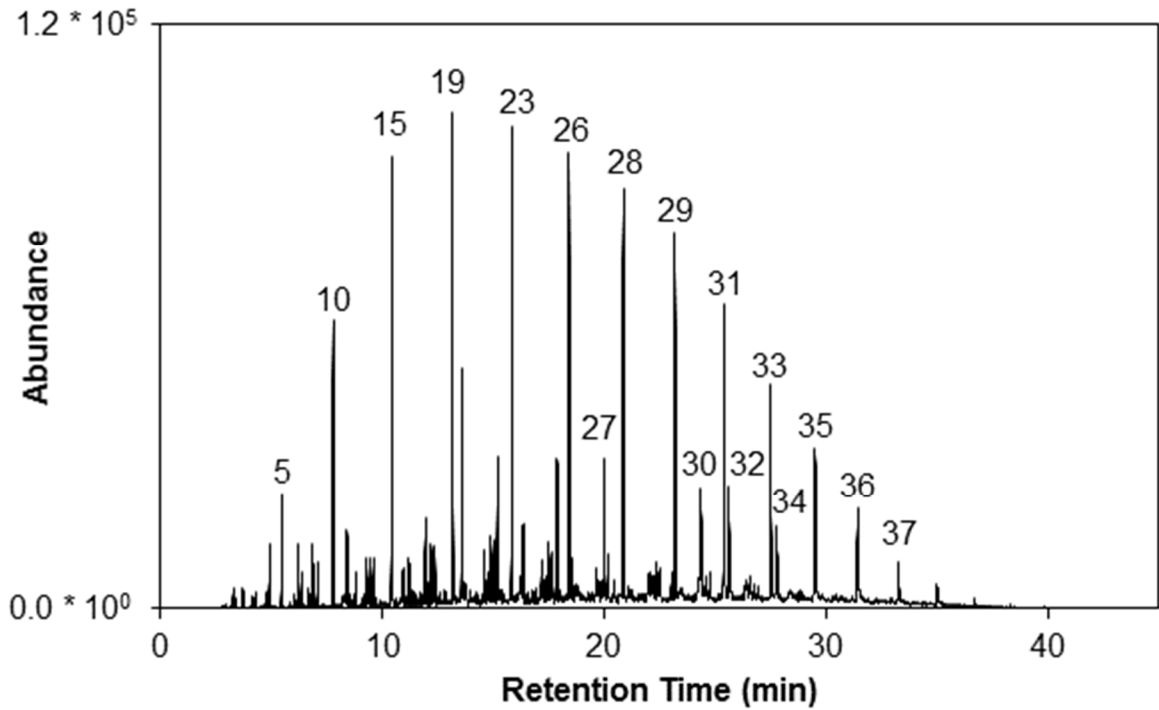


Figure 2-3. Extracted ion chromatogram of  $m/z$  57 for diesel fuel. The bottom trace is an expanded portion of the chromatogram, showing the region where more volatile compounds are observed. The peak numbers correspond to the compounds listed in Table 2-2.

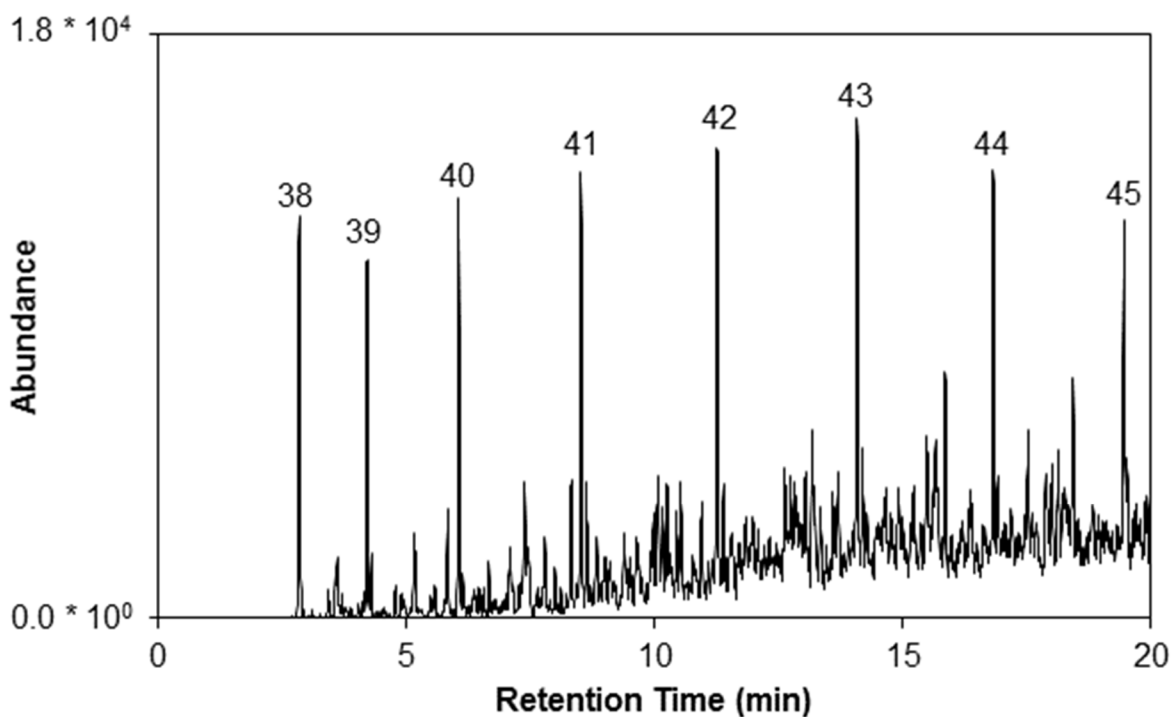
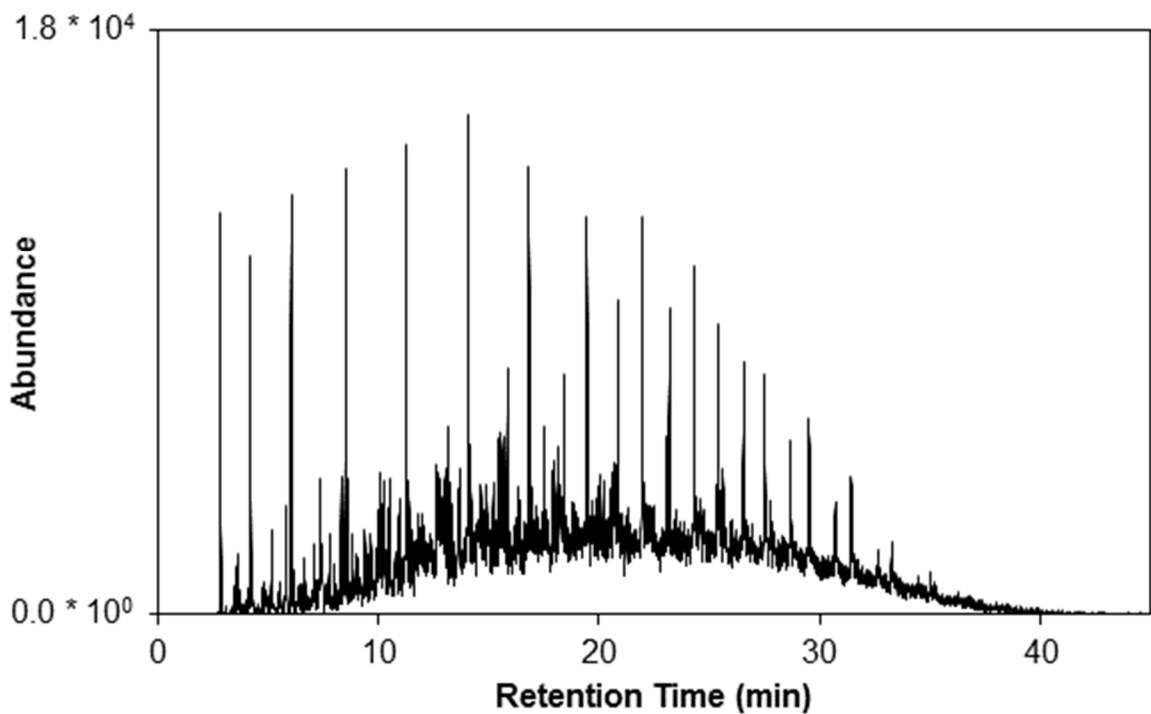


Figure 2-4. Extracted ion chromatogram of  $m/z$  83 for diesel fuel. The bottom trace is an expanded portion of the chromatogram, showing the region where more volatile compounds are observed. The peak numbers correspond to the compounds listed in Table 2-2.

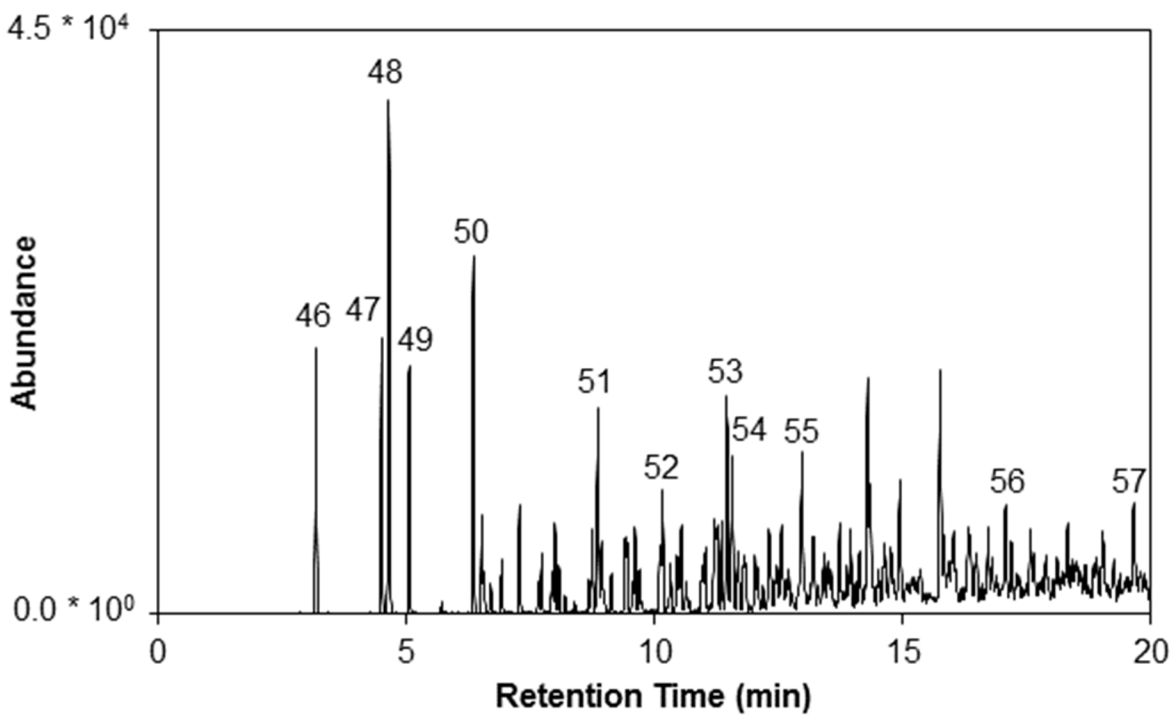
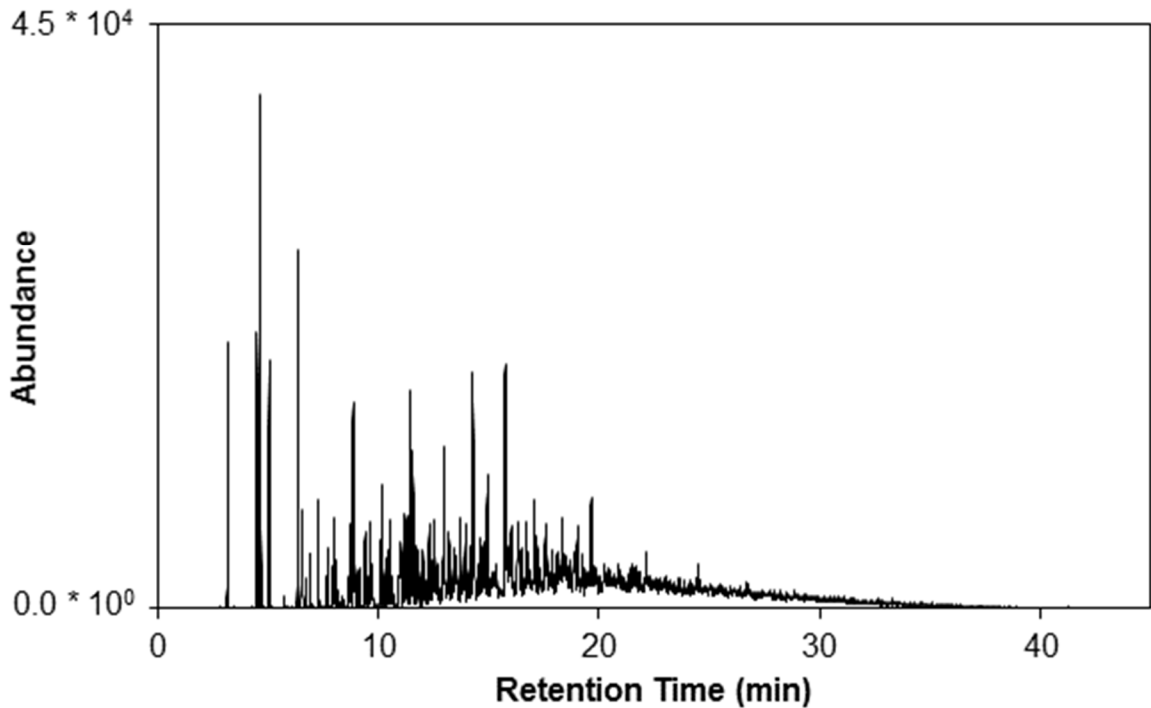


Figure 2-5. Extracted ion chromatogram of  $m/z$  91 for diesel fuel. The bottom trace is an expanded portion of the chromatogram, showing the region where more volatile compounds are observed. The peak numbers correspond to the compounds listed in Table 2-2.

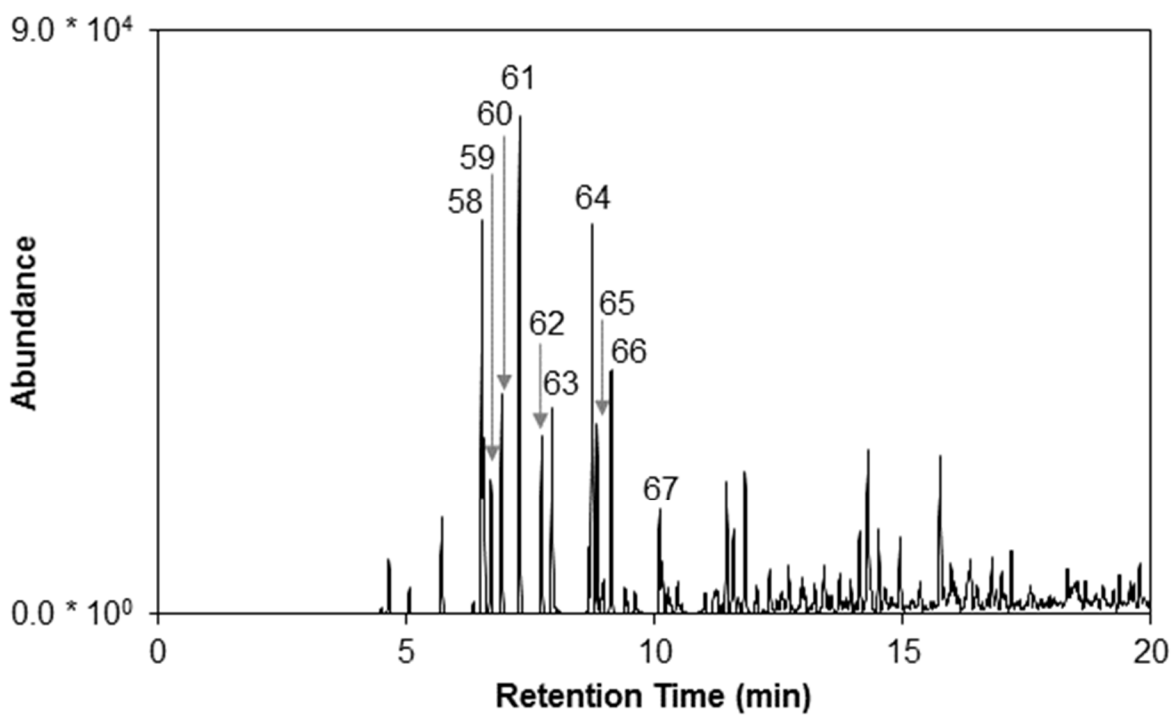
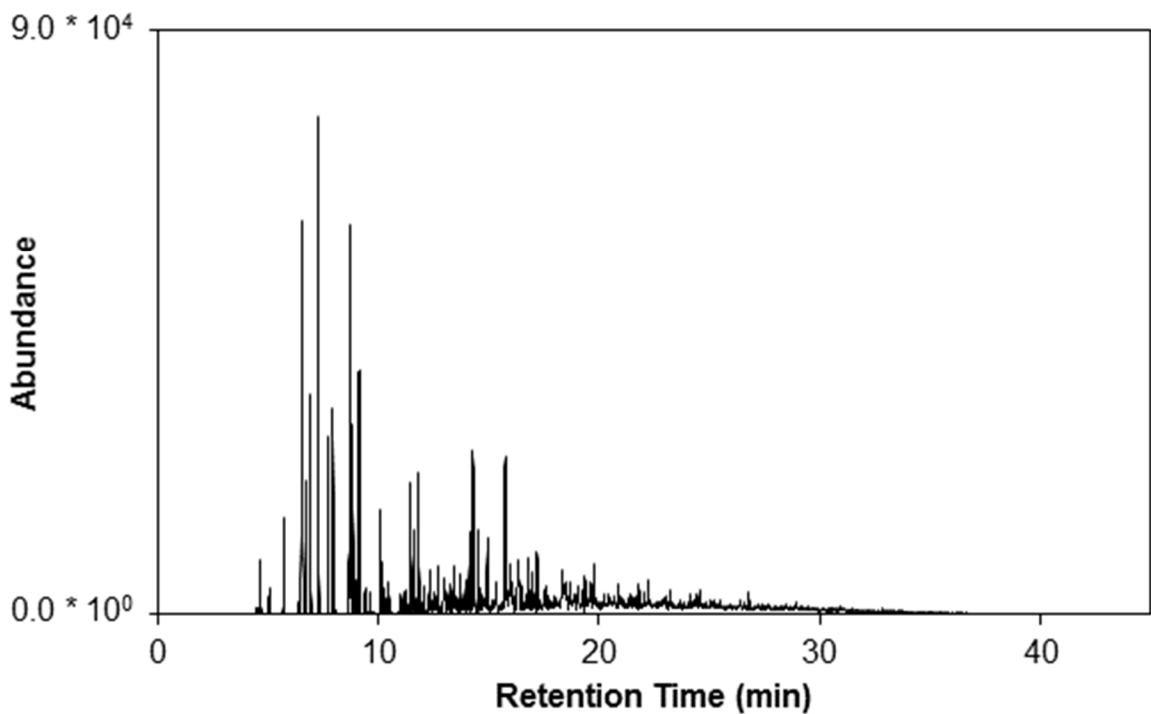


Figure 2-6. Extracted ion chromatogram of  $m/z$  105 for diesel fuel. The bottom trace is an expanded portion of the chromatogram, showing the region where more volatile compounds are observed. The peak numbers correspond to the compounds listed in Table 2-2.

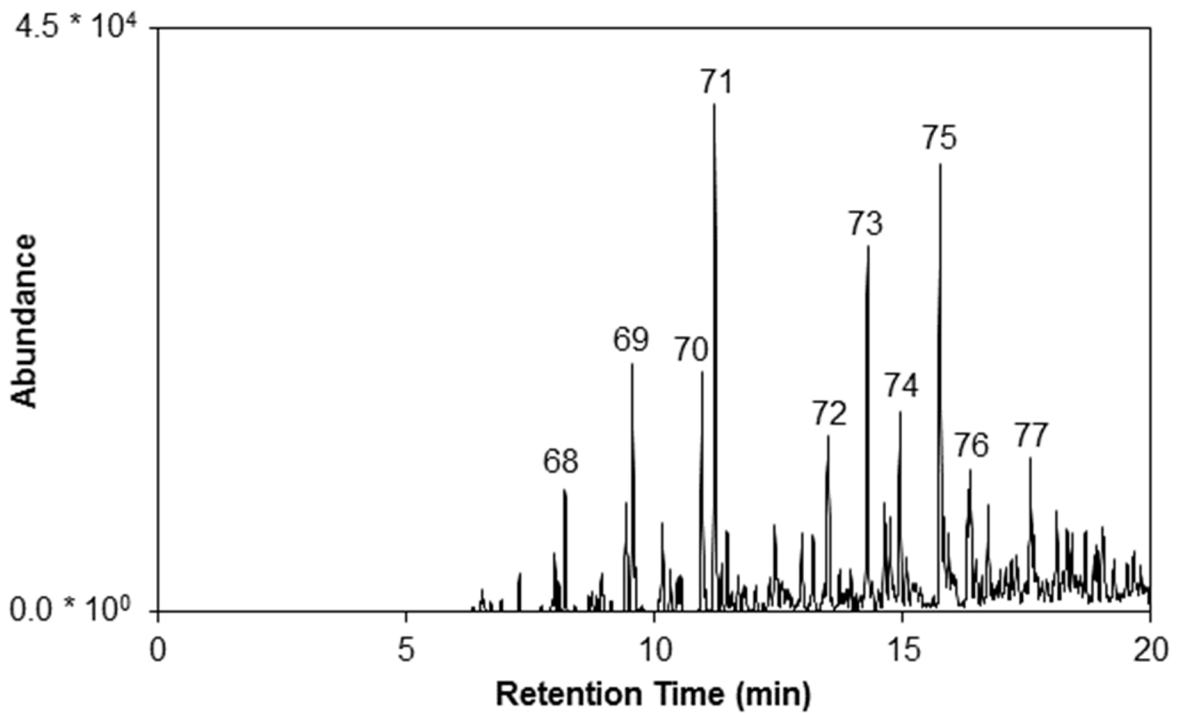
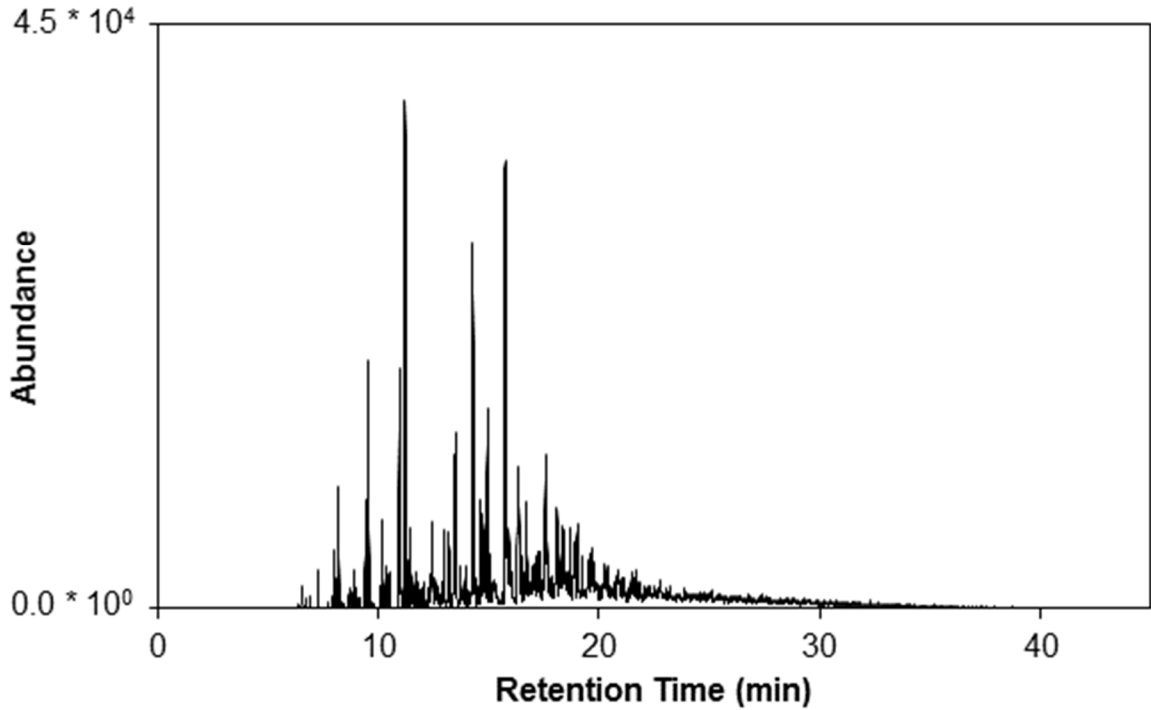


Figure 2-7. Extracted ion chromatogram of  $m/z$  117 for diesel fuel. The bottom trace is an expanded portion of the chromatogram, showing the region where more volatile compounds are observed. The peak numbers correspond to the compounds listed in Table 2-2.

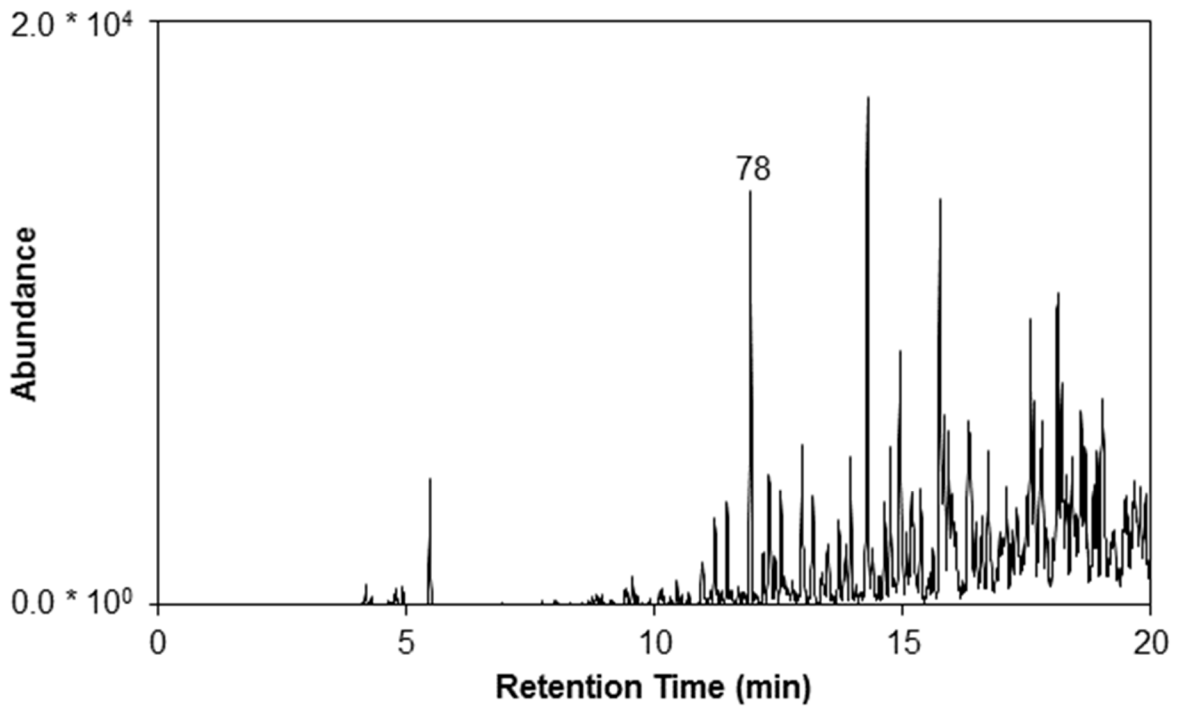
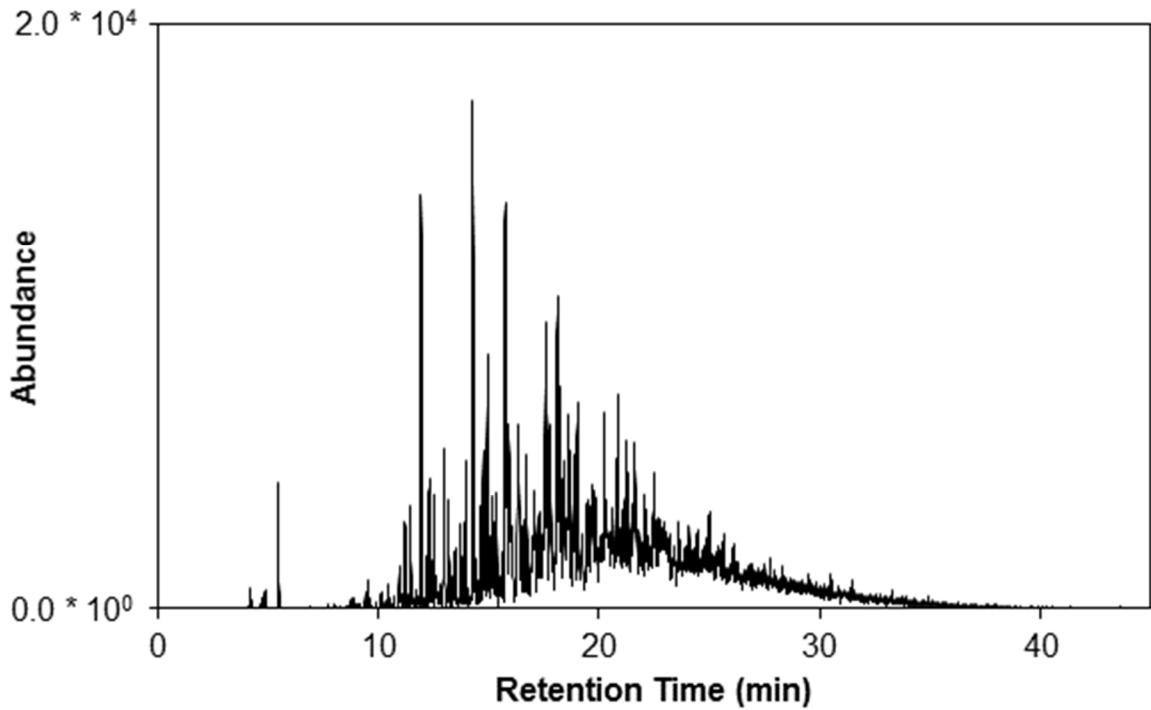


Figure 2-8. Extracted ion chromatogram of m/z 128 for diesel fuel. The bottom trace is an expanded portion of the chromatogram, showing the region where more volatile compounds are observed. The peak number corresponds to the compound listed in Table 2-2.

because many of the constituents in diesel fuel do not have known identities, boiling points, or vapor pressures, which are required for most currently available evaporation models. For the selected compounds, the identity, class membership, retention time, retention index, and boiling point are also summarized in Table 2-2.

In addition to these compounds used for model development, a second set that spanned the same range of retention times was selected for model validation. These compounds ( $n = 27$ ) were provisionally identified and assigned to one of the compound classes described above (branched alkane:  $m/z$  57,  $m/z$  97, alkyl aromatic:  $m/z$  105,  $m/z$  117,  $m/z$  119, polycyclic hydrocarbon:  $m/z$  117,  $m/z$  137,  $m/z$  138). For these compounds, the class membership, retention time, and retention index are summarized in Table 2-3.

For both the model development and validation sets, the compounds were quantified based on their peak heights in the EIC. Peak heights, rather than peak areas, were chosen for quantification because they were more precise. Precision was measured using RSD for all selected compounds in the EIC of  $m/z$  57 across nine replicates. The precision using peak heights was 8.4% compared to 11.3% for peak areas. For peaks that were not baseline resolved, reproducible determination of the baseline was challenging, leading to variability in determination of peak areas. To further improve precision, the peak heights of all selected compounds were normalized to the height of *n*-heneicosane ( $C_{21}$ ) in the EIC of  $m/z$  57. *n*-Heneicosane was selected for normalization since it was a late-eluting peak and was unaffected by evaporation during the time course

Table 2-3. Selected compounds monitored during evaporation of diesel fuel to validate the model. The following information is listed for each unidentified compound: compound class, mass-to-charge ratio ( $m/z$ ) of extracted ion chromatogram used for quantification, retention time ( $t_R^T$ ), retention index ( $I^T$ ), rate constant ( $k$ ), characteristic lifetime ( $\tau$ ), and number of  $\tau$  in 300 hours. The absolute percent error (APE) between the experimental and predicted rate constant is also shown.

<b>Class</b>	<b><math>m/z</math></b>	<b><math>t_R^T</math> (min)</b>	<b><math>I^T</math></b>	<b><math>k</math> (<math>h^{-1}</math>)</b>	<b><math>\tau</math> (h)</b>	<b># <math>t</math> in 300 h</b>	<b><math>k</math> (<math>h^{-1}</math>) predicted</b>	<b>APE</b>
Branched Alkane	57	12.094	1160	0.004	238.67	1.26	0.004	6.2
Branched Alkane	97	3.800	803	0.244	4.10	73.26	0.186	23.8
Branched Alkane	97	5.205	884	0.087	11.52	26.03	0.080	8.2
Branched Alkane	97	5.578	904	0.076	13.11	22.89	0.065	15.3
Branched Alkane	97	7.326	979	0.027	36.74	8.16	0.030	8.6
Branched Alkane	97	7.390	982	0.028	35.63	8.42	0.029	2.3
Branched Alkane	97	7.647	993	0.027	37.49	8.00	0.026	4.0
Branched Alkane	97	9.943	1081	0.010	98.74	3.04	0.010	0.5
Branched Alkane	97	10.241	1092	0.010	104.42	2.87	0.009	5.6
Alkyl Aromatic	105	5.723	910	0.075	13.32	22.51	0.061	19.3
Alkyl Aromatic	105	11.605	1142	0.006	156.74	1.91	0.005	16.0
Alkyl Aromatic	105	11.832	1151	0.006	160.77	1.87	0.005	21.0

Table 2-3 cont'd

<b>Class</b>	<b><i>m/z</i></b>	<b><i>t</i><sub>R</sub><sup>T</sup> (min)</b>	<b><i>I</i><sup>T</sup></b>	<b><i>k</i> (h<sup>-1</sup>)</b>	<b><i>τ</i> (h)</b>	<b># <i>t</i> in 300 h</b>	<b><i>k</i> (h<sup>-1</sup>) predicted</b>	<b>APE</b>
Alkyl Aromatic	117	14.641	1255	0.002	465.88	0.64	0.002	22.7
Alkyl Aromatic	119	8.002	1007	0.024	42.45	7.07	0.022	6.4
Alkyl Aromatic	119	8.084	1010	0.022	44.63	6.72	0.021	4.7
Alkyl Aromatic	119	8.864	1033	0.018	55.20	5.43	0.017	7.3
Alkyl Aromatic	119	8.941	1043	0.015	68.31	4.39	0.015	3.6
Alkyl Aromatic	119	9.617	1069	0.012	80.56	3.72	0.012	6.6
Alkyl Aromatic	119	11.686	1145	0.006	154.72	1.94	0.005	19.6
Alkyl Aromatic	119	11.797	1149	0.006	168.58	1.78	0.005	16.0
Alkyl Aromatic	119	12.036	1158	0.005	182.92	1.64	0.005	16.8
Polycyclic Hydrocarbon	119	10.650	1104	0.009	115.55	2.60	0.008	7.5
Polycyclic Hydrocarbon	119	11.360	1134	0.007	138.98	2.16	0.006	18.3
Polycyclic Hydrocarbon	137	10.532	1103	0.009	115.01	2.61	0.008	7.3
Polycyclic Hydrocarbon	137	13.645	1217	0.003	345.93	0.87	0.002	15.2
Polycyclic Hydrocarbon	137	13.907	1227	0.003	367.34	0.82	0.002	18.7
Polycyclic Hydrocarbon	138	9.052	1047	0.016	62.65	4.79	0.015	9.1

of these experiments. To confirm linear response for the purposes of quantification, calibration curves for 27 selected compounds were obtained over the range of concentrations typically found in diesel fuel (0 – 1.4 mM), with coefficients of determination ( $R^2$ ) in the range of 0.992 – 0.999 (Table 2-4).

## **2.3 Results and Discussion**

### *2.3.1 Determination of Kinetic Rate Constants*

Example TICs of diesel fuel evaporated for 0, 7, 30, and 300 h are shown in Figure 2-9. Early eluting compounds are the most volatile and evaporate first, whereas later eluting compounds remain relatively unchanged over the course of the evaporation experiment. For each compound of interest (Section 2.2.5), a decay curve was generated by plotting the normalized abundance as a function of evaporation time. Example decay curves for four normal alkanes are shown in Figure 2-10. As expected, abundances of the more volatile compounds, such as *n*-octane (Figure 2-10a), decay more quickly than less volatile compounds, such as *n*-tetradecane (Figure 2-10d).

Table 2-4. Compounds utilized to confirm linearity of calibration curves. For each compound, the retention time ( $t^T_R$ ), concentration range, slope ( $m$ ), intercept ( $b$ ), and coefficient of determination ( $R^2$ ) are shown.

Compound	$t^T_R$ (min)	Concentration (M)	$m$	$b$	$R^2$
Toluene	3.141	2.34E-04 – 1.17E-03	3E+10	-1E+06	0.997
Ethylbenzene	4.514	2.32E-04 – 1.16E-03	3E+10	-2E+05	0.998
<i>p</i> -Xylene	4.660	2.28E-04 – 1.14E-03	3E+10	-2E+05	0.997
<i>o</i> -Xylene	5.105	2.36E-04 – 1.18E-03	3E+10	-6E+05	0.998
Nonane	5.178	2.30E-04 – 1.15E-03	2E+10	3E+05	0.997
Propylbenzene	6.408	2.34E-04 – 1.17E-03	4E+10	-2E+06	0.997
1,2,4- Trimethylbenzene	7.366	2.29E-04 – 1.15E-03	4E+10	-1E+06	0.997
Decane	7.471	2.24E-04 – 1.12E-03	3E+10	9E+05	0.998
Butyl Cyclohexane	8.314	2.26E-04 – 1.13E-03	4E+10	5E+05	0.998
Indan	8.448	2.31E-04 – 1.15E-03	4E+10	-1E+05	0.997
Butylbenzene	8.976	2.29E-04 – 1.15E-03	5E+10	-3E+06	0.997
Undecane	10.114	2.29E-04 – 1.15E-03	3E+10	-3E+05	0.998
1,2,4,5- Tetramethylbenzene	10.590	2.31E-04 – 1.16E-03	5E+10	-1E+06	0.996
Tetralin	11.853	2.27E-04 – 1.14E-03	5E+10	-4E+05	0.998
Naphthalene	12.463	2.30E-04 – 1.15E-03	5E+10	-3E+06	0.992

Table 2-4 cont'd

<b>Compound</b>	<b><math>t_R^T</math> (min)</b>	<b>Concentration (M)</b>	<b><math>m</math></b>	<b><math>b</math></b>	<b><math>R^2</math></b>
Dodecane	12.856	2.70E-04 – 1.35E-03	3E+10	-3E+05	0.998
Tridecane	15.555	2.28E-04 – 1.14E-03	4E+10	-1E+06	0.998
Tetradecane	18.147	2.27E-04 – 1.14E-03	5E+10	-1E+06	0.998
Pentadecane	20.618	2.29E-04 – 1.15E-03	5E+10	-2E+06	0.998
Fluorene	22.611	2.28E-04 – 1.14E-03	8E+10	-7E+06	0.995
Hexadecane	22.964	2.28E-04 – 1.14E-03	6E+10	-1E+06	0.998
Heptadecane	25.197	2.29E-04 – 1.15E-03	6E+10	-3E+06	0.998
Octadecane	27.322	2.22E-04 – 1.11E-03	7E+10	-4E+06	0.999
Nonadecane	29.348	2.27E-04 – 1.14E-03	7E+10	-5E+06	0.999
Eicosane	31.283	2.27E-04 – 1.13E-03	8E+10	-6E+06	0.999
Pyrene	33.405	2.27E-04 – 1.13E-03	1E+11	-8E+06	0.997

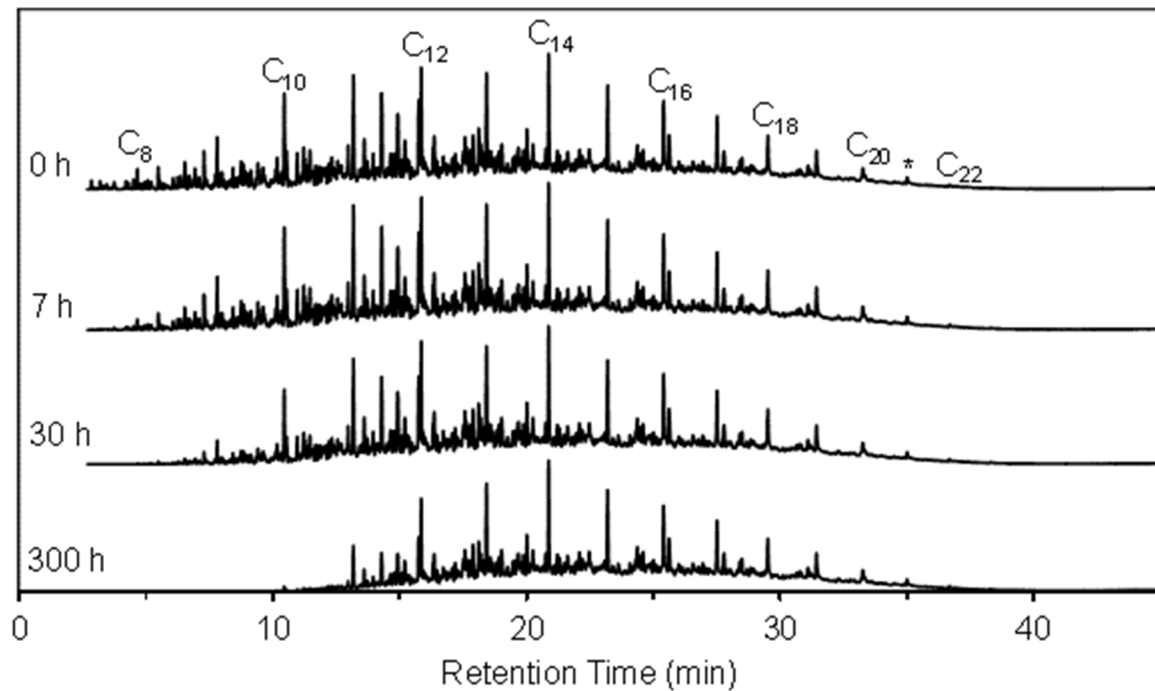


Figure 2-9. Total ion chromatograms of diesel fuel evaporated at 20 °C for 0 – 300 h. For reference, selected *n*-alkanes are labeled by carbon number. *n*-Heneicosane (C<sub>21</sub>) was used for normalization (\*).

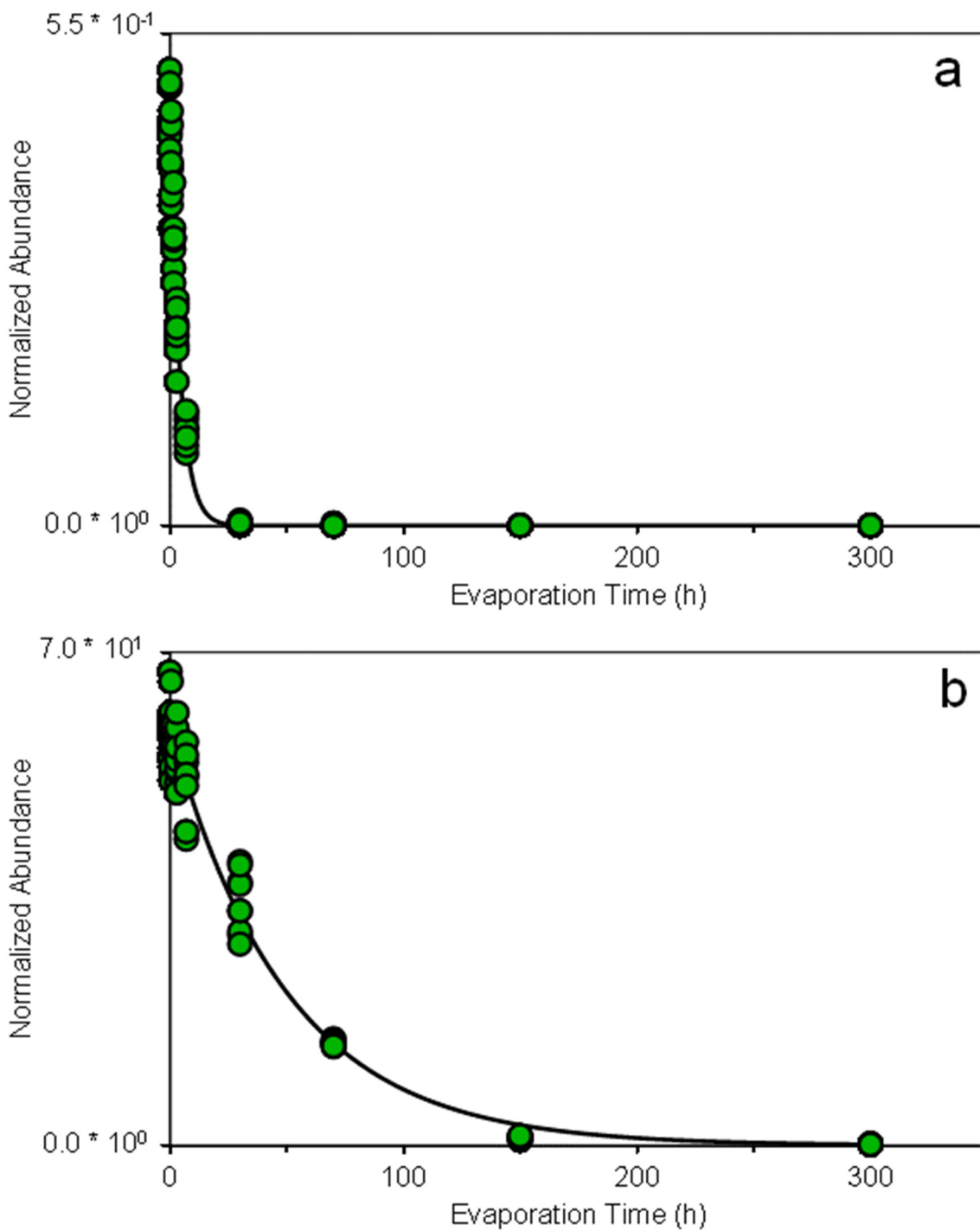
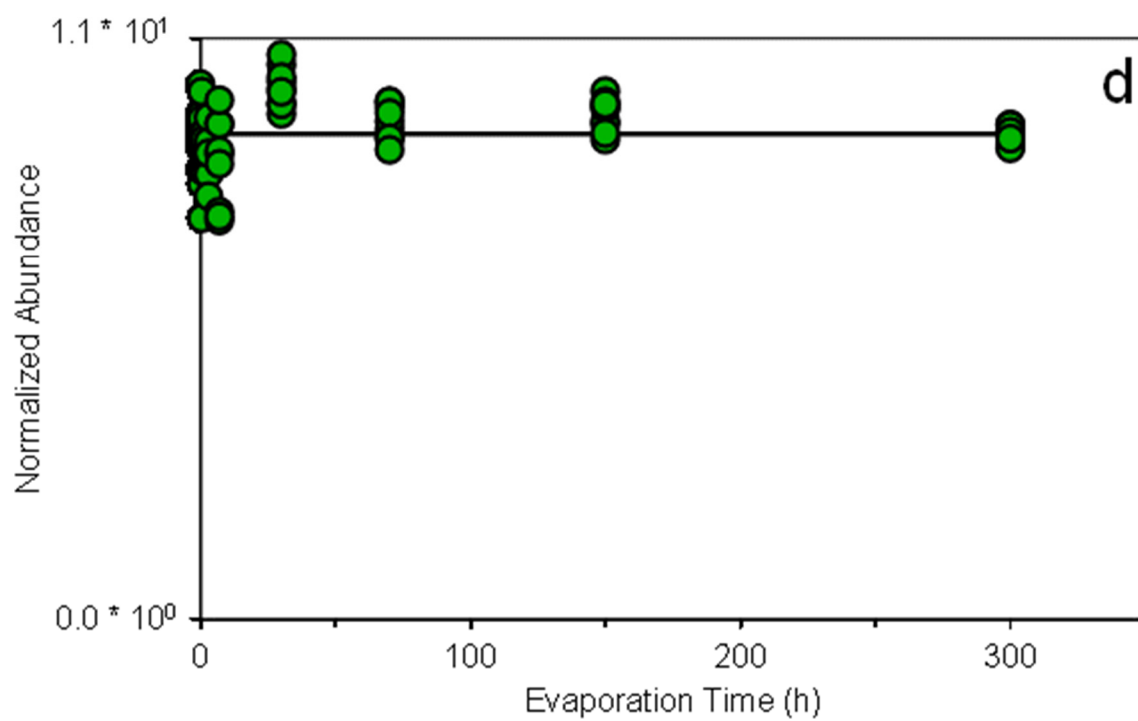
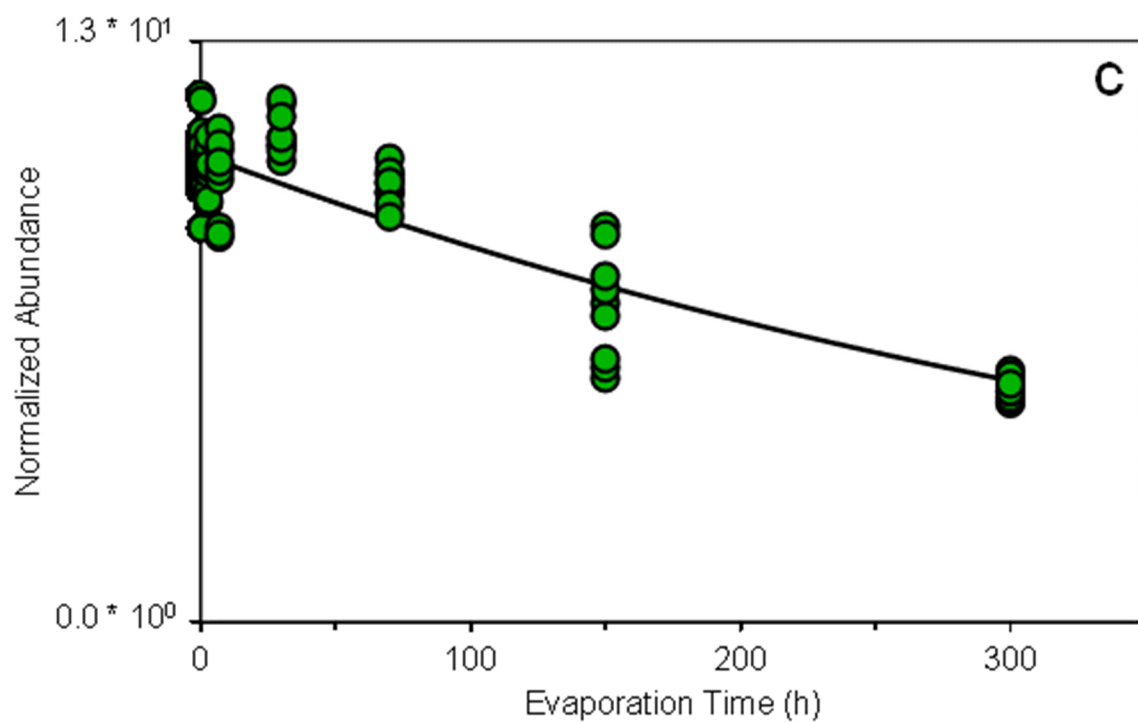


Figure 2-10. Residual abundances of *n*-octane (a), *n*-decane (b), *n*-dodecane (c), and *n*-tetradecane (d) as a function of evaporation time normalized to the peak height of *n*-heneicosane in the EIC at *m/z* 57. Linear regression equations: *n*-octane:  $C_t = 0.448 * \exp(-\underline{2.26 * 10^{-1}} * t)$ ,  $R^2 = 0.980$ ,  $F = 3882$ ; *n*-decane:  $C_t = 5.926 * \exp(-\underline{2.01 * 10^{-2}} * t)$ ,  $R^2 = 0.982$ ,  $F = 4359$ ; *n*-dodecane:  $C_t = 10.475 * \exp(-\underline{2.20 * 10^{-3}} * t)$ ,  $R^2 = 0.807$ ,  $F = 330$ ; *n*-tetradecane:  $C_t = 9.276 * \exp(-\underline{0.00 * 10^0} * t)$ ,  $R^2 = 0.000$ ,  $F = 0$ . The rate constant, *k*, is underlined in each equation.

Figure 2-10 cont'd



Based on the decay curve for each compound, the kinetic rate constant,  $k$ , was determined by non-linear regression (TableCurve 2D, version 5.01, Jandel Scientific, San Rafael, CA). All compounds were assumed to have a first-order kinetic decay [20],

$$C_t = C_0 \exp(-k t) \quad \text{Equation 2-2}$$

where  $C_t$  is the concentration at time  $t$  and  $C_0$  is the initial concentration [11, 32]. The resulting decay curve and regression line for the normal alkanes is shown in Figure 2-10. Based on the curve fitting, the evaporation rate constant for  $n$ -octane (Figure 2-10a) was determined to be  $2.3 \times 10^{-1} \text{ h}^{-1}$  with a coefficient of determination ( $R^2$ ) of 0.98, indicating a good quality of fit [33]. The rate constants for  $n$ -decane (Figure 2-10b) and  $n$ -dodecane (Figure 2-10c) were  $2.0 \times 10^{-2} \text{ h}^{-1}$  ( $R^2 = 0.98$ ) and  $2.2 \times 10^{-3} \text{ h}^{-1}$  ( $R^2 = 0.81$ ), respectively. The rate constant for  $n$ -tetradecane (Figure 2-10d) was  $0.0 \text{ h}^{-1}$ , indicating that the concentration did not change measurably over the course of 300 h. Rate constants for all selected compounds are available in Table 2-2. As demonstrated by the rate constants in the tables, compounds with larger  $I^T$  values and, hence, lower volatility, exhibited smaller rate constants. An increase in retention index of about 200 (or two methylene groups) resulted in approximately one order-of-magnitude decrease in  $k$ .

In order to accurately determine the rate constant, it is important that experimental data represent an adequate portion of the decay curve. The completeness of a decay curve can be expressed in terms of the characteristic lifetime,  $\tau$ , which is equal to  $1/k$ . A minimum of  $5 \tau$  (99.3% completion for a first-order decay) is considered necessary to adequately fit the decay curve [34]. However, in 300 h, many of the selected compounds

had less than 5  $\tau$  (Table 2-2). A chromatogram which highlights the regions with decay curves corresponding to various number of  $\tau$  is shown in Figure 2-11.

In order to include more compounds in the development of the model, the error introduced when fitting decay curves with less than 5  $\tau$  was investigated. For 14 selected compounds, each yielding measurements spanning more than 5  $\tau$ , the number of  $\tau$  was altered by removing the last time point of the decay curves. The rate constant was then recalculated, based on fewer  $\tau$ , using the curve-fitting software. This process was repeated until only three points remained in each curve, resulting in a number of  $\tau$  ranging from approximately 0.01  $\tau$  to 163  $\tau$ .

The error calculation for this work was based on the mean absolute percent error (MAPE) [35, 36]. The absolute error is calculated between the rate constant from the complete decay curve ( $k$ ) and the observed rate constant from the truncated decay curve ( $k_{obs}$ ), and then averaged across all observations ( $n$ ).

$$MAPE = \frac{\sum_{i=1}^n \left| \frac{k_i - k_{obs,i}}{k_i} \right|}{n} 100 \quad \text{Equation 2-3}$$

While there are a number of valid methods for calculating error, the MAPE is commonly applied and easy to interpret [36].

The MAPE between the original  $k$  (fit over 300 h) and the new  $k$  (< 300 h) was

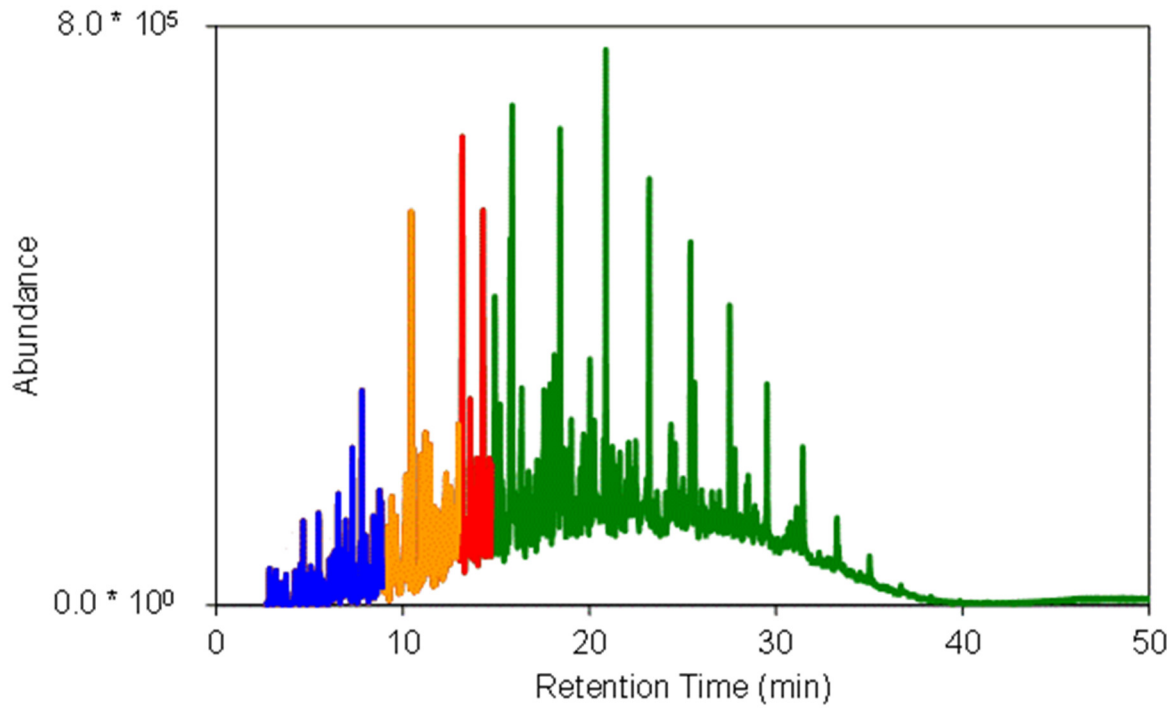


Figure 2-11. A chromatogram of unevaporated diesel fuel showing the compounds with decay curves corresponding to  $>5 \tau$  (blue),  $5 - 1 \tau$  (yellow),  $1 - 0.5 \tau$  (red), and  $<0.5 \tau$  (green).

calculated for each iteration. When more than  $5 \tau$  was used for the curve fitting, there was little difference (0.0003%) between the newly determined rate constant and the original. When  $1 - 5 \tau$  was used for the curve fitting, 1% error in  $k$  was observed and for the evaporation rate constant, with a mean average percent error of 3%. When  $0.5 - 1 \tau$  was used, 13% error was observed. When less than  $0.5 \tau$  was used, the error in  $k$  increased significantly to 38%. Therefore, compounds with more than  $0.5 \tau$  were selected for inclusion in the development of the predictive model

When the decay curves for selected compounds were fit, the coefficient of determination ( $R^2$ ) and the F-statistic were found to scale with the number of  $\tau$  (Figure 2-12). The coefficient of determination consistently increased with an increase in the number of  $\tau$ . More spread is observed for the F-statistic. This likely arise from the increased uncertainty when the decay occurs quickly, and there are only a few points before the decay is completed. When less than  $0.5 \tau$  was used to determine the rate constant, the  $R^2$  was constantly below 0.7 (Figure 2-12a) and the F-statistic was consistently below 200 (Figure 2-12b), at which point curves were considered to have a questionable fit. When greater than  $0.5 \tau$  was used in the decay curve, the  $R^2$  was consistently above 0.7 and maximized at 0.98 while the F-statistic was over 200, and maximized at 6800. The relative standard deviation was consistently below 8% when using greater than  $0.5 \tau$ . This demonstrates that a decay curve with greater than  $0.5 \tau$  provided sufficient data to obtain an appropriate fitting with minimal error.

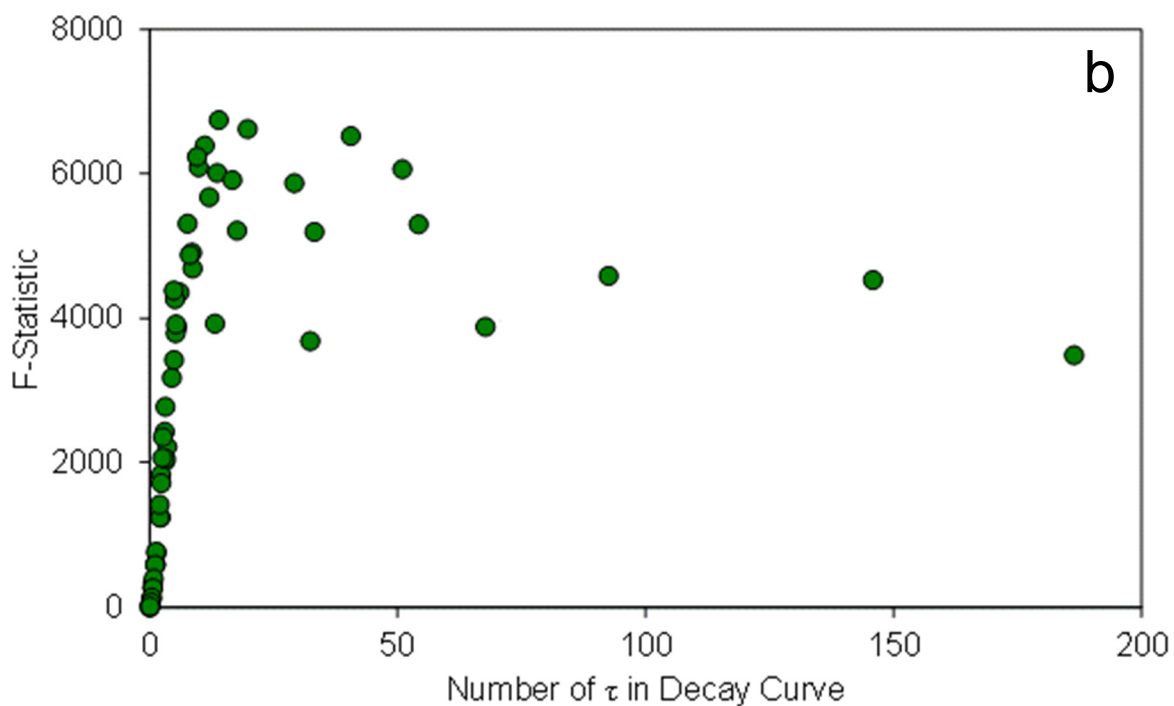
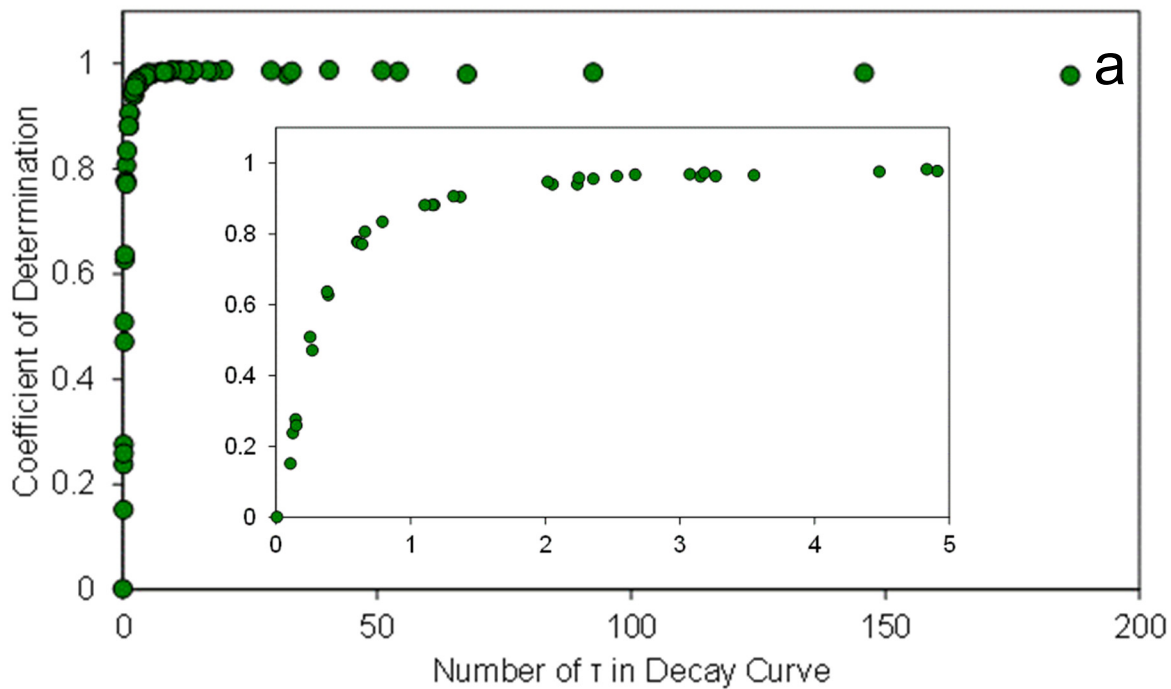


Figure 2-12. The coefficient of determination (a) F-statistic (b), and relative standard deviation for each compound *versus* the number of tau ( $\tau$ ) in the decay curve. The inset in a shows an expanded region, from 0 – 5 $\tau$ .



For the 300 h evaporation time, only those compounds eluting during the first 15% of the chromatogram ( $I^T < 1040$ ) yielded data with greater than 5  $\tau$  (Figure 2-11). This corresponded to 29 of the selected compounds. By utilizing rate constants generated from decay curves with greater than 0.5  $\tau$  (rather than 5  $\tau$ ), 30% of the chromatogram ( $I^T < 1260$ ) could be used for model development (Figure 2-11). This corresponded to 51 of the selected compounds, with rate constants varying from 0.002 to 0.621 h<sup>-1</sup>. The cutoff of 0.5  $\tau$  allows for the inclusion of more compounds, while still enabling the accurate determination of rate constants, which is critical for the development of robust predictive models. The values for  $I^T$ ,  $k$ ,  $\tau$ , and number  $\tau$  in 300 h are summarized in Table 2-2 for all selected compounds.

### 2.3.2 Predicting Kinetic Rate Constant Based on Boiling Point

Initially, a model was developed to predict the evaporation rate constant based on known boiling points. Figure 2-13a shows the natural logarithm of the rate constant as a function of boiling point for five normal alkanes (C<sub>8</sub> – C<sub>12</sub>). For a homologous series (in this case, normal alkanes), correlation is observed between the number of methylene groups and physical properties such as boiling point. This relationship exists because the change in free energy of evaporation upon addition of each methylene group is constant [37, 38]. The natural logarithm of the rate constant *versus* boiling point plot is linear for the normal alkanes with a high coefficient of determination ( $R^2 = 0.999$ ), indicating that boiling point is an appropriate predictor for the rate constant. A linear relationship ( $R^2 = 0.961$ ) is still observed when additional compounds from other classes (normal alkanes, branched and cyclic alkanes, alkyl aromatics, and polycyclic

hydrocarbons) were included in the plot (Figure 2-13b). This demonstrates that the boiling point of a compound can reliably be used to predict the rate constant for evaporation.

In order to develop a widely applicable model, the basis of the model must be derived from an easily obtained property. However, physical properties such as boiling point present a substantial challenge when used as the basis of a model, because the compound must be identified and the boiling point must be known. Unambiguous identification by GC-MS is often challenging, especially when structural and positional isomers are present. In addition, values of the physical properties are not available for many compounds found in diesel fuel.

### *2.3.3 Predicting Kinetic Rate Constant Based on Retention Index*

An empirical surrogate for boiling point would provide a promising basis for predictive models of evaporation, because definitive identification would not be necessary. In this work, a 100% poly(dimethylsiloxane) stationary phase was utilized in the GC-MS analysis. Molecular interactions with this stationary phase are dominated by weak London dispersion forces, such that compounds elute from the column based on their boiling points [39]. Figure 2-13c shows the relationship between boiling point and chromatographic retention index for 23 compounds from the four compounds classes previously discussed. A linear relationship exists between the boiling point and retention index ( $R^2 = 0.991$ ), which demonstrates that retention index is a suitable surrogate for boiling point.

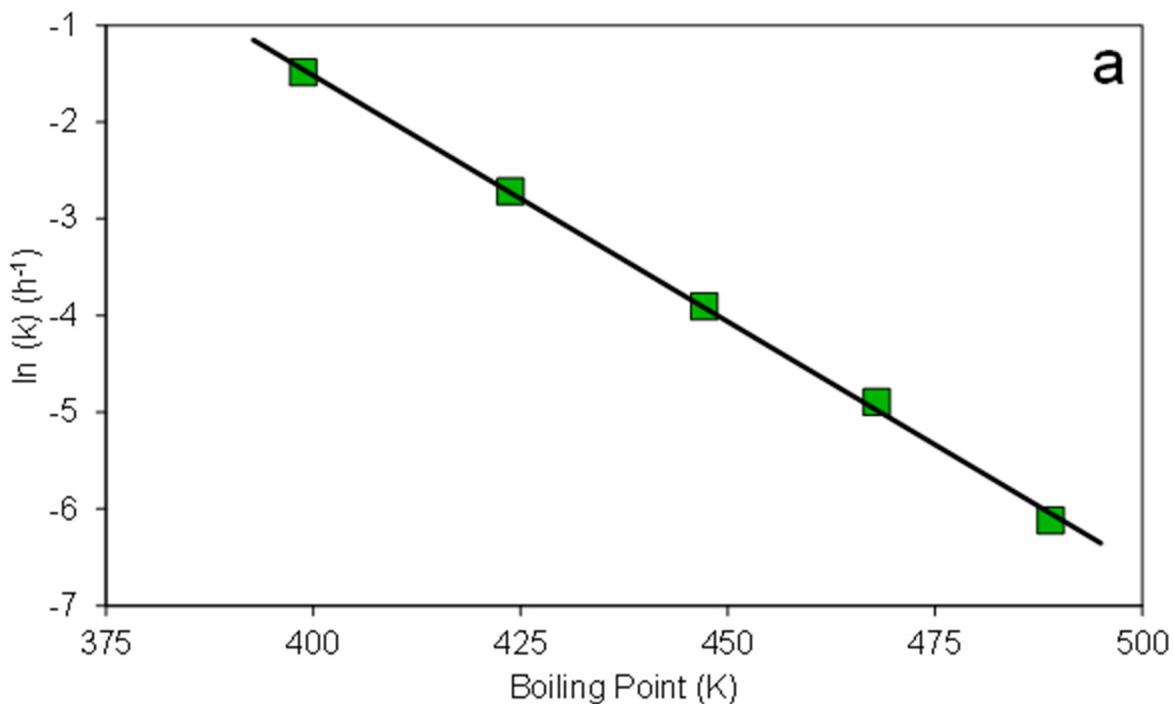
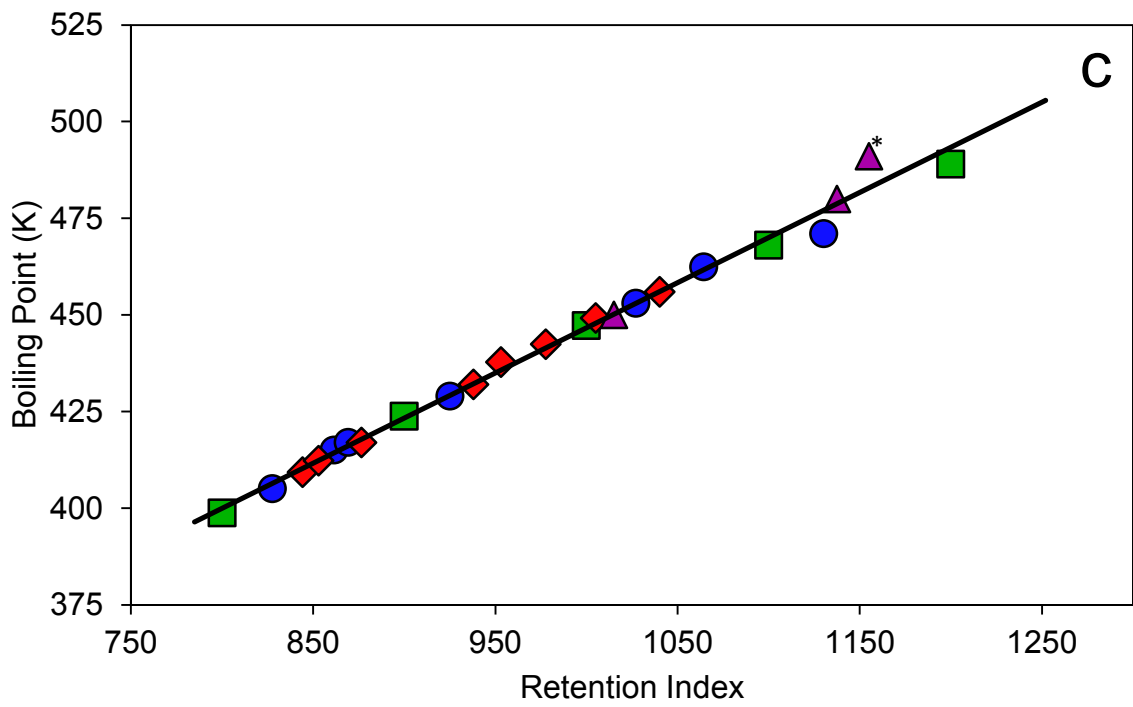
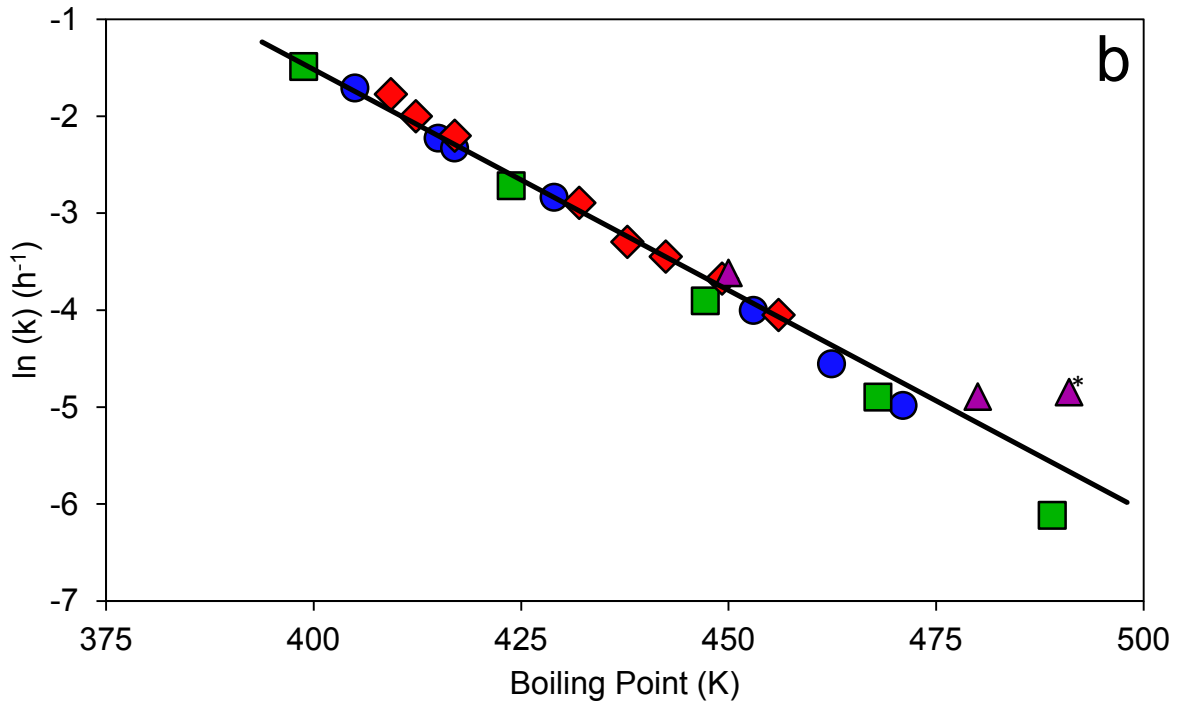


Figure 2-13. Natural logarithm of evaporation rate constant ( $\ln(k)$ ) versus boiling point for normal alkanes (a). Linear regression equation:  $y = -5.09 \times 10^{-2} \times x + 18.83$ ,  $R^2 = 0.999$ ,  $n = 5$ . Natural logarithm of evaporation rate constant ( $\ln(k)$ ) versus boiling point for all selected compound classes (b): normal alkanes ( $\blacksquare$ ), branched alkanes ( $\bullet$ ), alkyl benzenes ( $\blacklozenge$ ), and polycyclic hydrocarbons ( $\blacktriangle$ ). Linear regression equation:  $y = -4.51 \times 10^{-2} \times x + 16.71$ ,  $R^2 = 0.961$ ,  $n = 23$ . Compound with the \* indicates naphthalene, which sublimates and likely contains large error in the boiling point. Boiling point versus chromatographic retention index on HP-1MS stationary phase (c). Linear regression equation:  $y = 2.33 \times 10^{-1} \times x + 213.2$ ,  $R^2 = 0.991$ ,  $n = 23$ .

Figure 2-13 cont'd



Models were developed to predict evaporation rate constants by linear regression of the natural logarithm of the experimentally determined rate constant ( $\ln(k)$ ) *versus* the retention index ( $I^T$ )

$$\ln(k) = m I^T + b \quad \text{Equation 2-4}$$

where  $m$  and  $b$  are the slope and intercept determined from the regression. When the regression was performed using only the normal alkanes, there was a strong linear relationship with a high coefficient of determination ( $R^2 = 0.999$ ), which is expected for a homologous series based on linear free energy relationships [37, 38, 40]. The regression of other homologous series behaved similarly. For example, the alkyl-substituted cyclohexanes (methyl to hexyl) from the branched alkane class and the mono-substituted alkyl benzenes (methyl to pentyl) from the alkyl aromatic class demonstrated a similar coefficient of determination ( $R^2 = 0.999$ ) for the linear regression of Equation 2-4 to that of the normal alkanes.

Class-specific models were developed to predict evaporation rate constants (Table 2-5). The goodness of fit to the linear regression model for the branched alkane ( $R^2 = 0.994$ ), alkyl aromatic ( $R^2 = 0.992$ ), and polycyclic hydrocarbon ( $R^2 = 0.992$ ) classes was lower than that for the homologous series discussed above. The coefficient of determination was expected to decrease in the absence of a repeating structural unit. The  $R^2$  value from the linear regression of the boiling point *versus* the retention index (Figure 2-13c,  $R^2 = 0.991$ ) serves as a measure of the expected goodness of fit for a non-homologous series. Each of the class-specific models had coefficients of determination equal to or greater than the expected value. A plot showing the regression for each compound class is shown in Figure 2-14.

Table 2-5. Class-specific models developed to predict the rate constant, based on the *uncorrected* retention index. For each model, the number of compounds used to create the model (n) as well as the slope (m), intercept (b), and coefficient of determination (R<sup>2</sup>) for Equation 2-3 are shown. In addition, the mean absolute percent error (MAPE) for predicting compounds in each class is shown. For the compound class the following abbreviations were used: normal alkane (Norm), branched alkane (Bran), alkyl aromatic (Arom), polycyclic hydrocarbon (Poly).

Model Basis	n	m <sup>a</sup>	b <sup>b</sup>	R <sup>2</sup>	MAPE in <i>k</i> for Compounds in Each Class				
					Norm	Bran	Arom	Poly	All
Norm	5	-1.14 * 10 <sup>-2</sup>	7.61	0.999	4.9	10	19	43	19
Bran	19	-1.08 * 10 <sup>-2</sup>	7.05	0.994	12	8.2	14	32	15
Arom	17	-1.08 * 10 <sup>-2</sup>	7.20	0.992	26	17	5.7	22	15
Poly	10	-1.00 * 10 <sup>-2</sup>	6.47	0.992	44	36	15	4.0	23
All	51	-1.04 * 10 <sup>-2</sup>	6.70	0.981	24	15	6.9	20	14

a. Slope (h<sup>-1</sup>)

b. Intercept (h<sup>-1</sup>)

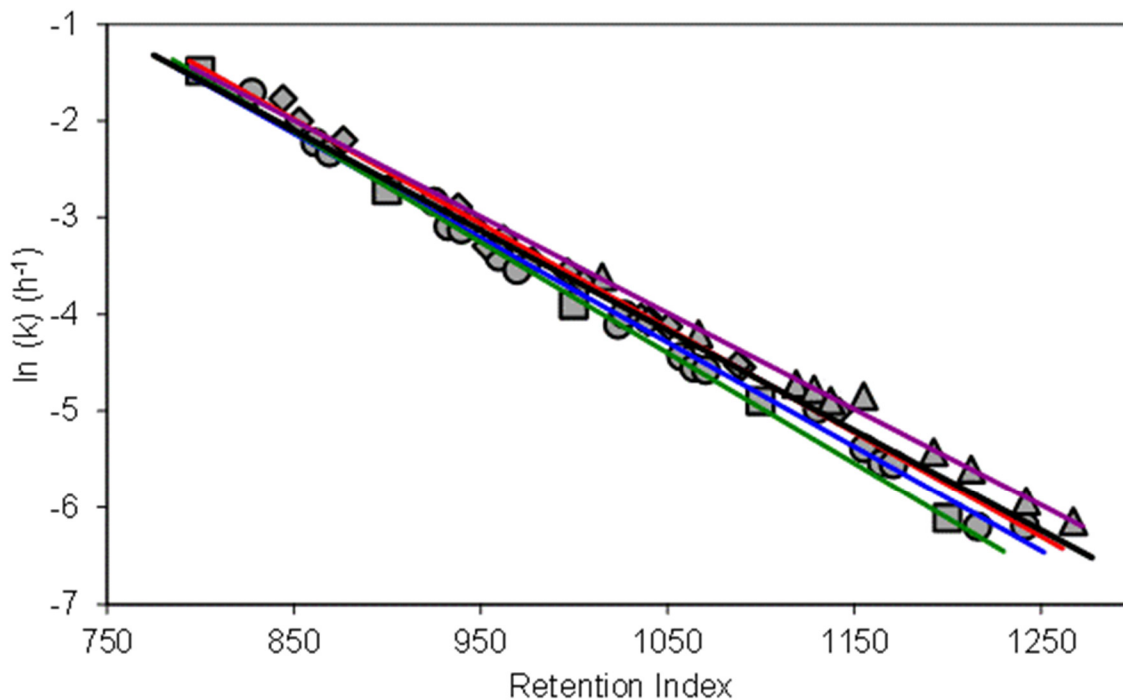


Figure 2-14. Natural logarithm of evaporation rate constant ( $\ln(k)$ ) *versus* chromatographic retention index on HP-1MS stationary phase for all selected compound classes: normal alkanes (■), branched alkanes (●), alkyl benzenes (◆), and polycyclic hydrocarbons (▲). The linear regression of each model is shown: normal alkanes (green), branched alkanes (blue), alkyl benzenes (red), polycyclic hydrocarbons (purple), and comprehensive (black). The regression equations are shown in Table 2-5.

A comprehensive model was also developed that incorporated compounds from all classes (Figure 2-15). When the linear regression was performed, an unexpected decrease in the coefficient of determination ( $R^2 = 0.981$ ) was observed, relative to the class specific models. In order to test the origin of this discrepancy, each class (normal alkane, branched alkane, branched aromatic, and polycyclic hydrocarbon) was sequentially added into the comprehensive model (Table 2-5). The decrease in  $R^2$  was observed after the aromatic and polycyclic hydrocarbon classes were included. Many of the alkyl aromatic and polycyclic hydrocarbons were positioned above the regression line (Figure 2-15), indicating that these compounds behaved differently than the normal and branched alkanes, the origin of which will be discussed in Section 3.4.

The four class-specific models and the comprehensive model were used to predict evaporation rate constants for the selected compounds ( $n = 5 - 19$ , Table 2-2 and Table 2-5). The absolute percent error between the predicted and observed rate constant was determined, and the mean absolute percent error (Equation 2-3) for each model was calculated (Table 2-5). The lowest errors were observed when a class-specific model was used to predict the rate constants for compounds in that class. For example, when the model for normal alkanes was used to predict the rate constants for normal alkanes, the average error was 4.9%. Using the branched alkane, alkyl aromatic, and polycyclic hydrocarbon models to predict the rate constant for compounds from those classes, the MAPE was 8.2%, 5.7%, and 4.0%, respectively. However, when the incorrect class-

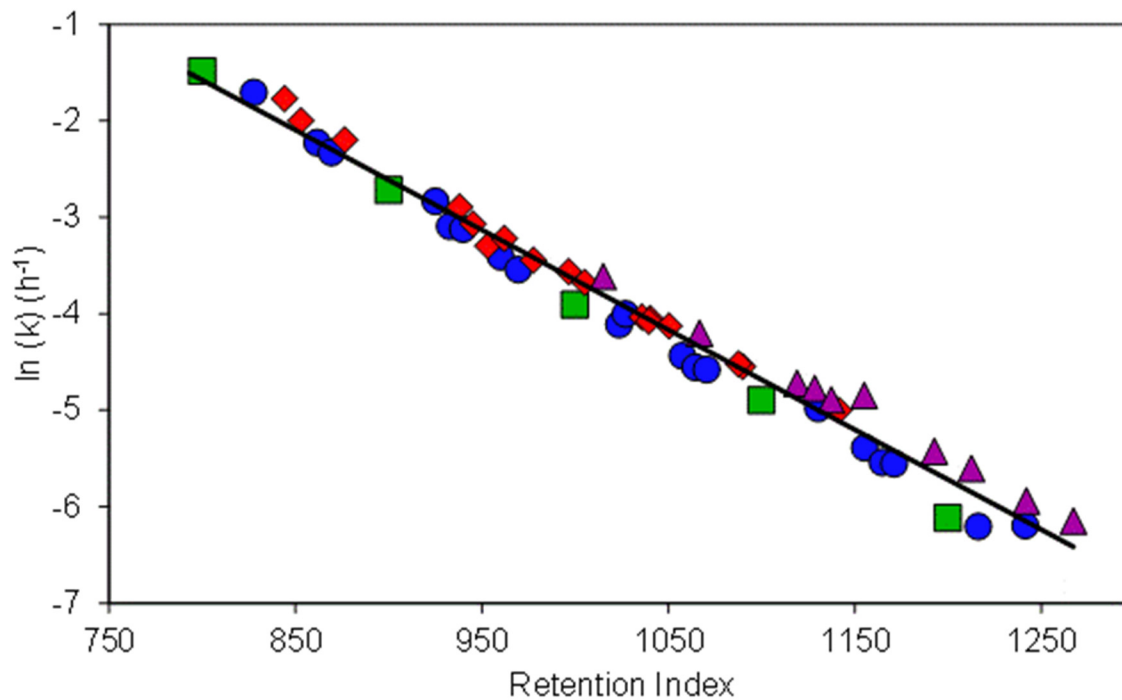


Figure 2-15. Natural logarithm of evaporation rate constant ( $\ln (k)$ ) versus chromatographic retention index on HP-1MS stationary phase for all compound classes: normal alkanes ( $\blacksquare$ ), branched alkanes ( $\bullet$ ), alkyl benzenes ( $\blacklozenge$ ), and polycyclic hydrocarbons ( $\blacktriangle$ ). Linear regression equation:  $y = -1.04 \cdot 10^{-2} \cdot x + 6.70$ ,  $R^2 = 0.981$ ,  $n = 51$ .

specific model was applied to predict the rate constant, the error was much larger. For example, when the normal alkane model was used to predict compounds from the polycyclic hydrocarbon class, the MAPE was 43%. This illustrates the importance of proper classification of compounds when applying class-specific models. However, classification can be challenging for many compounds found in complex samples such as diesel fuel.

If class membership is not known, the comprehensive model allows prediction of the evaporation rate constant with a mean absolute percent error of 14.2%. When the comprehensive model was used, there was greater error than with the correct class-specific model. The largest error was observed for the prediction of compounds from the normal alkane class (24.3%). The mean absolute percent error for the branched alkane, alkyl aromatic, and polycyclic hydrocarbon classes was 15.0%, 6.9%, and 19.7%, respectively. The greater error observed for the normal alkane class is likely due to the relatively few compounds included in that class ( $n = 5$ ). The lower error observed for the alkyl aromatic class is likely due to the large number of compounds ( $n = 17$ ), observed over a narrow retention index range ( $844 \leq I^T \leq 1141$ ). In addition, many of these compounds are volatile, which means that a greater number of  $\tau$  is included in the decay curve to determine the rate constant. The comprehensive model is advantageous since knowledge of class membership is not necessary. However, if class membership is known, the class-specific models result in approximately 10% less error in the determination of the rate constant.

#### 2.3.4 Correction of Retention Indices using McReynolds Constants

As noted above, many of the compounds from the alkyl aromatic and polycyclic hydrocarbon classes are positioned above the regression line in the plot of the natural logarithm of the rate constant *versus* the retention index (Figure 2-15). This error in position occurs because many of these compounds are more retained on the stationary phase than expected, based on the compound's boiling point. Using a 100% poly(dimethylsiloxane) stationary phase, compounds are expected to elute based on boiling point. However, some compounds appear to be more retained than expected due to additional analyte/stationary phase interactions. To evaluate the extent of this additional retention, the McReynolds constants ( $\Delta I^T$ ) were utilized. The McReynolds constant for a particular probe molecule is calculated by subtracting the retention index of that probe on a stationary phase of interest from that on squalane. Squalane is a nonpolar, purely hydrocarbon stationary phase capable only of London forces [39]. For example, the McReynolds number for benzene on a 100% poly(dimethylsiloxane) stationary phase (specifically OV-101) is 17 [41]. A shift of 100  $I^T$  units corresponds to a shift of one methylene group. Therefore, an increase in retention index of 17 indicates that the compound is more retained by approximately 0.17 methylene units on the 100% poly(dimethylsiloxane) stationary phase. The additional retention is likely due to electron donor/acceptor interactions between benzene and the oxygen atoms in the backbone of the polysiloxane stationary phase. This suggests that alkyl aromatic and polycyclic hydrocarbons also have additional interactions with the stationary phase.

To correct the retention index for these additional interactions, the McReynolds constant for benzene on the 100% poly(dimethylsiloxane) stationary phase ( $\Delta I^T = 17$ ) was

subtracted from the retention indices for all compounds from the alkyl aromatic and polycyclic hydrocarbon classes. Within the McReynolds system, benzene is considered to be the representative probe for aromatic hydrocarbons. Specific probes do not exist for alkyl aromatic and polycyclic aromatic hydrocarbons; however the difference in retention index between the 100% poly(dimethylsiloxane) and squalane stationary phases for these compounds is very similar to that for benzene [28]. When this correction is applied, the retention index more accurately represents the boiling point for these compounds, which improves the performance of the model.

The class-specific and comprehensive models were reconstructed using the corrected retention indices (Figure 2-16 and Figure 2-17). The class-specific models had the same coefficient of determination and prediction error as those prior to retention index correction (Table 2-6). However, the coefficient of determination for the comprehensive model increased from  $R^2 = 0.981$  to  $R^2 = 0.990$  when the corrected  $I^T$  values were utilized. This coefficient of determination was more similar to those for the class-specific models. This improvement in goodness of fit for the comprehensive model resulted in an increase in prediction accuracy (Table 2-6). The mean absolute percent error for all compounds decreased from 14.2% to 10.3%.

These results suggest that the methodologies developed in this work may be more broadly applicable to chromatographic separations on other stationary phases. To test this hypothesis, retention indices of all selected compounds were experimentally determined on a 5%-phenyl-95%-methylpolysiloxane stationary phase (HP-5MS, 30 m x

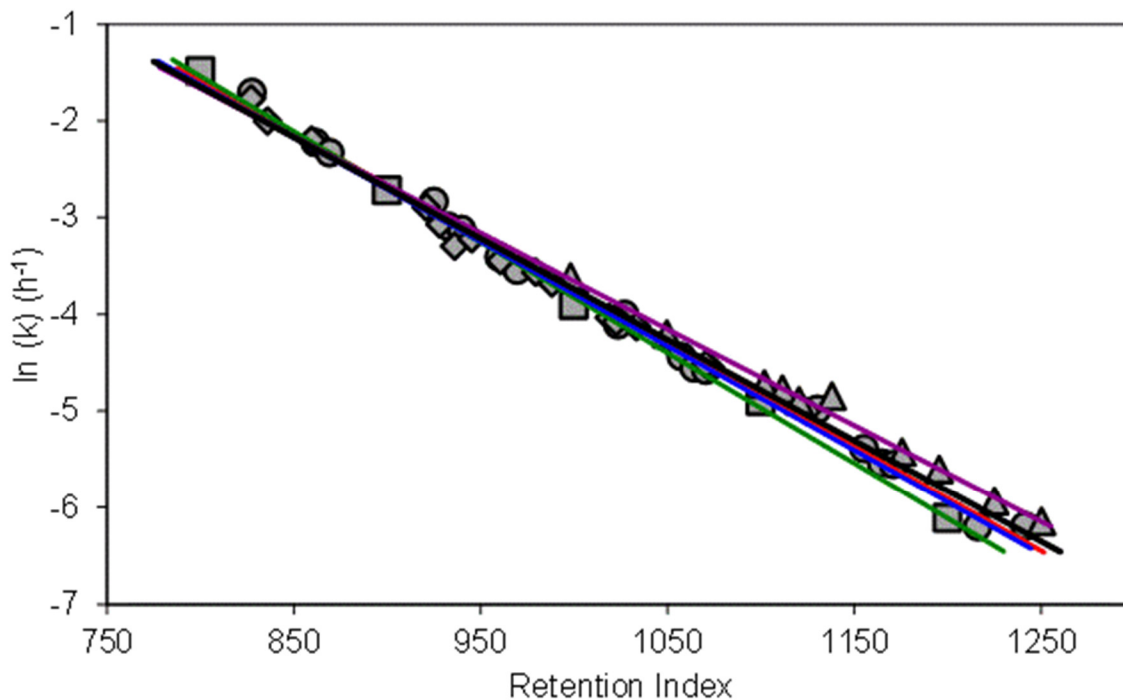


Figure 2-16. Natural logarithm of evaporation rate constant ( $\ln(k)$ ) versus corrected chromatographic retention index on HP-1MS stationary phase for all selected compound classes: normal alkanes ( $\blacksquare$ ), branched alkanes ( $\bullet$ ), alkyl benzenes ( $\blacklozenge$ ), and polycyclic hydrocarbons ( $\blacktriangle$ ). The linear regression of each model is shown: normal alkanes (green), branched alkanes (blue), alkyl benzenes (red), polycyclic hydrocarbons (purple), and comprehensive (black).

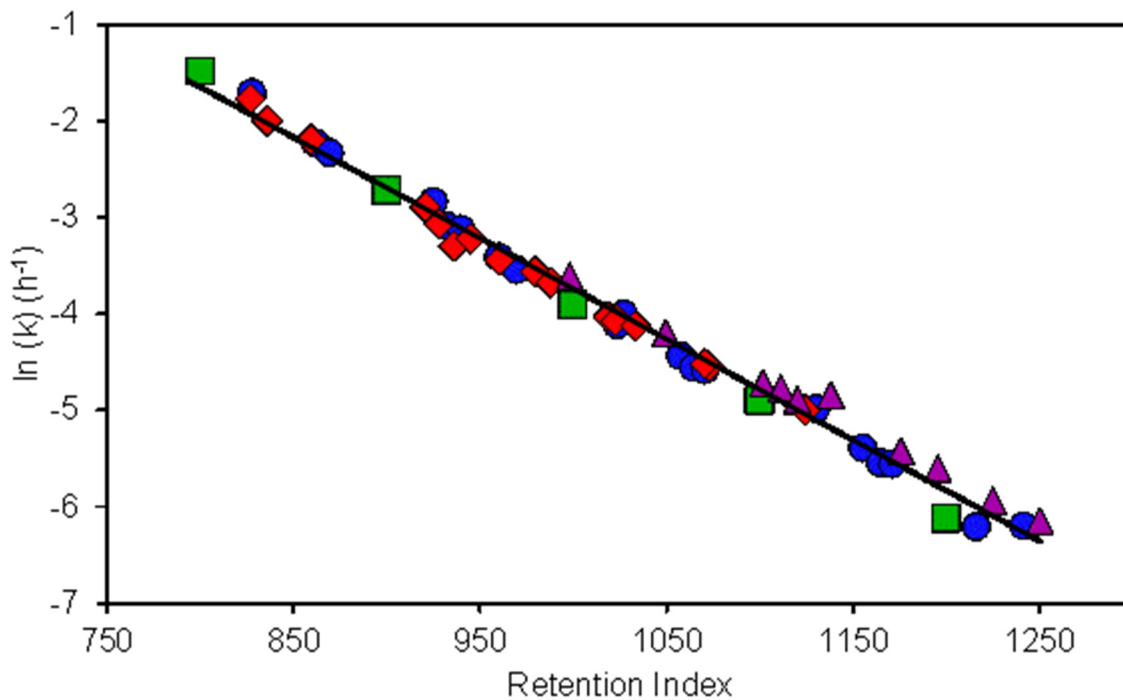


Figure 2-17. Natural logarithm of evaporation rate constant ( $\ln(k)$ ) versus corrected chromatographic retention index on HP-1MS stationary phase for all compound classes: normal alkanes (■), branched alkanes (●), alkyl benzenes (◆), and polycyclic hydrocarbons (▲). Linear regression equation:  $y = -1.05 \cdot 10^{-2} \cdot x + 6.71$ ,  $R^2 = 0.990$ ,  $n = 51$ .

Table 2-6. Class-specific models developed to predict the rate constant, based on the *corrected* retention index. For each model, the number of compounds used to create the model (n) as well as the slope (m), intercept (b), and coefficient of determination ( $R^2$ ) for Equation 2-3 are shown. In addition, the mean absolute percent error (MAPE) for predicting compounds in each class is shown. For the compound class the following abbreviations were used: normal alkane (Norm), branched alkane (Bran), alkyl aromatic (Arom), polycyclic hydrocarbon (Poly).

Model Basis	n	m <sup>a</sup>	b <sup>b</sup>	R <sup>2</sup>	MAPE in <i>k</i> for Compounds in Each Class				
					Norm	Bran	Arom	Poly	All
Norm	5	-1.14 * 10 <sup>-2</sup>	7.61	0.999	4.9	10	6.8	30	13
Bran	19	-1.08 * 10 <sup>-2</sup>	7.05	0.994	12	8.2	6.8	19	10
Arom	17	-1.08 * 10 <sup>-2</sup>	7.02	0.992	9.7	8.1	5.7	22	10
Poly	10	-1.00 * 10 <sup>-2</sup>	6.31	0.992	28	18	15	4.0	15
All	51	-1.05 * 10 <sup>-2</sup>	6.71	0.990	16	9.3	7.8	14	10

a. Slope (h<sup>-1</sup>)

b. Intercept (h<sup>-1</sup>)

0.25 mm x 0.25  $\mu\text{m}$ , Agilent Technologies). These retention indices were corrected based on the McReynolds constant for benzene on an equivalent stationary phase (specifically, OV-73,  $\Delta I^T = 40$ ) in the same manner as described above. The model developed for the 5% phenyl stationary phase ( $y = -1.04 * 10^{-2} I^T + 6.59$ ,  $R^2 = 0.984$ ) was not statistically different ( $\alpha = 0.005$ ) from that for the 100% poly(dimethylsiloxane) stationary phase ( $y = -1.05 * 10^{-2} I^T + 6.71$ ,  $R^2 = 0.990$ ). This demonstrates that retention indices measured on any stationary phase can be utilized in this model, provided there are appropriate McReynolds constants available for the stationary phase and compounds of interest.

### 2.3.5 Model Validation

Twenty seven additional compounds were selected for model validation from the branched alkane, alkyl benzene, and polycyclic hydrocarbon classes. Kinetic rate constants were experimentally determined in the same manner as those used to develop the model (Section 2.3.1). The experimental rate constants were compared to the values predicted by using Equation 2-4, after retention index correction (Table 2-3). The MAPE was 7.6%, with a range of 0.3% – 23.8%. This is comparable to or better than the 10.3% MAPE observed for the prediction of the rate constant of the 51 compounds used to generate the model (Table 2-6).

## 2.4 Applications of the Models

The models developed in Section 1.3 allow prediction of the evaporation rate constant ( $k$ ) for each compound based on retention index ( $I^T$ ). Once  $k$  is determined, the fraction remaining ( $F_{iT}$ ) can be predicted at time  $t$  by rearranging Equation 2-2.

$$F_{I^T} = C_{I^T,t} / C_{I^T,0} = \exp(-k t) \quad \text{Equation 2-5}$$

The equation to predict the rate constant (Equation 2-4) can be substituted in Equation 2-5 to generate a predictive model for the fraction remaining of an individual compound

$$F_{I^T} = \exp(-(\exp(m I^T + b) t)) \quad \text{Equation 2-6}$$

where the slope ( $m$ ) and intercept ( $b$ ) are model specific (Tables 2 and 3). For example, the fraction remaining predicted by using the comprehensive model with retention index correction is

$$F_{I^T} = \exp(-(\exp(-0.105 I^T + 6.71) t)) \quad \text{Equation 2-7}$$

To test the accuracy of predicting the fraction remaining of a compound, a validation set of six diesel samples, evaporated at 20 °C, was used. The predicted fraction remaining of each compound was calculated based on Equation 2-7, using the corrected retention index ( $I^T$ ) and evaporation time ( $t$ ) of 100 h. The fraction remaining (ranging from 0 – 1) can be plotted as a function of the retention index, showing the fraction remaining for each compound. Figure 2-18 shows the fraction remaining at each retention index, superimposed over a chromatogram of diesel fuel. For example, the predicted fraction remaining of *n*-undecane ( $I^T = 1100$ ) was calculated as 0.434, indicating that 43% of *n*-undecane remains after 100 h of evaporation.

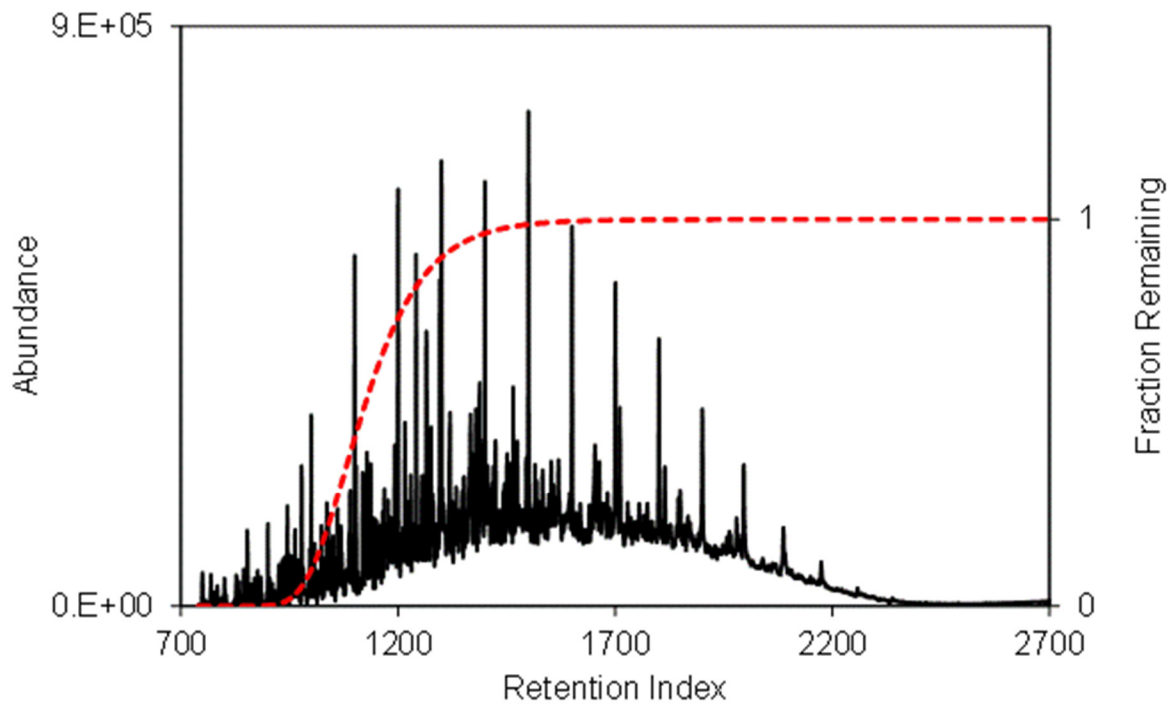


Figure 2-18. Total ion chromatogram of diesel fuel with the fraction remaining at each retention index (red dashed line) for evaporation at 20 °C for 100 h.

The experimental fraction remaining was calculated by dividing the average normalized peak height in the EIC of each selected compound in the evaporated samples by that in the unevaporated samples. For *n*-undecane, the fraction remaining based on the EIC of *m/z* 57 was 0.413, a 5.0% absolute error from the predicted value. For all compounds, the absolute percent error (APE) ranged from 0.0 to 300% and had a MAPE of 55% (Table 2-7). When  $F_{IT}$  was less than 0.1 ( $I^T < 1050$ ), the MAPE was 131%. The large error in  $F_{IT}$  at retention indices below 1050 was due to the very small fraction remaining (Table 2-7). When a relative error calculation is used for small numbers, the error appears inflated [36]. The mean absolute error in this region was only 0.03. When  $F_{IT}$  was 0.1 – 0.5 ( $1050 < I^T < 1150$ ), the MAPE was 42%. The higher error in this region was not surprising as this is where the fraction remaining curve increases sharply at the inflection point (Figure 7). In this region, small variations in the retention index of a compound could result in larger errors in the fraction remaining. When  $F_{IT}$  was greater than 0.5 ( $I^T > 1150$ ), the MAPE was 5.9%. The change in the fraction remaining curve in this region is relative small, leading to the lower error. When the low abundance compounds are excluded from the MAPE calculation, ( $F_{IT} = 0.1 - 1$ ), the MAPE was 13%.

In addition to the fraction remaining of individual compounds of interest, the models developed in this work can also be utilized to predict the total fraction remaining ( $F_{tot}$ ). The  $F_{tot}$  is calculated by summing Equation 2-7 over the relevant range of retention indices (for this study,  $I^T_i = 739$  and  $I^T_f = 3238$ )

Table 2-7. Fraction remaining ( $F_{IT}$ ) for selected compounds in evaporated diesel fuel (20 °C, 100 h), experimental and predicted using the comprehensive model with retention index ( $I^T$ ) correction. The absolute percent error (APE) is also shown.

Compound	$I^T$ Corrected	$F_{IT}$ Experimental	$F_{IT}$ Predicted	APE
Octane	800	2.39E-03	4.56E-09	100
Ethyl benzene	827	1.09E-03	5.19E-07	100
Ethyl cyclohexane	828	8.84E-04	5.63E-07	100
<i>m/p</i> -Xylene	836	9.49E-04	1.85E-06	100
<i>o</i> -Xylene	859	1.54E-03	3.30E-05	98
4-Methyl octane	862	1.47E-03	4.15E-05	97
3-Methyl octane	869	7.11E-04	9.09E-05	87
Nonane	900	1.20E-03	1.17E-03	2.8
Propyl benzene	921	2.46E-03	4.39E-03	79
Propyl cyclohexane	925	2.27E-03	5.56E-03	145
Ethyl methyl benzene isomer	928	3.22E-03	6.52E-03	102
Dimethyl octane isomer	933	2.40E-03	8.33E-03	246
1,3,5-Trimethyl benzene	936	7.53E-03	9.74E-03	29
Ethyl methyl heptane isomer	940	2.92E-03	1.17E-02	299
Ethyl methyl benzene isomer	945	5.78E-03	1.48E-02	155

Table 2-7 cont'd

<b>Compound</b>	<b><math>I^T</math> Corrected</b>	<b><math>F_{IT}</math> Experimental</b>	<b><math>F_{IT}</math> Predicted</b>	<b>APE</b>
Methyl nonane isomer	960	8.72E-03	2.72E-02	212
1,2,4-Trimethyl benzene	961	1.14E-02	2.77E-02	143
Unidentified	970	1.30E-02	3.82E-02	195
Unidentified	979	1.54E-02	5.27E-02	243
1,2,3-Trimethyl benzene	988	2.73E-02	6.79E-02	149
Indane	998	2.56E-02	8.87E-02	246
Decane	1000	4.30E-02	9.30E-02	116
Methyl propyl benzene isomer	1019	7.32E-02	1.42E-01	94
Methyl propyl benzene isomer	1023	7.90E-02	1.53E-01	94
Butyl benzene	1023	7.94E-02	1.55E-01	95
4-Methyl decane	1024	8.19E-02	1.56E-01	91
Butyl cyclohexane	1027	6.16E-02	1.67E-01	171
Methyl propyl benzene isomer	1033	9.41E-02	1.87E-01	99
Methyl indane isomer	1050	1.13E-01	2.43E-01	116
5-Methyl decane	1058	1.86E-01	2.72E-01	46

Table 2-7 cont'd

<b>Compound</b>	<b><math>I^T</math> Corrected</b>	<b><math>F_{IT}</math> Experimental</b>	<b><math>F_{IT}</math> Predicted</b>	<b>APE</b>
2-Methyl decane	1064	2.31E-01	2.98E-01	29
Unidentified	1071	2.11E-01	3.21E-01	52
3-Methyl decane	1071	2.45E-01	3.22E-01	31
Unidentified	1073	2.42E-01	3.30E-01	36
Undecane	1100	4.13E-01	4.34E-01	5.0
Unidentified	1102	2.96E-01	4.41E-01	49
Unidentified	1111	3.28E-01	4.77E-01	45
1,2,3,4-Tetrahydro- naphthalene	1120	3.75E-01	5.09E-01	36
Pentyl benzene	1124	4.41E-01	5.24E-01	19
Pentyl cyclohexane	1130	4.34E-01	5.44E-01	25
Naphthalene	1138	3.52E-01	5.70E-01	62
Unidentified	1155	6.15E-01	6.26E-01	1.8
Methyl undecane isomer	1165	6.80E-01	6.54E-01	3.8
Unidentified	1171	6.86E-01	6.72E-01	2.0
Methyl tetralin isomer	1176	6.06E-01	6.84E-01	13

Table 2-7 cont'd

<b>Compound</b>	<b><math>I^T</math> Corrected</b>	<b><math>F_{IT}</math> Experimental</b>	<b><math>F_{IT}</math> Predicted</b>	<b>APE</b>
Unidentified	1195	6.47E-01	7.35E-01	14
Dodecane	1200	8.24E-01	7.45E-01	10
2,6-Dimethyl undecane	1216	8.29E-01	7.80E-01	5.9
Methyl tetralin isomer	1225	7.56E-01	7.98E-01	5.5
Hexyl cyclohexane	1241	8.17E-01	8.27E-01	1.2
Methyl tetralin isomer	1250	7.87E-01	8.40E-01	6.8
Unidentified	1254	9.09E-01	8.46E-01	7.0
Unidentified	1276	9.35E-01	8.76E-01	6.4
Methyl tetralin isomer	1280	8.65E-01	8.80E-01	1.8
Tridecane	1300	1.01E+00	9.02E-01	10
Methyl tetralin isomer	1302	9.28E-01	9.04E-01	2.6
Unidentified	1330	9.85E-01	9.27E-01	5.9
Heptyl cyclohexane	1338	9.57E-01	9.33E-01	2.5
Methyl tetralin isomer	1351	1.00E+00	9.41E-01	6.3
Unidentified	1365	1.03E+00	9.49E-01	8.1

Table 2-7 cont'd

<b>Compound</b>	<b><math>I^T</math> Corrected</b>	<b><math>F_{IT}</math> Experimental</b>	<b><math>F_{IT}</math> Predicted</b>	<b>APE</b>
2,6,10-Trimethyl decane	1379	1.03E+00	9.56E-01	7.3
Tetradecane	1400	1.04E+00	9.64E-01	7.3
Unidentified	1433	1.04E+00	9.75E-01	6.4
Octyl cyclohexane	1442	1.04E+00	9.77E-01	6.3
Unidentified	1465	1.04E+00	9.82E-01	5.8
Pentadecane	1500	1.06E+00	9.87E-01	6.7
Hexadecane	1600	1.05E+00	9.96E-01	5.3
2,6,10-Trimethyl pentadecane	1654	1.06E+00	9.97E-01	5.9
Heptadecane	1700	1.02E+00	9.98E-01	1.6
Pristane	1711	1.05E+00	9.99E-01	4.8
Octadecane	1800	1.01E+00	9.99E-01	1.5
Phytane	1815	1.02E+00	1.00E+00	2.4
Nonadecane	1900	9.94E-01	1.00E+00	0.6
Eicosane	2000	1.01E+00	1.00E+00	1.3
Heneicosane	2100	1.00E+00	1.00E+00	0.0

Table 2-7 cont'd

<b>Compound</b>	<b><math>I^T</math> Corrected</b>	<b><math>F_{IT}</math> Experimental</b>	<b><math>F_{IT}</math> Predicted</b>	<b>APE</b>
Docosane	2200	1.03E+00	1.00E+00	3.0
Tricosane	2300	1.07E+00	1.00E+00	6.8
Tetracosane	2400	1.08E+00	1.00E+00	7.7
Pentacosane	2500	1.14E+00	1.00E+00	12

$$F_{\text{tot}} = \frac{\sum_{j=I_i}^{I_t} F_j A_j}{\sum_{j=I_i}^{I_t} A_j}$$

Equation 2-8

where  $A_j$  is the normalized abundance at each retention index in the chromatogram of the unevaporated fuel sample.

To test the accuracy of predicting the fraction remaining, three aliquots of diesel fuel were evaporated at 20 °C for 100 h without water in order to obtain accurate masses of the remaining fuel. The average fraction remaining based on the mass of the three diesel samples was 0.8176. Using the comprehensive, retention index corrected model, the predicted total fraction remaining is 0.8627, a 5.5% error. This error is lower than the MAPEs for the individual compounds discussed above. Many of the selected compounds used to develop and test the model were volatile, with a correspondingly higher APE because of their low abundance after evaporation. However, when calculating the total fraction remaining, the contributing compounds are relatively unaffected by evaporation, thereby reducing the error in the model.

To demonstrate the applicability of the model to other fuels, kerosene and marine fuel stabilizer were also utilized Figure 2-19 a and b respectively. These fuels differ significantly from diesel in chemical composition. A petri dish containing only the fuel was weighed before and after evaporation at 20 °C for 100 h. For kerosene, the fraction remaining by mass was 0.6171. The predicted fraction remaining using the comprehensive, retention index corrected model was 0.7253, a 17.5% error. For marine

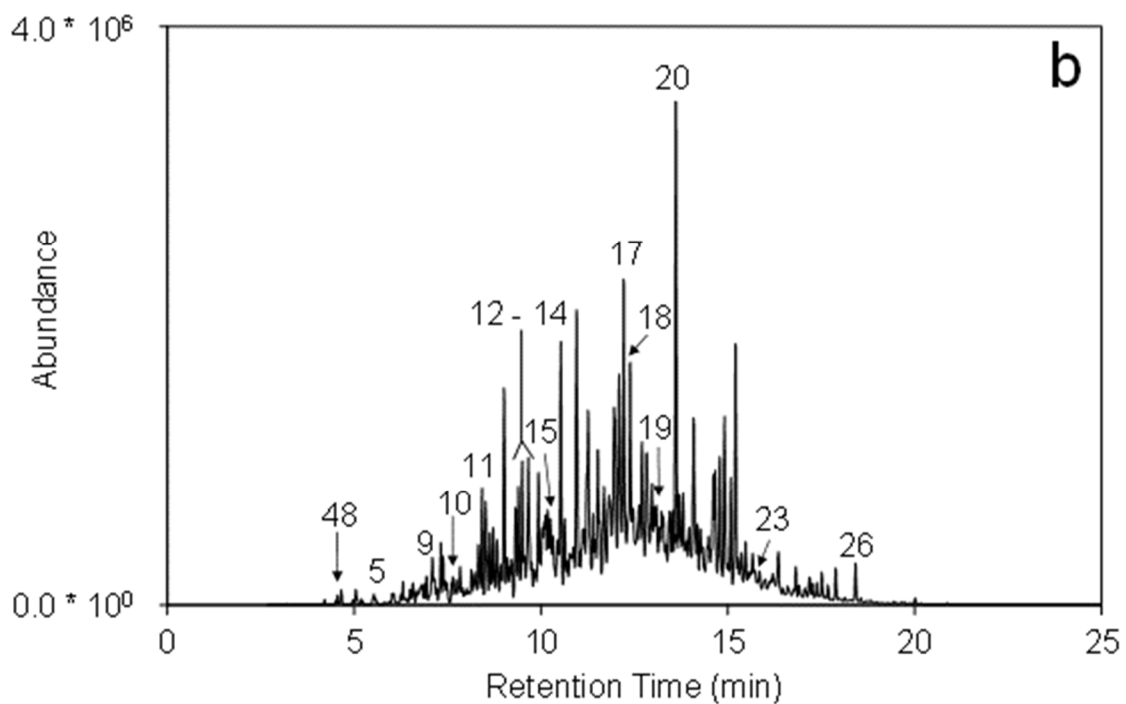
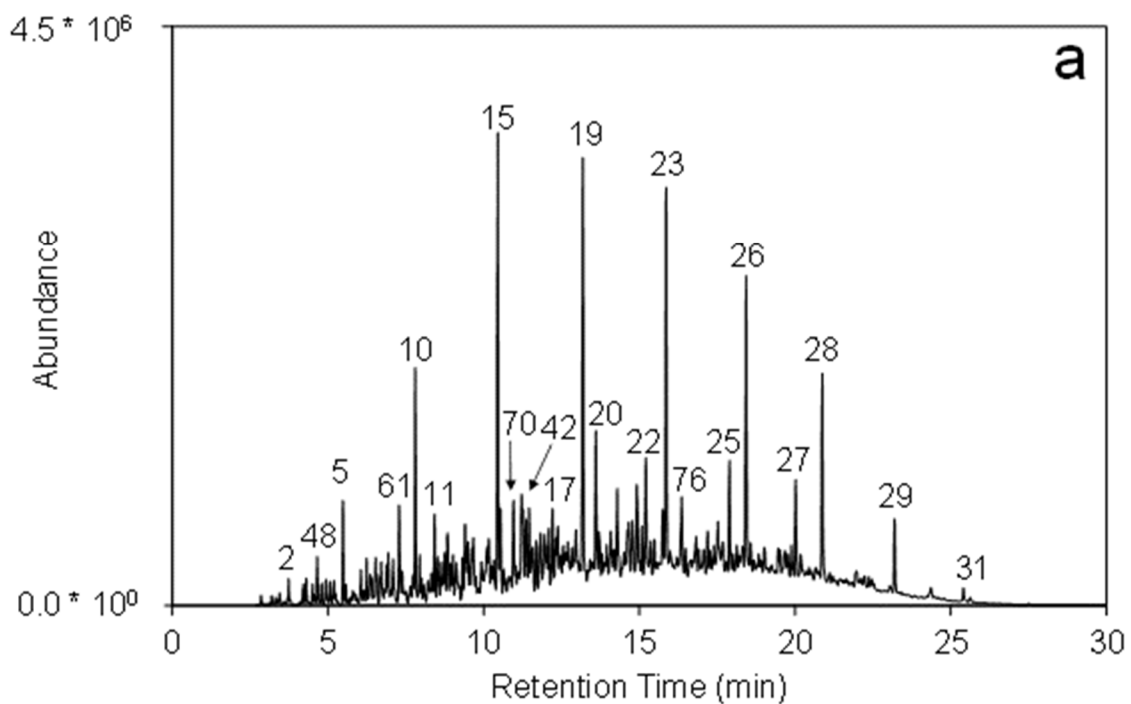


Figure 2-19. Total ion chromatogram for kerosene (a) and marine fuel stabilizer (b). The peak numbers correspond to the compounds listed in Table 2-2.

fuel stabilizer, the fraction remaining by mass was 0.5576. The predicted fraction remaining was 0.6108, resulting in a 9.5% error. These errors are of similar magnitude to those for prediction of the individual rate constants as well as for the total fraction remaining of diesel fuel, demonstrating that the model is extensible to other petroleum products.

## **2.5 Conclusions**

This study has demonstrated that models based on retention index of a compound can accurately predict its evaporation rate constant. The class-specific models are more accurate, but require assigning each compound to a structural class. The comprehensive model, based on all compound classes, is advantageous because knowledge of class membership is not required. Utilizing the developed models, the fraction remaining of an individual compound, as well as the total fraction remaining of the fuel, can be accurately predicted based on the retention index and evaporation time. This can be done without any prior knowledge of the fuel's composition or physical properties, which is critical in environmental and petrochemical applications where exact composition of a fuel is often unknown.

McReynolds constants were applied to further refine the comprehensive model to correct for differences in retention indices that resulted from interactions of the aromatic compounds with the polysiloxane stationary phase. The retention index correction strategies resulted in a closer representation of boiling point and resulted in a more accurate model. In addition chromatographic data generated on a number of widely available stationary phases could be utilized in the model after retention index correction.

Model flexibility, including the input GC data and models for different compound classes, will allow end-users to decide which is most appropriate based on the available data.

While this work has been developed for evaporation of petroleum products, the methodologies have many other potential applications. Other weathering processes on petroleum spills, such as dissolution, could be predicted using similar kinetic models. These methodologies could also be applied for explosives detection, where the vapor pressure and rate of decomposition are critical aspects in the development of detection schemes. Tracking the release and exposure of chemical warfare agents could be accomplished with similar kinetic models. In addition, monitoring and predicting the fate of other pollutants released into the environment, for which there is no established model, could be accomplished using these methodologies. These potential applications are worthy of additional investigation.

## REFERENCES

## REFERENCES

- [1] J. Kemsley, *Chem. Eng. News*, 91 (2013) 12.
- [2] L.M.V. Malmquist, R.R. Olsen, A.B. Hansen, O. Andersen, J.H. Christensen, *J. Chromatogr. A*, 1164 (2007) 262.
- [3] M.F. Fingas, *J. Hazard. Mater.*, 42 (1995) 157.
- [4] M.F. Fingas, *J. Hazard. Mater.*, 56 (1997) 227.
- [5] M.F. Fingas, *J. Hazard. Mater.*, 57 (1998) 41.
- [6] M.R. Riazi, M. Edalat, *J. Pet. Sci. Eng.*, 16 (1996) 291.
- [7] W. Stiver, D. Mackay, *Environ. Sci. Technol.*, 18 (1984) 834.
- [8] P.M.L. Sandercock, E. Du Pasquier, *Forensic Sci. Int.*, 140 (2004) 43.
- [9] W. Lehr, R. Jones, M. Evans, D. Simecek-Beatty, R. Overstreet, *Environ. Modell. Softw.*, 17 (2002) 191.
- [10] N.J. Nielsen, D. Ballabio, G. Tomasi, R. Todeschini, J.H. Christensen, *J. Chromatogr. A*, 1238 (2012) 121.
- [11] U.H. Yim, S.Y. Ha, J.G. An, J.H. Won, G.M. Han, S.H. Hong, M. Kim, J.H. Jung, W.J. Shim, *J. Hazard. Mater.*, 197 (2011) 60.
- [12] M. Reed, O. Johansen, P.J. Brandvik, P. Daling, A. Lewis, R. Fiocco, D. Mackay, R. Prentki, *Spill Sci. Technol. Bull.*, 5 (1999) 3.
- [13] Z. Wang, J.H. Christensen, in: R.D. Morrison, B.L. Murphy (Eds.), *Environmental Forensics Contaminant Specific Guide*, Elsevier, Burlington, MA, 2006.

- [14] B.M. Zorzetti, J.J. Harynuk, *Anal. Bioanal. Chem.*, 401 (2011) 2423.
- [15] B.M. Zorzetti, J.M. Shaver, J.J. Harynuk, *Anal. Chim. Acta*, 694 (2011) 31.
- [16] J.H. Christensen, G. Tomasi, *J. Chromatogr. A*, 1169 (2007) 1.
- [17] Z.D. Wang, M. Fingas, D.S. Page, *J. Chromatogr. A*, 843 (1999) 369.
- [18] R.B. Gaines, G.J. Hall, G.S. Frysinger, W.R. Gronlund, K.L. Juaire, *Environ. Forensics*, 7 (2006) 77.
- [19] Z.R. Regnier, B.F. Scott, *Environ. Sci. Technol.*, 9 (1975) 469.
- [20] R.L. Smith, *Ann. Occup. Hyg.*, 45 (2001) 437.
- [21] A.R. Katritzky, M. Kuanar, S. Slavov, C.D. Hall, M. Karelson, I. Kahn, D.A. Dobchev, *Chem. Rev.*, 110 (2010) 5714.
- [22] A.R. Katritzky, U. Maran, V.S. Lobanov, M. Karelson, *J. Chem. Inf. Comput. Sci.*, 40 (2000) 1.
- [23] N. Ulrich, G. Schuurmann, W. Brack, *J. Chromatogr. A*, 1285 (2013) 139.
- [24] J.S. Arey, R.K. Nelson, L. Xu, C.M. Reddy, *Anal. Chem.*, 77 (2005) 7172.
- [25] C. Eiserbeck, R.K. Nelson, K. Grice, J. Curiale, C.M. Reddy, *Geochim. Cosmochim. Acta*, 87 (2012) 299.
- [26] R.K. Nelson, B.M. Kile, D.L. Plata, S.P. Sylva, L. Xu, C.M. Reddy, R.B. Gaines, G.S. Frysinger, S.E. Reichenbach, *Environ. Forensics*, 7 (2006) 33.
- [27] R.M. Smith, *Anal. Chem.*, 54 (1982) 1399.
- [28] S.E. Stein, in: P.J. Linstrom, W.G. Mallard (Eds.), *NIST Chemistry Webbook*, NIST Standard Reference Database Number 69, National Institute of Standards and

Technology, Mass Spec Data Center, Gaithersburg, MD, 2011. <http://webbook.nist.gov>, (retrieved February 26, 2014).

[29] H. Vandendool, P.D. Kratz, *J. Chromatogr.*, 11 (1963) 463.

[30] IUPAC, *Compendium of Chemical Terminology (the "Gold Book")*, Blackwell Scientific Publications, Oxford, 1997.

[31] R.L. Brown, S.E. Stein, in: P.J. Linstrom, W.G. Mallard (Eds.), *NIST Chemistry Webbook, NIST Standard Reference Database Number 69*, National Institute of Standards and Technology, Gaithersburg, MD, 2011. <http://webbook.nist.gov>, (retrieved February 26, 2014).

[32] W.C. Yang, H. Wang, *Water Res.*, 11 (1977) 879.

[33] J.L. Devore, *Probability and Statistics for Engineering and the Sciences*, Duxbury Press, Belmont, CA, 1991.

[34] J.D. Ingle Jr., S.R. Crouch, *Spectrochemical Analysis*, Prentice-Hall, Englewood Cliffs, NJ, 1988.

[35] S. Makridakis, *Int. J. Forecast.*, 9 (1993) 527.

[36] S. Makridakis, M. Hibon, *Evaluating Accuracy (or Error) Measures*, INSEAD, Fontainebleau, France, 1995.

[37] N.H. Snow, *J. Chem. Educ.*, 73 (1996) 592.

[38] J. Novak, J. Vejrosta, M. Roth, J. Janak, *J. Chromatogr.*, 199 (1980) 209.

[39] P.J. Marriott, in: E. Heftmann (Ed.), *Chromatography*, Elsevier, New York, NY, 2004.

[40] J. Cazes, R.P.W. Scott, *Chromatography Theory*, Marcel Dekker, New York, NY, 2002.

[41] G. Zweig, J. Sherma, in: R.C. Weast (Ed.), Handbook of Chromatography: Volume II, CRC Press, Cleveland, OH, 1972.

### **3. Variable-Temperature Model for Predicting Environmental Evaporation Rates of Petroleum Products using Gas Chromatographic Retention Indices**

#### **3.1 Introduction**

Effective remediation and impact assessment of environmental releases of petroleum fuels depends upon reliable modeling of their fate. Because these devastating releases can occur anywhere in the world, variations in environmental conditions, particularly temperature, must be incorporated into predictive models to facilitate accurate predictions [1-5]. In the previous chapter, a novel kinetic method was proposed to predict evaporation of petroleum constituents. An extensive set of empirical rate constants was determined at 20 °C, which was then fit to a regression equation based on the gas chromatographic retention index. This chapter expands on the previous efforts by incorporating variable temperature into the predictive model. Fixed-temperature models were initially developed from empirical measurements at five temperatures (5, 10, 20, 30, 35 °C). Multiple linear regression of the rate constants determined for each compound at each temperatures was used to create a variable temperature model. The variable temperature model could be used to predict the fraction remaining of an individual compound or the entire fuel. The variable-temperature model was also used to estimate the length of time the fuel has been evaporated from an experimental chromatogram, to predict the chromatogram of the fuel after evaporation for a given time, and to predict the time to reach a specific percent evaporated for an individual compound or for the entire fuel.

## 3.2 Materials and Methods

### 3.2.1 Sample Collection

Diesel fuel was utilized for model development because it contains a wide range of compounds (normal alkanes, branched and cyclic alkanes, alkyl aromatics, and polycyclic aromatics), representative of the compound classes in crude oil. The range of boiling points in diesel fuel (~100 – 400 °C) is appropriate for analysis by gas chromatography-mass spectrometry (GC-MS). A large volume (~5 gallons) of diesel fuel was collected from a service station in East Lansing, MI, placed into acid-washed amber bottles, and stored at ~5 °C. This fuel sample was used over the entire course of the study. Kerosene was also collected from a local service station and stored in amber bottles at ~5 °C until use. Marine fuel stabilizer (Pennzoil, Houston, TX) was purchased and stored in its original container until use.

### 3.2.2 Evaporation of Fuel Samples

Diesel fuel samples were evaporated in an evaporation chamber designed in house [6]. Temperature was controlled by an Ambi-Hi-Lo incubator (5 – 50 °C ± 0.5 °C, model 3550DT, Lab-Line, Melrose Park, IL). Relative humidity (RH) was controlled by placing trays of water, totaling approximately 300 mL, inside the chamber. Temperature and humidity were monitored and recorded at two-minute intervals using a data logger (0 – 55 °C ± 0.3 °C, 10 – 95% RH ± 5% RH, TR-74Ui, T & D Corporation, Nagano, Japan). Glass Petri dishes (60 mm diameter x 15 mm high) with a thin film of diesel fuel (1.0 mL, ~0.5 mm) on distilled water (15 mL) were used to simulate an environmental spill. The

samples were evaporated in triplicate for nine different lengths of time (0 – 300 h) at each temperature (5, 10, 20, 30, and 35 °C).

For model validation, several other evaporation experiments were performed. In one experiment, three diesel fuel samples were prepared as previously described, while three additional samples were prepared without the water layer. The latter fuel samples were weighed before and after evaporation at 20 °C for 100 h to determine the mass loss. In separate experiments, three samples of kerosene and marine fuel stabilizer were evaporated at 20 °C for 100 h. In each experiment, two dishes contained the fuel and water, while the third dish contained the fuel alone. To test the model under fluctuating temperatures, three samples of diesel fuel with water and three samples with fuel alone were evaporated. The temperature was varied in the range of 12 – 27 °C approximately every 12 h, for a total time of 100 h, in order to simulate diurnal variations.

### *3.2.3 Gas Chromatography-Mass Spectrometry Analysis*

The evaporated diesel residues were extracted from water using dichloromethane. The contents of the Petri dish were quantitatively transferred to a separatory funnel and the dish was rinsed several times with approximately 1 mL of dichloromethane. The organic layer was then transferred to a 10.0 mL volumetric flask. An additional dilution (1:50) was performed prior to GC-MS analysis [6].

The analytical system consisted of a gas chromatograph (model 7890N, Agilent Technologies, Santa Clara, CA) with an automatic liquid sampler (model 7693, Agilent Technologies), coupled to a single-quadrupole mass spectrometer (model 5975, Agilent Technologies). The GC separation was performed on a capillary column with 100%

poly(dimethylsiloxane) stationary phase (HP-1MS, 30 m x 0.25 mm x 0.25  $\mu$ m, Agilent Technologies), using ultra-high purity helium (1 mL/min) as the carrier gas. The diluted diesel extract was introduced *via* a pulsed (15 psi for 0.25 min), split (50:1) injection at 280  $^{\circ}$ C. The GC temperature program had an initial temperature of 50  $^{\circ}$ C, linear ramp of 5  $^{\circ}$ C/min to a final temperature of 280  $^{\circ}$ C, with a 4-min hold. In the mass spectrometer, the samples were ionized (70 eV) and the fragment ions were separated using a quadrupole mass analyzer, which scanned mass-to-charge ( $m/z$ ) ratios of 40 – 550 at 2.91 scans/s. Compounds were identified by means of the  $m/z$  ratio of prominent ions as well as the GC retention indices [6]. They were quantified by means of the abundance from extracted ion chromatograms (EIC), normalized to the abundance of heneicosane ( $C_{21}$ ) in the EIC at  $m/z$  57 [6]. A list of the 78 compounds selected for model development and 29 compounds selected for model validation is provided in Table 3-1 and Table 3-2.

#### 3.2.4 Data Analysis

The first-order rate constants ( $k$ ) were determined by using the methodology developed in the previous work [17]. The first-order kinetic rate constant ( $k$ ) can be used to calculate the concentration of a compound ( $C_t$ ) at time ( $t$ ), given its initial concentration ( $C_0$ ).

$$C_t = C_0 \exp(-k t)$$

Equation 3-1

Table 3-1. Selected compounds monitored during evaporation of diesel fuel for development of fixed-temperature and variable-temperature models. The following information is listed for each compound: Peak number in Table 3-3 – Table 3-12 (Peak #), the identity of the compound, the class to which the compound was assigned, the mass-to-charge ( $m/z$ ) ratio of the extracted ion chromatogram (EIC) used to quantify the compound, the retention time ( $t^T_R$ ), the boiling point ( $T_b$ ), and retention index ( $I^T$ ) before and after correction.

Peak #	Compound	Class	$m/z$	$t^T_R$ (min)	$T_b$ (K) <sup>1</sup>	$I^T$	$I^T$ Corrected <sup>2</sup>
1	2-Methyl heptane	Branched Alkane	57	3.398			
2	Octane	Normal Alkane	57	3.748	399	800	800
3	4-Methyl octane	Branched Alkane	57	4.814	415	862	862
4	3-Methyl octane	Branched Alkane	57	4.948	417	869	869
5	Nonane	Normal Alkane	57	5.479	424	900	900
6	Dimethyl octane isomer	Branched Alkane	57	6.248		933	933
7	Ethyl methyl heptane isomer	Branched Alkane	57	6.411		940	940
8	Methyl nonane isomer	Branched Alkane	57	6.883		960	960
9	Unidentified	Branched Alkane	57	7.105		970	970

Table 3-1 cont'd

Peak #	Compound	Class	<i>m/z</i>	<i>t</i> <sub>R</sub> <sup>T</sup> (min)	<i>T</i> <sub>b</sub> (K) <sup>1</sup>	<i>I</i> <sup>T</sup>	<i>I</i> <sup>T</sup> Corrected <sup>2</sup>
10	Decane	Normal Alkane	57	7.816	447	1000	1000
11	4-Methyl decane	Branched Alkane	57	8.434	460	1024	1024
12	5-Methyl decane	Branched Alkane	57	9.326		1058	1058
13	2-Methyl decane	Branched Alkane	57	9.506	462	1064	1064
14	3-Methyl decane	Branched Alkane	57	9.670		1071	1071
15	Undecane	Normal Alkane	57	10.439	468	1100	1100
16	Unidentified	Branched Alkane	57	11.960		1155	1155
17	Methyl undecane isomer	Branched Alkane	57	12.217		1165	1165
18	Unidentified	Branched Alkane	57	12.392		1171	1171
19	Dodecane	Normal Alkane	57	13.184	489	1200	1200
20	2,6-Dimethyl undecane	Branched Alkane	57	13.616		1216	1216

Table 3-1 cont'd

Peak #	Compound	Class	<i>m/z</i>	<i>t</i> <sub>R</sub> <sup>T</sup> (min)	<i>T</i> <sub>b</sub> (K) <sup>1</sup>	<i>I</i> <sup>T</sup>	<i>I</i> <sup>T</sup> Corrected <sup>2</sup>
21	Unidentified	Branched Alkane	57	14.618		1254	1254
22	Unidentified	Branched Alkane	57	15.213		1276	1276
23	Tridecane	Normal Alkane	57	15.848	507	1300	1300
24	Unidentified	Branched Alkane	57	17.527		1365	1365
25	2,6,10-Trimethyl decane	Branched Alkane	57	17.900		1379	1379
26	Tetradecane	Normal Alkane	57	18.430	523	1400	1400
27	Unidentified	Branched Alkane	57	20.027		1465	1465
28	Pentadecane	Normal Alkane	57	20.890	540	1500	1500
29	Hexadecane	Normal Alkane	57	23.186	554	1600	1600
30	2,6,10-Trimethyl pentadecane	Branched Alkane	57	24.369		1654	1654
31	Heptadecane	Normal Alkane	57	25.395	575	1700	1700

Table 3-1 cont'd

Peak #	Compound	Class	<i>m/z</i>	<i>t</i> <sub>R</sub> <sup>T</sup> (min)	<i>T</i> <sub>b</sub> (K) <sup>1</sup>	<i>I</i> <sup>T</sup>	<i>I</i> <sup>T</sup> Corrected <sup>2</sup>
32	Pristane	Branched Alkane	57	25.628		1711	1711
33	Octadecane	Normal Alkane	57	27.488	589	1800	1800
34	Phytane	Branched Alkane	57	27.791		1815	1815
35	Nonadecane	Normal Alkane	57	29.539		1900	1900
36	Eicosane	Normal Alkane	57	31.400	616	2000	2000
37	Heneicosane	Normal Alkane	57	33.276	635	2100	2100
38	Methyl cyclohexane	Branched Alkane	83	2.856	374		
39	Ethyl cyclohexane	Branched Alkane	83	4.226	405	828	828
40	Propyl cyclohexane	Branched Alkane	83	6.067	429	925	925
41	Butyl cyclohexane	Branched Alkane	83	8.527	453	1027	1027
42	Pentyl cyclohexane	Branched Alkane	83	11.272	477	1130	1130

Table 3-1 cont'd

Peak #	Compound	Class	<i>m/z</i>	<i>t</i> <sub>R</sub> <sup>T</sup> (min)	<i>T</i> <sub>b</sub> (K) <sup>1</sup>	<i>I</i> <sup>T</sup>	<i>I</i> <sup>T</sup> Corrected <sup>2</sup>
43	Hexyl cyclohexane	Branched Alkane	83	14.288	498	1241	1241
44	Heptyl cyclohexane	Branched Alkane	83	16.833	510	1338	1338
45	Octyl cyclohexane	Branched Alkane	83	19.462	528	1442	1442
46	Toluene	Alkyl Aromatic	91	3.194	384		
47	Ethyl benzene	Alkyl Aromatic	91	4.511	409	844	827
48	m/p-Xylene	Alkyl Aromatic	91	4.663	412	853	836
49	o-Xylene	Alkyl Aromatic	91	5.071	417	876	859
50	Propyl benzene	Alkyl Aromatic	91	6.365	432	938	921
51	Butyl benzene	Alkyl Aromatic	91	8.871	456	1040	1023
52	Unidentified	Alkyl Aromatic	91	10.171		1090	1073
53	1,2,3,4-Tetrahydro-naphthalene	Polycyclic Hydrocarbon	91	11.465	490	1137	1120

Table 3-1 cont'd

Peak #	Compound	Class	<i>m/z</i>	<i>t</i> <sub>R</sub> <sup>T</sup> (min)	<i>T</i> <sub>b</sub> (K) <sup>1</sup>	<i>I</i> <sup>T</sup>	<i>I</i> <sup>T</sup> Corrected <sup>2</sup>
54	Pentyl benzene	Alkyl Aromatic	91	11.576		1141	1124
55	Methyl tetralin isomer	Polycyclic Hydrocarbon	91	12.980		1193	1176
56	Unidentified	Polycyclic Hydrocarbon	91	17.066		1347	1330
57	Unidentified	Polycyclic Hydrocarbon	91	19.660		1450	1433
58	Ethyl methyl benzene isomer	Alkyl Aromatic	105	6.534		945	928
59	1,3,5-Trimethyl benzene	Alkyl Aromatic	105	6.720	438	953	936
60	Ethyl methyl benzene isomer	Alkyl Aromatic	105	6.930		962	945
61	1,2,4-Trimethyl benzene	Alkyl Aromatic	105	7.291	442	978	961
62	Unidentified	Alkyl Aromatic	105	7.734		996	979
63	1,2,3-Trimethyl benzene	Alkyl Aromatic	105	7.950	449	1005	988

Table 3-1 cont'd

Peak #	Compound	Class	<i>m/z</i>	<i>t</i> <sub>R</sub> <sup>T</sup> (min)	<i>T</i> <sub>b</sub> (K) <sup>1</sup>	<i>I</i> <sup>T</sup>	<i>I</i> <sup>T</sup> Corrected <sup>2</sup>
64	Methyl propyl benzene isomer	Alkyl Aromatic	105	8.754		1036	1019
65	Methyl propyl benzene isomer	Alkyl Aromatic	105	8.854		1040	1023
66	Methyl propyl benzene isomer	Alkyl Aromatic	105	9.139		1050	1033
67	Unidentified	Alkyl Aromatic	105	10.113		1088	1071
68	Indane	Polycyclic Hydrocarbon	117	8.212	450	1015	998
69	Methyl indane isomer	Polycyclic Hydrocarbon	117	9.565		1067	1050
70	Unidentified	Polycyclic Hydrocarbon	117	10.958		1119	1102
71	Unidentified	Polycyclic Hydrocarbon	117	11.220		1128	1111
72	Unidentified	Polycyclic Hydrocarbon	117	13.516		1212	1195
73	Methyl tetralin isomer	Polycyclic Hydrocarbon	117	14.303	507	1242	1225

Table 3-1 cont'd

Peak #	Compound	Class	<i>m/z</i>	<i>t</i> <sub>R</sub> <sup>T</sup> (min)	<i>T</i> <sub>b</sub> (K) <sup>1</sup>	<i>I</i> <sup>T</sup>	<i>I</i> <sup>T</sup> Corrected <sup>2</sup>
74	Methyl tetralin isomer	Polycyclic Hydrocarbon	117	14.974		1267	1250
75	Methyl tetralin isomer	Polycyclic Hydrocarbon	117	15.760		1297	1280
76	Methyl tetralin isomer	Polycyclic Hydrocarbon	117	16.349		1319	1302
77	Methyl tetralin isomer	Polycyclic Hydrocarbon	117	17.591		1368	1351
78	Naphthalene	Polycyclic Hydrocarbon	128	11.949	490	1155	1138

<sup>1</sup> Source: R.L. Brown, S.E. Stein, in: P.J. Linstrom, W.G. Mallard (Eds.), NIST Chemistry WebBook, NIST Standard Reference Database Number 69, National Institute of Standards and Technology, Gaithersburg MD, 2011. <http://webbook.nist.gov>, (retrieved February 26, 2014).

<sup>2</sup> For compounds in the alkyl aromatic and polycyclic aromatic classes, retention index is corrected using the McReynolds constant for benzene on 100% poly(dimethylsiloxane) stationary phase.  $I^T \text{ corrected} = I^T - 17$

Table 3-2. Selected compounds monitored during evaporation of diesel fuel for validation of fixed-temperature and variable-temperature models. The following information is listed for each compound: Peak number in Table 3-3 – Table 3-12 (Peak #), the class to which the compound was assigned, the mass-to-charge ( $m/z$ ) ratio of the extracted ion chromatogram (EIC) used to quantify the compound, the retention time ( $t^T_{R}$ ), and retention index ( $I^T$ ) before and after correction.

Peak #	Class	$m/z$	$t^T_{R}$ (min)	$I^T$	$I^T$ Corrected <sup>1</sup>
79	Branched Alkane	57	12.094	1160	1160
80	Branched Alkane	57	15.078	1271	1271
81	Alkyl Aromatic	105	5.723	910	893
82	Alkyl Aromatic	105	11.605	1142	1125
83	Alkyl Aromatic	105	11.832	1151	1134
84	Alkyl Aromatic	117	14.641	1255	1238
85	Polycyclic Hydrocarbon	117	16.728	1334	1317
86	Branched Alkane	97	3.800	803	803
87	Branched Alkane	97	5.205	884	884

Table 3-2 cont'd

Peak #	Class	<i>m/z</i>	<i>t</i> <sub>R</sub> <sup>T</sup> (min)	<i>I</i> <sup>T</sup>	<i>I</i> <sup>T</sup> Corrected <sup>1</sup>
88	Branched Alkane	97	5.578	904	904
89	Branched Alkane	97	7.326	979	979
90	Branched Alkane	97	7.390	982	982
91	Branched Alkane	97	7.647	993	993
92	Branched Alkane	97	9.943	1081	1081
93	Branched Alkane	97	10.241	1092	1092
94	Alkyl Aromatic	119	8.002	1007	990
95	Alkyl Aromatic	119	8.084	1010	993
96	Alkyl Aromatic	119	8.864	1033	1016
97	Alkyl Aromatic	119	8.941	1043	1026
98	Alkyl Aromatic	119	9.617	1069	1052

Table 3-2 cont'd

Peak #	Class	<i>m/z</i>	<i>t</i> <sub>R</sub> <sup>T</sup> (min)	<i>I</i> <sup>T</sup>	<i>I</i> <sup>T</sup> Corrected <sup>1</sup>
99	Alkyl Aromatic	119	10.650	1104	1087
100	Alkyl Aromatic	119	11.360	1134	1117
101	Alkyl Aromatic	119	11.686	1145	1128
102	Alkyl Aromatic	119	11.797	1149	1132
103	Alkyl Aromatic	119	12.036	1158	1141
104	Polycyclic Hydrocarbon	137	10.532	1103	1086
105	Polycyclic Hydrocarbon	137	13.645	1217	1200
106	Polycyclic Hydrocarbon	137	13.907	1227	1210

<sup>1</sup> For compounds in the alkyl aromatic and polycyclic aromatic classes, retention index is corrected using the McReynolds constant for benzene on 100% poly(dimethylsiloxane) stationary phase.  $I^T$  corrected =  $I^T - 17$

The normalized abundance of each selected compound was plotted as a function of time, and the resulting decay curve was fit by nonlinear regression to Equation 3-1 (TableCurve 2D, version 5.01, Systat Software, Richmond, CA). The characteristic lifetime ( $\tau$ ), which is equal to  $1/k$ , is often used to describe the completeness of the decay curve. Only rate constants for compounds with greater than  $0.5 \tau$  in the decay curve were included in the models. This allowed for inclusion of 78 selected compounds, while introducing only minimal error of 2.9% [17].

For development of the fixed-temperature and variable-temperature kinetic models, linear and multiple linear regression were performed using Excel (Office 2013, version 15.0, Microsoft Corporation, Redmond, WA).

### 3.3 Results

Figure 3-1 shows representative total ion chromatograms (TIC) of diesel fuel prior to evaporation and after 300 h of evaporation at temperatures of 5, 10, 20, 30, and 35 °C. As expected, an increase in temperature resulted in additional evaporation. Some compounds, such as *n*-octane (C<sub>8</sub>), were completely evaporated after 300 h at all temperatures. Other compounds, such as *n*-tetradecane (C<sub>14</sub>), remained relatively unchanged at all temperatures. The rate constants for evaporation are summarized for all selected compounds at each temperature in Table 3-3 – Table 3-12.

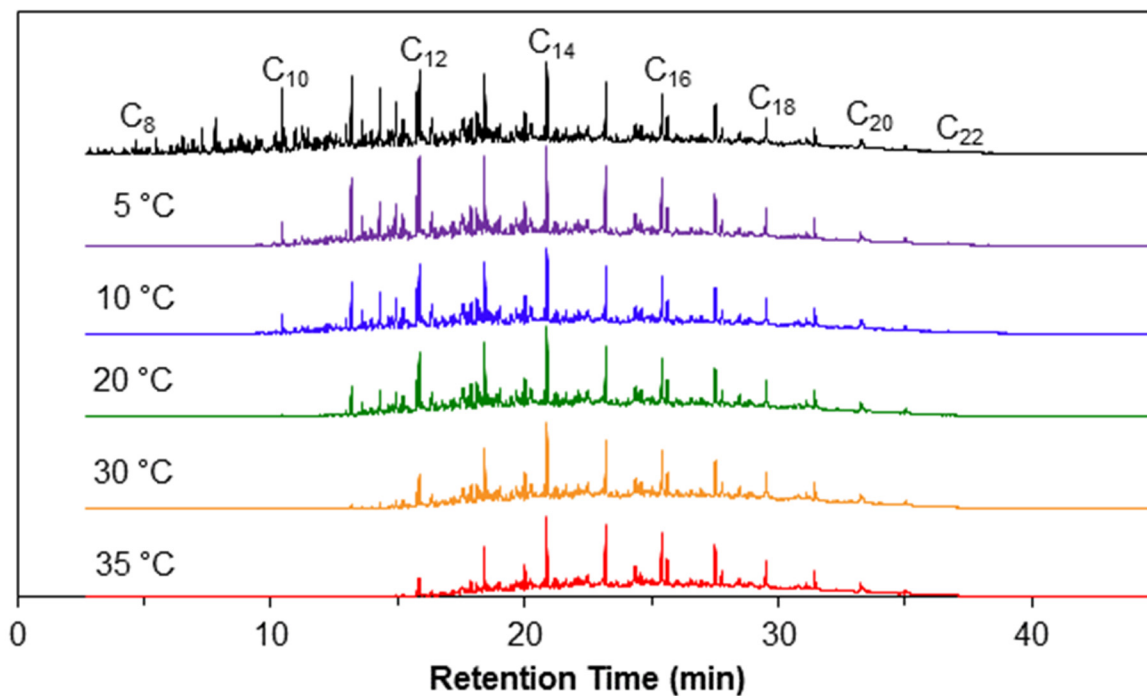


Figure 3-1. Representative total ion chromatograms of diesel samples prior to evaporation and after evaporation for 300 h at 5 – 35 °C. Even-numbered normal alkanes are labeled for reference.

Table 3-3. For model development, the experimental rate constant ( $k_{exp}$ ), characteristic lifetime ( $\tau$ ), and the number of  $\tau$  in 300 h for selected compounds monitored during the evaporation of diesel fuel at 5 °C. The predicted rate constant ( $k_{pred}$ ) and absolute percent error (APE) was calculated using the fixed-temperature (fixed T) and variable-temperature (variable T) models. Compounds with  $\tau > 0.5$  in 300 h were excluded from the table (peaks 16 – 37, 43 – 45, 72 – 77). Several compounds had retention indices less than 800 (peaks 1, 38, 46) and were also excluded, as the retention index could not be accurately extrapolated.

Peak #	$k_e$ ( $h^{-1}$ )	$\tau$ (h)	# $\tau$ in 300 h	$k_{pred}$ fixed T	$k_{pred}$ variable T	APE fixed T	APE variable T
1	1.83E-01	5.5	54.9				
2	1.28E-01	7.8	38.3	1.10E-01	7.36E-02	14.1	42.4
3	5.04E-02	19.8	15.1	5.49E-02	3.90E-02	9.0	22.6
4	4.97E-02	20.1	14.9	5.04E-02	3.60E-02	1.3	27.5
5	3.34E-02	29.9	10.0	3.57E-02	2.63E-02	6.7	21.4
6	2.32E-02	43.1	7.0	2.46E-02	1.87E-02	6.2	19.3
7	2.27E-02	44.0	6.8	2.28E-02	1.74E-02	0.4	23.2
8	1.63E-02	61.3	4.9	1.82E-02	1.42E-02	11.4	13.2
9	1.48E-02	67.7	4.4	1.63E-02	1.28E-02	10.5	13.1

Table 3-3 cont'd

Peak #	$k_e$ (h <sup>-1</sup> )	$\tau$ (h)	# $\tau$ in 300 h	$k_p$ fixed T	$k_p$ variable T	APE fixed T	APE variable T
10	1.02E-02	98.5	3.0	1.16E-02	9.38E-03	14.1	7.6
11	8.24E-03	121.3	2.5	8.90E-03	7.36E-03	7.9	10.7
12	5.56E-03	179.9	1.7	6.07E-03	5.19E-03	9.2	6.7
13	4.98E-03	201.0	1.5	5.62E-03	4.83E-03	12.9	2.8
14	4.79E-03	208.6	1.4	5.24E-03	4.53E-03	9.2	5.4
15	3.13E-03	320.0	0.9	3.77E-03	3.35E-03	20.5	7.3
16	1.51E-03	660.7	0.5	2.02E-03	1.89E-03		
17	1.31E-03	760.8	0.4	1.82E-03	1.72E-03		
18	1.26E-03	793.4	0.4	1.69E-03	1.61E-03		
19	6.96E-04	1437.5	0.2	1.22E-03	1.20E-03		
20	6.14E-04	1629.5	0.2	1.02E-03	1.01E-03		

Table 3-3 cont'd

Peak #	$k_e$ ( $h^{-1}$ )	$\tau$ (h)	# $\tau$ in 300 h	$k_p$ fixed T	$k_p$ variable T	APE fixed T	APE variable T
21	2.54E-04	3943.1	0.1	6.68E-04	6.88E-04		
22	1.41E-04	7107.7	0.0	5.20E-04	5.47E-04		
38	4.40E-01	2.3	132.1				
39	1.04E-01	9.6	31.3	8.05E-02	5.54E-02	23.0	47.0
40	2.98E-02	33.5	8.9	2.69E-02	2.03E-02	9.9	32.0
41	9.46E-03	105.7	2.8	8.55E-03	7.10E-03	9.6	24.9
42	2.86E-03	350.1	0.9	2.68E-03	2.45E-03	6.2	14.1
43	5.11E-04	1957.9	0.2	7.68E-04	7.81E-04		
46	3.04E-01	3.3	91.3				
47	9.70E-02	10.3	29.1	8.10E-02	5.57E-02	16.5	42.6
48	7.42E-02	13.5	22.3	7.34E-02	5.09E-02	1.1	31.4

Table 3-3 cont'd

Peak #	$k_e$ ( $h^{-1}$ )	$\tau$ (h)	# $\tau$ in 300 h	$k_p$ fixed T	$k_p$ variable T	APE fixed T	APE variable T
49	5.84E-02	17.1	17.5	5.63E-02	3.99E-02	3.6	31.7
50	2.94E-02	34.0	8.8	2.82E-02	2.12E-02	4.0	27.9
51	8.80E-03	113.6	2.6	8.93E-03	7.39E-03	1.4	16.1
52	5.00E-03	200.1	1.5	5.12E-03	4.44E-03	2.4	11.2
53	3.36E-03	297.5	1.0	3.00E-03	2.72E-03	10.9	19.1
54	2.74E-03	365.0	0.8	2.86E-03	2.61E-03	4.5	4.9
55	1.70E-03	589.0	0.5	1.61E-03	1.54E-03	5.1	9.3
58	2.42E-02	41.3	7.3	2.60E-02	1.97E-02	7.3	18.8
59	1.78E-02	56.3	5.3	2.38E-02	1.81E-02	33.8	2.0
60	2.02E-02	49.6	6.0	2.15E-02	1.65E-02	6.6	18.1
61	1.64E-02	61.0	4.9	1.81E-02	1.41E-02	10.1	14.1

Table 3-3 cont'd

Peak #	$k_e$ ( $h^{-1}$ )	$\tau$ (h)	# $\tau$ in 300 h	$k_p$ fixed T	$k_p$ variable T	APE fixed T	APE variable T
62	1.52E-02	66.0	4.5	1.46E-02	1.16E-02	3.7	23.5
63	1.19E-02	84.1	3.6	1.33E-02	1.06E-02	11.4	10.8
64	8.57E-03	116.7	2.6	9.39E-03	7.74E-03	9.5	9.7
65	8.80E-03	113.6	2.6	8.99E-03	7.44E-03	2.2	15.5
66	7.67E-03	130.3	2.3	7.96E-03	6.65E-03	3.7	13.3
67	5.00E-03	200.1	1.5	5.24E-03	4.54E-03	4.9	9.2
68	1.40E-02	71.3	4.2	1.18E-02	9.57E-03	15.5	31.7
69	7.43E-03	134.6	2.2	6.63E-03	5.63E-03	10.7	24.2
70	4.08E-03	245.1	1.2	3.69E-03	3.29E-03	9.6	19.5
71	3.77E-03	265.6	1.1	3.31E-03	2.98E-03	12.0	20.9
72	1.24E-03	809.4	0.4	1.29E-03	1.25E-03		

Table 3-3 cont'd

<b>Peak #</b>	<b><math>k_e</math> (<math>h^{-1}</math>)</b>	<b><math>\tau</math> (h)</b>	<b># <math>\tau</math> in 300 h</b>	<b><math>k_p</math> fixed T</b>	<b><math>k_p</math> variable T</b>	<b>APE fixed T</b>	<b>APE variable T</b>
73	8.51E-04	1174.6	0.3	9.24E-04	9.25E-04		
74	5.41E-04	1848.8	0.2	6.96E-04	7.14E-04		
75	2.19E-04	4569.2	0.1	5.00E-04	5.27E-04		
78	3.56E-03	281.2	1.1	2.46E-03	2.27E-03	30.9	36.3

Table 3-4. For model validation, the experimental rate constant ( $k_{\text{exp}}$ ), characteristic lifetime ( $\tau$ ), and the number of  $\tau$  in 300 h for selected compounds in diesel fuel evaporated at 5 °C. The predicted rate constant ( $k_{\text{pred}}$ ) and absolute percent error (APE) was calculated using the fixed-temperature (fixed T) and variable-temperature (variable T) models. Compounds with  $\tau > 0.5$  in 300 h were excluded from the table (peaks 80, 84, 85, 105, 106).

Peak #	$k_{\text{exp}}$ ( $\text{h}^{-1}$ )	$\tau$ (h)	# $\tau$ in 300 h	$k_{\text{pred}}$ fixed T	$k_{\text{pred}}$ variable T	APE fixed T	APE variable T
79	1.52E-03	657.5	0.5	1.91E-03	1.80E-03	25.8	18.5
81	2.94E-02	34.1	8.8	3.84E-02	2.81E-02	30.7	4.3
82	1.86E-03	538.5	0.6	2.83E-03	2.58E-03	52.4	38.9
83	1.90E-03	526.6	0.6	2.58E-03	2.37E-03	35.7	24.7
86	1.51E-01	6.6	45.3	1.06E-01	7.13E-02	29.8	52.8
87	4.52E-02	22.1	13.6	4.26E-02	3.09E-02	5.7	31.6
88	3.88E-02	25.8	11.6	3.40E-02	2.52E-02	12.3	35.1
89	1.45E-02	69.1	4.3	1.47E-02	1.16E-02	1.5	19.5
90	1.50E-02	66.7	4.5	1.42E-02	1.13E-02	5.1	24.5

Table 3-4 cont'd

Peak #	$k_{exp}$ ( $h^{-1}$ )	$\tau$ (h)	# $\tau$ in 300 h	$k_{pred}$ fixed T	$k_{pred}$ variable T	APE fixed T	APE variable T
91	1.39E-02	71.8	4.2	1.26E-02	1.01E-02	9.7	27.4
92	4.75E-03	210.7	1.4	4.66E-03	4.07E-03	1.9	14.2
93	4.66E-03	214.4	1.4	4.10E-03	3.62E-03	12.1	22.3
94	1.19E-02	83.8	3.6	1.30E-02	1.04E-02	8.6	12.9
95	1.14E-02	87.4	3.4	1.25E-02	1.01E-02	9.3	12.0
96	9.01E-03	111.0	2.7	9.67E-03	7.95E-03	7.3	11.8
97	7.14E-03	140.0	2.1	8.67E-03	7.19E-03	21.3	0.7
98	6.07E-03	164.7	1.8	6.49E-03	5.51E-03	6.8	9.2
99	3.85E-03	260.1	1.2	4.36E-03	3.83E-03	13.3	0.4
100	3.08E-03	324.8	0.9	3.13E-03	2.83E-03	1.6	8.2
101	2.51E-03	398.6	0.8	2.74E-03	2.50E-03	9.1	0.3

Table 3-4 cont'd

<b>Peak #</b>	<b><math>k_{\text{exp}}</math> (h<sup>-1</sup>)</b>	<b><math>\tau</math> (h)</b>	<b># <math>\tau</math> in 300 h</b>	<b><math>k_{\text{pred}}</math> fixed T</b>	<b><math>k_{\text{pred}}</math> variable T</b>	<b>APE fixed T</b>	<b>APE variable T</b>
102	2.32E-03	431.3	0.7	2.62E-03	2.40E-03	12.8	3.5
103	2.08E-03	480.5	0.6	2.37E-03	2.19E-03	13.9	5.4
104	4.13E-03	242.0	1.2	4.39E-03	3.86E-03	6.3	6.7
107	8.41E-03	119.0	2.5	8.26E-03	6.88E-03	0.7	18.1

Table 3-5. For model development, the experimental rate constant ( $k_{exp}$ ), characteristic lifetime ( $\tau$ ), and the number of  $\tau$  in 300 h for selected compounds monitored during the evaporation of diesel fuel at 10 °C. The predicted rate constant ( $k_{pred}$ ) and absolute percent error (APE) was calculated using the fixed-temperature (fixed T) and variable-temperature (variable T) models. Compounds with  $\tau > 0.5$  in 300 h were excluded from the table (peaks 19 – 37, 43 – 45, 73 – 77). Several compounds had retention indices lower than 800 (peaks 1, 38, 46) and were also excluded, as the retention index could not be accurately extrapolated.

Peak #	$k_e$ ( $h^{-1}$ )	$\tau$ (h)	# $\tau$ in 300 h	$k_p$ fixed T	$k_p$ variable T	APE fixed T	APE variable T
1	2.13E-01	4.7	63.8				
2	1.51E-01	6.6	45.2	1.05E-01	1.10E-01	30.2	26.8
3	5.49E-02	18.2	16.5	5.50E-02	5.85E-02	0.2	6.6
4	5.33E-02	18.8	16.0	5.07E-02	5.40E-02	4.9	1.4
5	3.47E-02	28.8	10.4	3.67E-02	3.94E-02	5.7	13.4
6	2.45E-02	40.8	7.4	2.60E-02	2.81E-02	5.9	14.4
7	2.35E-02	42.5	7.1	2.41E-02	2.61E-02	2.7	11.2
8	1.72E-02	58.1	5.2	1.95E-02	2.12E-02	13.4	23.4
9	1.59E-02	62.8	4.8	1.77E-02	1.93E-02	10.9	20.9

Table 3-5 cont'd

Peak #	$k_e$ ( $h^{-1}$ )	$\tau$ (h)	# $\tau$ in 300 h	$k_p$ fixed T	$k_p$ variable T	APE fixed T	APE variable T
10	1.08E-02	92.5	3.2	1.28E-02	1.41E-02	18.6	30.2
11	9.51E-03	105.2	2.9	1.00E-02	1.10E-02	5.2	16.2
12	6.82E-03	146.6	2.0	6.99E-03	7.78E-03	2.5	14.1
13	6.17E-03	162.1	1.9	6.50E-03	7.25E-03	5.5	17.6
14	6.06E-03	164.9	1.8	6.09E-03	6.80E-03	0.4	12.1
15	4.25E-03	235.5	1.3	4.47E-03	5.03E-03	5.3	18.4
16	2.31E-03	433.8	0.7	2.50E-03	2.84E-03	8.3	23.2
17	1.99E-03	502.3	0.6	2.26E-03	2.58E-03	13.6	29.6
18	1.90E-03	526.1	0.6	2.11E-03	2.42E-03	11.3	27.1
19	1.08E-03	924.5	0.3	1.56E-03	1.80E-03		
20	9.78E-04	1022.2	0.3	1.32E-03	1.52E-03		

Table 3-5 cont'd

Peak #	$k_e$ ( $h^{-1}$ )	$\tau$ (h)	# $\tau$ in 300 h	$k_p$ fixed T	$k_p$ variable T	APE fixed T	APE variable T
21	5.65E-04	1768.8	0.2	8.86E-04	1.03E-03		
22	4.00E-04	2497.0	0.1	7.00E-04	8.20E-04		
23	1.98E-04	5055.7	0.1	5.45E-04	6.41E-04		
38	5.10E-01	2.0	153.1				
39	1.13E-01	8.9	33.8	7.87E-02	8.30E-02	30.1	26.2
40	3.07E-02	32.6	9.2	2.82E-02	3.04E-02	8.3	1.0
41	1.00E-02	100.0	3.0	9.63E-03	1.06E-02	3.7	6.4
42	3.80E-03	263.1	1.1	3.25E-03	3.68E-03	14.5	3.3
43	9.85E-04	1014.9	0.3	1.01E-03	1.17E-03		
44	1.33E-04	7493.3	0.0	3.65E-04	4.33E-04		
46	3.62E-01	2.8	108.7				

Table 3-5 cont'd

Peak #	$k_e$ ( $h^{-1}$ )	$\tau$ (h)	# $\tau$ in 300 h	$k_p$ fixed T	$k_p$ variable T	APE fixed T	APE variable T
47	9.57E-02	10.5	28.7	7.91E-02	8.35E-02	17.3	12.7
48	7.23E-02	13.8	21.7	7.21E-02	7.63E-02	0.3	5.4
49	5.75E-02	17.4	17.3	5.63E-02	5.98E-02	2.1	4.0
50	2.83E-02	35.3	8.5	2.95E-02	3.18E-02	4.1	12.3
51	9.41E-03	106.2	2.8	1.00E-02	1.11E-02	6.6	17.7
52	5.55E-03	180.2	1.7	5.96E-03	6.65E-03	7.4	19.9
53	4.17E-03	239.7	1.3	3.61E-03	4.08E-03	13.5	2.3
54	3.59E-03	278.7	1.1	3.46E-03	3.91E-03	3.6	8.9
55	2.30E-03	434.1	0.7	2.02E-03	2.31E-03	12.4	0.2
58	2.33E-02	42.9	7.0	2.73E-02	2.95E-02	17.1	26.4
59	1.79E-02	56.0	5.4	2.51E-02	2.72E-02	40.6	52.1

Table 3-5 cont'd

Peak #	$k_e$ ( $h^{-1}$ )	$\tau$ (h)	# $\tau$ in 300 h	$k_p$ fixed T	$k_p$ variable T	APE fixed T	APE variable T
60	1.99E-02	50.1	6.0	2.28E-02	2.48E-02	14.5	24.2
61	1.58E-02	63.1	4.8	1.94E-02	2.11E-02	22.5	33.3
62	1.47E-02	67.9	4.4	1.59E-02	1.74E-02	8.1	18.1
63	1.26E-02	79.5	3.8	1.45E-02	1.59E-02	15.4	26.4
64	9.24E-03	108.2	2.8	1.05E-02	1.16E-02	13.8	25.6
65	9.11E-03	109.8	2.7	1.01E-02	1.12E-02	10.9	22.5
66	8.75E-03	114.3	2.6	9.01E-03	9.97E-03	3.0	14.0
67	6.09E-03	164.3	1.8	6.10E-03	6.81E-03	0.1	11.8
68	1.36E-02	73.6	4.1	1.31E-02	1.44E-02	3.7	5.7
69	8.00E-03	125.1	2.4	7.60E-03	8.44E-03	5.0	5.5
70	5.05E-03	198.1	1.5	4.38E-03	4.93E-03	13.1	2.3

Table 3-5 cont'd

Peak #	$k_e$ ( $h^{-1}$ )	$\tau$ (h)	# $\tau$ in 300 h	$k_p$ fixed T	$k_p$ variable T	APE fixed T	APE variable T
71	4.74E-03	211.0	1.4	3.96E-03	4.47E-03	16.3	5.7
72	1.77E-03	564.6	0.5	1.64E-03	1.88E-03	7.6	6.2
73	1.04E-03	960.1	0.3	1.20E-03	1.39E-03		
74	7.30E-04	1369.8	0.2	9.20E-04	1.07E-03		
75	2.81E-04	3559.8	0.1	6.75E-04	7.90E-04		
76	7.14E-05	14006	0.0	5.31E-04	6.26E-04		
78	4.82E-03	207.7	1.4	3.00E-03	3.40E-03	37.7	29.4

Table 3-6. For model validation, the experimental rate constant ( $k_{\text{exp}}$ ), characteristic lifetime ( $\tau$ ), and the number of  $\tau$  in 300 h for selected compounds in diesel fuel evaporated at 10 °C. The predicted rate constant ( $k_{\text{pred}}$ ) and absolute percent error (APE) was calculated using the fixed-temperature (fixed T) and variable-temperature (variable T) models. Compounds with  $\tau > 0.5$  in 300 h were excluded from the table (peaks 80, 84, 85, 105, 106).

Peak #	$k_{\text{exp}}$ ( $\text{h}^{-1}$ )	$\tau$ (h)	# $\tau$ in 300 h	$k_{\text{pred}}$ fixed T	$k_{\text{pred}}$ variable T	APE fixed T	APE variable T
79	2.18E-03	459.2	0.7	2.37E-03	2.70E-03	8.9	24.1
81	3.84E-02	26.0	11.5	3.93E-02	4.21E-02	2.4	9.7
82	3.51E-03	284.7	1.1	3.42E-03	3.87E-03	2.6	10.1
83	3.39E-03	295.2	1.0	3.14E-03	3.55E-03	7.4	4.8
86	1.61E-01	6.2	48.2	1.02E-01	1.07E-01	36.6	33.5
87	4.63E-02	21.6	13.9	4.34E-02	4.64E-02	6.2	0.2
88	3.91E-02	25.6	11.7	3.51E-02	3.77E-02	10.2	3.5
89	1.45E-02	68.8	4.4	1.60E-02	1.75E-02	10.0	20.2
90	1.50E-02	66.8	4.5	1.55E-02	1.70E-02	3.6	13.3

Table 3-6 cont'd

Peak #	$k_{\text{exp}}$ ( $\text{h}^{-1}$ )	$\tau$ (h)	# $\tau$ in 300 h	$k_{\text{pred}}$ fixed T	$k_{\text{pred}}$ variable T	APE fixed T	APE variable T
91	1.39E-02	72.0	4.2	1.38E-02	1.52E-02	0.4	9.1
92	5.87E-03	170.4	1.8	5.46E-03	6.10E-03	7.0	4.0
93	5.65E-03	176.9	1.7	4.84E-03	5.43E-03	14.3	3.9
94	1.19E-02	84.2	3.6	1.42E-02	1.56E-02	19.7	31.2
95	1.15E-02	86.8	3.5	1.38E-02	1.51E-02	19.4	30.9
96	9.48E-03	105.4	2.8	1.08E-02	1.19E-02	14.0	25.7
97	7.92E-03	126.2	2.4	9.76E-03	1.08E-02	23.2	36.1
98	6.98E-03	143.2	2.1	7.44E-03	8.27E-03	6.6	18.4
99	4.83E-03	207.0	1.4	5.13E-03	5.74E-03	6.1	18.9
100	3.96E-03	252.3	1.2	3.76E-03	4.24E-03	5.2	6.9
101	3.43E-03	291.5	1.0	3.32E-03	3.75E-03	3.3	9.4

Table 3-6 cont'd

<b>Peak #</b>	<b><math>k_{\text{exp}}</math> (h<sup>-1</sup>)</b>	<b><math>\tau</math> (h)</b>	<b># <math>\tau</math> in 300 h</b>	<b><math>k_{\text{pred}}</math> fixed T</b>	<b><math>k_{\text{pred}}</math> variable T</b>	<b>APE fixed T</b>	<b>APE variable T</b>
102	3.14E-03	318.3	0.9	3.18E-03	3.60E-03	1.1	14.5
103	2.87E-03	348.8	0.9	2.90E-03	3.29E-03	1.1	14.8
104	4.81E-03	207.7	1.4	5.16E-03	5.78E-03	7.2	20.1
107	8.78E-03	113.9	2.6	9.33E-03	1.03E-02	6.3	17.6

Table 3-7. For model development, the experimental rate constant ( $k_{exp}$ ), characteristic lifetime ( $\tau$ ), and the number of  $\tau$  in 300 h for selected compounds monitored during the evaporation of diesel fuel at 20 °C. The predicted rate constant ( $k_{pred}$ ) and absolute percent error (APE) was calculated using the fixed-temperature (fixed T) and variable-temperature (variable T) models. Compounds with  $\tau > 0.5$  in 300 h were excluded from the table (peaks 23-37, 44, 45, 57). Several compounds had retention indices lower than 800 (peaks 1, 38, 46) and were also excluded, as the retention index could not be accurately extrapolated.

Peak #	$k_e$ ( $h^{-1}$ )	$\tau$ (h)	# $\tau$ in 300 h	$k_p$ fixed T	$k_p$ variable T	APE fixed T	APE variable T
1	3.08E-01	3.2	92.5				
2	2.26E-01	4.4	67.7	1.92E-01	2.31E-01	14.9	2.3
3	1.08E-01	9.3	32.4	1.01E-01	1.22E-01	6.5	13.6
4	9.72E-02	10.3	29.2	9.31E-02	1.13E-01	4.2	16.4
5	6.58E-02	15.2	19.8	6.75E-02	8.25E-02	2.6	25.3
6	4.53E-02	22.1	13.6	4.79E-02	5.88E-02	5.7	29.8
7	4.39E-02	22.8	13.2	4.45E-02	5.47E-02	1.3	24.5
8	3.30E-02	30.3	9.9	3.60E-02	4.44E-02	9.2	34.6
9	2.88E-02	34.7	8.7	3.26E-02	4.03E-02	13.2	39.7

Table 3-7 cont'd

Peak #	$k_e$ ( $h^{-1}$ )	$\tau$ (h)	# $\tau$ in 300 h	$k_p$ fixed T	$k_p$ variable T	APE fixed T	APE variable T
10	2.01E-02	49.8	6.0	2.38E-02	2.95E-02	18.2	46.6
11	1.64E-02	61.1	4.9	1.86E-02	2.31E-02	13.4	41.2
12	1.18E-02	84.5	3.5	1.30E-02	1.63E-02	10.0	37.7
13	1.05E-02	95.2	3.2	1.21E-02	1.52E-02	15.3	44.4
14	1.02E-02	97.6	3.1	1.13E-02	1.42E-02	10.8	38.9
15	7.46E-03	134.1	2.2	8.35E-03	1.05E-02	12.0	41.1
16	4.56E-03	219.1	1.4	4.68E-03	5.95E-03	2.5	30.3
17	3.91E-03	255.5	1.2	4.24E-03	5.40E-03	8.5	38.0
18	3.87E-03	258.4	1.2	3.97E-03	5.06E-03	2.6	30.7
19	2.20E-03	453.8	0.7	2.94E-03	3.76E-03	33.3	70.5
20	2.02E-03	495.6	0.6	2.48E-03	3.18E-03	22.9	57.6

Table 3-7 cont'd

Peak #	$k_e$ ( $h^{-1}$ )	$\tau$ (h)	# $\tau$ in 300 h	$k_p$ fixed T	$k_p$ variable T	APE fixed T	APE variable T
21	1.30E-03	771.9	0.4	1.67E-03	2.16E-03		
22	8.46E-04	1182.5	0.3	1.33E-03	1.72E-03		
23	4.90E-04	2041.5	0.1	1.03E-03	1.34E-03		
38	6.21E-01	1.6	186.4				
39	1.81E-01	5.5	54.3	1.44E-01	1.74E-01	20.4	3.9
40	5.86E-02	17.1	17.6	5.19E-02	6.37E-02	11.4	8.6
41	1.83E-02	54.8	5.5	1.79E-02	2.23E-02	2.0	22.1
42	6.85E-03	146.1	2.1	6.08E-03	7.70E-03	11.2	12.4
43	2.04E-03	491.2	0.6	1.90E-03	2.45E-03	6.4	20.5
44	4.22E-04	2371.1	0.1	6.93E-04	9.06E-04		
46	4.86E-01	2.1	145.8				

Table 3-7 cont'd

Peak #	$k_e$ ( $h^{-1}$ )	$\tau$ (h)	# $\tau$ in 300 h	$k_p$ fixed T	$k_p$ variable T	APE fixed T	APE variable T
47	1.70E-01	5.9	51.0	1.45E-01	1.75E-01	14.8	2.9
48	1.35E-01	7.4	40.6	1.32E-01	1.60E-01	2.4	18.0
49	1.11E-01	9.0	33.2	1.03E-01	1.25E-01	6.9	13.0
50	5.54E-02	18.1	16.6	5.43E-02	6.65E-02	2.0	20.0
51	1.74E-02	57.4	5.2	1.86E-02	2.32E-02	6.9	33.0
52	1.06E-02	94.3	3.2	1.11E-02	1.39E-02	4.7	31.3
53	7.50E-03	133.3	2.3	6.75E-03	8.53E-03	10.0	13.7
54	6.73E-03	148.6	2.0	6.47E-03	8.18E-03	3.8	21.6
55	4.40E-03	227.4	1.3	3.79E-03	4.83E-03	13.8	9.9
56	5.05E-04	1980.2	0.2	7.54E-04	9.84E-04		
58	4.65E-02	21.5	14.0	5.03E-02	6.17E-02	8.2	32.7

Table 3-7 cont'd

Peak #	$k_e$ ( $h^{-1}$ )	$\tau$ (h)	# $\tau$ in 300 h	$k_p$ fixed T	$k_p$ variable T	APE fixed T	APE variable T
59	3.70E-02	27.0	11.1	4.63E-02	5.69E-02	25.0	53.5
60	4.00E-02	25.0	12.0	4.22E-02	5.18E-02	5.5	29.7
61	3.19E-02	31.4	9.6	3.59E-02	4.42E-02	12.6	38.8
62	2.83E-02	35.3	8.5	2.94E-02	3.64E-02	3.8	28.4
63	2.53E-02	39.5	7.6	2.69E-02	3.33E-02	6.2	31.5
64	1.77E-02	56.5	5.3	1.95E-02	2.43E-02	10.2	37.1
65	1.69E-02	59.0	5.1	1.88E-02	2.34E-02	10.7	37.8
66	1.61E-02	62.1	4.8	1.67E-02	2.09E-02	4.0	29.6
67	1.09E-02	91.9	3.3	1.14E-02	1.42E-02	4.4	30.9
68	2.69E-02	37.2	8.1	2.42E-02	3.00E-02	10.0	11.6
69	1.49E-02	67.0	4.5	1.41E-02	1.77E-02	5.4	18.3

Table 3-7 cont'd

Peak #	$k_e$ ( $h^{-1}$ )	$\tau$ (h)	# $\tau$ in 300 h	$k_p$ fixed T	$k_p$ variable T	APE fixed T	APE variable T
70	8.89E-03	112.5	2.7	8.19E-03	1.03E-02	7.9	16.0
71	8.44E-03	118.5	2.5	7.41E-03	9.35E-03	12.2	10.8
72	3.69E-03	271.4	1.1	3.08E-03	3.94E-03	16.4	6.9
73	2.64E-03	379.1	0.8	2.26E-03	2.91E-03	14.3	10.1
74	2.14E-03	468.1	0.6	1.74E-03	2.24E-03	18.6	4.9
75	1.27E-03	787.5	0.4	1.28E-03	1.65E-03		
76	9.00E-04	1111.0	0.3	1.01E-03	1.31E-03		
77	3.59E-04	2785.8	0.1	6.09E-04	7.98E-04		
78	7.85E-03	127.3	2.4	5.61E-03	7.11E-03	28.5	9.4

Table 3-8. For model validation, the experimental rate constant ( $k_{\text{exp}}$ ), characteristic lifetime ( $\tau$ ), and the number of  $\tau$  in 300 h for selected compounds in diesel fuel evaporated at 20 °C. The predicted rate constant ( $k_{\text{pred}}$ ) and absolute percent error (APE) was calculated using the fixed-temperature (fixed T) and variable-temperature (variable T) models. Compounds with  $\tau > 0.5$  in 300 h were excluded from the table (peaks 80, 85, 105, 106).

Peak #	$k_{\text{exp}}$ ( $\text{h}^{-1}$ )	$\tau$ (h)	# $\tau$ in 300 h	$k_{\text{pred}}$ fixed T	$k_{\text{pred}}$ variable T	APE fixed T	APE variable T
79	4.19E-03	238.7	1.3	4.45E-03	5.66E-03	6.2	35.0
81	7.50E-02	13.3	22.5	7.23E-02	8.82E-02	3.7	17.5
82	6.38E-03	156.7	1.9	6.40E-03	8.09E-03	0.3	26.9
83	6.22E-03	160.8	1.9	5.87E-03	7.43E-03	5.6	19.5
84	2.15E-03	465.9	0.6	1.98E-03	2.55E-03	7.7	18.8
86	2.44E-01	4.1	73.3	1.86E-01	2.24E-01	23.8	8.3
87	8.68E-02	11.5	26.0	7.97E-02	9.71E-02	8.2	11.9
88	7.63E-02	13.1	22.9	6.46E-02	7.90E-02	15.3	3.5
89	2.72E-02	36.7	8.2	2.96E-02	3.66E-02	8.6	34.3

Table 3-8 cont'd

Peak #	$k_{\text{exp}}$ ( $\text{h}^{-1}$ )	$\tau$ (h)	# $\tau$ in 300 h	$k_{\text{pred}}$ fixed T	$k_{\text{pred}}$ variable T	APE fixed T	APE variable T
90	2.81E-02	35.6	8.4	2.87E-02	3.55E-02	2.3	26.6
91	2.67E-02	37.5	8.0	2.56E-02	3.17E-02	4.0	19.0
92	1.01E-02	98.7	3.0	1.02E-02	1.28E-02	0.5	26.2
93	9.58E-03	104.4	2.9	9.04E-03	1.14E-02	5.6	18.8
94	2.36E-02	42.4	7.1	2.63E-02	3.26E-02	11.8	38.4
95	2.24E-02	44.6	6.7	2.55E-02	3.16E-02	13.8	41.0
96	1.81E-02	55.2	5.4	2.01E-02	2.50E-02	10.8	37.7
97	1.46E-02	68.3	4.4	1.81E-02	2.26E-02	23.8	54.1
98	1.24E-02	80.6	3.7	1.38E-02	1.73E-02	11.5	39.4
99	8.65E-03	115.5	2.6	9.56E-03	1.20E-02	10.5	38.9
100	7.20E-03	139.0	2.2	7.03E-03	8.87E-03	2.4	23.3

Table 3-8 cont'd

<b>Peak #</b>	<b><math>k_{\text{exp}}</math> (<math>\text{h}^{-1}</math>)</b>	<b><math>\tau</math> (h)</b>	<b># <math>\tau</math> in 300 h</b>	<b><math>k_{\text{pred}}</math> fixed T</b>	<b><math>k_{\text{pred}}</math> variable T</b>	<b>APE fixed T</b>	<b>APE variable T</b>
101	6.46E-03	154.7	1.9	6.21E-03	7.85E-03	4.0	21.5
102	5.93E-03	168.6	1.8	5.95E-03	7.53E-03	0.3	27.0
103	5.47E-03	182.9	1.6	5.43E-03	6.89E-03	0.6	26.0
104	8.69E-03	115.0	2.6	9.63E-03	1.21E-02	10.7	39.2
105	2.89E-03	345.9	0.9	2.93E-03	3.75E-03	1.3	29.6
106	2.72E-03	367.3	0.8	2.64E-03	3.39E-03	3.0	24.4
107	1.60E-02	62.6	4.8	1.73E-02	2.16E-02	8.6	35.3

Table 3-9. For model development, the experimental rate constant ( $k_{exp}$ ), characteristic lifetime ( $\tau$ ), and the number of  $\tau$  in 300 h for selected compounds monitored during the evaporation of diesel fuel at 30 °C. The predicted rate constant ( $k_{pred}$ ) and absolute percent error (APE) was calculated using the fixed-temperature (fixed T) and variable-temperature (variable T) models. Compounds with  $\tau > 0.5$  in 300 h were excluded from the table (peaks 24 – 37, 45, 77). Several compounds had retention indices lower than 800 (peaks 1, 38, 46) and were also excluded, as the retention index could not be accurately extrapolated.

Peak #	$k_e$ ( $h^{-1}$ )	$\tau$ (h)	# $\tau$ in 300 h	$k_p$ fixed T	$k_p$ variable T	APE fixed T	APE variable T
1	6.81E-01	1.5	204.2				
2	5.42E-01	1.8	162.5	4.40E-01	4.63E-01	18.8	14.5
3	2.26E-01	4.4	67.9	2.34E-01	2.46E-01	3.5	8.4
4	2.19E-01	4.6	65.8	2.17E-01	2.27E-01	1.2	3.4
5	1.62E-01	6.2	48.6	1.58E-01	1.65E-01	2.2	2.1
6	1.07E-01	9.3	32.2	1.13E-01	1.18E-01	5.3	9.7
7	1.04E-01	9.6	31.3	1.05E-01	1.10E-01	1.1	5.2
8	7.82E-02	12.8	23.4	8.57E-02	8.91E-02	9.7	14.0
9	7.17E-02	14.0	21.5	7.78E-02	8.08E-02	8.5	12.7

Table 3-9 cont'd

Peak #	$k_e$ ( $h^{-1}$ )	$\tau$ (h)	# $\tau$ in 300 h	$k_p$ fixed T	$k_p$ variable T	APE fixed T	APE variable T
10	5.03E-02	19.9	15.1	5.70E-02	5.91E-02	13.3	17.4
11	3.99E-02	25.1	12.0	4.48E-02	4.63E-02	12.3	16.1
12	2.87E-02	34.8	8.6	3.17E-02	3.26E-02	10.3	13.7
13	2.51E-02	39.9	7.5	2.95E-02	3.04E-02	17.8	21.4
14	2.44E-02	41.1	7.3	2.77E-02	2.85E-02	13.7	17.1
15	1.84E-02	54.3	5.5	2.05E-02	2.11E-02	11.6	14.6
16	1.08E-02	92.5	3.2	1.17E-02	1.19E-02	7.9	10.3
17	9.87E-03	101.4	3.0	1.06E-02	1.08E-02	7.4	9.8
18	9.34E-03	107.0	2.8	9.92E-03	1.01E-02	6.2	8.5
19	6.21E-03	161.0	1.9	7.39E-03	7.53E-03	19.0	21.3
20	6.12E-03	163.3	1.8	6.26E-03	6.38E-03	2.3	4.1

Table 3-9 cont'd

Peak #	$k_e$ ( $h^{-1}$ )	$\tau$ (h)	# $\tau$ in 300 h	$k_p$ fixed T	$k_p$ variable T	APE fixed T	APE variable T
21	4.38E-03	228.5	1.3	4.26E-03	4.33E-03	2.5	1.1
22	3.34E-03	299.8	1.0	3.39E-03	3.44E-03	1.8	3.1
23	2.24E-03	445.8	0.7	2.66E-03	2.69E-03	18.6	20.0
24	1.02E-03	984.0	0.3	1.37E-03	1.38E-03		
25	7.98E-04	1253.1	0.2	1.18E-03	1.19E-03		
38	1.41E+00	0.7	423.4				
39	4.07E-01	2.5	122.2	3.32E-01	3.48E-01	18.6	14.5
40	1.39E-01	7.2	41.8	1.22E-01	1.28E-01	12.1	8.4
41	4.42E-02	22.6	13.3	4.32E-02	4.47E-02	2.2	1.1
42	1.54E-02	64.9	4.6	1.51E-02	1.54E-02	2.2	0.2
43	5.33E-03	187.8	1.6	4.84E-03	4.92E-03	9.1	7.7

Table 3-9 cont'd

Peak #	$k_e$ ( $h^{-1}$ )	$\tau$ (h)	# $\tau$ in 300 h	$k_p$ fixed T	$k_p$ variable T	APE fixed T	APE variable T
44	1.89E-03	528.8	0.6	1.80E-03	1.82E-03	4.7	3.9
46	1.09E+00	0.9	325.8				
47	3.87E-01	2.6	116.1	3.34E-01	3.50E-01	13.8	9.5
48	3.09E-01	3.2	92.6	3.05E-01	3.20E-01	1.3	3.6
49	2.57E-01	3.9	77.2	2.40E-01	2.51E-01	6.9	2.5
50	1.37E-01	7.3	41.1	1.28E-01	1.33E-01	6.6	2.6
51	4.17E-02	24.0	12.5	4.50E-02	4.65E-02	7.7	11.4
52	2.53E-02	39.5	7.6	2.71E-02	2.79E-02	7.1	10.3
53	1.73E-02	57.8	5.2	1.67E-02	1.71E-02	3.7	1.2
54	1.51E-02	66.1	4.5	1.60E-02	1.64E-02	5.7	8.4
55	1.01E-02	99.5	3.0	9.49E-03	9.69E-03	5.6	3.6

Table 3-9 cont'd

Peak #	$k_e$ (h <sup>-1</sup> )	$\tau$ (h)	# $\tau$ in 300 h	$k_p$ fixed T	$k_p$ variable T	APE fixed T	APE variable T
56	1.92E-03	520.1	0.6	1.96E-03	1.97E-03	1.7	2.6
58	1.20E-01	8.3	36.1	1.19E-01	1.24E-01	1.2	3.0
59	9.14E-02	10.9	27.4	1.10E-01	1.14E-01	19.8	24.8
60	9.86E-02	10.1	29.6	9.99E-02	1.04E-01	1.3	5.4
61	7.99E-02	12.5	24.0	8.53E-02	8.87E-02	6.8	11.0
62	7.23E-02	13.8	21.7	7.03E-02	7.29E-02	2.7	0.9
63	6.12E-02	16.3	18.4	6.44E-02	6.67E-02	5.2	9.1
64	4.27E-02	23.4	12.8	4.71E-02	4.87E-02	10.1	13.9
65	4.08E-02	24.5	12.2	4.53E-02	4.68E-02	11.0	14.8
66	3.86E-02	25.9	11.6	4.05E-02	4.19E-02	4.9	8.4
67	2.48E-02	40.4	7.4	2.77E-02	2.86E-02	11.9	15.2

Table 3-9 cont'd

Peak #	$k_e$ ( $h^{-1}$ )	$\tau$ (h)	# $\tau$ in 300 h	$k_p$ fixed T	$k_p$ variable T	APE fixed T	APE variable T
68	6.59E-02	15.2	19.8	5.81E-02	6.02E-02	11.8	8.6
69	3.55E-02	28.2	10.6	3.43E-02	3.54E-02	3.3	0.2
70	2.10E-02	47.6	6.3	2.01E-02	2.07E-02	4.2	1.6
71	1.96E-02	51.1	5.9	1.83E-02	1.87E-02	6.7	4.2
72	8.76E-03	114.2	2.6	7.74E-03	7.89E-03	11.6	9.9
73	6.85E-03	146.0	2.1	5.73E-03	5.82E-03	16.4	15.0
74	5.51E-03	181.4	1.7	4.43E-03	4.49E-03	19.7	18.5
75	3.90E-03	256.4	1.2	3.27E-03	3.32E-03	16.0	15.0
76	2.92E-03	342.5	0.9	2.60E-03	2.63E-03	11.1	10.1
77	1.62E-03	617.6	0.5	1.59E-03	1.60E-03		
78	1.67E-02	59.9	5.0	1.39E-02	1.43E-02	16.6	14.5

Table 3-10. For model validation, the experimental rate constant ( $k_{exp}$ ), characteristic lifetime ( $\tau$ ), and the number of  $\tau$  in 300 h for selected compounds in diesel fuel evaporated at 30 °C. The predicted rate constant ( $k_{pred}$ ) and absolute percent error (APE) was calculated using the fixed-temperature (fixed T) and variable-temperature (variable T) models. Compounds with  $\tau > 0.5$  in 300 h were excluded from the table.

Peak #	$k_{exp}$ (h <sup>-1</sup> )	$\tau$ (h)	# $\tau$ in 300 h	$k_{pred}$ fixed T	$k_{pred}$ variable T	APE fixed T	APE variable T
79	1.03E-02	97.1	3.1	1.11E-02	1.13E-02	7.7	10.2
80	3.43E-03	291.2	1.0	3.57E-03	3.62E-03	4.1	5.5
81	1.75E-01	5.7	52.4	1.69E-01	1.77E-01	3.1	1.3
82	1.44E-02	69.4	4.3	1.58E-02	1.62E-02	9.9	12.7
83	1.45E-02	69.1	4.3	1.45E-02	1.49E-02	0.5	2.9
84	5.97E-03	167.6	1.8	5.03E-03	5.11E-03	15.7	14.3
85	2.75E-03	363.2	0.8	2.24E-03	2.26E-03	18.8	18.0
86	5.60E-01	1.8	168.0	4.27E-01	4.49E-01	23.8	19.8
87	1.98E-01	5.1	59.3	1.86E-01	1.95E-01	5.9	1.6
88	1.70E-01	5.9	51.0	1.52E-01	1.58E-01	10.9	7.0

Table 3-10 cont'd

Peak #	$k_{\text{exp}}$ ( $\text{h}^{-1}$ )	$\tau$ (h)	# $\tau$ in 300 h	$k_{\text{pred}}$ fixed T	$k_{\text{pred}}$ variable T	APE fixed T	APE variable T
89	6.70E-02	14.9	20.1	7.06E-02	7.33E-02	5.5	9.5
90	6.72E-02	14.9	20.1	6.87E-02	7.12E-02	2.2	6.0
91	6.24E-02	16.0	18.7	6.14E-02	6.36E-02	1.6	2.0
92	2.31E-02	43.3	6.9	2.49E-02	2.56E-02	7.7	10.8
93	2.22E-02	45.0	6.7	2.22E-02	2.28E-02	0.1	2.7
94	5.73E-02	17.5	17.2	6.31E-02	6.54E-02	10.1	14.1
95	5.38E-02	18.6	16.1	6.11E-02	6.33E-02	13.6	17.7
96	4.29E-02	23.3	12.9	4.84E-02	5.00E-02	12.6	16.5
97	3.54E-02	28.3	10.6	4.38E-02	4.52E-02	23.7	27.8
98	2.95E-02	33.9	8.8	3.36E-02	3.47E-02	14.2	17.8
99	1.99E-02	50.3	6.0	2.34E-02	2.41E-02	17.8	21.2

Table 3-10 cont'd

<b>Peak #</b>	<b><math>k_{\text{exp}}</math> (<math>\text{h}^{-1}</math>)</b>	<b><math>\tau</math> (h)</b>	<b># <math>\tau</math> in 300 h</b>	<b><math>k_{\text{pred}}</math> fixed T</b>	<b><math>k_{\text{pred}}</math> variable T</b>	<b>APE fixed T</b>	<b>APE variable T</b>
100	1.68E-02	59.7	5.0	1.73E-02	1.78E-02	3.4	6.1
101	1.45E-02	68.9	4.4	1.54E-02	1.57E-02	5.8	8.5
102	1.39E-02	71.8	4.2	1.47E-02	1.51E-02	5.8	8.5
103	1.27E-02	78.5	3.8	1.35E-02	1.38E-02	5.8	8.4
104	1.95E-02	51.3	5.8	2.36E-02	2.43E-02	21.0	24.5
105	7.39E-03	135.3	2.2	7.37E-03	7.51E-03	0.3	1.6
106	7.26E-03	137.7	2.2	6.66E-03	6.79E-03	8.2	6.6
107	3.92E-02	25.5	11.8	4.19E-02	4.33E-02	6.8	10.4

Table 3-11. For model development, the experimental rate constant ( $k_{exp}$ ), characteristic lifetime ( $\tau$ ), and the number of  $\tau$  in 300 h for selected compounds monitored during the evaporation of diesel fuel at 35 °C. The predicted rate constant ( $k_{pred}$ ) and absolute percent error (APE) was calculated using the fixed-temperature (fixed T) and variable-temperature (variable T) models. Compounds with  $\tau > 0.5$  in 300 h were excluded from the table (peaks 26 – 37, 45). Several compounds had retention indices lower than 800 (peaks 1, 38, 46) and were also excluded, as the retention index could not be accurately extrapolated.

Peak #	$k_e$ (h <sup>-1</sup> )	$\tau$ (h)	# $\tau$ in 300 h	$k_p$ fixed T	$k_p$ variable T	APE fixed T	APE variable T
1	1.44E+00	0.7	432.4				
2	1.00E+00	1.0	300.0	6.82E-01	6.46E-01	31.8	35.4
3	3.95E-01	2.5	118.5	3.68E-01	3.43E-01	6.8	13.3
4	3.79E-01	2.6	113.8	3.41E-01	3.16E-01	10.1	16.6
5	2.54E-01	3.9	76.1	2.51E-01	2.31E-01	1.2	9.1
6	1.75E-01	5.7	52.6	1.80E-01	1.64E-01	2.8	6.3
7	1.69E-01	5.9	50.7	1.68E-01	1.53E-01	0.4	9.5
8	1.26E-01	7.9	37.9	1.37E-01	1.24E-01	8.7	1.7

Table 3-11 cont'd

Peak #	$k_e$ ( $h^{-1}$ )	$\tau$ (h)	# $\tau$ in 300 h	$k_p$ fixed T	$k_p$ variable T	APE fixed T	APE variable T
9	1.11E-01	9.0	33.3	1.25E-01	1.13E-01	12.4	1.4
10	7.66E-02	13.0	23.0	9.22E-02	8.24E-02	20.2	7.5
11	6.34E-02	15.8	19.0	7.28E-02	6.46E-02	14.8	1.9
12	4.68E-02	21.3	14.1	5.18E-02	4.55E-02	10.6	2.8
13	4.20E-02	23.8	12.6	4.84E-02	4.24E-02	15.3	1.1
14	4.04E-02	24.8	12.1	4.54E-02	3.98E-02	12.5	1.5
15	2.89E-02	34.6	8.7	3.39E-02	2.94E-02	17.2	1.8
16	1.82E-02	54.9	5.5	1.95E-02	1.66E-02	6.9	8.6
17	1.61E-02	62.2	4.8	1.77E-02	1.51E-02	10.3	6.0
18	1.52E-02	65.9	4.6	1.66E-02	1.41E-02	9.6	6.8
19	1.10E-02	90.5	3.3	1.25E-02	1.05E-02	12.8	4.9

Table 3-11 cont'd

Peak #	$k_e$ ( $h^{-1}$ )	$\tau$ (h)	# $\tau$ in 300 h	$k_p$ fixed T	$k_p$ variable T	APE fixed T	APE variable T
20	9.98E-03	100.2	3.0	1.06E-02	8.89E-03	6.2	10.9
21	7.28E-03	137.5	2.2	7.27E-03	6.04E-03	0.1	17.0
22	5.87E-03	170.4	1.8	5.81E-03	4.80E-03	0.9	18.3
23	4.04E-03	247.7	1.2	4.58E-03	3.75E-03	13.4	7.0
24	2.41E-03	414.2	0.7	2.39E-03	1.92E-03	1.0	20.4
25	2.16E-03	463.4	0.6	2.07E-03	1.66E-03	4.2	23.3
26	1.48E-03	674.4	0.4	1.68E-03	1.34E-03		
27	7.43E-04	1345.9	0.2	8.79E-04	6.87E-04		
28	3.22E-04	3105.8	0.1	6.19E-04	4.79E-04		
38	2.86E+00	0.3	858.6				
39	7.52E-01	1.3	225.6	5.17E-01	4.86E-01	31.2	35.4

Table 3-11 cont'd

Peak #	$k_e$ ( $h^{-1}$ )	$\tau$ (h)	# $\tau$ in 300 h	$k_p$ fixed T	$k_p$ variable T	APE fixed T	APE variable T
40	2.14E-01	4.7	64.1	1.95E-01	1.78E-01	8.7	16.6
41	6.86E-02	14.6	20.6	7.03E-02	6.23E-02	2.4	9.2
42	2.55E-02	39.3	7.6	2.50E-02	2.15E-02	1.8	15.5
43	8.69E-03	115.1	2.6	8.23E-03	6.86E-03	5.3	21.1
44	3.91E-03	255.7	1.2	3.13E-03	2.53E-03	20.1	35.2
46	2.13E+00	0.5	637.9				
47	6.74E-01	1.5	202.1	5.20E-01	4.89E-01	22.8	27.5
48	5.46E-01	1.8	163.7	4.76E-01	4.46E-01	12.7	18.2
49	4.34E-01	2.3	130.1	3.76E-01	3.50E-01	13.3	19.3
50	2.11E-01	4.7	63.2	2.03E-01	1.86E-01	3.4	11.7
51	6.43E-02	15.5	19.3	7.31E-02	6.49E-02	13.6	0.8

Table 3-11 cont'd

Peak #	$k_e$ ( $h^{-1}$ )	$\tau$ (h)	# $\tau$ in 300 h	$k_p$ fixed T	$k_p$ variable T	APE fixed T	APE variable T
52	3.95E-02	25.3	11.8	4.45E-02	3.89E-02	12.7	1.4
53	2.75E-02	36.3	8.3	2.76E-02	2.39E-02	0.4	13.4
54	2.50E-02	40.0	7.5	2.65E-02	2.29E-02	6.2	8.5
55	1.64E-02	60.9	4.9	1.59E-02	1.35E-02	3.1	17.7
56	3.84E-03	260.6	1.2	3.39E-03	2.75E-03	11.7	28.3
58	1.75E-01	5.7	52.6	1.89E-01	1.73E-01	7.9	1.5
59	1.42E-01	7.1	42.5	1.75E-01	1.59E-01	23.4	12.4
60	1.49E-01	6.7	44.7	1.60E-01	1.45E-01	7.1	2.7
61	1.18E-01	8.5	35.3	1.37E-01	1.24E-01	16.2	5.0
62	1.06E-01	9.5	31.7	1.13E-01	1.02E-01	7.2	3.6
63	9.04E-02	11.1	27.1	1.04E-01	9.31E-02	14.9	3.0

Table 3-11 cont'd

Peak #	$k_e$ ( $h^{-1}$ )	$\tau$ (h)	# $\tau$ in 300 h	$k_p$ fixed T	$k_p$ variable T	APE fixed T	APE variable T
64	6.49E-02	15.4	19.5	7.64E-02	6.79E-02	17.7	4.6
65	6.30E-02	15.9	18.9	7.35E-02	6.53E-02	16.7	3.6
66	5.94E-02	16.8	17.8	6.60E-02	5.84E-02	11.1	1.7
67	4.03E-02	24.8	12.1	4.55E-02	3.98E-02	12.7	1.3
68	1.01E-01	9.9	30.3	9.39E-02	8.40E-02	7.0	16.9
69	5.42E-02	18.4	16.3	5.61E-02	4.94E-02	3.4	8.9
70	3.32E-02	30.1	10.0	3.32E-02	2.88E-02	0.0	13.2
71	3.06E-02	32.7	9.2	3.02E-02	2.61E-02	1.2	14.5
72	1.45E-02	68.8	4.4	1.30E-02	1.10E-02	10.3	24.2
73	1.09E-02	91.9	3.3	9.70E-03	8.12E-03	10.8	25.3
74	8.71E-03	114.7	2.6	7.54E-03	6.27E-03	13.5	28.1

Table 3-11 cont'd

<b>Peak #</b>	<b><math>k_e</math> (<math>h^{-1}</math>)</b>	<b><math>\tau</math> (h)</b>	<b># <math>\tau</math> in 300 h</b>	<b><math>k_p</math> fixed T</b>	<b><math>k_p</math> variable T</b>	<b>APE fixed T</b>	<b>APE variable T</b>
75	6.42E-03	155.7	1.9	5.61E-03	4.63E-03	12.6	28.0
76	5.19E-03	192.8	1.6	4.47E-03	3.66E-03	13.8	29.4
77	3.34E-03	299.2	1.0	2.76E-03	2.23E-03	17.3	33.3
78	2.82E-02	35.4	8.5	2.32E-02	1.99E-02	17.9	29.5

Table 3-12. For model validation, the experimental rate constant ( $k_{\text{exp}}$ ), characteristic lifetime ( $\tau$ ), and the number of  $\tau$  in 300 h for selected compounds in diesel fuel evaporated at 35 °C. The predicted rate constant ( $k_{\text{pred}}$ ) and absolute percent error (APE) was calculated using the fixed-temperature (fixed T) and variable-temperature (variable T) models. Compounds with  $\tau > 0.5$  in 300 h were excluded from the table.

Peak #	$k_{\text{exp}}$ ( $\text{h}^{-1}$ )	$\tau$ (h)	# $\tau$ in 300 h	$k_{\text{pred}}$ fixed T	$k_{\text{pred}}$ variable T	APE fixed T	APE variable T
79	1.73E-02	57.9	5.2	1.85E-02	1.58E-02	7.3	8.5
80	6.10E-03	163.9	1.8	6.11E-03	5.05E-03	0.2	17.2
81	2.92E-01	3.4	87.7	2.68E-01	2.47E-01	8.5	15.7
82	2.43E-02	41.1	7.3	2.63E-02	2.26E-02	7.9	7.0
83	2.35E-02	42.5	7.1	2.42E-02	2.08E-02	2.8	11.6
84	9.24E-03	108.2	2.8	8.54E-03	7.13E-03	7.6	22.9
85	4.86E-03	205.7	1.5	3.86E-03	3.15E-03	20.6	35.3
86	1.06E+00	0.9	317.7	6.62E-01	6.26E-01	37.5	40.9
87	3.10E-01	3.2	93.0	2.94E-01	2.71E-01	5.3	12.4
88	2.74E-01	3.7	82.2	2.40E-01	2.21E-01	12.3	19.4

Table 3-12 cont'd

Peak #	$k_{\text{exp}}$ ( $\text{h}^{-1}$ )	$\tau$ (h)	# $\tau$ in 300 h	$k_{\text{pred}}$ fixed T	$k_{\text{pred}}$ variable T	APE fixed T	APE variable T
89	1.05E-01	9.5	31.4	1.14E-01	1.02E-01	8.5	2.4
90	1.05E-01	9.5	31.5	1.11E-01	9.93E-02	5.2	5.5
91	9.82E-02	10.2	29.5	9.91E-02	8.87E-02	0.9	9.7
92	3.84E-02	26.0	11.5	4.09E-02	3.57E-02	6.6	7.0
93	3.65E-02	27.4	10.9	3.65E-02	3.18E-02	0.2	12.8
94	8.99E-02	11.1	27.0	1.02E-01	9.12E-02	13.2	1.4
95	8.43E-02	11.9	25.3	9.86E-02	8.83E-02	17.0	4.8
96	6.57E-02	15.2	19.7	7.84E-02	6.98E-02	19.4	6.2
97	5.60E-02	17.8	16.8	7.11E-02	6.31E-02	27.0	12.6
98	4.71E-02	21.2	14.1	5.50E-02	4.84E-02	16.8	2.8
99	3.22E-02	31.0	9.7	3.86E-02	3.36E-02	19.6	4.2

Table 3-12 cont'd

<b>Peak #</b>	<b><math>k_{\text{exp}}</math> (<math>\text{h}^{-1}</math>)</b>	<b><math>\tau</math> (h)</b>	<b># <math>\tau</math> in 300 h</b>	<b><math>k_{\text{pred}}</math> fixed T</b>	<b><math>k_{\text{pred}}</math> variable T</b>	<b>APE fixed T</b>	<b>APE variable T</b>
100	2.70E-02	37.0	8.1	2.87E-02	2.48E-02	6.2	8.2
101	2.46E-02	40.7	7.4	2.55E-02	2.20E-02	3.7	10.7
102	2.27E-02	44.0	6.8	2.45E-02	2.11E-02	7.7	7.4
103	2.07E-02	48.2	6.2	2.24E-02	1.93E-02	8.2	7.1
104	3.23E-02	31.0	9.7	3.88E-02	3.38E-02	20.4	4.9
105	1.16E-02	86.4	3.5	1.24E-02	1.05E-02	7.3	9.5
106	1.13E-02	88.9	3.4	1.13E-02	9.47E-03	0.0	15.9
107	5.87E-02	17.0	17.6	6.82E-02	6.04E-02	16.1	2.9

Based on these experimental data, several models were developed to predict the rate constants for evaporation. The fixed-temperature models were developed to predict rate constants at a single temperature at which the data were acquired (5 – 35 °C). The data from these experiments were then combined to develop the variable-temperature model. The variable-temperature model was utilized in two ways: under constant temperature, to compare with the performance of the fixed-temperature models, and under fluctuating temperature, to simulate diurnal and seasonal changes. Once developed, these models were applied to predict the fraction remaining of an individual compound and the entire fuel. Prior to model development, data were evaluated by constructing Arrhenius plots to determine evaluate the effect of temperature on the rate constant and determine the activation energy and pre-exponential term in the Arrhenius equation.

### 3.3.1 Arrhenius Plots

The dependence of the rate constant on temperature can be described by the Arrhenius equation

$$\ln k = \ln A - \frac{E_A}{RT} \quad \text{Equation 3-2}$$

where  $k$  is the rate constant,  $A$  is the pre-exponential factor,  $E_A$  is the activation energy,  $R$  is the gas constant and  $T$  is temperature. Arrhenius plots were constructed for seventeen selected compounds by plotting the  $\ln(k)$  vs  $1/T$ , and linear regression was performed. The activation energy was determined from the slope and the pre-exponential factor was determined from the intercept. The pre-exponential factor incorporates a

frequency factor, accounting for the number of collisions, as well as a steric factor, related to the cross-sectional area of a molecule.

Arrhenius plots were constructed using rate constants from all 5 temperatures (Table 3-13). There was a deviation from linearity at the lower temperatures ( $R^2 = 0.937 - 0.988$ ). This deviation may be due to an increased temperature experienced when the evaporation chamber was opened to place the samples inside. A phase change occurring at the lower temperatures could also explain the deviation from linearity. The temperature at which saturates form a wax and precipitate out of solution, or the cloud point, is approximately  $0 - 5\text{ }^\circ\text{C}$  for diesel fuel [7]. Therefore, at the lower temperatures, a phase change may be occurring. The activation energy determined for each compound was relatively similar (Table 3-13), however, due to the deviation in linearity, only limited conclusions can be made from these values.

Arrhenius plots were constructed using only the three highest temperatures (20, 30, and  $35\text{ }^\circ\text{C}$ ) where the plots were linear (TABLE,  $R^2 = 0.986 - 1.000$ ). The activation energy was similar for all the individual compounds. The pre-exponential factor was larger using the three highest temperatures, suggesting a lower frequency of collision when incorporating the lower temperatures may be due to a phase change. Using the activation energy, the activation enthalpy ( $H_A$ ) was determined from the temperature (T) the pressure (P) and the change in molar volume ( $\Delta V$ ).

Table 3-13. The activation energy ( $E_A$ ), pre-exponential factor ( $A$ ), coefficient of determination ( $R^2$ ) determined from the Arrhenius plot of using all temperatures (5, 10, 20, 30, 35 °C).

<b>Compound Identity</b>	<b><math>E_A</math></b>	<b><math>A</math></b>	<b><math>R^2</math></b>
Octane	49.25	1.87E+08	0.939
Ethyl benzene	48.54	9.85E+07	0.940
Ethyl cyclohexane	47.89	8.27E+07	0.937
Nonane	51.72	1.37E+08	0.961
Propyl benzene	51.14	9.09E+07	0.952
Propyl cyclohexane	50.43	7.05E+07	0.962
1,3,5 trimethyl benzene	53.60	1.62E+08	0.963
1,2,4 trimethyl benzene	51.66	6.39E+07	0.956
1,2,3 trimethyl benzene	52.26	6.30E+07	0.971
Indane	51.28	4.64E+07	0.954

Table 3-13 cont'd

<b>Compound Identity</b>	<b><math>E_A</math> (kJ/mol)</b>	<b><math>A</math> (s<sup>-1</sup>)</b>	<b><math>R^2</math></b>
Decane	51.63	4.05E+07	0.963
Butyl benzene	50.53	2.20E+07	0.965
4-methyl decane	50.79	2.37E+07	0.966
Butyl cyclohexane	50.35	2.18E+07	0.961
Undecane	54.36	4.51E+07	0.983
1,2,3,4 tetrahydronaphthalene	51.78	1.55E+07	0.980
Dodecane	66.77	2.17E+09	0.988

Table 3-14. The activation energy ( $E_A$ ), pre-exponential factor ( $A$ ), coefficient of determination ( $R^2$ ) determined from the Arrhenius plot of using the three highest temperatures (20, 30, 35 °C). The enthalpy of vaporization ( $H_{vap}$ ) from the literature and the enthalpy of activation ( $H_A$ ) determined from the Arrhenius plot and Equation 3-3 as well as the difference between the two values ( $H_{vap} - H_A$ ) are also shown.

Compound Identity	$H_{vap}$ (kJ/mol) <sup>1</sup>	$E_A$ (kJ/mol)	$A$ (s <sup>-1</sup> )	$R^2$	$H_A$ (kJ/mol)	$H_{vap} - H_A$
Octane	41.5	75.6	6.74E+12	0.990	73.22	31.7
Ethyl benzene	42.3	70.1	5.36E+11	0.992	67.74	25.5
Ethyl cyclohexane	40.6	72.1	1.26E+12	0.986	69.69	29.1
Nonane	46.4	69.8	1.83E+11	1.000	67.38	20.9
Propyl benzene	46.2	69.2	1.22E+11	1.000	66.81	20.6
Propyl cyclohexane	45.1	66.9	4.98E+10	1.000	64.49	19.4
1,3,5 trimethyl benzene	47.5	69.4	8.90E+10	1.000	67.02	19.5
1,2,4 trimethyl benzene	47.9	68.2	4.64E+10	0.999	65.78	17.8
1,2,3 trimethyl benzene	49.1	66.2	1.63E+10	1.000	63.79	14.7

Table 3-14 cont'd

Compound Identity	$H_{\text{vap}}$ (kJ/mol) <sup>1</sup>	$E_A$ (kJ/mol)	$A$ (s <sup>-1</sup> )	$R^2$	$H_A$ (kJ/mol)	$H_{\text{vap}} - H_A$
Indane	48.8	68.6	4.57E+10	1.000	66.17	17.4
Decane	51.4	69.5	5.05E+10	1.000	67.12	15.7
Butyl benzene	51.4	67.5	1.94E+10	1.000	65.14	13.8
4-methyl decane	53.8	69.9	4.80E+10	1.000	67.51	13.7
Butyl cyclohexane	49.4	68.5	2.98E+10	1.000	66.08	16.7
Undecane	56.4	70.1	2.32E+10	1.000	67.65	11.2
1,2,3,4 tetrahydronaphthalene	55.0	66.9	6.34E+09	0.999	64.49	9.5
Dodecane	61.5	82.9	1.33E+12	0.999	80.50	19.0

1. From reference [8].

$$E_A = H_A + (RT - P\Delta V) \quad \text{Equation 3-3}$$

The molar volume was calculated as 10 times the volume in the liquid phase, because the molecule is moving from the gas to liquid phase. The activation enthalpy was similar, but slightly lower than the activation energy, demonstrating that the temperature and change in volume only have minor contributions. The activation enthalpy was compared to the enthalpy of vaporization (TABLE). The enthalpy of vaporization is large, contributing 55 – 85% of the total enthalpy of activation.

### 3.3.2 Fixed-temperature Models

To develop the fixed-temperature models, the natural logarithm of the rate constant ( $\ln(k)$ ) was plotted *versus* the retention index for all selected compounds (Figure 3-2). Linear regression was used to calculate the slope ( $m$ ) and intercept ( $b$ ) of

$$\ln(k) = mI^T + b \quad \text{Equation 3-4}$$

as summarized in Table 3-15. At all temperatures, a high coefficient of determination ( $R^2 = 0.982 - 0.995$ ) indicated a good quality of fit to the linear equation. Slightly lower  $R^2$  values were observed at the lower temperatures of 5 and 10 °C, which may be due to a change in temperature when the evaporation chamber was opened to insert and remove the samples. It is noteworthy that both the slope ( $1.00 * 10^{-2} - 1.12 * 10^{-2}$ ) and the intercept (6.17 – 7.62) of Equation 3-4 were temperature dependent.

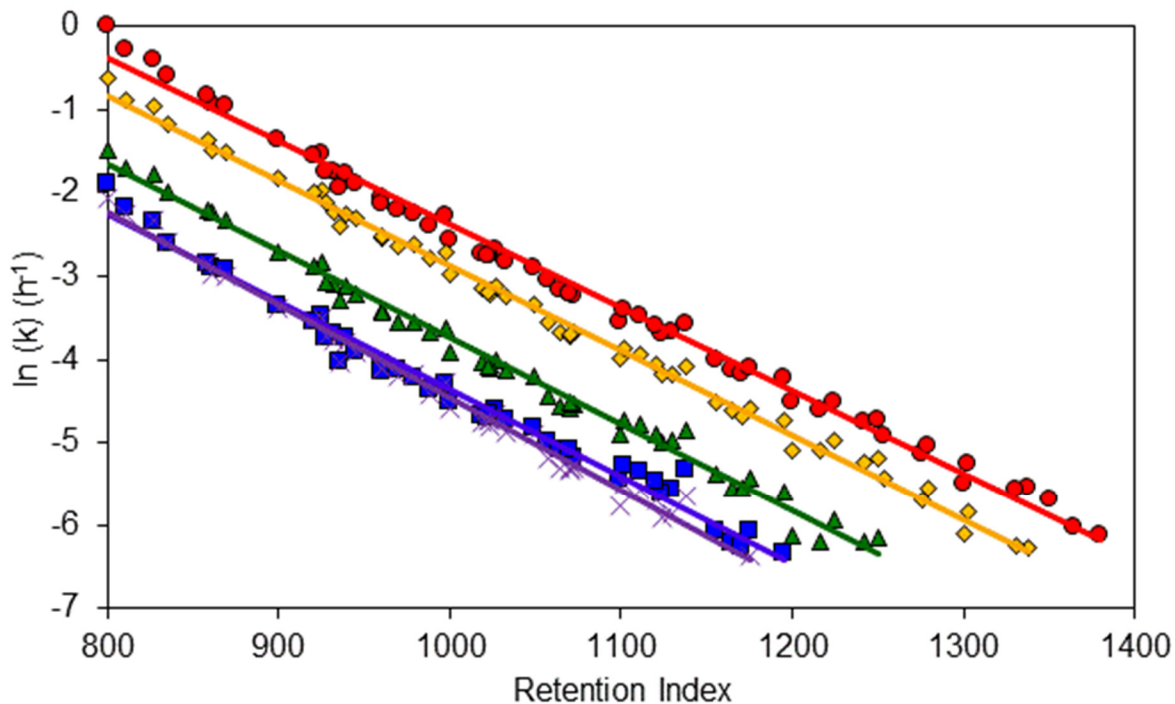


Figure 3-2. Natural logarithm of evaporation rate constant ( $\ln(k)$ ) versus retention index for selected compounds. Linear regression equations: 5 °C ( $\times$ )  $y = -1.12 \cdot 10^{-2} \cdot x + 6.78$ ,  $R^2 = 0.987$ ,  $n = 42$ ; 10 °C ( $\blacksquare$ ),  $y = -1.05 \cdot 10^{-2} \cdot x + 6.17$ ,  $R^2 = 0.982$ ,  $n = 46$ ; 20 °C ( $\blacktriangle$ ),  $y = -1.05 \cdot 10^{-2} \cdot x + 6.71$ ,  $R^2 = 0.990$ ,  $n = 51$ ; 30 °C ( $\blacklozenge$ ),  $y = -1.02 \cdot 10^{-2} \cdot x + 7.35$ ,  $R^2 = 0.995$ ,  $n = 58$ ; 35 °C ( $\bullet$ ),  $y = -1.00 \cdot 10^{-2} \cdot x + 7.62$ ,  $R^2 = 0.993$ ,  $n = 61$ .

Table 3-15. The fixed temperature models developed for each temperature, including the number of compounds (n), the slope (m), intercept (b), and coefficient of determination (R<sup>2</sup>) for linear regression with Equation 3-4 are shown. Also shown is the mean absolute percent error (MAPE) in the prediction of the rate constant for each temperature using the fixed temperature models as well as the variable temperature model (Equation 3-6).

Model Temperature (K)	n	m	b	R <sup>2</sup>	MAPE (%)	
					Fixed T	Variable T
278	42	-1.12 * 10 <sup>-2</sup>	6.78	0.987	9.6	19
283	46	-1.05 * 10 <sup>-2</sup>	6.17	0.982	10.8	16
293	51	-1.05 * 10 <sup>-2</sup>	6.71	0.990	10.3	26
303	58	-1.02 * 10 <sup>-2</sup>	7.35	0.995	8.6	9.4
308	61	-1.00 * 10 <sup>-2</sup>	7.62	0.993	10.5	13
Average					10.0	16.4

The performance of the fixed-temperature models was evaluated by calculating the predicted rate constant ( $k_{\text{pred}}$ ) and comparing it to the experimental evaporation rate constant ( $k_{\text{exp}}$ ) for each selected compound. The absolute percent error (APE) was calculated for each compound and then averaged to yield the mean absolute percent error (MAPE) [9].

$$MAPE = \frac{\sum_{i=1}^n \left| \frac{k_{\text{exp},i} - k_{\text{pred},i}}{k_{\text{exp},i}} \right|}{n} 100 \quad \text{Equation 3-5}$$

The APE for the selected compounds is summarized in the odd numbered tables between Table 3-3 – Table 3-12 and the MAPE is summarized in Table 3-15 for each fixed-temperature model. Errors for individual compounds ranged from 0.1 – 40.6%. The MAPE for each model ranged from 8.6 – 10.8%, with an overall average of 10.0%.

To validate the fixed-temperature models, 29 additional compounds were selected that spanned a similar range of retention indices as those used to develop the models. The rate constants were experimentally determined at temperatures of 5, 10, 20, 30, and 35 °C, as summarized in the even numbered tables between Table 3-3 – Table 3-12. The experimental rate constants were then compared to the values predicted by the fixed-temperature models at the corresponding temperature. As a representative example, the experimental and predicted rate constants for decalin ( $m/z = 138$ ,  $I^T = 1045$ ) are shown in Table 3-16. The APE for each model ranged from 0.5 – 17.4%, with an overall average



Table 3-16. The rate constant ( $k$ ) at each temperature for decalin ( $R/I = 1045$ ), which was not included in the original model. The observed rate constant ( $k_{\text{obs}}$ ) as well as the experimentally predicted ( $k_{\text{exp}}$ ) rate constant using the fixed temperature and variable model is also shown. The absolute percent error (APE) between the experimental and predicted rate constants are shown for each model.

Model Temperature (K)	$k_{\text{obs}}$ ( $\text{h}^{-1}$ )	$k_{\text{exp}}$ ( $\text{h}^{-1}$ ): Fixed T Model	APE (%)	$k_{\text{exp}}$ ( $\text{h}^{-1}$ ): Variable T Model	APE (%)
278	$8.41 \times 10^{-3}$	$6.95 \times 10^{-3}$	17	$5.87 \times 10^{-3}$	30
283	$8.78 \times 10^{-3}$	$7.93 \times 10^{-3}$	9.6	$8.80 \times 10^{-3}$	0.3
293	$1.60 \times 10^{-2}$	$1.48 \times 10^{-2}$	7.6	$1.84 \times 10^{-2}$	15
303	$3.92 \times 10^{-2}$	$3.58 \times 10^{-2}$	8.7	$3.69 \times 10^{-2}$	5.8
308	$5.87 \times 10^{-2}$	$5.84 \times 10^{-2}$	0.5	$5.15 \times 10^{-2}$	12
Average			8.8		13

of 8.8%. The MAPE for all validation compounds using the corresponding fixed-temperature models ranged from 0.02 – 52%, with an overall average of 10.1% (even numbered tables between Table 3-3 – Table 3-12). The error observed for the validation compounds is comparable to that for the selected compounds used to develop the model (Table 3-15). This demonstrates that the models are broadly applicable to a wide range of compounds, not only those used to develop the model. Extensibility of the model is critical because of the large number and wide variety of compounds in petroleum fuels.

### 3.3.3 Variable-Temperature Model

The models developed to this point were generated for five fixed temperatures (5 – 35 °C), but do not include temperature as a variable. Using the same experimental data, a variable-temperature model to predict the rate constant was developed. Multiple linear regression was performed to determine the fitting coefficients for the slopes ( $m_1$  and  $m_2$ ) and the intercept ( $b$ ). As for the fixed-temperature models, all selected compounds with greater than 0.5  $\tau$  in the 300 h evaporation experiment were included in the regression ( $n = 258$ ,  $R^2 = 0.979$ ) [6].

$$\ln(k) = -0.0103 I^T + -6410 \left( \frac{1}{T} \right) + 28.7 \quad \text{Equation 3-6}$$

The APE for predicting the rate constant for each selected compound is summarized in Table 3-3 – Table 3-12, and the MAPE is summarized in Table 3-15. Errors for individual compounds ranged from 0.2 – 71 %. The MAPE ranged from 9.4 – 26%, with an overall average of 16.4%. As expected, these errors are slightly greater than those for the fixed-temperature models.

The rate constants for the 29 validation compounds were also predicted at each temperature using the variable-temperature model. As a representative example, the experimental and predicted rate constants for decalin ( $m/z = 138$ ,  $I^T = 1045$ ) are shown in Table 3-16. The APE at each temperature ranged from 0.3 – 30%, with an overall average of 13%. The MAPE for all validation compounds ranged from 0.2 – 54%, with an overall average of 16.8% (Table 3-17 and even numbered tables between Table 3-3 – Table 3-12). Again, the error for the validation compounds using the variable-temperature model is consistent with that observed for the compounds used to develop the model (Table 3-15). This demonstrates that the variable-temperature model is broadly applicable to a wide range of compounds, not only those used to develop the model. This model can be utilized over a range of environmentally relevant temperatures with low error and only a 6.4% increase over the fixed-temperature models.

### 3.3.4 Applications of Model

#### 3.3.4.1 Calculation of Fraction Remaining with Fluctuating Temperatures

In Chapter 2, the fraction remaining of an individual compound ( $F_{I^T}$ ) was calculated by combining Equation 3-1 and Equation 3-4 [6]. To predict the fraction remaining at variable temperature, Equation 3-6 was combined with Equation 3-1.

$$F_{I^T} = \frac{C_{I^T,t}}{C_{I^T,0}} = \exp\left(-\left(\exp(-0.0103 I^T - 6410\left(\frac{1}{T}\right) + 28.7) t\right)\right) \quad \text{Equation 3-7}$$

Table 3-17. The mean absolute percent error (MAPE) for 29 compounds using the corresponding fixed temperature model (Table 3-15) and the variable temperature model (Equation 3-6).

Model Temperature (K)	MAPE (%) Fixed T Model	MAPE (%) Variable T Model
278	13.4	16.7
283	9.3	17.9
293	7.6	27.5
303	9.2	10.8
308	10.8	11.3
Average	10.1	16.8

The total fraction of fuel remaining ( $F_{\text{tot}}$ ), based on the individual compounds, could then be calculated

$$F_{\text{tot}} = \frac{\sum_{j=I_i}^{I_f} F_j C_{j,0}}{\sum_{j=I_i}^{I_f} C_{j,0}} \quad \text{Equation 3-8}$$

using Equation 3-7 for compounds with  $I_i = 739$  and  $I_f = 3238$ . with  $I_i = 739$  and  $I_f = 3238$ . The iterative calculations to determine the fraction remaining were performed using an algorithm written in house (Matlab, version 7.12.0.635 R2011a, Mathworks, Natick, MA).

This model was validated by evaporating three samples of diesel fuel with water and three samples of fuel alone under conditions of fluctuating temperature, in order to simulate diurnal variations. The temperature was varied in the range of 12 – 27 °C approximately every 12 h, for a total time of 100 h. The temperature profile, recorded in the evaporation chamber at 2-min intervals, is shown in Figure 3-3a (solid line). The experimental fraction remaining of diesel fuel was determined from the change in mass of the samples without water, before and after evaporation. The average fraction remaining was 0.83. Using the variable-temperature model with the temperatures recorded at 2-min intervals, the fraction remaining was predicted to be 0.87. The predicted fraction remaining represents only 5.4% error, compared with the experimental value (Table 3-18). The fraction remaining calculation is based on the change in GC-MS

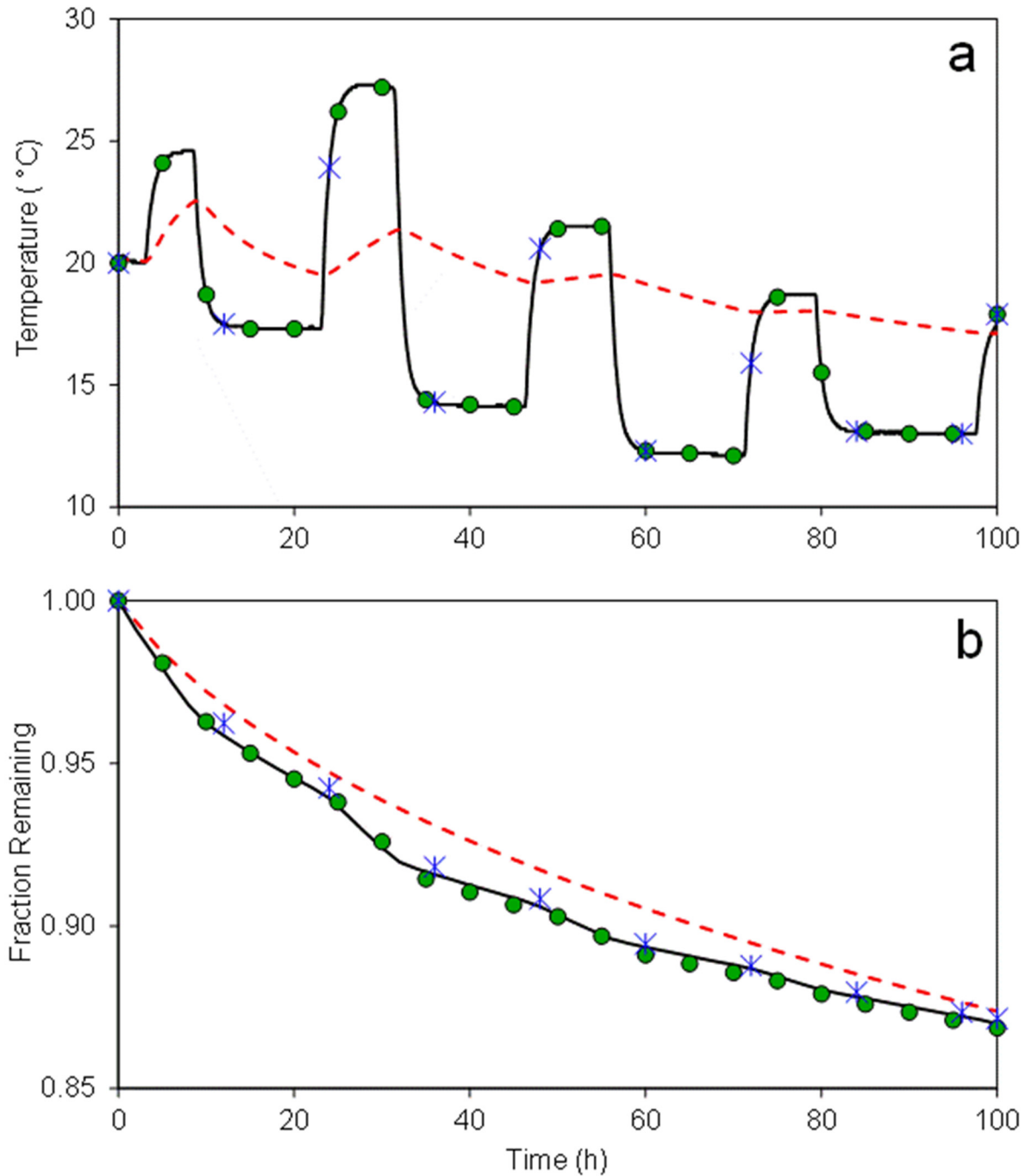


Figure 3-3. The temperature profile (a) of the fluctuating evaporation experiment with the temperature recorded every two minutes (solid line) and as a running average temperature (dashed line). The temperatures at 5-h intervals (circles) and 12-h intervals (stars) are also shown. The fraction of fuel remaining (b) calculated using the variable temperature model using the temperature at 2 min intervals (solid line) 5-h intervals (circles), 12-h intervals (stars), and running average temperature (dashed line). The percent fuel remaining is shown in Table 3-18.

Table 3-18. The fraction of fuel remaining predicted using the variable-temperature model with temperature data collected every two minutes, every five hours, every twelve hours, and the running average temperature (Figure 3-3). The experimental fraction of fuel remaining ( $F_{IT}$ ) based on the average change in mass was 0.83. The percent error between the experimental and predicted values using the model is also shown. In addition, the percent error between the models using the 2-min temperature interval compared to the longer intervals is shown.

<b>Temperature Interval</b>	<b>Predicted <math>F_{IT}</math></b>	<b>Error (%) from Prediction using 2-min Temperature Interval</b>	<b>Error (%) from Experimental Fraction Remaining</b>
2 min	0.870	0.00	5.4
1 h	0.870	0.01	5.4
5 h	0.869	-0.15	5.3
12 h	0.872	0.18	5.6
100 h Average	0.874	0.43	5.9

abundance between the evaporated and unevaporated chromatograms, whereas the experimental fraction remaining is based on the change in mass. This could account for some of the difference between the predicted and experimental values. The error in the prediction of the fraction remaining of fuel is similar to that observed using the fixed-temperature model (20 °C, 7.3% error) in our previous work [6]. This demonstrates that the variable-temperature model, using fluctuating temperature, can predict the fraction remaining of fuel with similar error to existing models that lack the temperature variable.

For many practical applications, such highly accurate and detailed temperature data may not be available. For example, temperature data are available at hourly intervals for many areas in the United States using the National Oceanic and Atmospheric Administration (NOAA) National Climatic Data Center [10]. In order to simulate temperature data that are more readily available, profiles with the temperature collected at 1-h, 5-h, and 12-h intervals were also utilized. The temperature at 5-h intervals (circles) and 12-h intervals (asterisks) are shown on Figure 3-3a. In addition, the running average temperature was calculated (dashed line). The variable-temperature model was used to calculate the fraction remaining using each temperature interval. The predicted fraction remaining over the duration of the 100-h experiment is shown in Figure 3-3b. The predicted fraction remaining for the 5-h and 12-h intervals is very similar to that for the 2-min interval at all times. When the running average temperature was used, the fraction remaining was slightly different because the average temperature was less sensitive to the high and low temperature fluctuations (Figure 3-3a). However, by 100 h, the predicted fraction remaining using the running average temperature became more similar to that from the other temperature profiles.

The predicted fraction remaining at the end of the 100-h experiment is summarized in Table 3-18. In general, the fraction remaining is similar ( $\pm 0.005$ ) for all temperature profiles. The 2-min interval is expected to be the most accurate ( $F_{IT} = 0.870$ ), since it most closely reflects the actual temperature. The running average temperature is expected to be the least accurate ( $F_{IT} = 0.874$ ), yet there was only a 0.43% difference between these two values. This suggests that the use of the average temperature over the course of an environmental spill is a reasonable approximation. This is advantageous because the average temperature is easier to obtain and allows for easier application of the predictive models.

#### 3.3.4.2 Compound Distribution

The variable-temperature model in Equation 3-6 can be utilized to predict the fraction remaining, ranging from 0 to 1, at each retention index. An example for diesel fuel is shown in Figure 3-4. In this example, the fraction remaining curve was calculated at the average temperature (17.1 °C) and time (100 h) for the temperature profile shown in Figure 3-3a. This fraction remaining curve can be employed to predict the chromatographic profile, or the distribution of all individual compounds in the chromatogram after evaporation. The fraction remaining at each retention index (Figure 3-4a) was multiplied by the corresponding normalized abundance from the chromatogram (Figure 3-4b) to generate the predicted distribution of compounds after evaporation

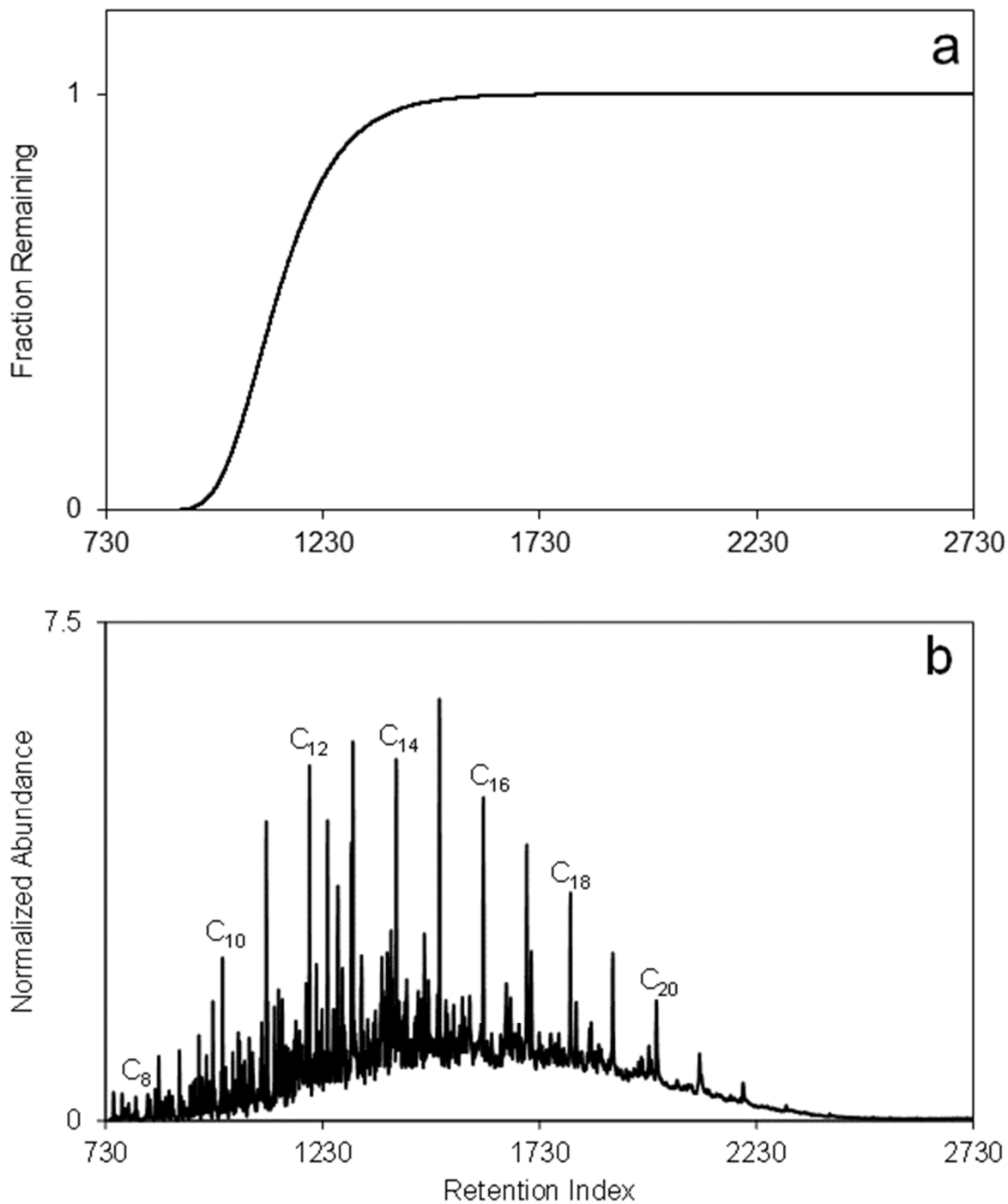
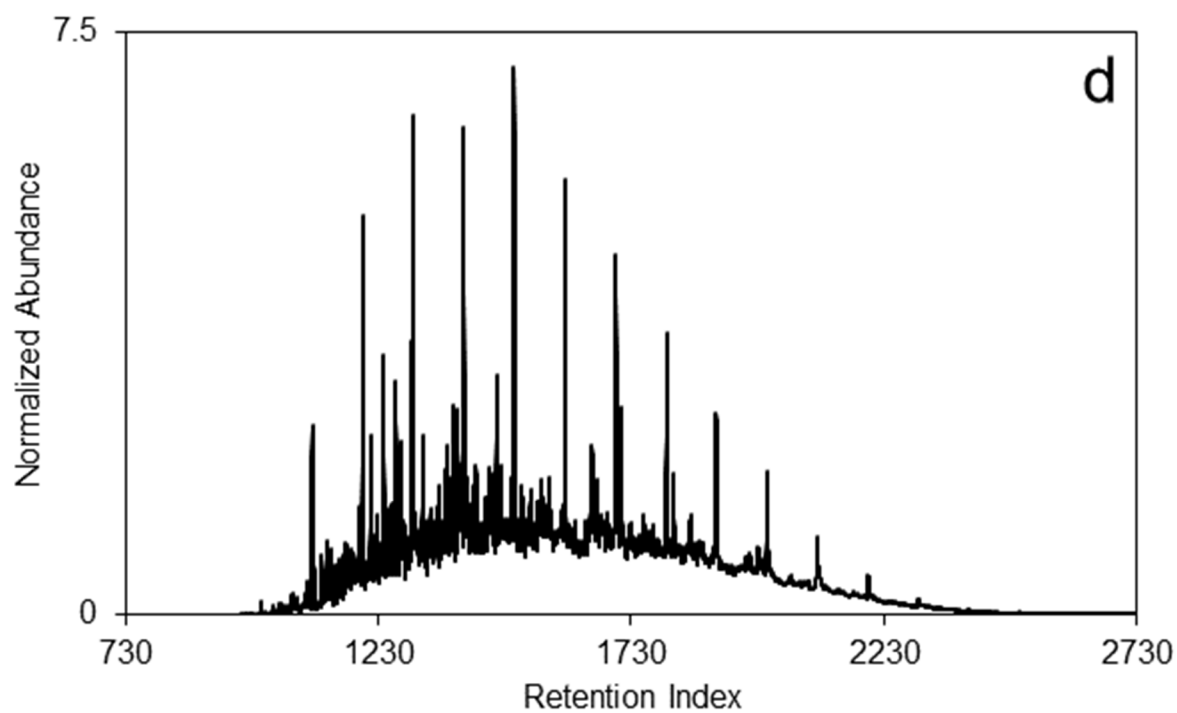
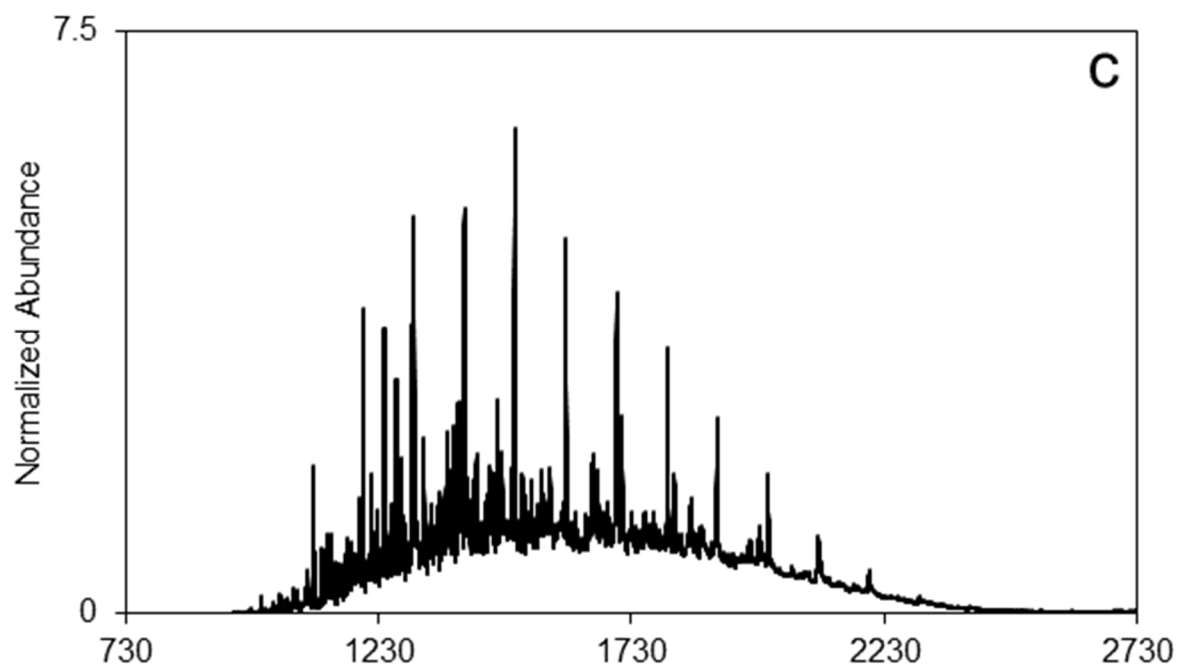


Figure 3-4. The fraction remaining curve (a) predicted using the variable temperature model, using the average temperature (17.1 °C) during the fluctuating temperature experiment (100 h). Also shown are chromatograms of diesel fuel (normalized to heneicosane), unevaporated (b), predicted by multiplying the unevaporated chromatogram (b) by the fraction remaining curve (a), and the actual chromatogram of diesel fuel after the fluctuating temperature experiment (d).

Figure 3-4 cont'd



(Figure 3-4c). The predicted chromatogram was compared to the experimental chromatogram (Figure 3-4d) generated from the fluctuating temperature experiment (Section 3.3.4.1).

A visual comparison of the predicted and experimental chromatograms (Figure 3-4c and Figure 3-4d) suggests a relatively high degree of similarity. In order to quantify this similarity, Pearson product-moment correlation (PPMC) coefficients were used. PPMC coefficients ( $r$ ) measure how two variables ( $x$  and  $y$ ) change with respect to one another (covariance), compared to the degree to which each variable changes independently (standard deviation) [11].

$$r = \frac{\sum [(x_i - \bar{x})(y_i - \bar{y})]}{\sqrt{\sum (x_i - \bar{x})^2 \sum (y_i - \bar{y})^2}} \quad \text{Equation 3-9}$$

PPMC coefficients can range from -1 – +1, where -1 indicates a negative correlation, and +1 indicates a positive correlation. Correlations can be classified as strong ( $0.8 \leq |r| \leq 1$ ), moderate, ( $0.5 < |r| < 0.8$ ) or weak ( $0.5 \leq |r| \leq 0.8$ ) [11]. For this case, the  $x$  and  $y$  variables are the abundances in the predicted and experimental chromatograms at each retention index. The PPMC coefficient was 0.991, indicating that the two chromatograms were strongly correlated. This demonstrates that this model can accurately predict the distribution of individual compounds after evaporation.

### 3.3.4.3 Evaporation Rates of Other Complex Mixtures

To demonstrate the applicability of the model to other complex mixtures, the variable-temperature model was applied to predict the fraction of fuel remaining and distribution of compounds for diesel fuel, kerosene, and marine fuel stabilizer, each

evaporated at a constant temperature near 20 °C for 100 h, similar to that discussed in Section 3.3.4.1. An example chromatogram of each liquid before and after evaporation is shown in Figure 3-5 – Figure 3-7. Kerosene has a similar composition and distribution of compounds compared to diesel fuel but contains more short-chain normal alkanes. Kerosene is therefore more volatile than diesel fuel. Marine fuel stabilizer contains mostly branched and cyclic alkanes, with very low abundances of normal alkanes or aromatic compounds. Marine fuel stabilizer is more volatile than diesel fuel or kerosene. For normalization, heneicosane was used for diesel, pentadecane was used for kerosene, and tetradecane was used for marine fuel stabilizer.

Based on the weight of the diesel fuel before and after evaporation, the fraction remaining was 0.82. The predicted fraction remaining, using the variable-temperature model was 0.84, a 3.1% absolute error. This error is similar to that observed when calculating the fraction remaining using the fluctuating temperature (5.4%). For kerosene, the fraction remaining based on weight was 0.62. Using the variable-temperature model, the predicted fraction remaining of kerosene was 0.70, a 12.7% difference. For marine fuel stabilizer, the fraction remaining based on weight was 0.56. Using the variable-temperature model, the predicted fraction remaining was 0.55, a 2.0% difference. The low errors demonstrate the success at applying these models to predict the fraction of fuel remaining for a range of petroleum products.

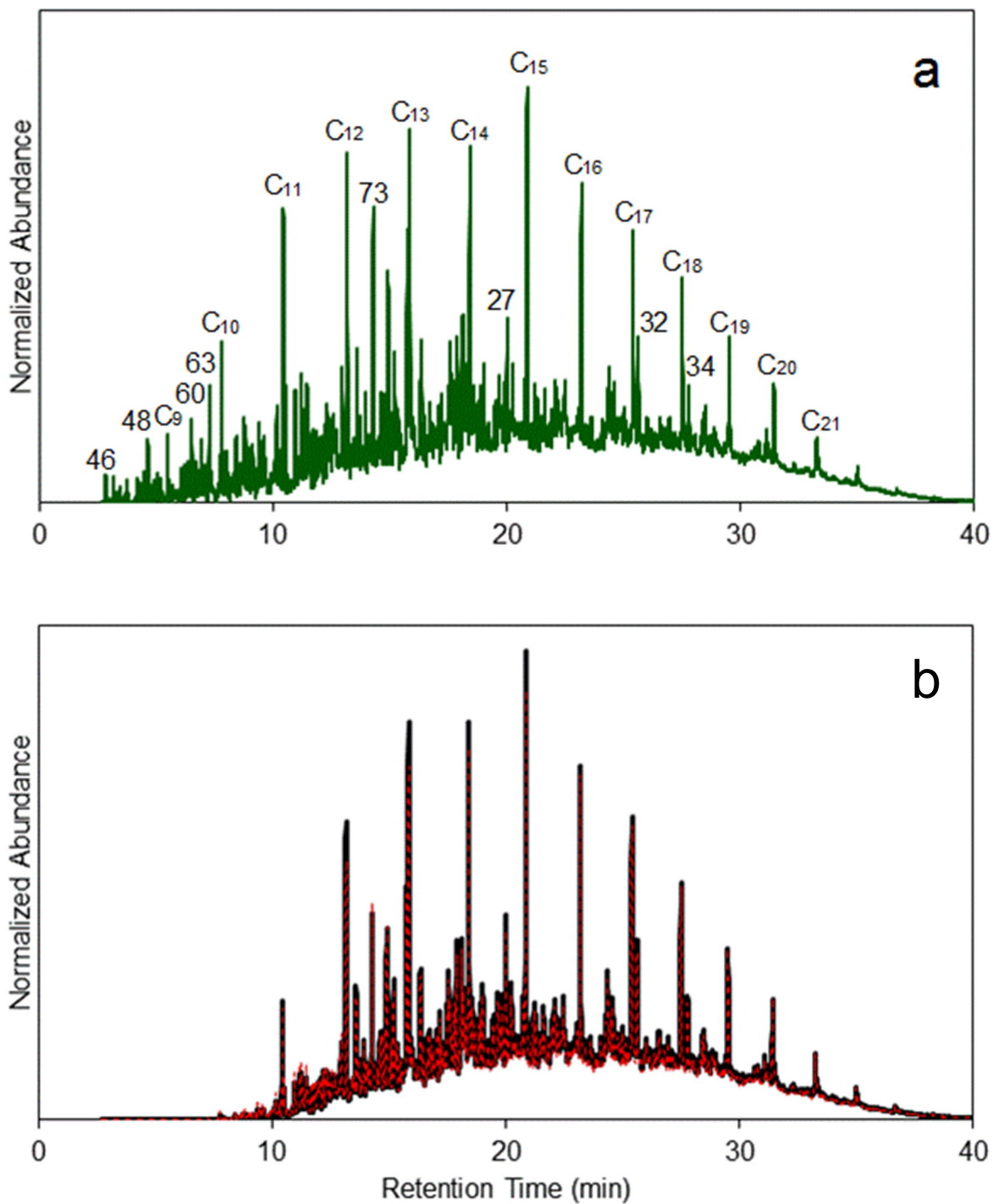


Figure 3-5. A chromatogram of diesel fuel prior to evaporation (a) and after 100 h evaporation at 20 °C (b). In part b, the solid black chromatogram represents the experimentally evaporated fuel, while the red dashed line represents the predicted distribution of compounds, using the variable temperature model. The numbers correspond to peak numbers given in Table 3-1.

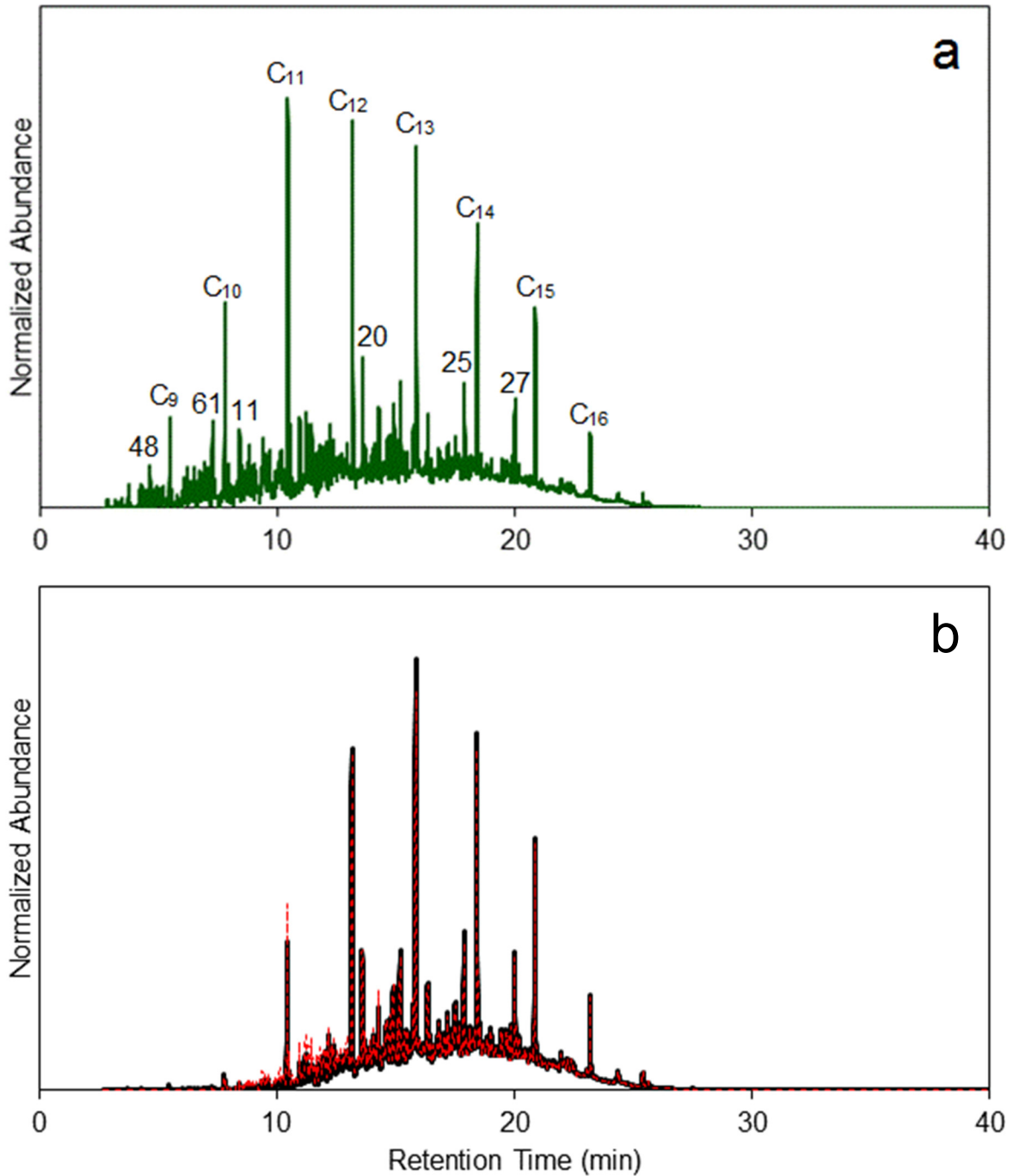


Figure 3-6. A chromatogram of kerosene prior to evaporation (a) and after 100 h evaporation at 20 °C (b). In part b, the solid black chromatogram represents the experimentally evaporated fuel, while the red dashed line represents the predicted distribution of compounds, using the variable temperature model. The numbers correspond to peak numbers given in Table 3-1.

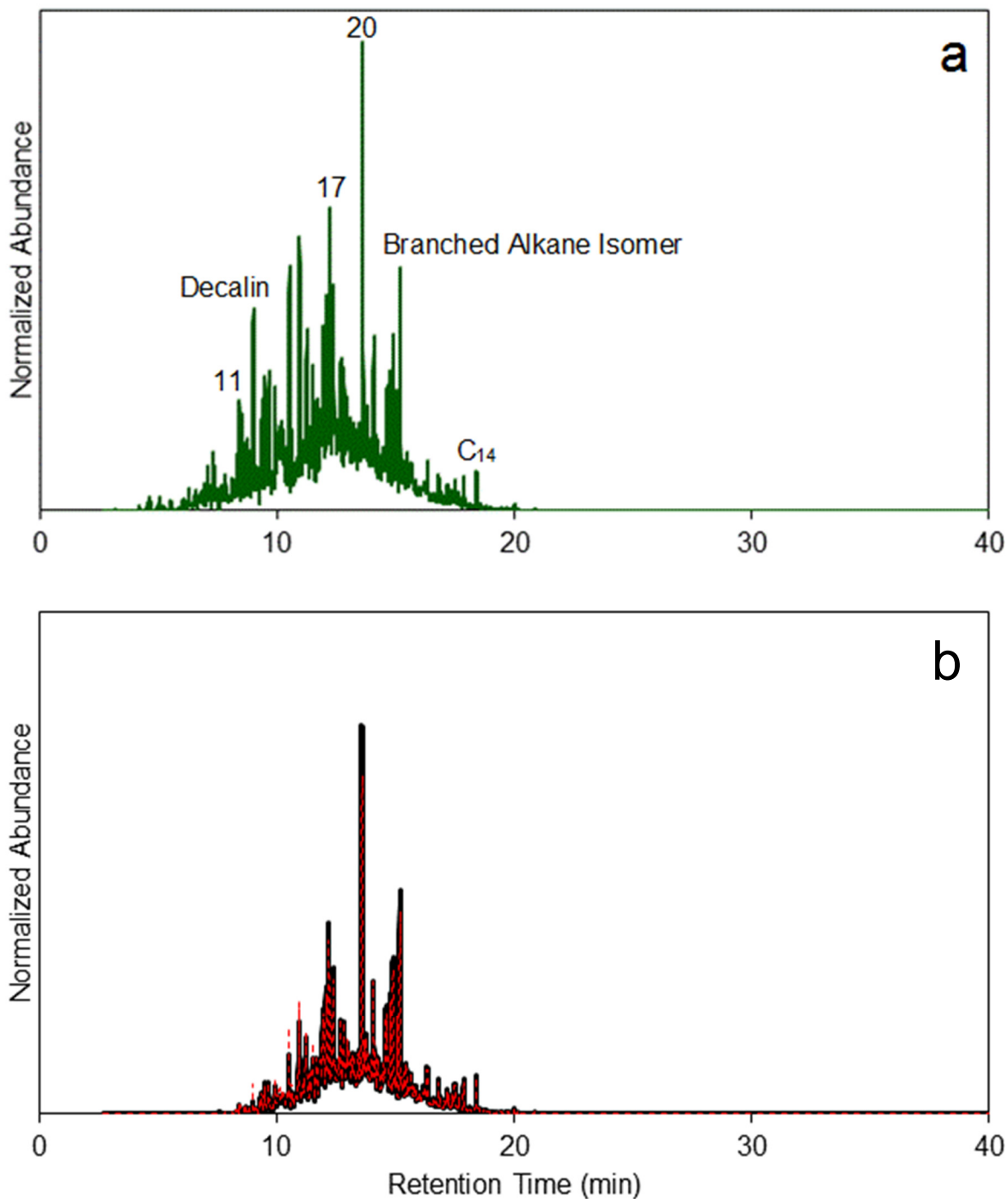


Figure 3-7. A chromatogram of marine fuel stabilizer prior to evaporation (a) and after 100 h evaporation at 20 °C (b). In part b, the solid black chromatogram represents the experimentally evaporated fuel, while the red dashed line represents the predicted distribution of compounds, using the variable temperature model. The numbers correspond to peak numbers given in Table 3-1.

The model was also used to predict the distribution of compounds for diesel, kerosene, and marine fuel stabilizer as discussed in Section 3.3.4.2. After prediction of the chromatogram, a visual comparison and quantitative comparison using PPMC coefficients were applied between the predicted and experimental chromatograms. For diesel fuel, the visual comparison of overlaid chromatograms (Figure 3-5) showed a good agreement between the evaporated and predicted chromatogram. The PPMC coefficient between these chromatograms was 0.9983, indicating strong correlation. For kerosene, the visual comparison of the chromatograms (Figure 3-6) showed that the more volatile compounds were at a higher abundance in the predicted chromatogram while the less volatile compounds were at a higher abundance in the experimental chromatogram. The PPMC coefficient between these chromatograms was 0.9874. In the comparison of the chromatograms for marine fuel stabilizer (Figure 3-7), similar trends were observed to those observed in kerosene. The PPMC coefficient between the predicted and experimentally determined chromatogram for evaporated marine fuel stabilizer was 0.9864. These results demonstrate that the model can be applied to other complex mixtures.

While this PPMC coefficient for kerosene and marine fuel stabilizer still indicates strong correlation, they were lower than observed in the predictions using diesel chromatogram predictions. There are several possible reasons for this. First, the model is based on retention index, which require normal alkanes in order to calculate. In particular for marine fuel stabilizer, the normal alkanes were at low abundance or were not present, requiring extrapolation of retention indices from other samples analyzed at the same time. Another possible problem arises from the increased volatility of kerosene

and marine fuel stabilizer. In order to correct for variation in sample preparation and analysis, normalization was applied. Ideally a nonvolatile compound would be used for normalization. However, in both kerosene and marine fuel stabilizer, it is possible that some of the compound used for normalization evaporated, which could have introduced additional variation into the prediction.

#### 3.3.4.4 Evaporation Time

The models developed in this work can also be used to estimate the evaporation time from the chromatograms of an unevaporated and evaporated fuel sample. This would be useful in environmental applications to estimate when a spill occurred. To do so, a fraction remaining curve is created for each possible evaporation time. The abundance at each retention time in the chromatogram of the unevaporated fuel sample is multiplied by the fraction remaining, to generate the predicted chromatogram (as discussed in Section 3.3.4.2). The predicted chromatogram at each possible evaporation time is compared to the actual evaporated chromatogram, using PPMC coefficients. The time at which the PPMC coefficient reaches a maximum value is considered the best estimate of the evaporation time.

This prediction was tested using the diesel fuel evaporated at 20 °C for 100 hours, discussed in Section 3.3.4.3. The diesel fuel was extracted from six different petri dishes, three containing water and three without water, and each was analyzed by GC-MS in triplicate, creating eighteen total trials. The variable-temperature model with the average temperature was used to predict the evaporated chromatograms at times from 0 – 1000 h, at 1 hour intervals. An example of the distribution of PPMC coefficients is

shown

in

Figure 3-8. There is a relatively large region with a similarly high PPMC coefficient ( $r > 0.998$ ), ranging from 89 – 151 h. While this region has similar PPMC coefficients, it brackets the actual evaporation time of 100 h. Also, the time at which this replicate had a maximum PPMC coefficient was 117 h ( $r = 0.9986$ ), a 17% error from the actual evaporation time. For all 18 replicates, the average predicted evaporation time was 105 h (range: 77 – 141), only a 5% error from the actual time, with an average PPMC coefficient of 0.9990 (range: 0.9986 – 0.9992). This demonstrated the utility of this model in predicting the length of time a sample has been evaporated, given the temperature and the original distribution of compounds.

#### 3.3.4.5 Time to Specific Fraction Remaining

These models have been shown to accurately predict the evaporation time (Section 3.3.4.4) and could therefore be used to estimate the time required for the entire fuel or an individual compound to reach a specific level, such as an LD<sub>50</sub> or a limit of detection. This information is critical for assessing safety at spill sites and predicting persistence in the environment. Using the total fraction remaining (Equation 3-8) with the variable-temperature model (Equation 3-7), numerical integration can be used to determine the time to reach a specific concentration. A plot of the fraction remaining *versus* time at 20 °C is shown in Figure 3-9 on a logarithmic scale. The fraction remaining decreases quickly for the first day and into the first week, then decreased more slowly. A plot such as this is useful in assessing temporal changes in the fuel due to evaporation.



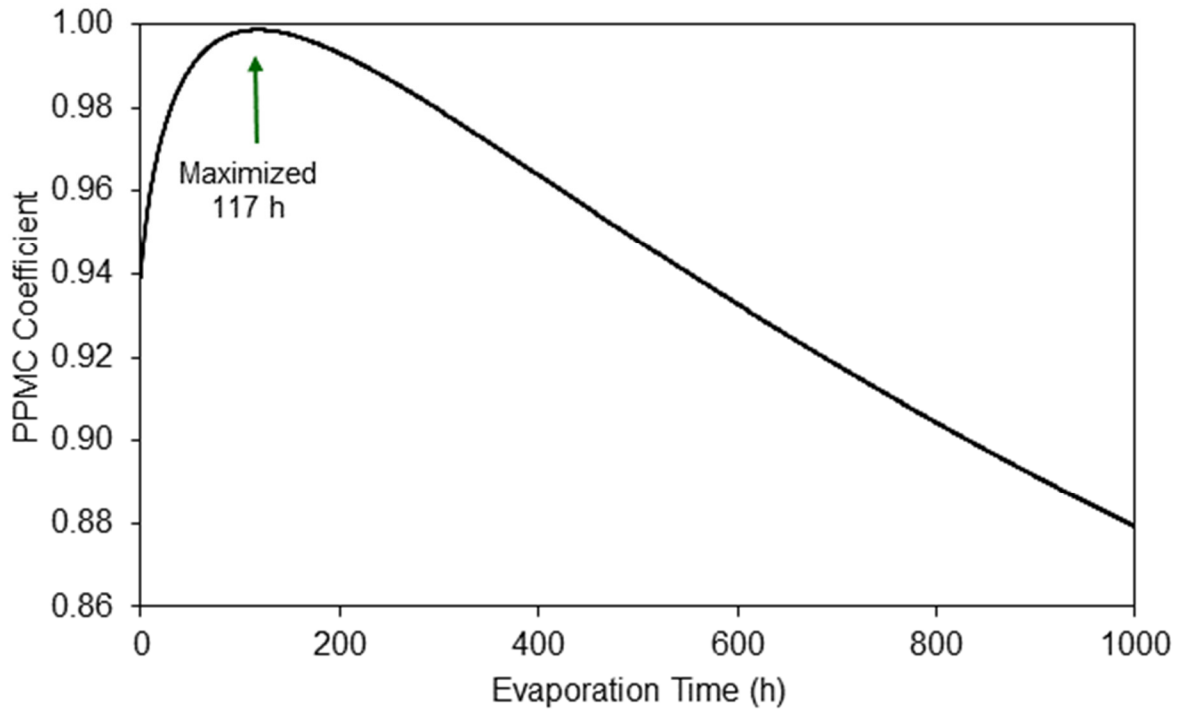


Figure 3-8. The Pearson product-moment correlation (PPMC) coefficients between a chromatogram of diesel fuel evaporated on water for 100 h at 20 °C and the predicted evaporation chromatogram, based on the variable-temperature model for 0 – 1000 h tested at 1-h intervals. The PPMC coefficient maximized at 117 h (0.9986), with values greater than 0.998 from 89 – 151 h.

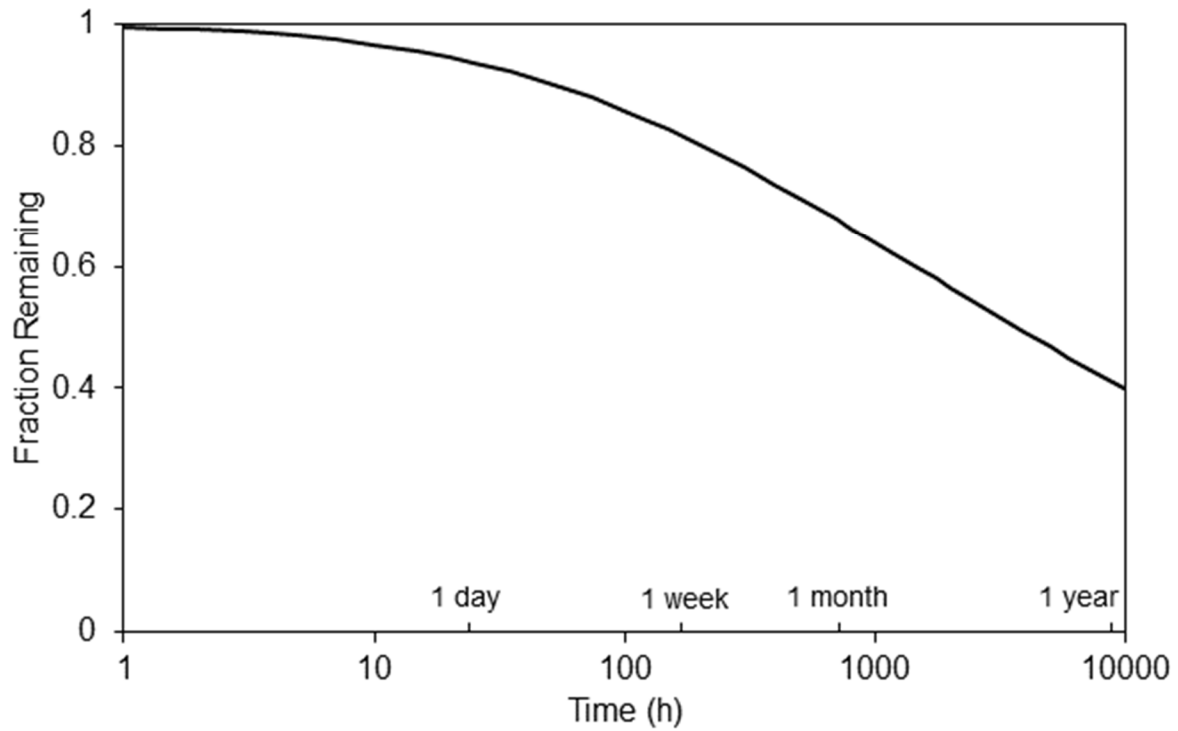


Figure 3-9. The predicted fraction remaining, using the variable-temperature model (Equation 10), over 10,000 h (approximately 1 year) at an average temperature of 20 °C.

A similar calculation can be performed for any compound in petroleum. For example, benzene is commonly highlighted due to its high toxicity in the environment. Benzene makes up approximately 1% of commercial gasoline by volume [12]. If 15 gallons of gasoline (approximately the size of a car's gas tank) leaked into a stream, there would be over 500,000 mg of benzene released into the environment. For rainbow trout, the lethal concentration (LC<sub>50</sub>) is approximately 22 mg/gal for 96 h [13]. In a pool of 10,000 gallons, the concentration is 50 mg/gal. The time until the concentration reaches below the LC<sub>50</sub> (approximately 0.44 remaining) can be solve using Equation 3-7 for benzene ( $I^T = 650$  [14]). The time to reach below the LC<sub>50</sub> is approximately 0.7 h and the time to reach 0.01 (or 1% remaining) is approximately 4 h. While this is a simple example, it serves to demonstrate the utility of the model in predicting removal of a compound from the environment due to evaporation.

#### 3.3.4.6 Comparison to Other Evaporation Models

The accuracy of the model developed in this work has been amply demonstrated in the previous sections. To further validate this model, fraction remaining predicted using this model was compared to an existing evaporation model. An empirical model developed by Fingas for southern diesel fuel evaporated for less than five days was used for the comparison [15]. The model for the percent evaporated ( $\%Evap$ ) is based on time ( $t$ , min) and temperature ( $T$ , °C).

$$\%Evap = (-0.02 + 0.013 T) \sqrt{t} \quad \text{Equation 3-10}$$

While this is the simplest evaporation model, Jones demonstrated that this model provides similar results to other commonly used evaporation models [16], including those

by MacKay (known as the analytical model) [17, 18] and Jones (known as the pseudo-component model) [3, 16].

The experimentally determined percent remaining by weight for diesel fuel allowed to evaporate at 20 °C for 100 h and was 82% (Section 3.3.4.3). Using the total fraction remaining and variable-temperature model the predicted percent remaining was 84%. Using the empirically developed model by Fingas (Equation 3-10) [15], the predicted percent remaining was 81%. The prediction using the model by Fingas is remarkably similar to the model developed in this work. Moreover, the model from this work also incorporated predicting the evaporation of individual compounds. This demonstrates that the model in this work can predict the evaporation comparably to other models, but also provides additional tools, such as the prediction of individual compounds, not available in existing models.

### **3.4 Discussion and Conclusions**

In this work, the model for predicting the rate constant based on retention index offers potential multiple applications in environmental modeling. The evaporation rate constant can be predicted based on retention index and temperature. The predicted rate constant can then be used to predict the fraction remaining of a fuel at a given time, with similar accuracy to existing models. Many existing models rely on estimations of physical properties, which are determined from the pure compound. As demonstrated using the enthalpy of vaporization, the physical property of a pure compound can vary greatly in a complex mixture. The development of a semi-empirical evaporation model is necessary in order to account of these differences.

The model has also been shown to be applicable to a range of petroleum fuels. Moreover, because the model was developed using individual compounds, further information accessible over existing models, which can only predict the evaporation of the entire fuel. Additionally, the use of many existing models, require knowledge of physical properties, such as the boiling point or vapor pressure. When these properties are not known, they must be estimated using information about the fuel, such as the distillation curve, which is not readily available for most refined petroleum products. In this model, only the retention index for the compounds of interest required. A simple GC-MS experiment can be used to determine the retention index of all compounds in a fuel sample. Alternatively, the retention index for many compounds is available in reference libraries, such as the NIST Webbook [14], negating the need the GC-MS experiment.

In addition to predicting the fraction remaining, the model develop in this work provides a method for determining the distribution of compounds at a given time (Section 3.3.4.2), the length of time over which the evaporation has occurred (Section 3.3.4.4), and the time to reach safe exposure levels (Section 3.3.4.5). Determination of the distribution of compound helps to assess what losses would be expected due to evaporation. The expected losses could be compared to losses experienced during remediation, to evaluate effectiveness. For example, if the application of a remediation method results in a greater reduction of compounds than expected from the model, it could be judged to be effective. This model also allows for a determination of exposure time, which would be necessary for determination of the source or blame for the spill. Last, the prediction of evaporation rates of potentially toxic and volatile compounds, such

as benzene, can be readily estimated, which is important for assessing hazards for cleanup workers [3].

For the implementation of this model, there are several other important considerations. First, this model only calculated the fraction remaining, therefore in order to obtain an absolute weight or concentration, the initial amount is required. The initial amount could be quantified using an analytical technique such as GC or may be known from the source. Second, determination of an appropriate compound for normalization is challenging in refined petroleum products that contain mostly volatile components. Lastly, this model has only been applied to petroleum distillates. Crude oil contains many compounds that are not volatile enough to be analyzed by GC-MS, including polar compounds such as resins and asphaltenes, which can account for up to 50% of the composition of crude oil [19, 20]. Therefore, a correction factor may be necessary to determine a total fraction remaining of crude oil.

In conclusion, the model presented in this work is capable of predicting a first-order kinetic constant for the evaporation of an individual compound, based on the retention index of that compound and the temperature. The rate constant can then be utilized to predict the fraction remaining of individual compounds and the fraction remaining of the entire fuel. Existing models cannot predict the fraction remaining of individual compounds and require the estimation of a physical properties of the fuel, making this model more versatile than existing models. The model developed in this work was shown to have a wide range of applications include to predict the distribution of compounds after evaporation, to predict the length of time since the evaporation began,

and predict the time to reach a specific fraction remaining. The model was also shown to be applicable to the evaporation of other complex mixtures.

## REFERENCES

## REFERENCES

- [1] J.K. Jolliff, T.A. Smith, S. Ladner, R.A. Arnone, *Ocean Model.*, 75 (2014) 84.
- [2] D.P. French-McCay, *Environ. Toxicol. Chem.*, 23 (2004) 2441.
- [3] W. Lehr, R. Jones, M. Evans, D. Simecek-Beatty, R. Overstreet, *Environ. Modell. Softw.*, 17 (2002) 191.
- [4] A. Berry, T. Dabrowski, K. Lyons, *Mar. Pollut. Bull.*, 64 (2012) 2489.
- [5] M. Reed, O.M. Aamo, P.S. Daling, *Spill Sci. Technol. Bull.*, 2 (1995) 67.
- [6] J.W. McIlroy, A.D. Jones, V.L. McGuffin, *Anal. Chim. Acta* (In press).
- [7] C. Corporation, Chevron Corporation, Diesel Fuels Technical Review, 2007. <<http://www.chevronwithtechron.com/products/diesel.aspx>>. May 1, 2014.
- [8] R.L. Brown, S.E. Stein, in: P.J. Linstrom, W.G. Mallard (Eds.), *NIST Chemistry Webbook*, NIST Standard Reference Database Number 69, National Institute of Standards and Technology, Gaithersburg, MD, 2011. <http://webbook.nist.gov>, (retrieved July 12, 2014).
- [9] S. Makridakis, *Int. J. Forecast.*, 9 (1993) 527.
- [10] N.O.a.A.A.N.N.C.D. Center, National Oceanic and Atmospheric Administration (NOAA) National Climatic Data Center <<http://www.ncdc.noaa.gov/>>. September 18, 2014.
- [11] J.L. Devore, *Probability and Statistics for Engineering and the Sciences*, Duxbury Press, Belmont, CA, 1991.
- [12] E.P. Agency, Summary and Analysis of the 2011 Gasoline Benzene Pre-Compliance Reports. <<http://www.epa.gov/otaq/regs/toxics/420r12007.pdf>>. 08/16/2014.

- [13] Sigma-Aldrich, Benzene Material Safety Data Sheet, 2014
- [14] S.E. Stein, in: P.J. Linstrom, W.G. Mallard (Eds.), NIST Chemistry Webbook, NIST Standard Reference Database Number 69, National Institute of Standards and Technology, Mass Spec Data Center, Gaithersburg, MD, 2011. <http://webbook.nist.gov>, (retrieved February 26, 2014).
- [15] M. Fingas, in: M. Fingas (Ed.), Oil Spill Science and Technology (Chapt. 9), Elsevier, Burlington, MA, 2011.
- [16] R.K. Jones, Proceedings; Environmental Canada Twentieth Arctic and Marine Oilspill Program Technical Seminar, 1 (1997) 43.
- [17] W. Stiver, D. Mackay, Environ. Sci. Technol., 18 (1984) 834.
- [18] W. Stiver, W.Y. Shiu, D. Mackay, Environ. Sci. Technol., 23 (1989) 101.
- [19] Z. Wang, M. Fingas, C. Yang, J. Christensen, in: R.D. Morrison, B.L. Murphy (Eds.), Environ. Forensics, Elsevier, Burlington, MA, 2006.
- [20] M. Fingas, in: M. Fingas (Ed.), Oil Spill Science and Technology (Chapt. 5), Elsevier, Burlington, MA, 2011.

## **4. Determination of Kinetic Rate Constants during Solar-Simulated Irradiation of Diesel Fuel by Gas Chromatography-Mass Spectrometry and High Resolution Mass Spectrometry**

### **4.1 Introduction**

Until recently, photooxidation of petroleum after an environmental release was considered an insignificant weathering process as it did not account for a substantial source of mass loss during weathering [1]. Photooxidation is not included in many comprehensive petroleum weathering models [1-3]. However, photooxidation of a compound increases its water solubility and toxicity, leading to increased rates of transport as well as environmental and health risks [4]. Photooxidation of oil can also change the physical properties of the oil, forming high-molecular weight tars and gum residues [1]. Therefore, understanding photooxidation is an important aspect of comprehensive environmental modeling of a petroleum spill.

In this work, the effect of photooxidation on diesel fuel was investigated. The goal of this work was to identify and quantify the degradation and formation of compounds. In order to accomplish this goal, both GC-MS and high resolution time-of-flight mass spectrometry (ToF-MS) were utilized and results were compared. Atmospheric pressure chemical ionization (APCI) was selected as it allows for improved detection of higher mass PAHs and oxygenated compounds that are either not sufficiently volatile or are obscured by more abundant substances when GC-MS analyses are performed [5]. After promising compounds were annotated, kinetic rate constants were determined in order to quantify the rate of decay and formation of the selected compounds. While previous

reports have described kinetic rate constants for the decay of compounds, little work has been done to determine rate constants for the compounds formed by photooxidation of petroleum products. Knowing the rates of formation and decay for compounds could be used to link precursors to oxygenated products.

## **4.2 Materials and Methods**

### *4.2.1 Collection of Diesel Fuel*

Refined petroleum products, such as diesel fuel have not been widely studied for photooxidation. Refined products are simpler than crude oil and have fewer compounds that contain heteroatoms, which will affect the photooxidation. Diesel fuel was chosen as an illustrative refined product because of its wide range of compounds compared to other refined products. Diesel fuel was collected from a local service station in East Lansing, MI in July 2010 and stored at 3 °C in acid washed amber bottles until used.

### *4.2.2 Irradiation of Diesel Fuel*

In order to irradiate the samples, a solar simulator with a commercially available xenon arc lamp was modified (Figure 4-1). The light source was a 300 W xenon arc lamp housing (Model SP66902-4000, Newport Corporation, Stratford, CT), with two 2-inch diameter plano-convex condenser lenses ( $f/\# = 2$ ), an ozone-free xenon lamp (model 6258, Newport Corporation) and power supply (model 69911, Newport Corporation). A 2-inch plano-convex lens ( $f/\# = 2$ ) in a lens holder was placed on the condenser assembly of the lamp housing to focus the light. A 2-inch beam turner (model 66246, Newport Corporation) was used to redirect the light at a 90° angle, towards the sample. A second 2-inch plano-convex lens ( $f/\# = 2$ ) in a lens holder was placed approximately 28 cm from

the source, using a filter holder as a spacer. The sample was a total distance of 49.3 cm away from the source. The sample was placed in a petri dish, which fit into a water-cooled, aluminum block, located inside a clear Plexiglas box. A recirculating water bath was used to maintain a constant 21 °C in the petri dish. A metal plate covered the top of the box to prevent extraneous light from reaching the sample. A hole (diameter = 2 in) in the box and metal was positioned directly above the sample. Two bandpass filters (model FSQ-KG2, Newport Corporation) covered the hole and helped to remove unwanted regions of the spectrum (discussed below). High-purity air was flowed into the box (~270 mL min<sup>-1</sup>) allowing for a continuous supply of oxygen.

In the selection and testing of the solar simulator, there were several important considerations including the temporal stability of the light source, the spatial uniformity of the beam, the similarity of the spectrum of the source relative to that of the sun, and the irradiance of the source. The temporal variation was reported by the manufacturer as < 5%. This was verified by taking periodic measurements using a thermopile (model 407A, Newport Corporation) and finding no measurable difference in the irradiance of the source. The intensities were measured 49.3 cm from the source. A 5.5 cm grid was used to evenly collect intensity measurements across the irradiated area, allowing the measurement of uniformity over the area of the petri dishes which contained the samples during irradiation (Figure 4-2). The intensity was measured at nine equally spaced points and the uniformity ( $U$ ) was calculated using the maximum ( $I_{\max}$ ) and minimum ( $I_{\min}$ ) intensities.

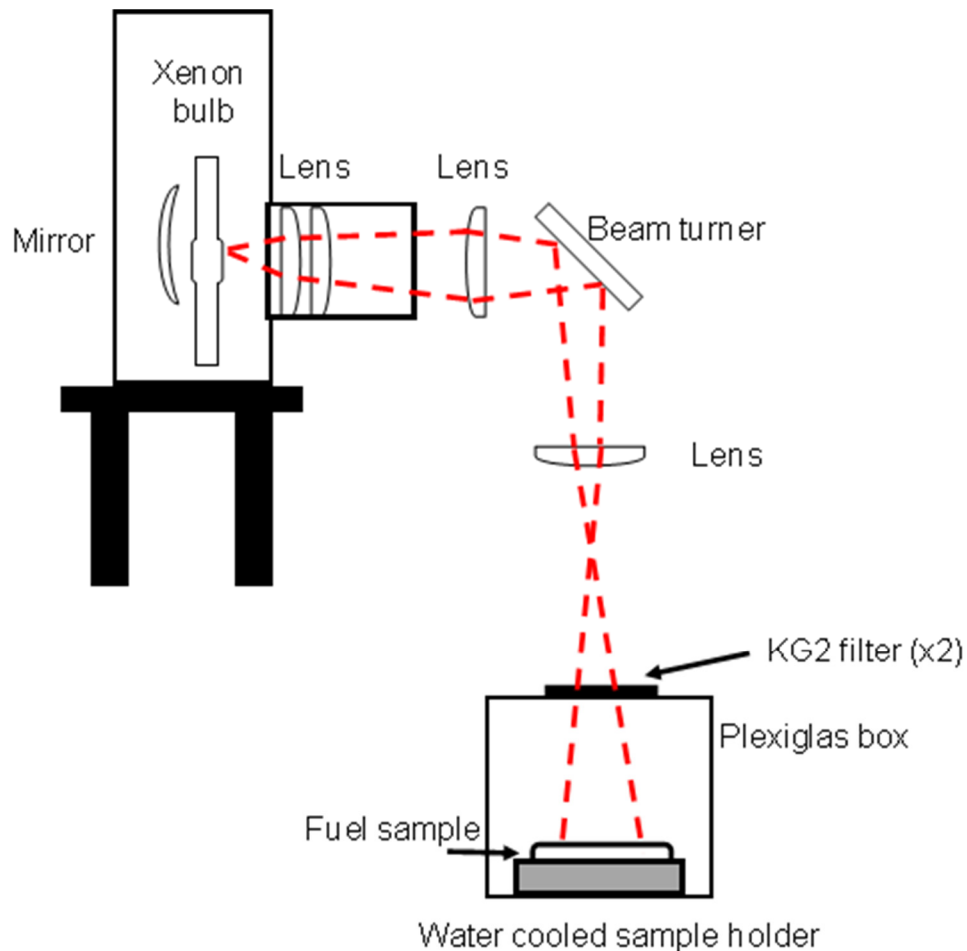


Figure 4-1. A diagram depicted the solar simulator used for irradiation. A commercially available xenon light source was utilized along with several plano-convex lens to homogenize the beam. A beam turner redirected the beam from the source to the sample. The sample was placed on an aluminum block, connected to a circulating water bath to maintain constant temperature. The sample and block were housed inside a Plexiglas box with a hole in the top to allow light to pass. Two filters (KG2) were placed over the hole to reduce the infrared light reaching the sample. A ray tracing is shown as the red dashed line.

$$U = \left( \frac{I_{\max} - I_{\min}}{I_{\max} + I_{\min}} \right) 100 \quad \text{Equation 4-1}$$

The spectral uniformity was monitored and was 5.0% ( $\pm 0.8$ ) over the course of the experiment.

The desired spectrum of the light source should closely match that of the sun at the Earth's surface, which will allow for simulation of solar photooxidation in the environment. Light from the sun contains x-ray through infrared radiation, however, much of that light is absorbed before reaching the Earth's surface [6]. X-ray and UVC wavelengths (from 100 – 280 nm) are absorbed by ozone, while much of the infrared light is absorbed by water, oxygen, and carbon dioxide [6].

A typical spectrum of sunlight, based on ASTM G-173-03 (National Renewable Energy Laboratory, SMARTS v. 2.9.2 [7]), is shown in Figure 4-3a (dotted black line). A spectrum of the xenon light source (Figure 4-3a, dashed blue line) was obtained using a spectrophotometer (Fluorolog 3, Jobin Yvon Horiba, Kyoto, Japan). The xenon arc lamp provided a continuum source, and its emission extends to wavelengths shorter than 280 nm and has several large peaks in the infrared region. Light with wavelengths shorter than 280 nm will deposit more energy per photon (115 kcal/mol at 250 nm *versus* 95 kcal/mol at 300 nm) than is experienced at the Earth's surface, which could lead to environmentally atypical photoreactions and has been a weakness in previous studies [8]. Energy in the infrared region (32 kcal/mol at 900 nm) is too low to induce electronic excitation in petroleum constituents, but can heat the water and sample, and such heating

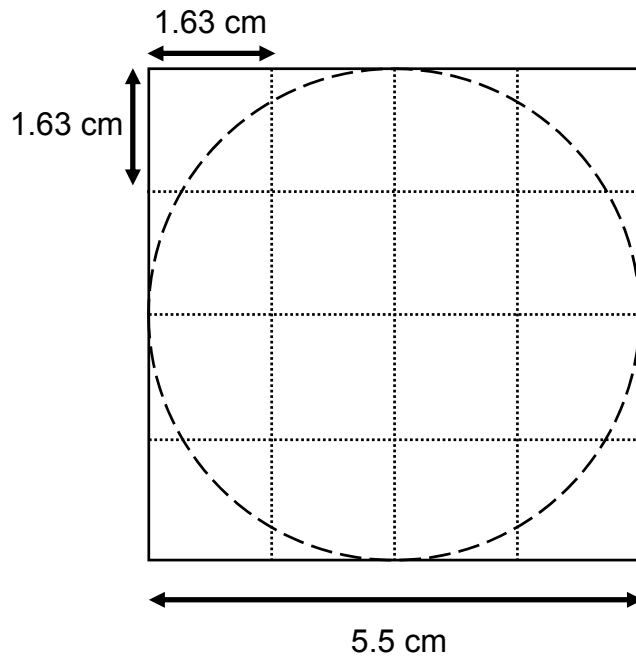


Figure 4-2. A diagram showing how uniformity was measured. The irradiated sample was contained in a petri dish (dashed line, diameter ~5.5 cm). Intensity measurements were taken at the points where the grid lines intersect.

could increase evaporation. In the environment, this heat would be easily dissipated into the surrounding, but in the experimental setup this heating could make maintaining constant temperature challenging. Two bandpass KG2 filters were used to remove the light of wavelengths shorter than 280 nm and 95% of the light with wavelengths longer than 800 nm, including the large peaks in the infrared region. The spectrum of the xenon source with the KG2 filters in place is also shown in Figure 4-3a (solid red line) and is in agreement with the sun spectrum. Between 280 – 330 nm, which is the region most likely to cause photochemical reactions, the spectrum of light delivered to the sample by the solar simulator closely agrees with the spectrum of the sun. The normalized abundance from the solar simulator is higher from 330 – 450 nm, while the abundance in sun's spectrum is higher at wavelengths greater than 550 nm. In order to provide direct comparisons between the xenon source and the sun, a portable spectrometer was used (USB4000, Ocean Optics, Dunedin, Florida). The resulting spectra are shown in Figure 4-3b. The solar simulator and sun are again in good agreement, except for the increased abundance between 350 – 450 nm for the solar simulator. This spectrometer had a short wavelength cutoff at 350 nm so shorter wavelengths could not be evaluated.

Last, the spectral irradiance of the source was measure and compared to that of the sun. Using a thermopile, the irradiance of the source was 0.69 W (304 mW/cm<sup>2</sup>) without the KG2 filters and 0.1 W (44 mW/cm<sup>2</sup>) with the KG2 filters in place. This demonstrates the large contribution from the infrared region being removed by the filters. The irradiance of the sun was measured as 0.2 W (88 mW/cm<sup>2</sup>) using the same

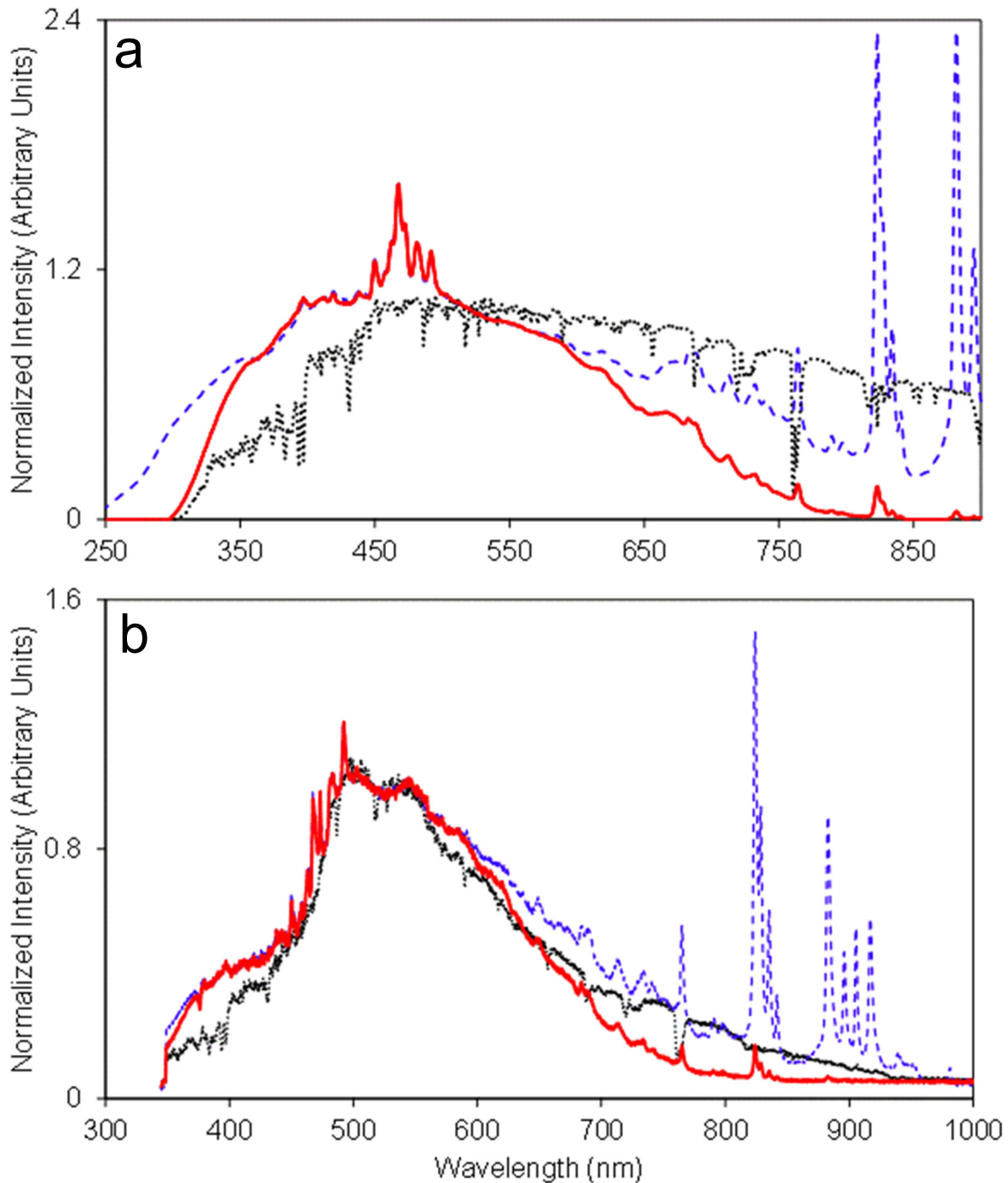
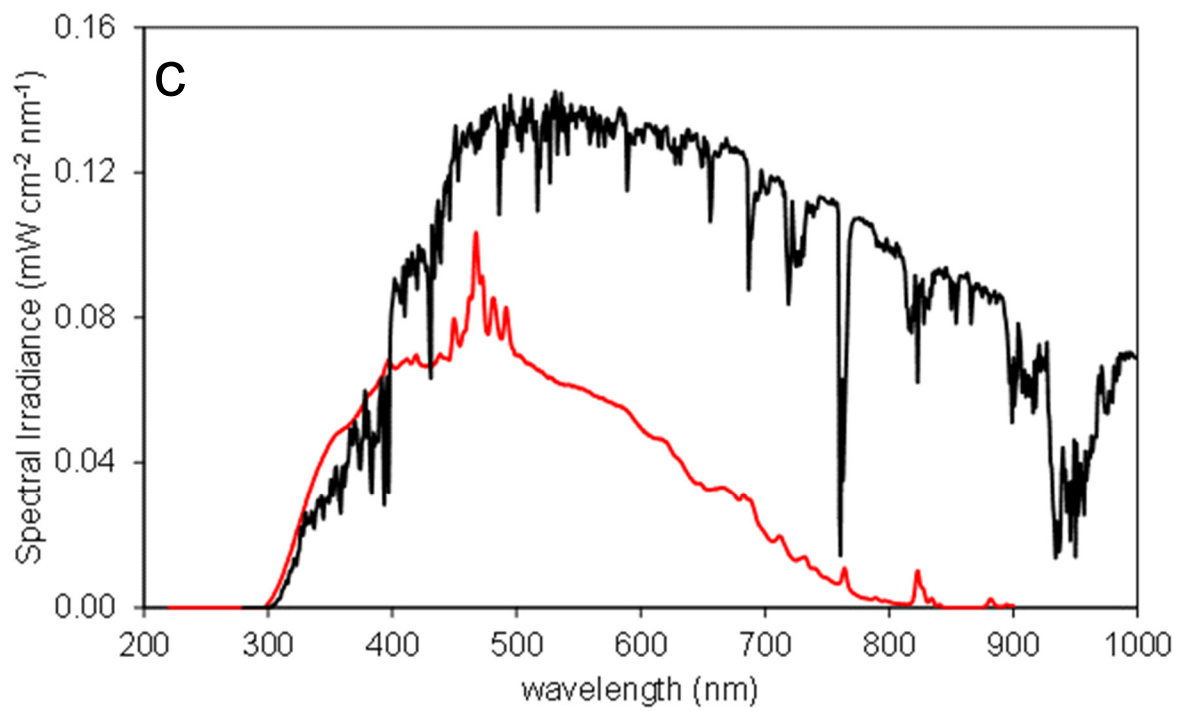


Figure 4-3. A spectrum of the sun [7] (black dotted line) compared to the spectrum of a xenon light source (dashed blue line) and the xenon light source with 2 KG2 filters (solid red line) (a). The same spectra are shown in b, but all were collected using the same spectrometer. The spectra were normalized to the average intensity between 500 – 550 nm. The spectral irradiance of the sun and the xenon source with the 2 KG2 filters is shown in part c.

Figure 4-3 cont'd



thermopile (measured July 12, 2014 at 1500 hrs in East Lansing, MI, USA). This is consistent with literature values of approximately 97 mW/cm<sup>2</sup> for irradiation at the Earth's surface [7]. With the two KG2 filters in place, the irradiance of the sun was 0.5 W (22 mW/cm<sup>2</sup>). The spectral irradiance was calculated using the spectra and thermopile measurements. The fraction of the total signal in the spectra was determined at each wavelength, for the sun and the xenon source with the KG2 filters in place. The total irradiance, measured using the thermopile, was multiplied by the fraction at each wavelength to calculate the spectral irradiance (Figure 4-3c). The irradiance of the sun and solar simulator were approximately equal from 280 – 330 nm. The solar simulator had an approximately 1.5 times higher irradiance from approximately 330 – 400 nm. Above 400 nm the irradiance of the sun was higher. However, this region of the spectrum is expected to induce fewer photochemical reactions. This demonstrates that the solar simulator is approximately equivalent to the irradiance of the sun over the region that is likely to cause photochemical reactions.

A thin film of diesel fuel (1.0 mL, ~0.5 mm) on distilled water (10 mL) was irradiated in glass petri dishes (60 mm ID x 15 mm). The irradiance of the source was measured as 0.1 W (corresponding to ~44 mW/cm<sup>2</sup>), measured using a thermopile. A circulating water bath maintained nearly constant temperature (~21 °C). Samples were irradiated in triplicate for at 7 different lengths of time (0 – 10 h).

#### *4.2.3 Sample Extraction*

After irradiation, the diesel residues were extracted from the petri dish. Prior to extraction, 1 mL of cyclohexane containing 8.4 \*10<sup>-3</sup> M quinoline-*d*<sub>7</sub> was added as a reference standard and as a lock mass for mass spectrometric analysis. Cyclohexane

was selected as the solvent as it was more amenable to the MS analysis than dichloromethane used previously. The diesel/water/cyclohexane mixture was quantitatively transferred to a separatory funnel. The petri dish was rinsed with approximately 1 mL of cyclohexane, which was then quantitatively transferred to the separatory funnel. The water layer and interface were removed, then the cyclohexane layer was transferred to a 10.0 mL volumetric flask, which was filled to the line with cyclohexane. The extract was further diluted (1:50) and transferred to an autosampler vial for GC-MS and MS analysis.

#### *4.2.4 Selection of an Internal Standard*

Selection of an appropriate internal standard for this work was challenging. Ideally, the internal standard should be added to the fuel prior to irradiation, meaning that the internal standard must be resistant to photooxidation. Saturated hydrocarbons, such as normal alkanes, are resistant to photooxidation, however, they are not efficiently ionized by APCI. For analysis by APCI, an unsaturated hydrocarbon or a compound containing a heteroatom is necessary. These compounds likely undergo photooxidation, so they must be added after the irradiation experiment. In order to differentiate the internal standard from a native compound, a deuterated analogue is desirable. Many deuterated PAHs, such as phenanthrene- $d_{10}$ , were found to have masses that correspond to compounds already in the fuel. Naphthalene- $d_8$  did not have a compound with a corresponding mass, but naphthalene was not efficiently ionized, and was not observed using APCI.

Deuterated quinoline was selected as an internal standard because it ionized effectively by APCI and has a mass that does not correspond to a compound already in

diesel. However, quinoline can adsorb onto tubing and surfaces in the MS instrument. Initial studies indicated that analyzing pyridine before each analysis could minimize these effects. However, during the analysis of the irradiated samples, the signal from quinoline- $d_7$  was highly variable, even within replicate analyses, indicating that quinoline- $d_7$  was not appropriate internal standard. In this work, quinoline- $d_7$  was used as a lock mass for the ToF-MS.

For normalization,  $m/z$  199.1487 was used, because it remained relatively constant over the 10 hour irradiation. The mass was assigned an elemental formula of  $C_{15}H_{19}$  ( $M+H^+$ ) and had 7 double bond equivalences (DBE). This compound is consistent with naphthalene with five methylene groups. Prior to normalization, many compounds with 7 DBE were unchanged after irradiation for 10 hours. The GC-MS experiment also showed no change for the alkyl naphthalene, which indicates that it may be more resistant to photooxidation than other PAHs.

#### *4.2.5 Gas Chromatography-Mass Spectrometry*

The gas chromatography-mass spectrometry analysis was performed using a gas chromatograph (model 7890N, Agilent Technologies, Santa Clara, CA) with an automatic liquid sampler (model 7693, Agilent Technologies) coupled to a mass spectrometer (model 5975, Agilent Technologies). Ultra-high-purity helium was flowed (1 mL/min) through a capillary column containing a 100% poly(dimethylsiloxane) stationary phase (HP-1MS, 30 m x 0.25 mm x 0.25  $\mu$ m, Agilent Technologies). The diesel extract was injected (1  $\mu$ L) using a pulsed (15 psi for 0.25 min) split (50:1) injection at 280 °C. The initial GC oven temperature was 50 °C and was ramped at 5 °C/min<sup>-1</sup> to 280 °C where the temperature was held for 4 min. The transfer line temperature was 300 °C. The

quadrupole mass analyzer employed electron ionization (70 eV) and scanned mass-to-charge ratios ( $m/z$ ) from 40 – 550 at a rate of 2.91 scans/s.

#### *4.2.6 Time of Flight-Mass Spectrometry*

Mass spectrometry experiments were conducted using a LCT Premier (Waters Corporation, Milford, MA) time-of-flight mass spectrometer (TOF-MS). The diluted diesel samples (10  $\mu$ L) were introduced using flow injection analysis with hexanes pumped at 0.5 mL/min for 2 min. The sample was ionized using atmospheric pressure chemical ionization (APCI) in positive ion mode with the corona current at 20  $\mu$ A. The capillary voltage was 1000 V and the sample cone voltage was 10 V. The probe and source temperatures were 500 °C and 100 °C, respectively. The cone gas flow was 40 mL/min and the desolvation gas flow was 350 mL/min. The mass analyzer was operated in “W-mode”, which yields mass resolution of about 9000 ( $m/\Delta m$ , full width, half maximum) and scanned  $m/z$  90 –  $m/z$  1000, with data acquisition in centroid mode using extended dynamic range acquisition.

### **4.3 Results**

#### *4.3.1 Visual Observations and Mass Change of Diesel Residue*

Irradiation resulted in visible changes in the diesel fuel. Prior to irradiation, the diesel a light yellow and was not turbid. After 1 h of irradiation, the fuel became darker yellow. After 3 h, a precipitate was observed at the water/fuel interface, and the turbidity increased through 10 h. For one analysis, the weight was recorded to determine the change in mass of the fuel and mass of precipitate formed during irradiation (Section 4.3.7). Prior to irradiation, 1 mL of diesel fuel (0.906 g) was placed into a petri dish

(without water). The fuel was irradiated for 10 h and weighed (0.8222 g; 90.7% of the original mass). To determine the mass of precipitate formed, the liquid diesel was extracted using pentane, then the precipitate was dried under nitrogen, and the residual was weighed (0.0371 g). For the fuel sample, nearly 5% (by mass) had formed a precipitate after 10 h of irradiation. The precipitate was insoluble in hexane, dichloromethane, and water, but was soluble in methanol, acetone, and acetonitrile, suggesting that the precipitate had an increased polarity, which would be consistent with increased oxygen content. This demonstrated that photooxidation is a more substantial source of mass loss from the liquid than previously thought and results in considerable chemical change in the fuel. The formation of a precipitate after photooxidation has not been widely reported in the literature, except for a few laboratory experiments. Larson *et al.* [9] reported the formation of a precipitate in diesel fuel after less than 12 h of irradiation and King *et al.* [10] reported the formation of a solid layer in crude oil within 6 h irradiation. The precipitate is likely not observed in the environment due to the physical mixing that occurs from wave action and wind.

#### 4.3.2 Gas Chromatography-Mass Spectrometry of Diesel Residue

Example total ion chromatograms (TIC) of diesel fuel irradiated from 0 – 10 h (Figure 4-4a) show a progressive decrease in the most volatile compounds, similar to that observed for evaporation. The same decrease is observed for the dark control (Figure 4-4a), indicating that there was no detectible change due to photooxidation, based on the TIC. The chromatograms were normalized to the peak height of nonadecane from  $m/z$  57 to correct for variation in extraction and analysis. Nonadecane has a low volatility and normal alkanes have been shown to be resistant to photooxidation, so this peak was

expected to be unchanged during the experiment. The aliphatic compounds, which dominate the GC-MS TIC, are resistant to photooxidation and previous studies have shown that the changes in the fuel due to photooxidation are not observed in the GC-MS chromatogram [11-13]. However, the decrease of some GC-amiable PAHs, such as fluorene and phenanthrene, were hypothesized to change during irradiation. Extracted ion chromatograms (EICs) were employed to look for specific classes of compounds which may be present at a low abundance and not observed in the TIC. The EIC of  $m/z$  216 (Figure 4-4b) shows a decrease in abundance of two peaks (corresponding to isomers of methylpyrene) over the 10 h irradiation. A corresponding decrease was not observed in the dark control, indicated that the loss was due to photooxidation. A complete list of compound monitored by GC-MS is shown in Table 4-1. The oxidized products were not expected to be observed by GC-MS, because they would be present in low abundance and the addition of an oxygen would decrease volatility.

The most volatile normal alkanes in diesel ( $C_8 - C_{10}$ ) completely evaporated which was consistent with the dark control. The fraction remaining after 10 hours of irradiation was not significantly different from the dark control for the larger normal alkanes ( $C_{12} - C_{20}$ ). However, a statistically significant ( $\alpha = 0.05$ ) decrease in abundance was observed for most other selected compounds, compared with the dark control, indicating accelerated evaporation or photooxidation. It is hard to differentiate which process is occurring. For the more volatile compounds, accelerated evaporation due to irradiation the likely process. For substituted PAHs and less volatile compounds, the losses are likely due to photooxidation. These changes were quantified in Section 4.3.6.

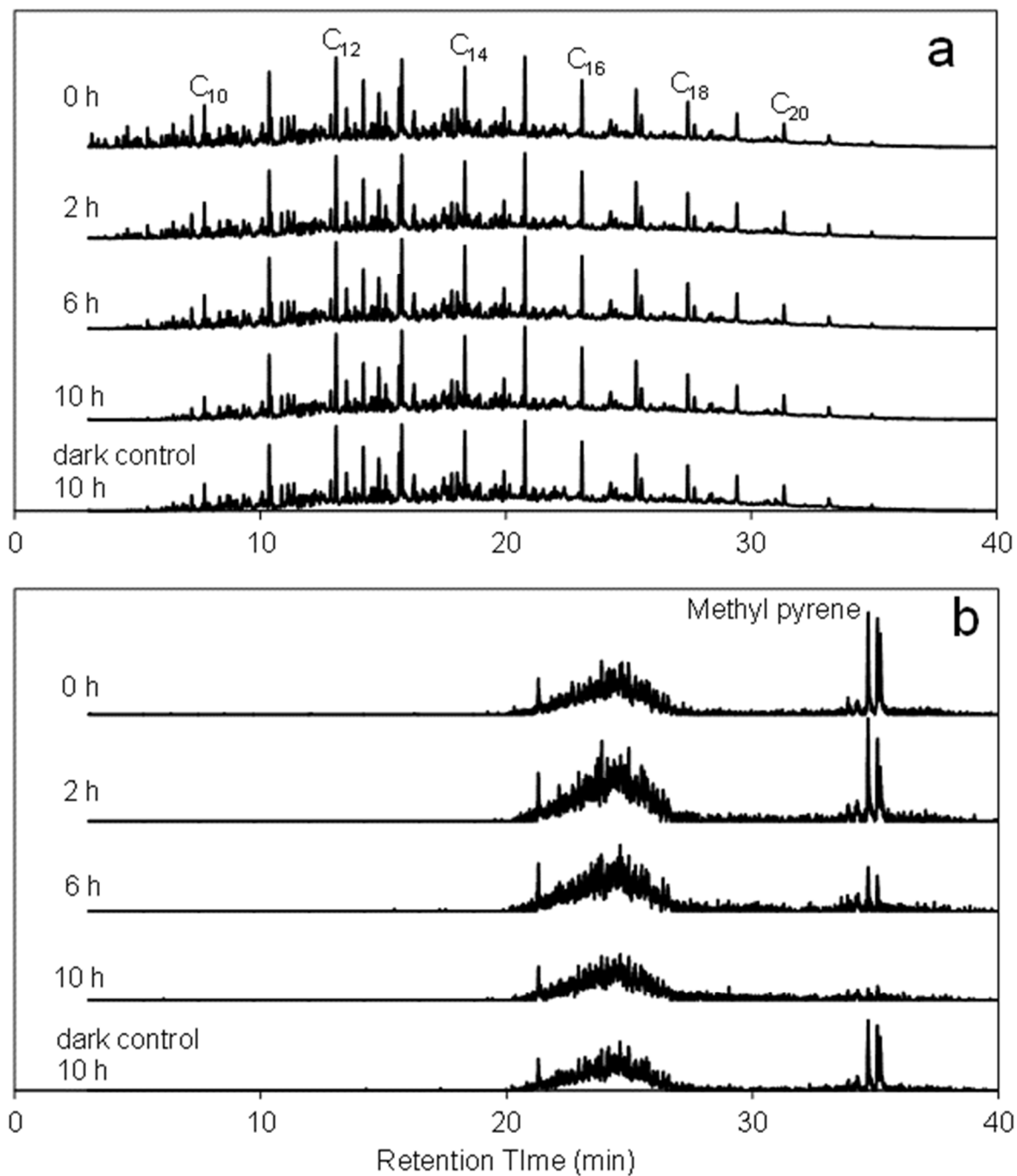


Figure 4-4. Total ion chromatograms (a) and extracted ion chromatograms (b) of  $m/z$  216 of diesel fuel irradiated for 0 – 10 h as well as a 10 h dark control. In the total ion chromatogram the even numbered normal alkanes are labeled for reference. The peaks at 34.39 min and 34.77 min correspond to methyl pyrenes.

Table 4-1. A list of compounds monitored by the GC-MS experiment. For each compound the mass-to-charge ( $m/z$ ) ratio for the extracted ion chromatogram, the retention time ( $t_R$ ), retention index ( $I^T$ ), the observed rate constant ( $k_{obs}$ ), and a predicted rate constant ( $k_{pre}$ ) for evaporation available from Chapter 3.

Compound	$m/z$ of EIC	$t_R$ (min)	$I^T$	$k_{obs}$ ( $h^{-1}$ )	Uncertainty	$k_{pre}$ ( $h^{-1}$ ) <sup>a</sup>
Toluene	91	3.137	768	1.211	0.067	0.379
Octane	57	3.686	800	0.572	0.020	0.274
Ethyl benzene	91	4.443	844	0.419	0.014	0.175
<i>m/p</i> -Xylene	91	4.593	853	0.340	0.011	0.160
<i>o</i> -Xylene	91	4.997	876	0.274	0.009	0.126
Nonane	57	5.413	900	0.170	0.006	0.098
Propyl benzene	91	6.285	938	0.138	0.006	0.067
Ethyl methyl benzene isomer	105	6.458	945	0.118	0.005	0.062
1,3,5-Trimethyl benzene	105	6.637	953	0.091	0.005	0.057
Ethyl Methyl benzene isomer	105	6.857	963	0.099	0.005	0.052
1,2,4-Trimethyl benzene	105	7.209	978	0.078	0.004	0.044
Methyl propyl benzene isomer	105	7.648	997	0.069	0.004	0.037
Decane	57	7.723	1000	0.045	0.003	0.035
1,2,3-Trimethyl benzene	105	7.862	1005	0.058	0.004	0.034

Table 4-1 cont'd

Compound	<i>m/z</i> of EIC	<i>t<sub>R</sub></i> (min)	<i>I<sup>T</sup></i>	<i>k<sub>obs</sub></i> (h <sup>-1</sup> )	Uncertainty	<i>k<sub>pre</sub></i> (h <sup>-1</sup> ) <sup>a</sup>
Indane	117	8.121	1015	0.070	0.005	0.030
Methyl propyl benzene isomer	105	8.682	1036	0.037	0.004	0.024
Methyl propyl benzene isomer	105	8.763	1039	0.035	0.004	0.024
Methyl propyl benzene isomer	105	9.051	1050	0.032	0.003	0.021
Alkyl indane isomer	117	9.473	1066	0.049	0.004	0.018
Diethyl benzene isomer	105	10.027	1087	0.019	0.004	0.015
Undecane	57	10.362	1100	0.007	0.003	0.013
Methyl decalin isomer	117	10.876	1119	0.028	0.004	0.011
Alkyl indane isomer	117	11.130	1128	0.023	0.003	0.010
1,2,3,4- Tetrahydro- naphthalene	91	11.373	1137	0.011	0.003	0.009
Naphthalene	128	11.852	1155	0.007	0.004	0.007
Methyl tetralin isomer	91	12.875	1192	0.010	0.004	0.005
Dodecane	57	13.094	1200	n/c <sup>b</sup>	n/c	0.000
Alkyl indane isomer	117	13.406	1212	0.012	0.004	0.000

Table 4-1 cont'd

Compound	<i>m/z</i> of EIC	<i>t<sub>R</sub></i> (min)	<i>I<sup>T</sup></i>	<i>k<sub>obs</sub></i> (h <sup>-1</sup> )	Uncertainty	<i>k<sub>pre</sub></i> (h <sup>-1</sup> ) <sup>a</sup>
Alkyl indane isomer	145	13.625	1220	0.020	0.003	0.000
Alkyl tetralin isomer	117	14.197	1241	0.015	0.003	0.000
Alkyl decalin isomer	165	14.469	1251	n/c	n/c	0.000
Alkyl tetralin isomer	117	15.641	1295	0.006	0.003	0.000
Tridecane	57	15.768	1300	n/c	n/c	0.000
Alkyl tetralin isomer	145	15.826	1302	0.022	0.004	0.000
Alkyl biphenyl isomer	179	16.553	1331	n/c	n/c	0.000
Alkyl tetralin isomer	132	16.623	1333	0.014	0.004	0.000
Alkyl tetralin isomer	145	17.483	1367	0.018	0.003	0.000
Alkyl tetralin isomer	145	17.541	1369	0.026	0.004	0.000
Dimethyl naphthalene isomer	128	18.015	1387	n/c	n/c	0.000
Tetradecane	57	18.338	1400	n/c	n/c	0.000
Alkyl tetralin isomer	132	18.754	1417	0.013	0.003	0.000
Alkyl tetralin isomer	132	18.823	1420	0.014	0.003	0.000
Alkyl tetralin isomer	132	18.916	1424	0.016	0.003	0.000

Table 4-1 cont'd

<b>Compound</b>	<b><i>m/z</i> of EIC</b>	<b><i>t<sub>R</sub></i> (min)</b>	<b><i>I<sup>T</sup></i></b>	<b><i>k<sub>obs</sub></i> (h<sup>-1</sup>)</b>	<b>Uncertainty</b>	<b><i>k<sub>pre</sub></i> (h<sup>-1</sup>)<sup>a</sup></b>
Alkyl biphenyl isomer	165	19.58	1451	n/c	n/c	0.000
Pentadecane	57	20.781	1500	n/c	n/c	0.000
Fluorene	165	21.751	1542	0.011	0.003	0.000
Alkyl biphenyl isomer	165	22.000	1552	0.020	0.003	0.000
Hexadecane	57	23.108	1600	n/c	n/c	0.000
Methyl fluorene isomer	165	24.367	1657	0.014	0.003	0.000
Methyl fluorene isomer	165	24.494	1663	0.035	0.004	0.000
Alkyl biphenyl isomer	179	24.783	1676	0.059	0.003	0.000
Heptadecane	57	25.315	1700	n/c	n/c	0.000
Phenanthrene	178	25.904	1728	n/c	n/c	0.000
Dimethyl fluorene isomer	179	26.857	1773	0.033	0.003	0.000
Dimethyl fluorene isomer	179	26.972	1779	0.034	0.003	0.000
Dimethyl fluorene isomer	179	27.099	1785	0.045	0.003	0.000
Octadecane	57	27.417	1800	n/c	n/c	0.000
Alkyl hopanes isomer	192	28.306	1844	0.006	0.002	0.000

Table 4-1 cont'd

Compound	<i>m/z</i> of EIC	<i>t<sub>R</sub></i> (min)	<i>I<sup>T</sup></i>	<i>k<sub>obs</sub></i> (h <sup>-1</sup> )	Uncertainty	<i>k<sub>pre</sub></i> (h <sup>-1</sup> ) <sup>a</sup>
Alkyl hopanes isomer	192	28.393	1849	0.004	0.002	0.000
Alkyl hopanes isomer	192	28.739	1866	0.009	0.003	0.000
Alkyl hopanes isomer	192	28.837	1871	0.006	0.002	0.000
Nonadecane	57	29.421	1900	n/c	n/c	0.000
Eicosane	57	31.332	2000	n/c	n/c	0.000
Pyrene	202	32.181	2047	0.174	0.005	0.000
Heneicosane	57	33.157	2100	n/c	n/c	0.000
Alkyl pyrene isomer	216	34.388	2170	0.218	0.014	0.000
Alkyl pyrene isomer	216	34.774	2192	0.243	0.010	0.000

a. Model obtained in Chapter 3

b. n/c =  $k_{obs} < 0.002 \text{ h}^{-1}$ , which was not significantly different from 0.0 ( $\alpha = 0.05$ )

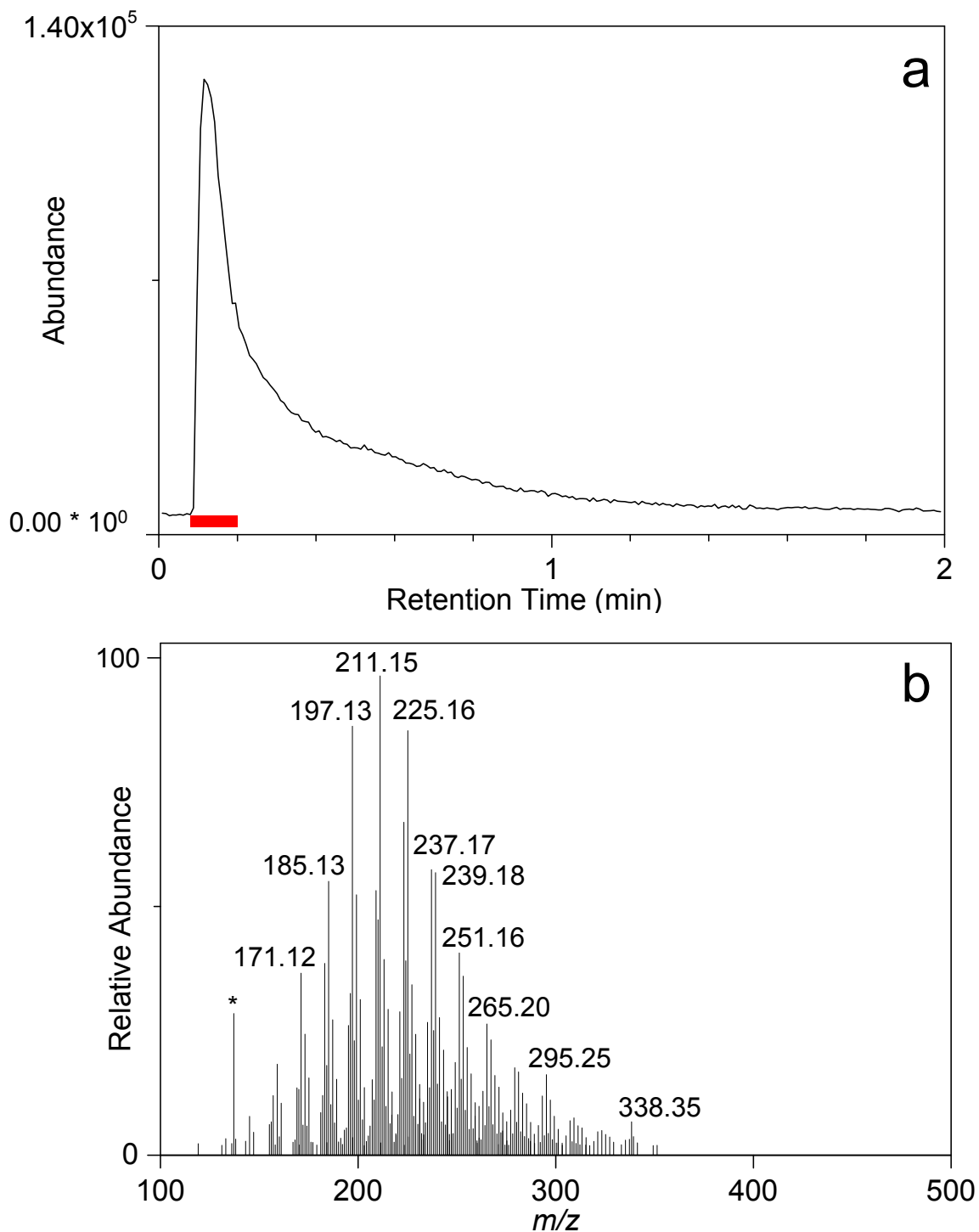
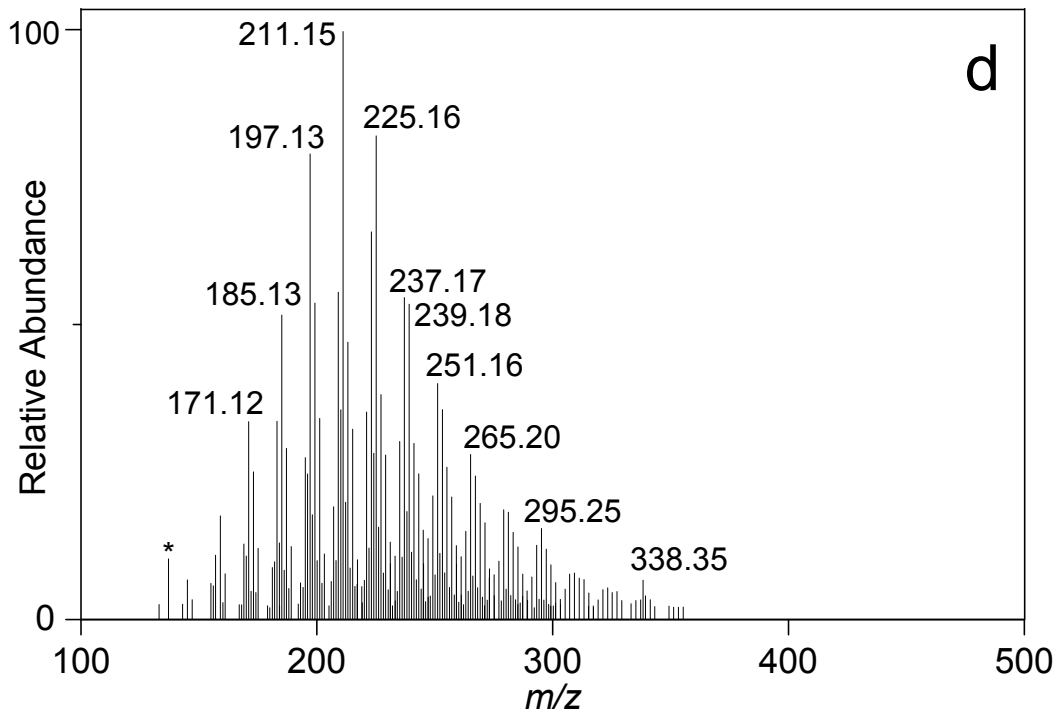
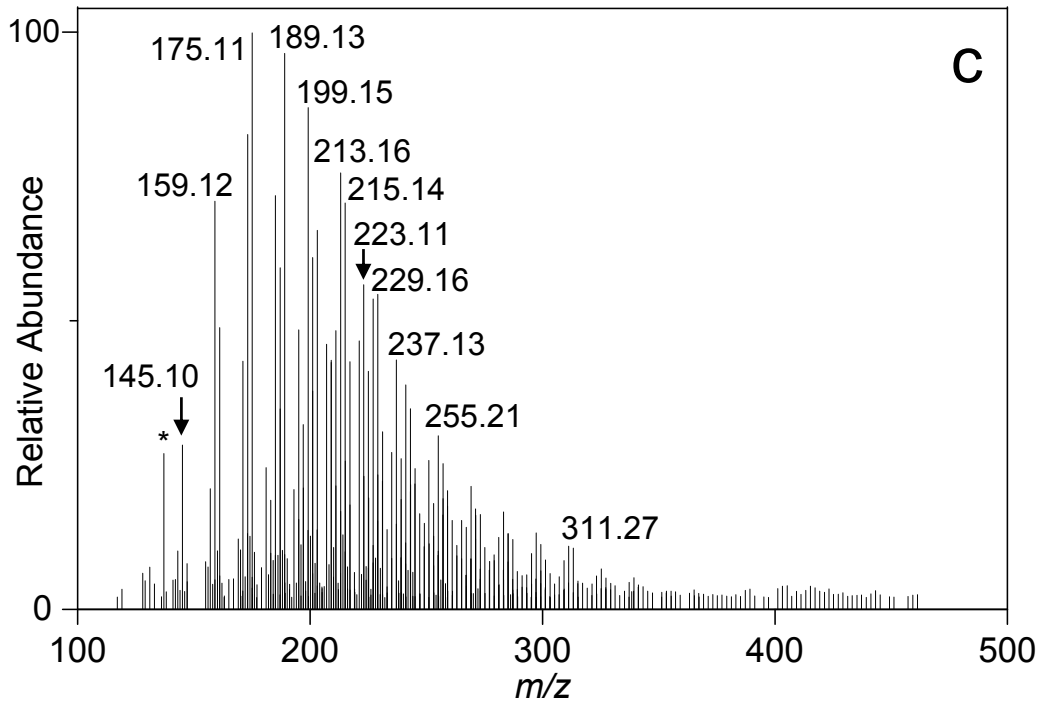


Figure 4-5. The output from mass spectrometry analysis of diesel fuel. An example TIC chromatogram (a) is representative of all chromatograms indicating the region over which the spectra were averaged (red line). The mass spectrum prior to irradiation (b) and after irradiation for 10 h (c) and the 10 hour dark control (d) are also shown. Quinoline-d7 (\*) was used at the lock mass. The formulas for each mass is in Table 4-2 and Table 4-3.

Figure 4-5 cont'd



### 4.3.3 Determination of Elemental Formulas by High Resolution Mass Spectrometry

The high resolution mass spectrometry (HR-MS) analyses used flow injection analysis, resulting in a total ion chromatogram with a single peak (Figure 4-5a). To obtain the mass spectrum, 12 spectra from 0.09 to 0.20 min were averaged (MassLynx, Waters Corporation). A lock mass of  $m/z$  137.1091 Da corresponding to quinoline- $d_7$ , was used to correct for mass drift. Only masses between  $m/z$  100 –  $m/z$  500 were evaluated as spectra did not have meaningful ions greater than  $m/z$  500. The threshold was set at 2% of the base peak.

The MS analysis of the fuel sample yielded hundreds of masses (Figure 4-5b and c). Elemental formulas were assigned using MassLynx, with element ranges of C (1 – 500), H (1 – 1000), N (0 – 4), O (0 – 4), and S (0 – 4). Even using a mass error of less than 3 mDa, the Elemental Composition algorithm of MassLynx frequently reported multiple possible formulas. Because diesel fuel is a refined petroleum product, many of the compounds containing heteroatoms typically found in crude oil would not be present in the fuel before irradiation. Moreover, diesel fuel goes through additional refining to create ultra-low sulfur diesel (<15 ppm sulfur) [14]. Therefore, it is unlikely that these heteroatoms are present at high abundance, except for oxygen after photooxidation. Elemental formulas were then assigned using C (1 – 500), H (1 – 1000), and O (0 – 4) with a mass error of 10 mDa. This allowed the assignment of one or two elemental compositions to most compounds. The typical mass error was 3 – 7 mDa, but was as high 20 mDa in some cases.

A list of masses and elemental compositions were exported to Excel (2013, Microsoft Corporation, Redmond, WA). In cases where two elemental formulas were

possible, each were evaluated based on the mass error and whether that formula was present in other replicates. Masses for which an elemental formula did not match within the 10 mDa error window were omitted. This allowed for the assignment of a single elemental formula for each mass. This resulted in over 850 elemental formulas, ranging from 8 – 49 carbons, 7 – 59 hydrogens, 0 – 4 and oxygens, with 0 – 30 double bond equivalences (rings or double bonds).

In the mass spectrum of diesel prior to irradiation (Figure 4-5b), Over 99% of the elemental formulas suggest the compounds contain only carbons and hydrogens. Clusters of peaks separated by approximately 2 Da are observed. These regions correspond to compounds that have the same number of carbons, but differ by 2 hydrogen atoms, or 1 double bond equivalent (DBE). Each of these clusters are separated by approximately 14 Da, corresponding to differences of a CH<sub>2</sub> group as expected from alkyl homologs. This repeating pattern is common in the MS of petroleum products [15, 16]. A similar pattern, but with different masses, was observed in the spectrum of diesel fuel after 10 h of irradiation (Figure 4-5c). After irradiation, the dominant masses that were observed still have varying DBE and CH<sub>2</sub> groups, but now contain at least one oxygen atom. These new masses were not observed in the dark control (Figure 4-5d), indicating that they were formed by photooxidation. Quantification of the changes in abundance for specific masses will be discussed in Section 4.3.6.

#### *4.3.4 Kendrick Mass Defect*

In the analysis of petroleum products, the Kendrick mass defect (KMD) is commonly applied to simplify the interpretation of high resolution MS data [17]. The KMD is calculated from the Kendrick mass ( $m_K$ ), which rescales the exact monoisotopic mass

( $m_E$ ) so that the mass of  $\text{CH}_2$  is set to equal exactly 14, rather than the IUPAC mass scale, based upon the atomic mass of  $^{12}\text{C}$  equaling exactly 12 [18] (Equation 4-2).

$$m_K = m_E * \frac{14.00000}{14.01565} \quad \text{Equation 4-2}$$

The KMD is calculated as difference between the Kendrick mass and the nominal mass ( $m_N$ ), as shown in Equation 4-3.

$$KMD = m_K - m_N \quad \text{Equation 4-3}$$

Using the Kendrick mass defect, compounds with the same double bond equivalency (DBE) and heteroatoms will have the same mass defect [18]. When the nominal mass is plotted against the Kendrick mass defect, compounds with the same DBE and heteroatom, but different numbers of methyl groups will appear as horizontal lines allowing for the rapid determination of structurally related compounds [18].

Using the elemental formulas determined in Section 4.3.3, Kendrick mass defects were calculated using Equation 4-2 and Equation 4-3. The Kendrick mass was plotted against the Kendrick mass defect to identify structurally related compounds (Figure 4-6a). On this plot, compounds with the same Kendrick mass defect, (*i.e.* differing by a methylene group) form a straight horizontal line, 14 Da apart. In Figure 4-6a, only hydrocarbons are present, so the Kendrick mass defect corresponds to differences in DBE. Compounds with the same number of carbons, form diagonal lines, with points that differ by 2 Da, indicating differences in the number of hydrogen atoms.

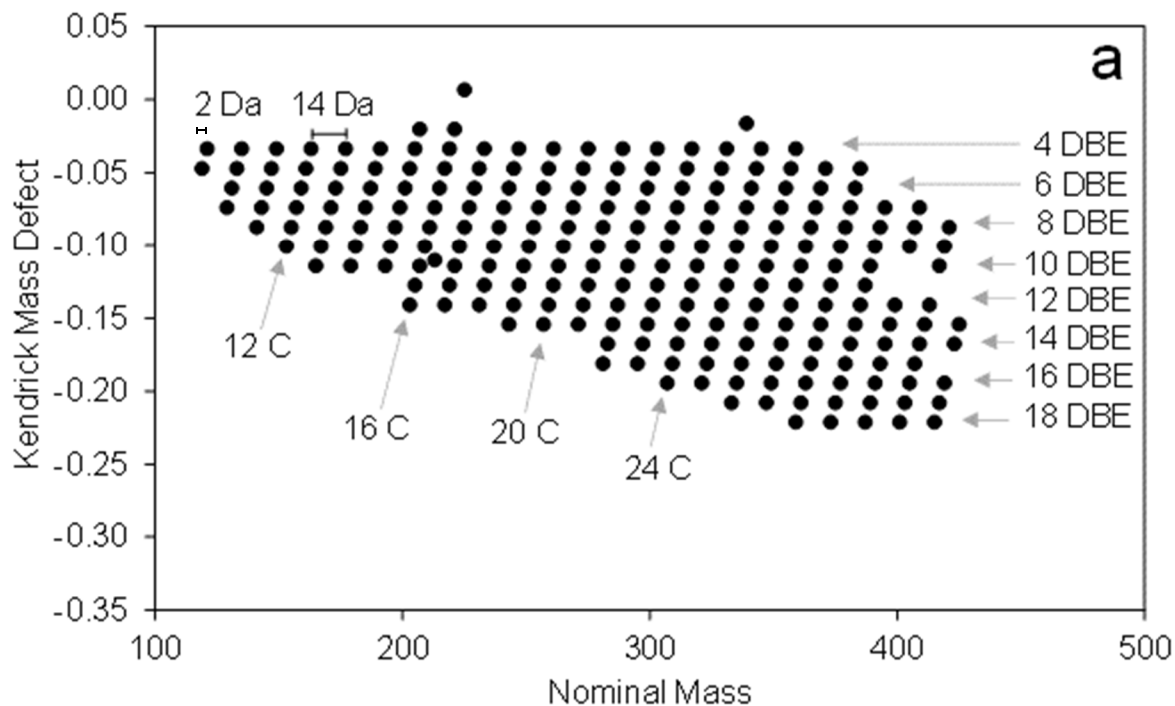
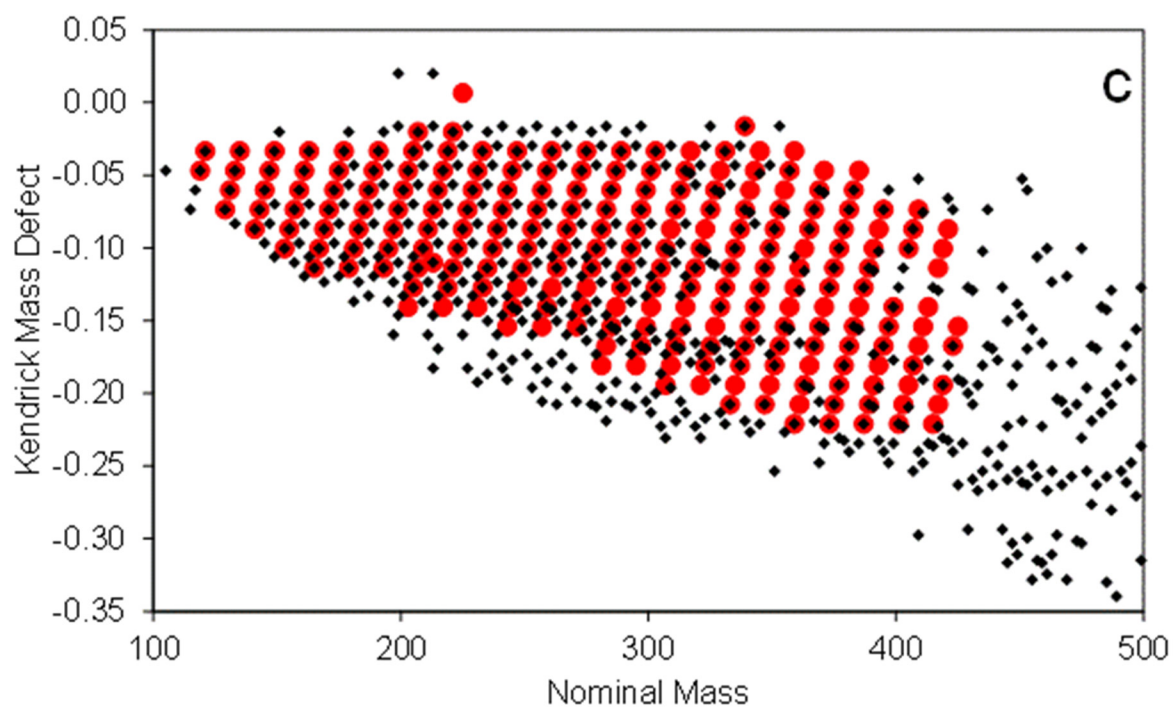
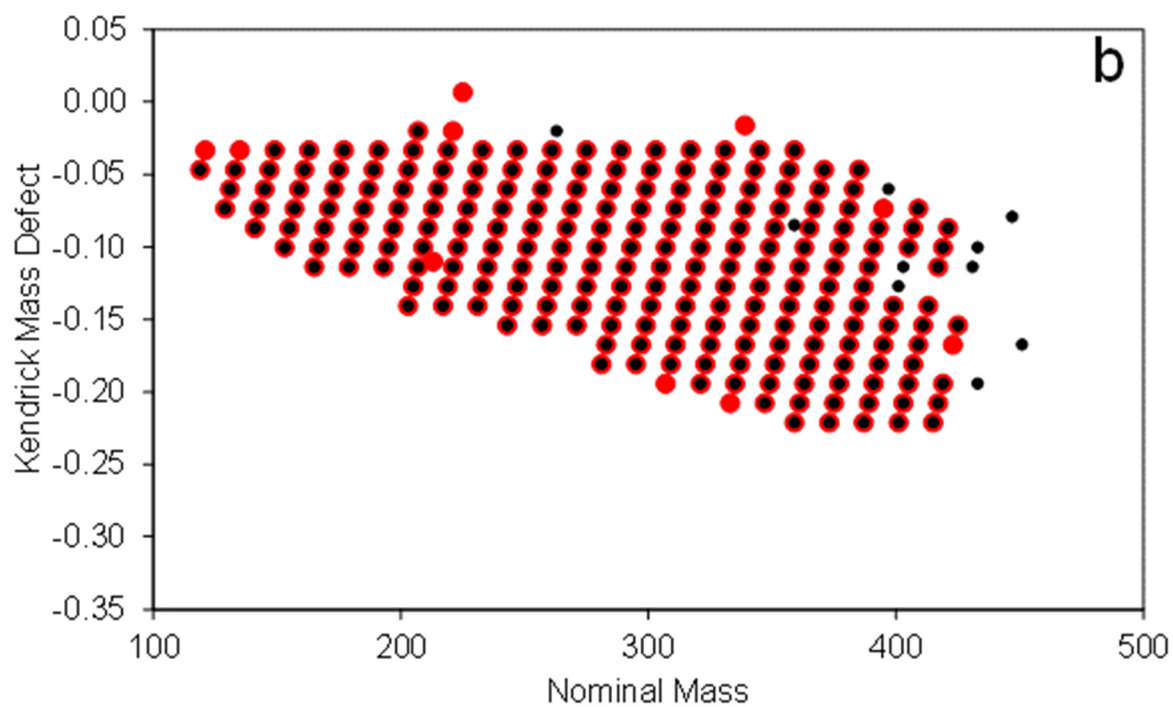


Figure 4-6. The Kendrick mass defect *versus* the nominal mass for an unirradiated diesel sample (a). Compounds in a horizontal row have the same double bond equivalence (DBE) and differ by 14 Da, indicating a difference in one methylene group. Compounds in a diagonal line, indicate the same number of carbon atoms, and differ by 2 Da, indicating a difference in 2 hydrogen atoms. The Kendrick mass defect *versus* the nominal mass for the unirradiated diesel fuel (large red circles) overlaid with the 10 hour dark control (small black circles) (b), and the 10 hour irradiated sample (small black diamonds) (c).

Figure 4-6 cont'd



The plot of the Kendrick mass defect *versus* the nominal mass for diesel fuel irradiated for 10 hours and the corresponding dark control were compared to the plot of the unirradiated diesel sample (Figure 4-6 b and c). In the unirradiated sample (larger red circles), 228 elemental formulas were assigned, only two of which contained an oxygen. In the 10 hour dark control (smaller black circles), 228 elemental formulas were also assigned (Figure 4-6b). In this case, two different elemental formulas contained oxygen. When overlaid, all but 10 formulas from each sample agree. This demonstrates that the unirradiated sample and dark control are similar and newly formed compounds can be attributed to photooxidation. By comparison, the diesel sample irradiated for 10 hour contained 574 elemental formulas, or about 2.5 times as many as in the untreated fuel. In the plot of the Kendrick mass defect *versus* nominal mass (Figure 4-6c), a large number of new elemental formulas are present in the irradiated sample (black diamonds). In addition to the large number of newly formed compounds, approximately 58 compounds (about 25% of the original diesel constituents) were no longer present, suggesting complete degradation from photooxidation or evaporation. This demonstrates that even over a relatively short period of time, there are substantial changes due to photooxidation.

#### 4.3.5 *Principal Component Analysis*

In order to determine which masses were changing during the irradiation, principal component analysis (PCA) was performed (Pirouette v. 4.0, Infometrix, Bothell, WA). PCA organizes sample data based on the greatest sources of variance and has two main outputs, scores plots and loadings plots (Figure 4-7). The scores plot shows a visual

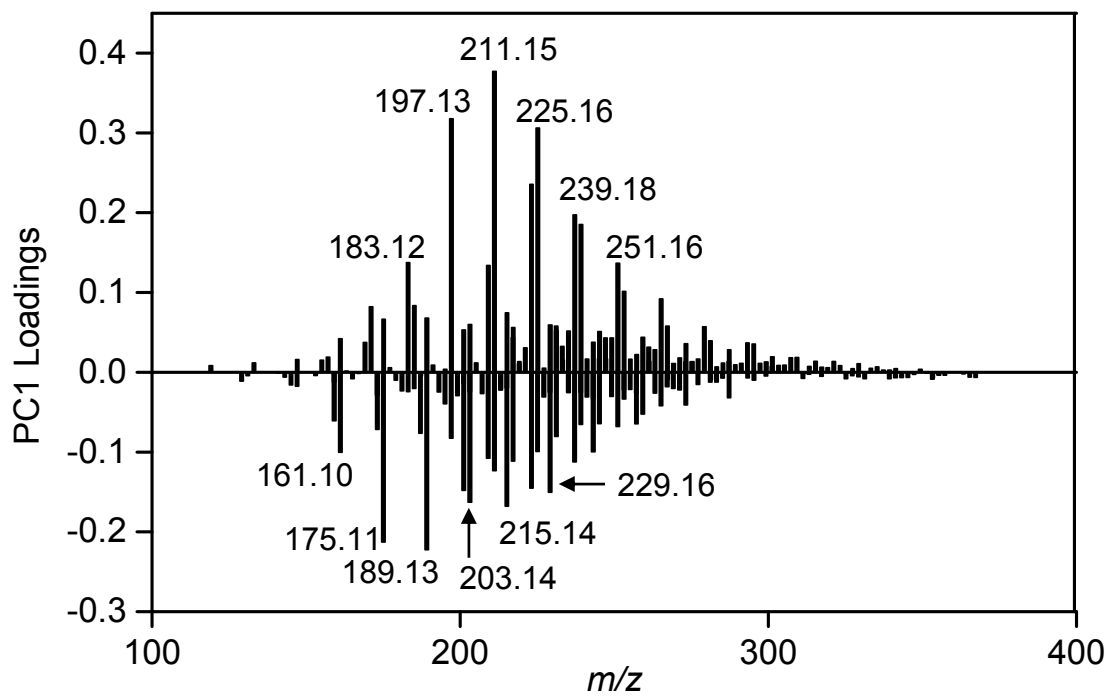
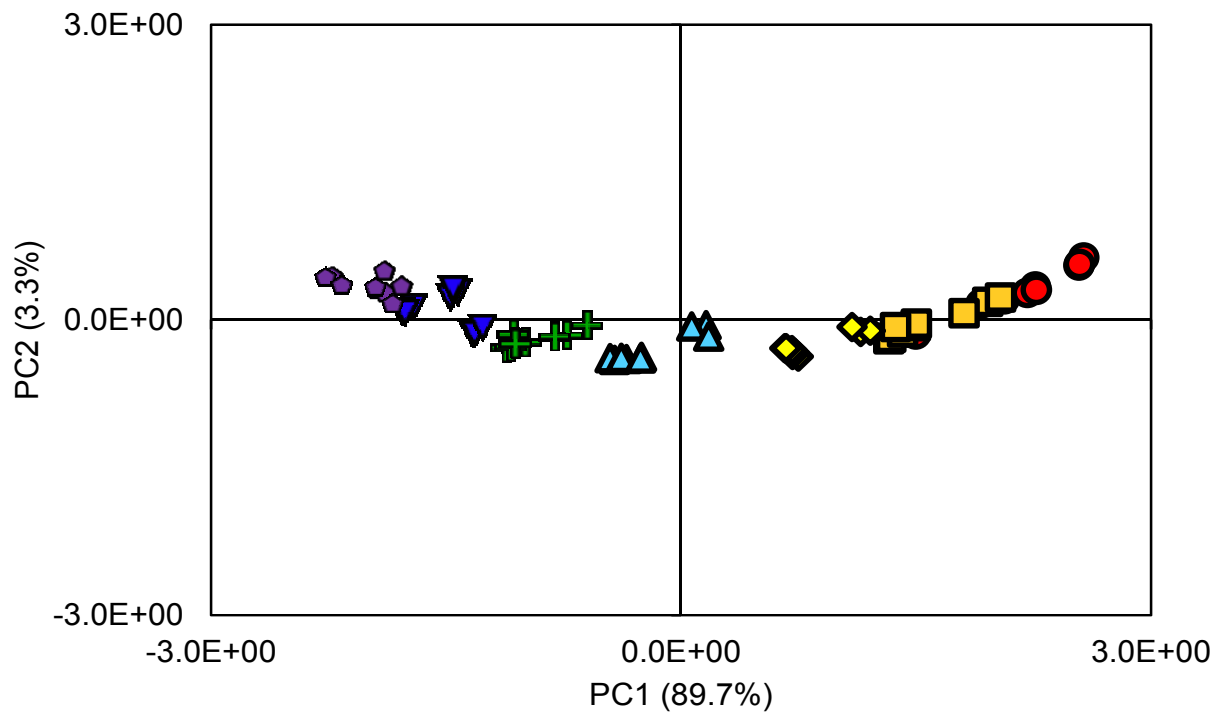


Figure 4-7. The PCA scores plot (a) and loadings plot (b) for samples irradiated for 0 h (●), 1 h (■), 2 h (◆), 4 h (▲), 6 h (+), 8 (▼), and 10 h (◆).

relationship between samples; samples that are positioned close together are more chemically similar than those positioned further apart. The PCA in this work was performed using the abundances (peak heights) for each exact mass, based on the elemental formulas discussed in Section 4.3.3, after normalizing abundances to  $m/z$  199.1487. The scores plot (Figure 4-7a) shows the first principal component (PC1) accounts for 89.7% of the variance and the second principal component (PC2) accounts for 3.2% of the variance. Because PC1 accounts for such a large amount of the variance, most of the chemical differences are accounted for on this PC. The unirradiated diesel samples are positioned positively on PC1. As irradiation time increased, the diesel samples were positioned progressively more negative until 10 h, which are positioned the most negatively on PC1. This demonstrates that PC1 is accounting for difference in irradiation time.

The loadings plots show which variables are influencing the positioning of the samples on the scores plot. The loadings plot for PC1, which is the loadings *versus* the  $m/z$ , is shown in Figure 4-7b. The masses that are most abundant in the unirradiated fuel (Figure 4-5b) are loading positively on PC1, while the masses that are most abundant after 10 h of irradiation (Figure 4-5c) are loading negatively on PC1. Therefore, on the PC1 loadings plot, the masses that are loading positive correspond to compounds that are decaying, while masses that are loading negatively likely correspond to compounds that are forming during irradiation.

PCA results demonstrated several important points. First, PCA was useful in demonstrating differences in sample composition as a function of irradiation time. Experimental replicates are clustered close together, indicating that the irradiation

experiments were reproducible. Second, PCA was useful in identifying characteristic masses corresponding to compounds that were undergoing formation or decay. Compounds that loaded positively were hydrocarbons that decayed in abundance during photooxidation while compounds that loaded negatively were oxygenated compounds that formed during irradiation.

#### 4.3.6 Determination of Photooxidation Rate Constants

In order to quantify the rate of change from both the GC-MS and HR-MS experiments, kinetic rate constants were determined. In the GC-MS experiment, peak abundances were normalized to nonadecane and in the HR-MS experiments the peak abundances were normalized to  $m/z$  199.1487, which had 7 DBE, equivalent to a naphthalene with 5 methylene groups.

Decay or formation curves (Figure 4-8) were plotted for individual compounds by plotting the normalized abundance *versus* time. Kinetic rate constants were then determined by nonlinear regression (TableCurve 2D, version 5.01, Jandel Scientific, San Rafael, CA). Zeroth- and first-order kinetics were considered, based on previous research [8, 9, 19]. A zeroth-order rate constant results in a reaction that is independent of concentration. This may occur when the reactant is at a low concentration or is being replenished by another reaction. Zeroth order kinetics could also arise when light serves as the limiting reactant [20]. A first-order rate constant results in a reaction that is directly proportional to the concentration of the reactant. Also possible are pseudo-first-order reactions in which the reaction is dependent upon the concentration of two

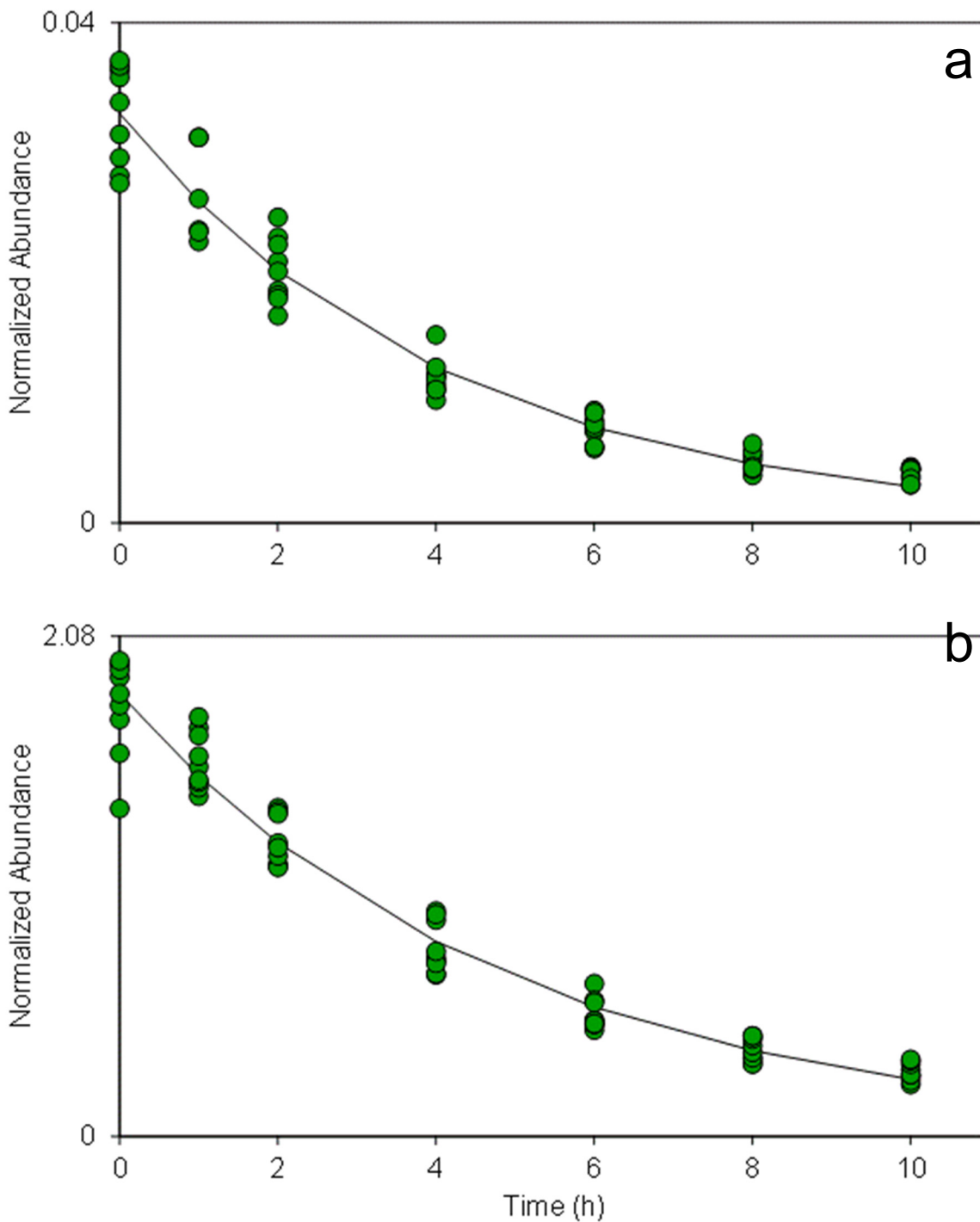
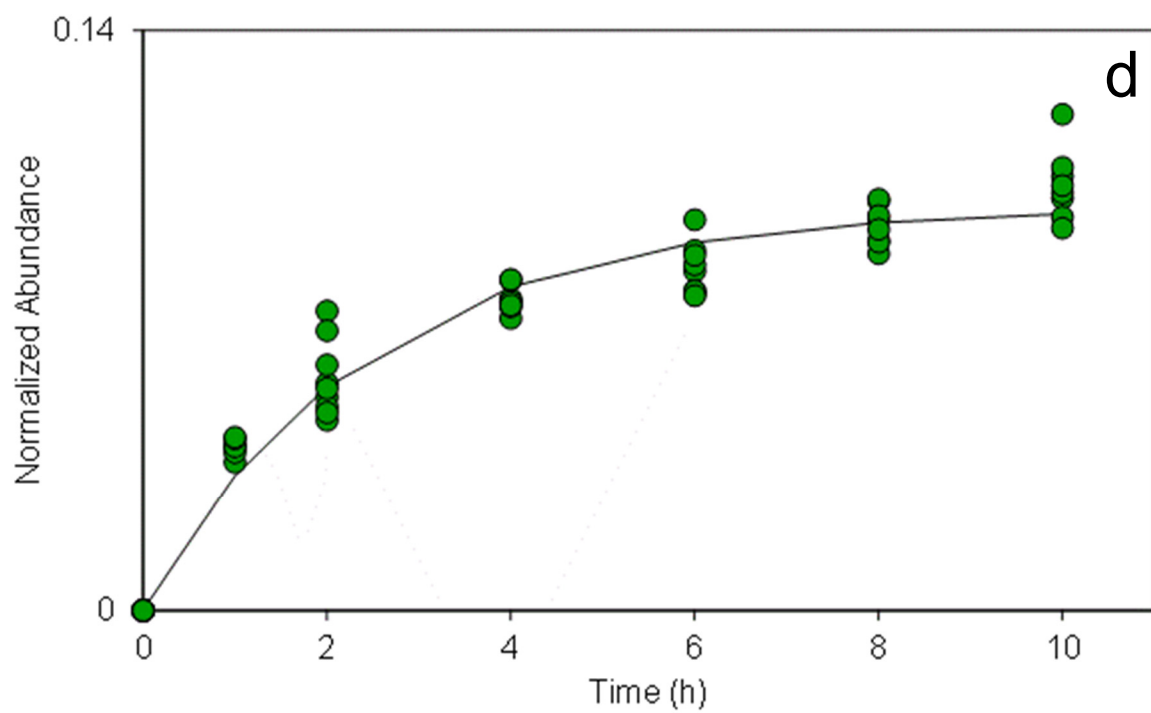
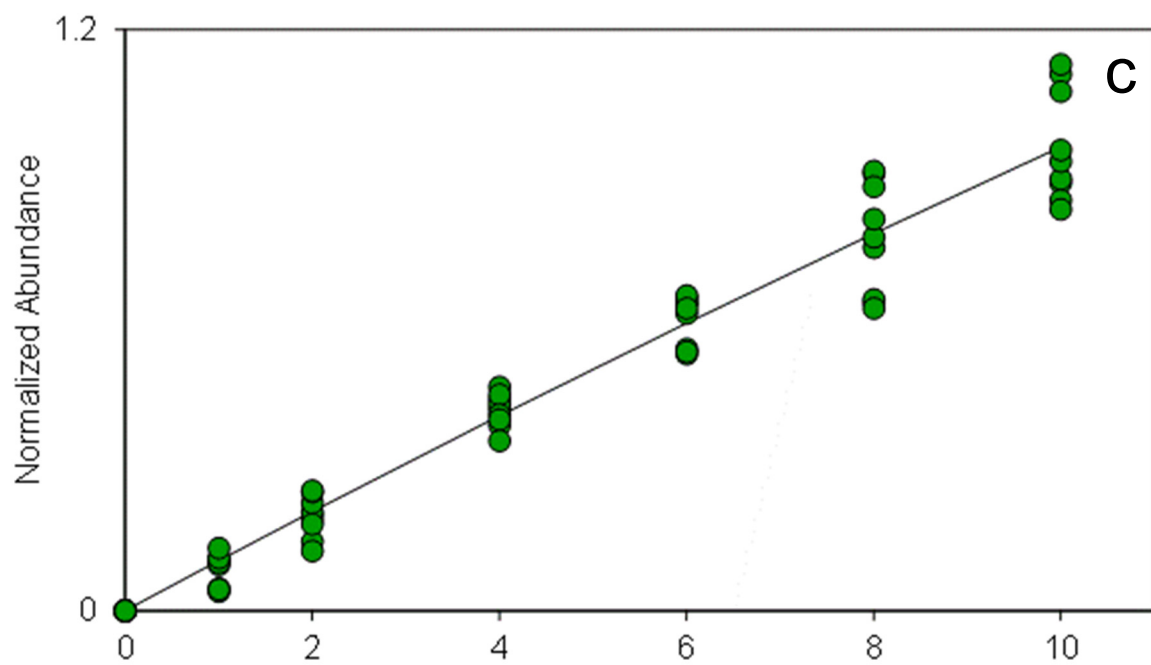


Figure 4-8. Decay and formation curves for various compounds. The regression equation is shown and the first order rate constant is underlined. From the GC-MS analysis: methyl pyrene (a) (retention time 34.77 min,  $y = 0.033 * \exp(-\underline{0.243} * t)$ ). From the HR-MS analysis:  $C_{16}H_{19}$  (b) ( $m/z$ : 211.15,  $y = 1.840 * \exp(-\underline{0.205} * t)$ ),  $C_{13}H_{17}O_1$  (c) ( $m/z$ : 189.13,  $y = 6.291 * \exp(-\underline{0.0165} * t)$ ),  $C_{18}H_{21}O_2$  (d) ( $m/z$ : 269.15,  $y = 0.097 * \exp(-\underline{0.045} * t)$ ).

Figure 4-8 cont'd



reactants. However, one reactant is at a much higher concentration and can be thought of as constant, so that the kinetics can be thought of as first-order. The first-order formation of a compound is the inverse of the first-order decay of a precursor, even when the identity of the precursor is unknown. Previous reports suggested that the decay due to photooxidation was likely first-order or pseudo-first-order [21-23], while other investigations have suggested formation was zeroth-order [24]. It is likely that the kinetics of photooxidation of diesel fuel and other complex petroleum products are not simple, and depend on the concentrations of the compound as well as the sensitizer. However, the total abundance of all sensitizers may be large compared to the abundance of any single compound, allowing pseudo-first-order kinetic equations to provide an accurate depiction of the rate constants.

#### 4.3.6.1 Kinetic Rate Constants Determined from Gas Chromatography-Mass Spectrometry

Using the GC-MS chromatographic data, 61 compounds were quantified and decay curves were generated. An example decay curve for methyl pyrene (retention time: 34.77 min, from Figure 4-4b) is shown in Figure 4-8a. A decrease in abundance over time was observed for 41 of the 61 compounds, and first-order rate constants were determined for each. The experimental rate constants were compared with rate constants predicted for evaporation alone, using a model based on the retention index of the compound on a nonpolar stationary phase and temperature (Chapter 3). The temperature of the water was 21 °C and retention indices were calculated from the GC-MS experiment. Surprisingly, the experimental rate constants determined during photooxidation ( $0.004 - 1.211 \text{ h}^{-1}$ ) were nearly twice as large as the rate constants

predicted by the evaporation model ( $0.000 - 0.379 \text{ h}^{-1}$ ) for the compounds expected to evaporate (with retention indices greater than about 1200).

It is unlikely that the increase in the rate constant is due to photooxidation, because a similar increase was observed for all compound classes, including the normal alkanes, which are not expected to decay by photooxidation owing to their lower reactivity relative to alkyl aromatics toward free radicals [11, 12]. This increase in the disappearance rates is likely to result from increased deposition of energy deposited into the molecules during irradiation that results in warming rather than electronic excitation. This observation demonstrates the interconnection between weathering processes; even though the compounds are not being degraded by photooxidation, increased rates of evaporation are observed.

Other compounds that were not expected to evaporate, decreased in abundance over the 10 h irradiation experiment due to photooxidation. The compounds that underwent photooxidation were typically larger and alkyl substituted PAHs, however, compounds that were provisionally identified as alkyl indanes and tetralins also were oxidized. Naphthalene, methyl naphthalene, phenanthrene, and alkyl biphenyl compounds did not undergo photooxidation over the course of this experiment as judged by their minimal changes in abundances. For the compounds that did oxidize, those with more alkyl substituents had a higher rate constant. This is consistent with results reported by Prince *et al.* who observed more degradation due to photooxidation in compounds with more aromatic rings and more alkyl substitutions, consistent with the notion that electron-donating groups add to the photo-reactivity of benzene rings [12]. In addition, structural isomers that were more retained than other isomers, based on retention index ( $I^T$ ), also

often had an increased rate constant. For example, the rate constant for pyrene ( $I^T = 2047$ ,  $k = 0.174 \text{ h}^{-1}$ ) was lower than that of methyl pyrene ( $I^T = 2170$ ,  $k = 0.218 \text{ h}^{-1}$ ). The rate constant for the methyl pyrene was lower than the rate constant for the more retained structural isomer ( $I^T = 2192$ ,  $k = 0.243 \text{ h}^{-1}$ ). A similar trend is observed for fluorene ( $I^T = 1542$ ,  $k = 0.011 \text{ h}^{-1}$ ) and the methyl fluorenes ( $I^T = 1657$ ,  $k = 0.014 \text{ h}^{-1}$  and  $I^T = 1663$ ,  $k = 0.036 \text{ h}^{-1}$ ) and dimethyl fluorenes ( $I^T = 1773$ ,  $k = 0.033 \text{ h}^{-1}$  and  $I^T = 1779$ ,  $k = 0.034 \text{ h}^{-1}$  and  $I^T = 1785$ ,  $k = 0.045 \text{ h}^{-1}$ ). Identification of additional isomers would help to elucidate additional underlying patterns however, this identification was not feasible given the small sample size, the complexity of the sample, and the relatively low abundance of many of the isomers.

#### 4.3.6.2 Kinetic Rate Constants Determined from High Resolution Mass Spectrometry

In the HR-MS experiments, over 850 unique masses were identified in the photooxidized diesel, however, many were only present in a few samples. Only masses that were present in at least 27 of the 63 total analyses (equivalent data collected at three time points) were considered for the rate determination, resulting in 201 masses. Changes in abundance were observed for 121 of the 201 masses, for which rate constants were determined using either decay ( $k_d$ ,  $n = 67$ ) or formation ( $k_f$ ,  $n = 54$ ) curves. An example decay curve of  $m/z$  211.15 ( $\text{C}_{16}\text{H}_{19}$ ) and example formation curves of  $m/z$  189.13 ( $\text{C}_{13}\text{H}_{17}\text{O}_1$ ) and  $m/z$  269.15 ( $\text{C}_{18}\text{H}_{21}\text{O}_2$ ) are shown in Figure 4-8 b – d respectively. All of the newly formed compounds suggest the presence of at least one oxygen atom. There do not appear to be any high molecular weight ions ( $m/z > 300$ ) that does not contain oxygen, suggesting dimerization is not occurring.

All of the determined rate constants were considered first-order or pseudo-first-order. Rate constants ranged from 0.003 – 0.210 h<sup>-1</sup> for decay, 0.000 – 0.221 h<sup>-1</sup> for formation of a compound containing one oxygen atom, and 0.017 – 1.173 h<sup>-1</sup> for formation of a compound containing two oxygen atoms. A complete list of the rate for decay and formation are in Table 4-2 and Table 4-3, respectively. Some formation rate constants appeared to be zeroth-order and could not be reasonably fit to a first-order formation equation (n = 25). The zeroth-order formation is consistent with observations by Larson *et al.* [24], however, it is possible these formations are first-order, but only a small portion of the formation curve is seen over the 10 hour experiments. The zeroth-order rate constants for all formed compounds that form are also available on Table S3. The uncertainty measurement in  $k_f$  was as high as 0.13, larger than many of the first-order rate constants for formation, supporting that the compounds may not form by zeroth-order. In addition, a reaction involving singlet oxygen or free radicals would likely not result in zeroth-order kinetics, as the rate constant is dependent on concentration [25]. These compounds were excluded from further consideration, however many of the trends discussed below for the first-order rate constant for formation were also observed when using the zeroth-order rate constants. Of note, there were also three hydrocarbons that were shown to grow during irradiation. These hydrocarbons are related with differing alkyl substitution. These hydrocarbons are like a rearrangement of an oxygenated compound, with a loss of water, occurring during ionization. These compounds also showed zeroth-order formation and were excluded from further consideration.

Table 4-2. The exact mass, the number of carbon atoms (C), the number of hydrogen atoms (H), the number of oxygen atoms (O), the double bond equivalence (DBE), the Kendrick mass defect (KMD), the rate constant for decay ( $k_d$ ), and the uncertainty in the rate constant for compounds identified using mass spectrometry.

<b>Mass</b>	<b>C</b>	<b>H</b>	<b>O</b>	<b>DBE</b>	<b>KMD</b>	<b><math>k_d</math> (<math>h^{-1}</math>)</b>	<b>Uncertainty</b>
163.149	12	19	0	4	-0.0335	n/c <sup>a</sup>	n/c
177.164	13	21	0	4	-0.0335	n/c	n/c
191.18	14	23	0	4	-0.0335	n/c	n/c
205.196	15	25	0	4	-0.0335	0.100	0.009
219.211	16	27	0	4	-0.0335	0.113	0.008
233.227	17	29	0	4	-0.0335	0.117	0.008
247.243	18	31	0	4	-0.0335	0.112	0.009
261.258	19	33	0	4	-0.0335	0.104	0.010
275.274	20	35	0	4	-0.0335	0.091	0.010
289.29	21	37	0	4	-0.0335	0.080	0.010
303.305	22	39	0	4	-0.0335	n/c	n/c
317.321	23	41	0	4	-0.0335	n/c	n/c
119.086	9	11	0	5	-0.0469	0.096	0.013
133.102	10	13	0	5	-0.0469	0.094	0.010

Table 4-2 cont'd

<b>Mass</b>	<b>C</b>	<b>H</b>	<b>O</b>	<b>DBE</b>	<b>KMD</b>	<b><math>k_d</math> (h<sup>-1</sup>)</b>	<b>Uncertainty</b>
147.117	11	15	0	5	-0.0469	0.105	0.009
161.133	12	17	0	5	-0.0469	0.153	0.008
175.149	13	19	0	5	-0.0469	0.196	0.009
189.164	14	21	0	5	-0.0469	0.205	0.010
203.18	15	23	0	5	-0.0469	0.197	0.010
217.196	16	25	0	5	-0.0469	0.206	0.014
231.211	17	27	0	5	-0.0469	0.186	0.009
245.227	18	29	0	5	-0.0469	0.185	0.009
259.243	19	31	0	5	-0.0469	0.171	0.010
273.258	20	33	0	5	-0.0469	0.158	0.011
287.274	21	35	0	5	-0.0469	0.153	0.012
301.29	22	37	0	5	-0.0469	0.129	0.011
315.305	23	39	0	5	-0.0469	0.084	0.013
329.321	24	41	0	5	-0.0469	0.074	0.014
131.086	10	11	0	6	-0.0603	n/c	n/c

Table 4-2 cont'd

<b>Mass</b>	<b>C</b>	<b>H</b>	<b>O</b>	<b>DBE</b>	<b>KMD</b>	<b><math>k_d</math> (h<sup>-1</sup>)</b>	<b>Uncertainty</b>
145.102	11	13	0	6	-0.0603	n/c	n/c
159.117	12	15	0	6	-0.0603	n/c	n/c
173.133	13	17	0	6	-0.0603	n/c	n/c
187.149	14	19	0	6	-0.0603	n/c	n/c
201.164	15	21	0	6	-0.0603	0.044	0.003
215.18	16	23	0	6	-0.0603	0.078	0.003
229.196	17	25	0	6	-0.0603	0.074	0.003
243.211	18	27	0	6	-0.0603	0.050	0.003
257.227	19	29	0	6	-0.0603	0.033	0.004
271.243	20	31	0	6	-0.0603	0.026	0.004
285.258	21	33	0	6	-0.0603	0.018	0.005
299.274	22	35	0	6	-0.0603	0.019	0.005
313.29	23	37	0	6	-0.0603	n/c	n/c
327.305	24	39	0	6	-0.0603	n/c	n/c
341.321	25	41	0	6	-0.0603	n/c	n/c

Table 4-2 cont'd

<b>Mass</b>	<b>C</b>	<b>H</b>	<b>O</b>	<b>DBE</b>	<b>KMD</b>	<b><math>k_d</math> (h<sup>-1</sup>)</b>	<b>Uncertainty</b>
355.336	26	43	0	6	-0.0603	n/c	n/c
129.07	10	9	0	7	-0.0737	n/c	n/c
143.086	11	11	0	7	-0.0737	n/c	n/c
157.102	12	13	0	7	-0.0737	n/c	n/c
171.117	13	15	0	7	-0.0737	0.058	0.005
185.133	14	17	0	7	-0.0737	0.038	0.003
199.149	15	19	0	7	-0.0737	n/c	n/c
213.164	16	21	0	7	-0.0737	n/c	n/c
227.18	17	23	0	7	-0.0737	n/c	n/c
241.196	18	25	0	7	-0.0737	n/c	n/c
255.211	19	27	0	7	-0.0737	n/c	n/c
269.227	20	29	0	7	-0.0737	n/c	n/c
283.243	21	31	0	7	-0.0737	n/c	n/c
297.258	22	33	0	7	-0.0737	n/c	n/c
311.274	23	35	0	7	-0.0737	n/c	n/c

Table 4-2 cont'd

<b>Mass</b>	<b>C</b>	<b>H</b>	<b>O</b>	<b>DBE</b>	<b>KMD</b>	<b><math>k_d</math> (h<sup>-1</sup>)</b>	<b>Uncertainty</b>
325.29	24	37	0	7	-0.0737	n/c	n/c
339.305	25	39	0	7	-0.0737	n/c	n/c
353.321	26	41	0	7	-0.0737	n/c	n/c
141.07	11	9	0	8	-0.0871	n/c	n/c
155.086	12	11	0	8	-0.0871	0.046	0.011
169.102	13	13	0	8	-0.0871	0.073	0.008
183.117	14	15	0	8	-0.0871	0.136	0.008
197.133	15	17	0	8	-0.0871	0.184	0.007
211.149	16	19	0	8	-0.0871	0.205	0.007
225.164	17	21	0	8	-0.0871	0.210	0.007
239.18	18	23	0	8	-0.0871	0.172	0.006
253.196	19	25	0	8	-0.0871	0.124	0.006
267.211	20	27	0	8	-0.0871	0.099	0.006
281.227	21	29	0	8	-0.0871	0.080	0.005
295.243	22	31	0	8	-0.0871	0.099	0.006

Table 4-2 cont'd

<b>Mass</b>	<b>C</b>	<b>H</b>	<b>O</b>	<b>DBE</b>	<b>KMD</b>	<b><math>k_d</math> (h<sup>-1</sup>)</b>	<b>Uncertainty</b>
309.258	23	33	0	8	-0.0871	0.041	0.004
323.274	24	35	0	8	-0.0871	0.040	0.005
337.29	25	37	0	8	-0.0871	0.018	0.004
351.305	26	39	0	8	-0.0871	n/c	n/c
365.321	27	41	0	8	-0.0871	n/c	n/c
153.07	12	9	0	9	-0.1005	n/c	n/c
167.086	13	11	0	9	-0.1005	n/c	n/c
181.102	14	13	0	9	-0.1005	n/c	n/c
195.117	15	15	0	9	-0.1005	n/c	n/c
209.133	16	17	0	9	-0.1005	0.072	0.004
223.149	17	19	0	9	-0.1005	0.158	0.006
237.164	18	21	0	9	-0.1005	0.190	0.007
251.18	19	23	0	9	-0.1005	0.184	0.007
265.196	20	25	0	9	-0.1005	0.162	0.008
279.211	21	27	0	9	-0.1005	0.131	0.006

Table 4-2 cont'd

<b>Mass</b>	<b>C</b>	<b>H</b>	<b>O</b>	<b>DBE</b>	<b>KMD</b>	<b><math>k_d</math> (h<sup>-1</sup>)</b>	<b>Uncertainty</b>
293.227	22	29	0	9	-0.1005	0.104	0.006
307.243	23	31	0	9	-0.1005	0.069	0.004
321.258	24	33	0	9	-0.1005	0.062	0.005
335.274	25	35	0	9	-0.1005	0.050	0.005
349.29	26	37	0	9	-0.1005	0.041	0.005
363.305	27	39	0	9	-0.1005	n/c	n/c
221.133	17	17	0	10	-0.1139	n/c	n/c
235.149	18	19	0	10	-0.1139	0.052	0.005
249.164	19	21	0	10	-0.1139	0.065	0.006
263.18	20	23	0	10	-0.1139	0.056	0.007
277.196	21	25	0	10	-0.1139	0.047	0.007
291.211	22	27	0	10	-0.1139	0.046	0.006
305.227	23	29	0	10	-0.1139	0.040	0.005
319.243	24	31	0	10	-0.1139	n/c	n/c
333.258	25	33	0	10	-0.1139	n/c	n/c

Table 4-2 cont'd

<b>Mass</b>	<b>C</b>	<b>H</b>	<b>O</b>	<b>DBE</b>	<b>KMD</b>	<b><math>k_d</math> (h<sup>-1</sup>)</b>	<b>Uncertainty</b>
347.274	26	35	0	10	-0.1139	n/c	n/c
219.117	17	15	0	11	-0.1273	n/c	n/c
233.133	18	17	0	11	-0.1273	0.112	0.015
247.149	19	19	0	11	-0.1273	0.077	0.009
261.164	20	21	0	11	-0.1273	n/c	n/c
275.18	21	23	0	11	-0.1273	n/c	n/c
289.196	22	25	0	11	-0.1273	n/c	n/c
303.211	23	27	0	11	-0.1273	n/c	n/c
317.227	24	29	0	11	-0.1273	n/c	n/c
331.243	25	31	0	11	-0.1273	n/c	n/c
345.258	26	33	0	11	-0.1273	n/c	n/c
217.102	17	13	0	12	-0.1407	0.097	0.014
231.117	18	15	0	12	-0.1407	n/c	n/c
245.133	19	17	0	12	-0.1407	n/c	n/c
259.149	20	19	0	12	-0.1407	n/c	n/c

Table 4-2 cont'd

<b>Mass</b>	<b>C</b>	<b>H</b>	<b>O</b>	<b>DBE</b>	<b>KMD</b>	<b><math>k_d</math> (h<sup>-1</sup>)</b>	<b>Uncertainty</b>
273.164	21	21	0	12	-0.1407	n/c	n/c
287.18	22	23	0	12	-0.1407	n/c	n/c
301.196	23	25	0	12	-0.1407	n/c	n/c
315.211	24	27	0	12	-0.1407	n/c	n/c
329.227	25	29	0	12	-0.1407	n/c	n/c
343.243	26	31	0	12	-0.1407	n/c	n/c
357.258	27	33	0	12	-0.1407	n/c	n/c
285.164	22	21	0	13	-0.1541	n/c	n/c
299.18	23	23	0	13	-0.1541	n/c	n/c
313.196	24	25	0	13	-0.1541	n/c	n/c
327.211	25	27	0	13	-0.1541	n/c	n/c
341.227	26	29	0	13	-0.1541	n/c	n/c
355.243	27	31	0	13	-0.1541	n/c	n/c
311.18	24	23	0	14	-0.1675	n/c	n/c
325.196	25	25	0	14	-0.1675	n/c	n/c

Table 4-2 cont'd

<b>Mass</b>	<b>C</b>	<b>H</b>	<b>O</b>	<b>DBE</b>	<b>KMD</b>	<b><math>k_d</math> (h<sup>-1</sup>)</b>	<b>Uncertainty</b>
339.211	26	27	0	14	-0.1675	n/c	n/c
353.227	27	29	0	14	-0.1675	n/c	n/c
367.243	28	31	0	14	-0.1675	n/c	n/c

a. n/c =  $k_{obs} < 0.002 \text{ h}^{-1}$ , which was not significantly different from 0 ( $\alpha = 0.05$ )

Table 4-3. The exact mass, the number of carbon atoms (C), the number of hydrogen atoms (H), the number of oxygen atoms (O), the double bond equivalence (DBE), the Kendrick mass defect (KMD), the first (1<sup>st</sup>) and zeroth (0<sup>th</sup>) rate constant for formation ( $k_f$ ), and the uncertainty in the rate constant for compounds identified using mass spectrometry.

Mass	C	H	O	DBE	KMD	$k_f$ 1 <sup>st</sup> (h <sup>-1</sup> )	Uncertainty	$k_f$ 0 <sup>th</sup> (h <sup>-1</sup> )	Uncertainty
165.07	13	9	0	10	-0.114	0.958	0.153	0.003	0.0002
179.086	14	11	0	10	-0.114	0.647	0.119	0.005	0.0003
193.102	15	13	0	10	-0.114	0.758	0.138	0.012	0.0009
147.081	10	11	1	6	-0.083	0.000	0.036	0.008	0.0004
161.097	11	13	1	6	-0.083	0.028	0.026	0.043	0.0019
175.112	12	15	1	6	-0.083	0.033	0.020	0.092	0.0031
189.128	13	17	1	6	-0.083	0.017	0.015	0.097	0.0024
203.144	14	19	1	6	-0.083	0.000	0.017	0.073	0.0016
217.159	15	21	1	6	-0.083	0.000	0.027	0.051	0.0017
231.175	16	23	1	6	-0.083	0.000	0.030	0.037	0.0013
245.191	17	25	1	6	-0.083	0.000	0.030	0.030	0.0011
259.206	18	27	1	6	-0.083	0.000	0.028	0.025	0.0008
273.222	19	29	1	6	-0.083	0.000	0.029	0.020	0.0006
287.237	20	31	1	6	-0.083	0.000	0.031	0.015	0.0005

Table 4-3 cont'd

Mass	C	H	O	DBE	KMD	$k_f$ 1 <sup>st</sup> (h <sup>-1</sup> )	Uncertainty	$k_f$ 0 <sup>th</sup> (h <sup>-1</sup> )	Uncertainty
159.081	11	11	1	7	-0.097	0.000	0.031	0.005	0.0002
173.097	12	13	1	7	-0.097	0.000	0.024	0.012	0.0005
187.112	13	15	1	7	-0.097	0.000	0.019	0.033	0.0011
201.128	14	17	1	7	-0.097	0.000	0.015	0.065	0.0016
215.144	15	19	1	7	-0.097	0.000	0.013	0.079	0.0014
229.159	16	21	1	7	-0.097	0.000	0.021	0.068	0.0018
243.175	17	23	1	7	-0.097	0.000	0.032	0.046	0.0017
257.191	18	25	1	7	-0.097	0.000	0.049	0.031	0.0017
183.081	13	11	1	9	-0.123	0.002	0.029	0.010	0.0005
197.097	14	13	1	9	-0.123	0.064	0.021	0.035	0.0013
211.112	15	15	1	9	-0.123	0.142	0.018	0.052	0.0019
225.128	16	17	1	9	-0.123	0.221	0.024	0.041	0.0020
239.144	17	19	1	9	-0.123	0.111	0.027	0.028	0.0013
253.159	18	21	1	9	-0.123	0.000	0.037	0.016	0.0008
195.081	14	11	1	10	-0.137	0.000	0.023	0.017	0.0005

Table 4-3 cont'd

Mass	C	H	O	DBE	KMD	$k_f$ 1 <sup>st</sup> (h <sup>-1</sup> )	Uncertainty	$k_f$ 0 <sup>th</sup> (h <sup>-1</sup> )	Uncertainty
209.097	15	13	1	10	-0.137	0.017	0.013	0.047	0.0010
223.112	16	15	1	10	-0.137	0.055	0.012	0.063	0.0014
237.128	17	17	1	10	-0.137	0.101	0.015	0.048	0.0014
251.144	18	19	1	10	-0.137	0.104	0.016	0.029	0.0009
265.159	19	21	1	10	-0.137	0.038	0.021	0.019	0.0007
235.112	17	15	1	11	-0.150	0.002	0.001	0.011	0.0006
249.128	18	17	1	11	-0.150	0.074	0.021	0.013	0.0005
263.144	19	19	1	11	-0.150	0.045	0.024	0.012	0.0004
203.107	13	15	2	7	-0.120	0.013	0.043	0.014	0.0009
201.092	13	13	2	8	-0.133	0.000	0.035	0.006	0.0003
215.107	14	15	2	8	-0.133	0.070	0.034	0.011	0.0006
229.123	15	17	2	8	-0.133	0.215	0.035	0.015	0.0008
243.139	16	19	2	8	-0.133	0.909	0.095	0.014	0.0017
257.154	17	21	2	8	-0.133	1.173	0.130	0.011	0.0017
271.17	18	23	2	8	-0.133	1.045	0.121	0.010	0.0014

Table 4-3 cont'd

<b>Mass</b>	<b>C</b>	<b>H</b>	<b>O</b>	<b>DBE</b>	<b>KMD</b>	<b><math>k_f</math> 1<sup>st</sup> (h<sup>-1</sup>)</b>	<b>Uncertainty</b>	<b><math>k_f</math> 0<sup>th</sup> (h<sup>-1</sup>)</b>	<b>Uncertainty</b>
213.092	14	13	2	9	-0.146	0.000	0.023	0.008	0.0002
227.107	15	15	2	9	-0.146	0.063	0.022	0.013	0.0005
241.123	16	17	2	9	-0.146	0.065	0.065	0.014	0.0005
255.139	17	19	2	9	-0.146	0.131	0.022	0.011	0.0005
269.154	18	21	2	9	-0.146	0.405	0.029	0.009	0.0006
283.17	19	23	2	9	-0.146	0.427	0.042	0.007	0.0006
239.107	16	15	2	10	-0.160	0.000	0.030	0.012	0.0005
253.123	17	17	2	10	-0.160	0.129	0.026	0.010	0.0005
267.139	18	19	2	10	-0.160	0.141	0.024	0.008	0.0004
281.154	19	21	2	10	-0.160	0.017	0.032	0.006	0.0003

The compounds that decayed and formed were organized by KMD, so that the rate constant for compounds with the same DBE but varying alkyl substitution could be evaluated. As observed in the GC-MS experiment, for a compound with the same DBE, more alkyl substitution resulted in an increase in the rate constant. As alkyl substitution continues, the rate constant then decreases (Figure 4-9a). This decrease was not observed in the GC-MS experiment because the compounds with sufficient alkyl substitution were not amenable to GC-MS analysis. The increase in the rate constant could be due to the alkyl groups donating additional electrons to the ring or the addition of benzylic hydrogen presenting more reactive sites, which would be consistent with photooxidation with free radicals. Electron donating groups, such as additional alkyl groups, enhance free radical reactions. Reactions with free radicals often proceed through abstraction of hydrogen atoms, and making alkyl PAHs attractive candidates for free radical oxidation [26]. It has been proposed that alkyl olefins, such as a dimethyl indene, would initiate a free radical reaction [24]. However, other authors suggested that the initiator required for free radical mechanisms is not present in petroleum, but it could be formed from reactions with singlet oxygen [27, 28].

More extensive alkyl substitution resulted in a decrease in photooxidation rate constants. Steric effects and decreases in the number of benzylic hydrogens may explain the resulting decrease in the rate constant for larger homologs. Most compounds with DBE greater than 11 showed no decay over the 10 hour of irradiation, which is consistent

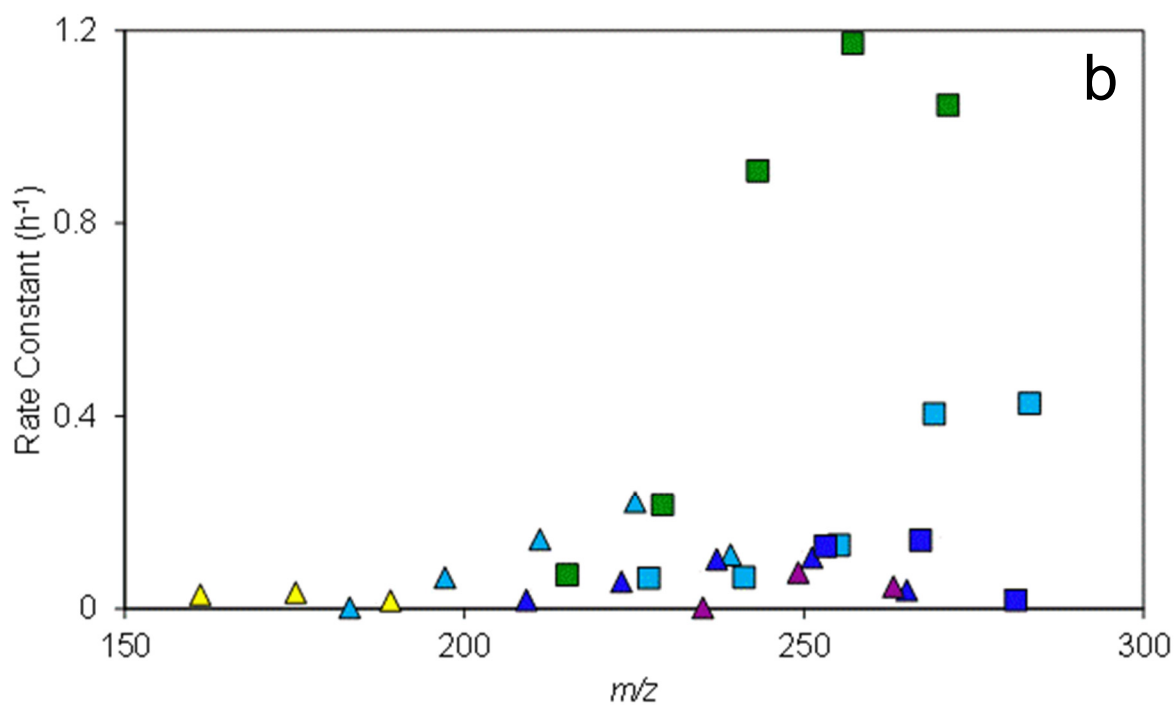
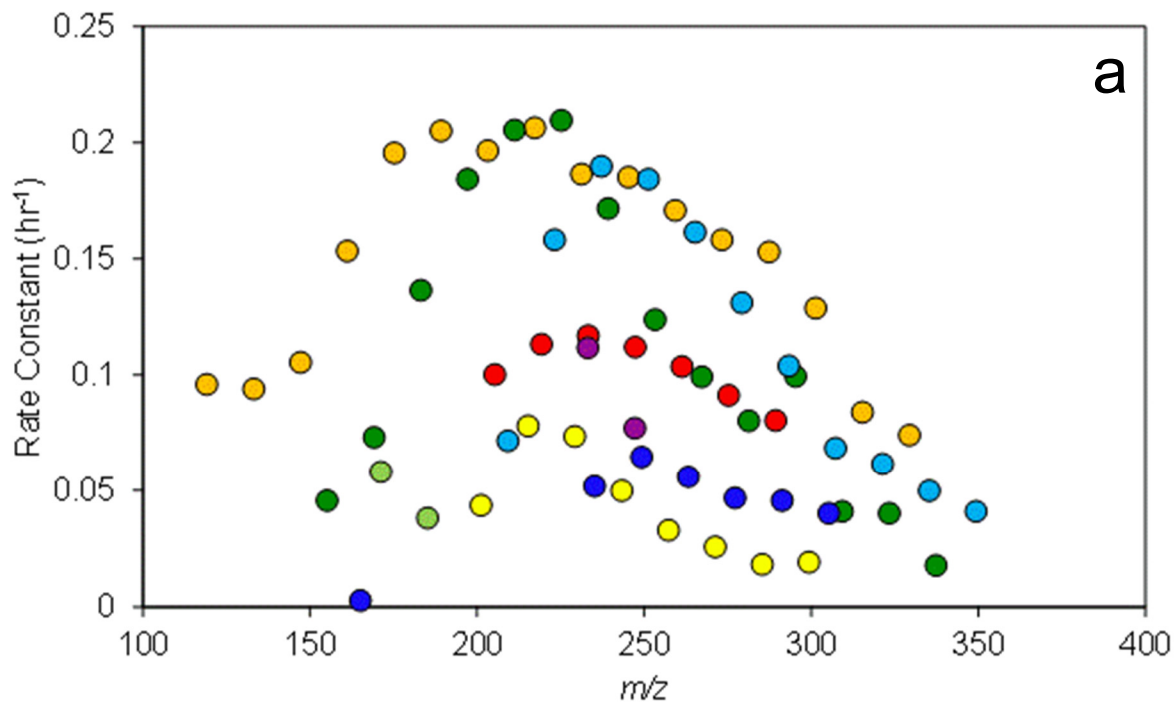


Figure 4-9. The rate constant for decay (a) and formation (b) of selected compounds *versus* the mass of the compound. Compounds are classified based on the number of double bond equivalences (4: red, 5: orange, 6: yellow, 7: light green, 8: dark green, 9: light blue, 10: dark blue, 11: purple) and number of oxygens (0: •, 1: ▲, 2: ■).

with results reported for crude oil [29]. Large PAHs typically have large gaps between the lowest unoccupied molecular orbital (LUMO) and highest occupied molecular orbital (HOMO). A large HOMO-LUMO gap has been shown to result in decreased reactivity, because it is energetically unfavorable to remove electrons from a low HOMO and add electrons to a high HOMO [30, 31]. Addition of alkyl substitution reduces the HOMO-LUMO gap, also helping to explain the increased reactivity with alkyl substitution [31]. Many of the PAHs with DBE greater than 11 were detected at very low abundances, which also made quantification of changes challenging.

The formation rate constants showed a similar increase then decrease with additional alkyl substitution (Figure 4-9b). The rate constants for decay maximized between  $m/z$  150 –  $m/z$  250, while the rate constants for formation maximized between  $m/z$  175 –  $m/z$  275, a mass difference consistent with the addition of an oxygen. The compounds that contained two oxygen atoms typically had higher rate constants for formation than those that only contained one oxygen atom. This could be a result of the mechanism of photooxidation. The reaction with singlet oxygen typically results in the addition of two oxygen atoms, forming a quinone, peroxide, or hydroperoxide, each of which contain two oxygen atoms [8, 26, 32]. The peroxides can then further react, forming an alcohol or other stable oxygen-containing species. Many of the compounds containing two oxygen atoms reached a constant abundance after the first few hours (Figure 4-8d). This indicates that either the reactant(s) have been depleted or that another reaction is occurring and the species containing 2 oxygen atoms are only intermediates that achieve steady-state concentrations. The formation curves for several compounds containing one oxygen show a delayed onset of formation (up to 4 hours), indicating that it may be formed

from an intermediate. There were also several compounds containing 3 or 4 oxygen atoms, but were only present at the latest time points. These were excluded from the rate determination, but suggest that additional oxidation is occurring.

#### *4.3.7 Analysis of Precipitate formed during Irradiation of Diesel Fuel*

The precipitate that was formed during irradiation was analyzed using infrared spectroscopy to identify functional groups and mass spectrometry to determine an elemental formula. Fourier transform infrared spectroscopy attenuated total reflectance (Spectrum One, Perkin Elmer, Waltham, MA) allowed for the analysis of the solid precipitate without any additional sample preparation. The instrument acquired four scans at a resolution of  $4\text{ cm}^{-1}$ , from  $4000 - 650\text{ cm}^{-1}$ . The resulting spectrum (Figure 4-10) indicates oxygenated compounds. There was a broad peak at  $3400\text{ cm}^{-1}$ , consistent with O-H stretch, a large peak at  $1703\text{ cm}^{-1}$ , consistent with a carbonyl stretch, and a peak at  $1262\text{ cm}^{-1}$ , consistent with a C-O stretch. There is also several peaks around  $2929\text{ cm}^{-1}$ , which are consistent with alkyl stretches. These peaks indicates that the precipitate contains hydrocarbons with oxygen functional groups, which would be expected from photooxidation.

The precipitate was also dissolved in acetonitrile for MS analysis. Flow injection analysis was used, with methanol as the mobile phase instead of hexane. There were over 620 masses observed in the precipitate (Figure 4-11). Many of the masses observed

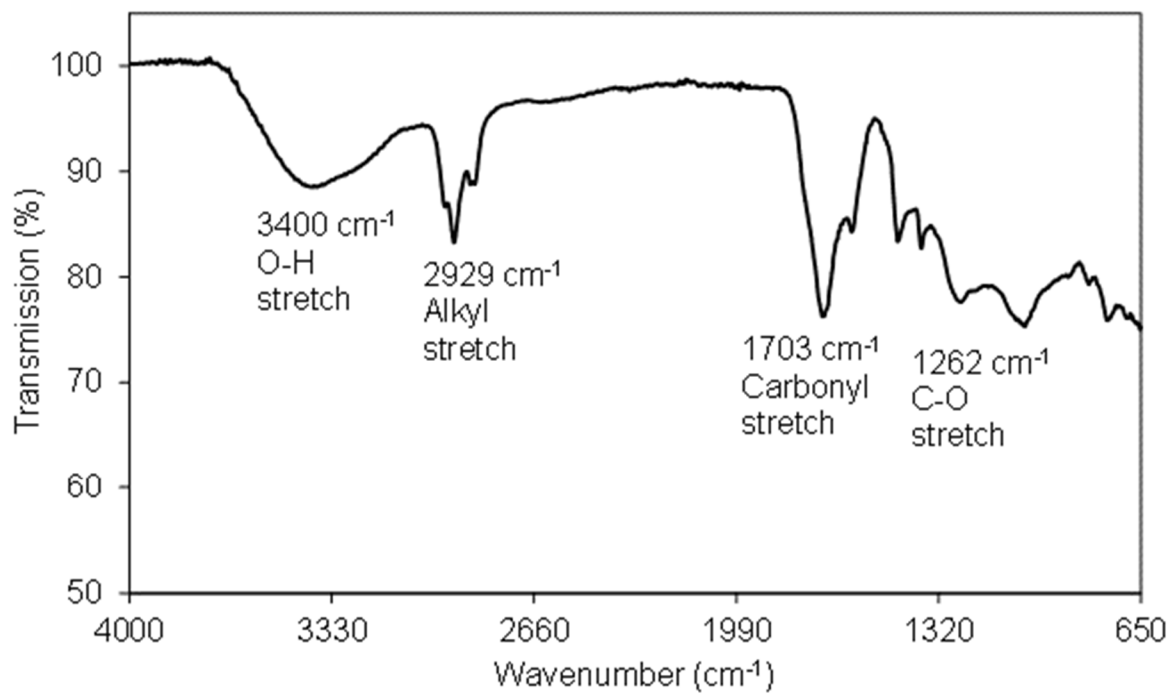


Figure 4-10. An infrared spectrum of the precipitate formed from diesel after 10 hours of irradiation. Several peaks are labeled for reference.

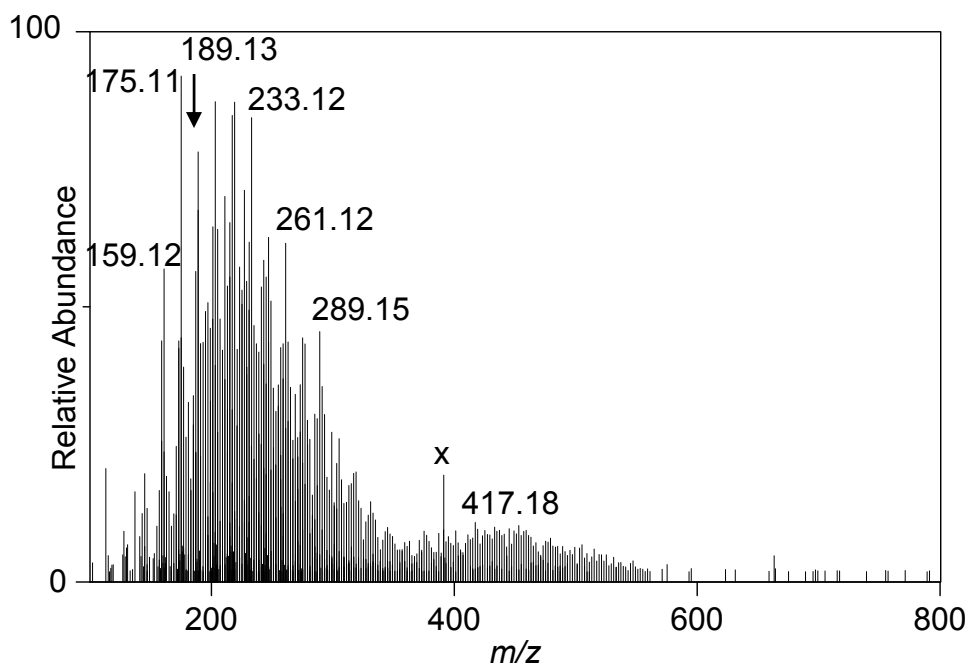


Figure 4-11. The mass spectrum of the precipitate formed from diesel fuel after 10 h of irradiation. The peak marked with “x” at 391.28 is from a phthalate and is present in the blank. It was used as a lock mass in this analysis.

in the precipitate were also observed in the 10 hour irradiated diesel sample. A number of additional masses were observed, many of which contain 3 or more oxygen atoms. The same masses being present in both the fuel and the precipitate suggest that the precipitate is made up of weakly-bonded clusters of oxygenated compounds that dissolve in solution rather than large dimerized compounds.

Several small studies were designed to try to determine the origin of the precipitate. In one experiment, ascorbic acid (Columbus Chemical Industries, Columbus, WI) was added to water (0.8 g/mL) as a free radical scavenger. Peroxides are likely formed in the water layer which could lead to reactions at the oil water interface. Diesel fuel (1 mL) was added on top of the water with ascorbic acid (10mL) and irradiated for 8 hours. In another study, the water layer was completely omitted and 1 mL of diesel fuel was irradiated. In both cases, the precipitate formed as in previous experiments. In addition the mass spectra of the extracted fuel residue in both case contained the same masses at similar abundances to that observed in normal 8 hour irradiation of diesel on distilled water. This demonstrates that the water layer does not significantly influence the rate of photooxidation. However, natural waters which contain additional sensitizers could result in an increased rate of photooxidation.

In another study, diesel fuel was diluted 5-fold by hexadecane. For irradiation, 5 mL of diesel fuel (thickness = 19mm) was placed on 10 mL of distilled water. In this case, the number of compounds from diesel fuel are the same, but at a lower concentration. After 8 hours of irradiation, the fuel became a darker yellow and was slightly turbid, but the precipitate was not formed. The mass spectrum of the extracted diesel fuel was compared to spectra irradiated for 0 – 10 hours. The ratio of masses present in the

spectrum of the diluted diesel fuel was similar to that of non-diluted diesel fuel irradiated for 2 – 4 hours. This demonstrates that the rate of photooxidation is affected by concentration of the reactants, indicating that the rate constants for photooxidation are not zeroth-order. This could also suggest a free-radical mechanism, because free radicals have very short lifetimes to react. In a dilute solution, free-radicals would not encounter as many compounds to react with as in the undiluted sample.

Diesel fuel (100 mL) was redistilled using rotary evaporation, to remove nonvolatile and heteroatom containing compounds. In addition, distillation should have removed any antioxidants or other additives. Approximately 90% of the diesel was recovered after rotary evaporation. The residuum was a dark brown, and likely contained the sulfur and nitrogen containing compounds. In an additional step to remove additives and heteroatom containing compounds, 5 mL of the redistilled diesel was filtered through a C<sub>18</sub> sep-pak cartridge (Waters Associates, Milford, MA). This filtration should remove the volatile polar compounds (antioxidants or other additives) that were distilled. The distilled and filtered diesel fuel was analyzed by GC-MS and APCI-ToF-MS. The TIC from the GC-MS experiment showed no identifiable difference between the fuels. This was expected because the compounds removed by distillation and filtration are likely not amenable to GC-MS. The APCI-ToF-MS spectra also did not show any differences between the two fuels. This is likely to the relatively low abundance of the compounds that were removed. The distilled and filtered fuel was also exposed to irradiation for 5 hours. A precipitate was observed at the end of the experiment. The APCI-ToF-MS spectra of the irradiated diesel samples both with and without distillation and filtration

were also similar. This indicates that the polar and heavy molecular weight compounds likely had little effect on the photooxidation experiment.

The photooxidation of kerosene, which contains more volatile hydrocarbons and fewer PAHs than diesel fuel, was also investigated. The PAHs are the compounds undergoing photooxidation and likely resulting in the precipitate. There are fewer PAHs in kerosene which would making the characterization more straight-forward. The kerosene was evaporated by 50% to reduce the volatility and minimize risk of ignition during the experiment. This also resulted in an increased concentration the less volatile compounds, such as PAHs. Kerosene (1 mL) on water (10 mL) was irradiated for 5 hours. Kerosene is a clear liquid and no color change was observed, however, there was a small amount of turbidity after irradiation. The mass spectra of kerosene prior to irradiation contained fewer masses than the mass spectrum for diesel fuel, indicating that there are fewer PAHs in the kerosene. The mass spectrum of kerosene after irradiation did not suggest the formation of new compounds or decay of existing compounds. However, only limited information can be taken from this experiment as no replicate analyses were performed. It did show that photooxidation of kerosene is sufficiently slow that kerosene would not be well suited for the photooxidation experiments. It also demonstrated the variability in photooxidation between different petroleum products.

#### **4.4 Discussion and Conclusions**

This work has demonstrated the significance of photooxidation in the weathering of petroleum products. While photooxidation may not account for significant mass loss (it may actually add mass, because the oxidized products are heavier), it does lead to the formation of oxidized products that are often more toxic and water-soluble than the parent

compound. In addition, the results from this work suggest that photooxidation occurs much faster than discussed previously. In this work, a color change in the fuel was observed within an hour, and a precipitate formed after 3 hours. Using high resolution mass spectrometry, the diesel samples that were irradiated for 10 hours showed the formation of over 300 new compounds. For these experiments, there were not any photosensitizers added to the water, as there would be in the environment, though the possibility that dissolved CO<sub>2</sub> could be converted to peroxy carbonate and associated radicals cannot be discounted. The photosensitizers present in natural waters would likely lead to additional reactions, with the potential for formation of more compounds and an increase in reaction rates. Diesel fuel and other refined products often contain antioxidants (10-25 ppm) added to help prevent degradation of the fuel prior to use [14]. While these antioxidants were not observed during the analysis, they were likely present and could also affect the rates of degradation.

Even though substantial chemical changes were occurring, few differences due to photooxidation were observed by GC-MS. Using EICs, PAHs such as fluorene and methyl pyrene, were shown to decrease over the course of 10 hours, but no oxidized products were seen. GC-MS is useful in analyzing volatile, nonpolar compounds, but was not effective for analyzing polar oxygenated compounds. Using high resolution mass spectrometry with APCI, the less volatile and oxygenated compounds were detected. APCI allows for a soft ionization of moderately polar compounds including PAHs and oxygenated compounds. This makes APCI an appropriate ionization method for the analysis of petroleum and for monitoring photooxidation. When coupled to a high resolution mass spectrometer, unique elemental formulas can often be assigned. This

demonstrates the need for complementary instrumental techniques to account for the physical and chemical changes that occur during wreathing of petroleum.

The rate constants determined using GC-MS and HR-MS also provided complementary data regarding the rate and mechanism at which the oxidized compounds form. GC-MS allowed for the separation of isomers, demonstrating structural isomers have different rates at which photooxidation occurs. One of the limitations of using the flow injection analysis is that there is no separation of structural isomers. Previous research has shown that different isomers can have nearly a 2-fold difference in their rate constants [23]. In the HR-MS experiment, multiple isomers, each of which react at different rates, could be contributing apparent rate constant. This makes determination of the rate constant challenging and does not allow for a direct comparison of rate constants determined using GC-MS and HR-MS experiments or from the decay and formation of compounds. The GC-MS data also showed that for the decay of a series of compounds, increased alkyl substitution resulted in an increase in the first-order rate constant. A similar trend was observed in the MS data, where an increase in alkyl substitution (with the same KMD) resulted in an increase the photooxidation rate constants. Without chromatographic separation of isomers, it is challenging to assess the number or type of alkyl substitutions, but the rate constants maximized for substitutions between 4 and 8 methylene groups.

In this work, abundances were normalized prior to determination of the rate constant. By normalizing, all calculated concentrations are relative, but for environmental applications, it may be necessary to obtain absolute concentrations. This is challenging using many ionization methods in mass spectrometry unless authentic standards are

available for all compounds of interest. The signal from each compound is dependent on the ionization efficiency of that compound. In APCI, the oxygenated compound was found to ionize more efficiently than pure hydrocarbon PAHs. For example, at equal molar concentrations, phenanthraquinone resulted in a 50 time larger signal than phenanthrene. Similarly, larger PAHs also ionized more efficiently. Pyrene resulted in a 10 times higher signal than that of phenanthrene at equal molar concentrations. For quantification by mass spectrometry, often deuterated or isotopically labeled analogues are required. In a complex mixture such as petroleum, it is impossible to use analogues of every compound. However, specific compounds of interest can be quantified, then the rate constants determined by this approach could be utilized to determine a final concentration.

Exact reaction mechanisms explaining photooxidation of petroleum are still elusive, but it is likely that both singlet oxygen and free radicals are involved in the photooxidation of crude oil and the significance of each process depends on the starting material and the sensitizers in the environment [8, 24, 26]. A recent study by Correa *et al.* showed that diesel fuel was more effective at generating singlet oxygen during irradiation than crude oil [33]. Therefore, singlet oxygen reactions may account for more photodegradation in refined petroleum products, as opposed to crude oil. It is also possible that singlet oxygen is the initiating step in a free radical chain reaction. Determination of the rates of decay and formation due to photooxidation is further complicated by the multiple mechanisms are occurring simultaneously and likely some of the same products are formed by different mechanisms. Miller and Olejnik demonstrated a synergic effect in photodegradation when PAHs are added together [34]. This further complicates the understanding of photooxidation because the pathways and rates may

be highly sample dependent. There are also other mechanisms have been suggested involving electron transfer and the formation of ions at the oil water interface leading to heterogeneous solutions, further complicating mechanistic studies [35, 36].

In conclusion, this work has demonstrated that photooxidation is a significant weathering process for refined petroleum products, such as diesel fuel. This work also proposed a large number of kinetic rate constants determined using GC-MS and APCI-MS as a tool to help quantify the rates of weathering. A large number of oxygenated compounds were formed in a shorter period of time than previously thought. Utilizing complementary analytical techniques, capable of monitoring volatile nonpolar (GC-MS) and nonvolatile, moderately polar molecules (APCI-MS), provided a more complete picture of the changes in the fuel during weathering. This work has also demonstrated the importance of understanding the interdependence of weathering process, such as the increased evaporation resulting from irradiation during photooxidation. Last, the kinetic information on the formation and decay would be useful for developing a model to predict changes in petroleum products due to photooxidation. However, in order to develop the models, work is still needed to understand the mechanism by which photooxidation occurs.

## REFERENCES

## REFERENCES

- [1] National Research Council, Oil in the Sea III : Inputs, Fates, and Effects, National Academy Press, Washington, D.C., 2003.
- [2] M. Fingas, The Basics of Oil Spill Cleanup, CRC Press, Boca Raton, FL, 2013.
- [3] A. Berry, Development of OILTRANS Model Code, 2011. <[http://www.arcopol.eu/arcopol/archivos/documentacion/102/Development\\_OILTRANS\\_model\\_code.pdf](http://www.arcopol.eu/arcopol/archivos/documentacion/102/Development_OILTRANS_model_code.pdf)>. 2/17/2014.
- [4] R.F. Lee, Spill Sci. Technol. Bull., 8 (2003) 157.
- [5] C. Le Vot, C. Afonso, C. Beaugrand, J.C. Tabet, Int. J. Mass Spectrom., 367 (2014) 35.
- [6] C. Frohlich, J. Lean, Astron. Astrophys. Rev., 12 (2004) 273.
- [7] C. Honsberg, S. Bowden, PV Education, Standard Solar Spectra. <<http://www.pveducation.org/pvcdrom/appendices/standard-solar-spectra>>. 08/14/2014.
- [8] J.R. Payne, C.R. Phillips, Environ. Sci. Technol., 19 (1985) 569.
- [9] R.A. Larson, L.L. Hunt, D.W. Blankenship, Environ. Sci. Technol., 11 (1977) 492.
- [10] S.M. King, P.A. Leaf, A.C. Olson, P.Z. Ray, M.A. Tarr, Chemosphere, 95 (2014) 415.
- [11] R.M. Garrett, I.J. Pickering, C.E. Haith, R.C. Prince, Environ. Sci. Technol., 32 (1998) 3719.
- [12] R.C. Prince, R.M. Garrett, R.E. Bare, M.J. Grossman, T. Townsend, J.M. Suflita, K. Lee, E.H. Owens, G.A. Sergy, J.F. Braddock, J.E. Lindstrom, R.R. Lessard, Spill Sci. Technol. Bull., 8 (2003) 145.

- [13] C. Aeppli, C.A. Carmichael, R.K. Nelson, K.L. Lemkau, W.M. Graham, M.C. Redmond, D.L. Valentine, C.M. Reddy, *Environ. Sci. Technol.*, 46 (2012) 8799.
- [14] C. Corporation, Chevron Corporation, Diesel Fuels Technical Review, 2007. <<http://www.chevronwithtechron.com/products/diesel.aspx>>. May 1, 2014.
- [15] A.M. McKenna, R.K. Nelson, C.M. Reddy, J.J. Savory, N.K. Kaiser, J.E. Fitzsimmons, A.G. Marshall, R.P. Rodgers, *Environ. Sci. Technol.*, 47 (2013) 7530.
- [16] C.A. Hughey, C.L. Hendrickson, R.P. Rodgers, A.G. Marshall, *Energy Fuels*, 15 (2001) 1186.
- [17] A.G. Marshall, R.P. Rodgers, *Accounts Chem. Res.*, 37 (2004) 53.
- [18] L. Sleno, *J. Mass Spectrom.*, 47 (2012) 226.
- [19] T. Saeed, L.N. Ali, A. Al-Bloushi, H. Al-Hashash, M. Al-Bahloul, A. Al-Khabbaz, A. Al-Khayat, *Mar. Environ. Res.*, 72 (2011) 143.
- [20] D. Dabrowska, A. Kot-Wasik, J. Namiesnik, *Pol. J. Environ. Stud.*, 17 (2008) 17.
- [21] R.G. Zepp, D.M. Cline, *Environ. Sci. Technol.*, 11 (1977) 359.
- [22] R.P. Schwarzenbach, P.M. Gschwend, D.M. Imboden, *Environmental Organic Chemistry*, John Wiley & Sons, Hoboken, NJ, 2003.
- [23] D.L. Plata, C.M. Sharpless, C.M. Reddy, *Environ. Sci. Technol.*, 42 (2008) 2432.
- [24] R.A. Larson, T.L. Bott, L.L. Hunt, K. Rogenmuser, *Environ. Sci. Technol.*, 13 (1979) 965.
- [25] M.E. Sigman, E.A. Chevis, A. Brown, J.T. Barbas, R. Dabestani, E.L. Burch, J. *Photochem. Photobiol. A-Chem.*, 94 (1996) 149.
- [26] F. ThomINETTE, J. Verdu, *Marine Chemistry*, 15 (1984) 91.

- [27] D.E. Nicodem, M.C.Z. Fernandes, C.L.B. Guedes, R.J. Correa, *Biogeochemistry*, 39 (1997) 121.
- [28] J.F. Rontani, P.J.P. Giral, *Int. J. Environ. Anal. Chem.*, 42 (1990) 61.
- [29] M.T. Griffiths, R. Da Campo, P.B. O'Connor, M.P. Barrow, *Anal. Chem.*, 86 (2014) 527.
- [30] J. Aihara, *J. Phys. Chem. A*, 103 (1999) 7487.
- [31] G.N. Lu, Z. Dang, X.Q. Tao, P.A. Peng, D.C. Zhang, *J. Theor. Comput. Chem.*, 4 (2005) 811.
- [32] H.T. Yu, *J. Environ. Sci. Health Pt. C-Environ. Carcinog. Ecotoxicol. Rev.*, 20 (2002) 149.
- [33] R.J. Correa, D. Severino, R.D. Souza, E.F. de Santana, L.L. Mauro, S.D.S. Alvarenga, D.E. Nicodem, *J. Photochem. Photobiol. A-Chem.*, 236 (2012) 9.
- [34] J.S. Miller, D. Olejnik, *Water Res.*, 35 (2001) 233.
- [35] M.E. Sigman, S.P. Zingg, R.M. Pagni, J.H. Burns, *Tetrahedron Lett.*, 32 (1991) 5737.
- [36] A.E. Klein, N. Pilpel, *Journal of the Chemical Society-Faraday Transactions I*, 70 (1974) 1250.

## 5. Conclusions and Future Works

### 5.1 Evaporation

#### 5.1.1 Conclusions

When a petroleum release occurs, it is critical to have accurate fate and transport models in order to assess potential impacts and guide remediation. Evaporation is one of the most significant sources of mass loss during a petroleum spill and evaporative loss can alter many physical properties of the fuel. Therefore the ability to predict evaporation is a critical aspect of oil spill models. Many current evaporation models require a physical property, such as vapor pressure, which are not readily available for most oils. Therefore, an estimation of the physical properties are required. Moreover, the physical property can change over time, complicating the estimation. In this work, a model was developed to predict the evaporation rate constant for an individual compound, based on the retention index of that compound on a nonpolar stationary phase and the temperature. The first-order rate constant was used to determine a fraction remaining for an individual compound. The total fraction remaining of the fuel was then determined using the sum of the fraction remaining of each individual compound. This predictive model was in good agreement with other evaporation models (percent difference = 4%) as well as experimental measurements (percent difference = 2%).

Current predictive models for evaporation result in a percent evaporated for the total fuel, however, this model also includes the ability to predict the fraction remaining of individual compounds. This provides powerful new tools, not available from other models. Using the fraction remaining of individual compounds, this model can be used to predict

the distribution of compound abundances in a fuel at a given time (*i.e.* create a chromatographic profile), determine the length of time over which the evaporation has occurred, and determine the time it would take for a fuel or an individual compound to reach a specific fraction remaining, which are tools not typically available in oil spill modeling. The prediction of a chromatogram allows users to compare the weathered fuel directly to the neat fuel for identification and forensic purposes. The evaporation time can be estimated using a chromatogram of the evaporated fuel and predicted chromatograms from the model. The predicted chromatograms can be iteratively compared to the evaporated sample. The evaporation time corresponds to the predicted chromatogram that is most similar to the evaporated sample. In this work, the similarity was compared using Pearson product moment correlation coefficients. Currently, the length of time over which evaporation has occurred is estimated using peak ratios of several volatile compounds compared to a nonvolatile compound. The evaporation model developed in this work uses the entire chromatogram, leading to a more accurate determination of evaporation time.

Most evaporation models allow iterative calculations to predict the time it would take to reach a specific fraction remaining or percent evaporated for the fuel. The evaporation model in this work can predict this time for the fuel as well as for individual compounds. This allows for additional assessment of the individual toxic compounds, such as benzene, which could pose additional risks to first responders or marine life. This demonstrates the increased versatility of the kinetic evaporation model developed in this work compared to existing evaporation models. Enhanced models provide a more

accurate and detailed assessment to guide decision making, risk assessment, and remediation.

### *5.1.2 Limitations*

There are a few additional investigations that must be addressed before wide implementation of this model for oil spill fate determination. First, the only variable changed in this work was temperature, however, some research suggests that wind speed, thickness of the film, and surface area may also influence the rate of evaporation [1]. Jones demonstrated using three different predictive models that varying wind speed resulted in an approximately 10% difference in the amount of crude oil evaporated in 48 hours and varying initial thicknesses resulted in an approximately 20% difference. While the influence of these variables are still debated, they require investigation prior to implementation.

Second, in this work the model was developed and validated using fuels with containing different chemical constituents, but with a moderately similar distribution of compounds. The fuels were a complex mixture (more than 100 compounds in each fuel) with boiling points for the majority of the compounds ranging from approximately 100 °C to over 400 °C. However, there are other environmentally relevant fuel samples that have a different distribution of compound abundances and boiling points. For example, gasoline is considerably more volatile than diesel fuel, containing compounds with boiling points lower than 80 °C. As a result, in the GC-MS analysis, several compounds elute prior to typical solvent delays, meaning that these compounds would not be included in the calculation of the fraction remaining of the total fuel, predicting less evaporation than actually occurred. In a similar manner, oils with low volatility (e.g. bunker C or crude oil)

which are not amenable to GC-MS analysis, would also not be included in the total fraction remaining calculation, resulting in predicting more evaporation than actually occurred. In some cases, more than 75% of the compounds in oil would not be sufficiently volatile for GC-MS analysis [2]. Therefore, further investigation of these petroleum products are necessary to determine how to correct the total fraction remaining for compounds not observed in the GC-MS analysis. However, the use of the model to predict the fraction remaining of an individual compound is unaffected by the problem, as long as a retention index can be determined.

Last, this model has not been applied to simple mixtures or pure liquids. For pure liquids, evaporation proceeds linearly with time, indicating zeroth order kinetics [3, 4]. As the mixture becomes more complex, the evaporation kinetics becomes first order. First order kinetics arise because a compound is evaporated, the mole fraction will decrease, resulting in a decrease in the vapor pressure, based on Raoult's Law. However, the methodologies developed in this work could be used to assess evaporation rate and develop new models if necessary.

### 5.1.3 Future Directions

In addition to addressing the limitations discussed above, there are numerous applications of the methodologies discussed in this work both in environmental and forensic applications.

Additional weathering processes could be modeled using similar methodologies to those developed in this work. Arey *et al.* demonstrated that aqueous solubilities and octanol-water partition coefficients could be determined for diesel fuel hydrocarbons using

a column with a mid-polarity stationary phase (50% phenyl polysilphenylene-siloxane) in two dimensional gas chromatography [5]. A model to predict dissolution of compounds from the oil into water could be developed. The hydrocarbon compounds likely to undergo dissolution are the small molecules such as benzene. These compounds frequently are toxic, and determining their fate is critical in effective remediation.

The model developed in this work could have significant implications in the analysis of fire debris. In a forensic laboratory, the detection of an accelerant in fire debris analysis is typically performed using GC-MS. The fire debris is extracted, analyzed, and the resulting chromatogram is compared to reference standards of known fuels [6]. Because burning also leads to the loss of volatile compounds, evaporated standards of the fuels are also used. Typically, these evaporated standards are prepared at several evaporation levels (e.g. 0%, 50%, 75%, 90%) by an analyst in the lab. Preparing and analyzing a large number of standards is very time consuming. By applying the evaporation model, the predicted evaporated chromatogram could be determined from the neat fuel, without the need for evaporating and analyzing the sample, saving time and money.

Another application of this work would be for improved training for explosive detection canines, where the vapor pressure and rate of decomposition are critical aspects of detection. Canines use multiple volatile organic compounds released from an explosive to locate it [7]. When developing training aids for the dogs, it is important to have reproducible vapor-time profiles for each explosive to ensure proper training. The vapor-time profile is related to the vapor pressure of the compounds that compose the explosive. However, the vapor profile is constantly changing due to environmental

transport [8]. Target compounds are often from similar classes, which should allow for the development of a model, using the same methodologies applied in this work, capable of predicting the vapor profile for new compounds and monitoring temporal changes in the profile. This would allow for better real-time understanding of the vapors to which the canines are exposed, leading to a better understanding canine scent training and the development of better and more representative training aids.

## **5.2 Photooxidation**

### *5.2.1 Conclusions*

The photooxidation study highlighted the need for a better understanding of photooxidation as well as the interdependence of weathering processes. Some research suggests that photooxidation is not a significant source of weathering, however, this work showed the formation of hundreds of oxygenated compounds after only 10 hours irradiation of light similar to the sun and without the sensitizers that would be present in natural waters. The new formed oxygenated products have increased toxicity and water solubility. This poses an increased risk to sea life and humans, because the toxins are often bioaccumulated in fish which are ingested by humans. Visual and chemical changes in the diesel fuel were observed, even after the first hour of irradiation, far faster than previously believed [9]. This work highlights the critical need to understand photooxidation because of the early onset at which these toxic compounds form.

The kinetic rate constants determined for photooxidation were useful in assessing rates of change in comparing weathering. In the photooxidation experiments, a large number of first-order kinetic rate constants never previously discussed in the literature,

were calculated for compounds quantified using gas chromatography-mass spectrometry (GC-MS) and atmospheric pressure chemical ionization-time of flight-mass spectrometry (APCI-ToF-MS). In the GC-MS experiment, there was an observed decrease in the volatile compounds, as would be expected due to evaporation. However, when compared to predicted evaporation rate constants (Chapter 3), many of the compounds decayed nearly twice as fast as expected. While this could be explained by photooxidation for some compounds, this phenomenon was observed for a range of compounds, including normal alkanes, which are less reactive toward photooxidation. Therefore, the increased rate of evaporation was likely due to the increased energy deposition from the light source. In the APCI-ToF-MS experiment, the rate constants for structurally related compounds increased with greater alkyl substitution, until 4 – 8 methylene units, then decreased. Larger PAHs, with more than 11 double bond equivalences, were shown to not change over the 10 hours of irradiation. Kinetic rate constants provide valuable information which allows for the comparisons of rates of change for various weathering processes and could be useful in predictive models and determining mechanism of reaction.

### *5.2.2 Limitations*

The development of a predictive model for the photooxidation of petroleum is a challenging task. Most photooxidation proceeds through sensitizers. The sensitizers in the environment can vary greatly between locations. Moreover, the sensitizers in the fuel can vary depending on the composition of the oil. The sensitizers can change over the course of the spill depending on other weathering processes and remediation. Also complicating the development of the model is the changing intensity and spectrum of the

light. Diurnal and seasonal variations change the intensity of the sunlight the surface film of oil changes the intensity and the spectrum of light, complicating model development [9]. To date, no one has developed a predictive model for photooxidation incorporating all of these variables.

One of the major challenges in understanding photooxidation comes from the lack of a comprehensive analytical tool for the analysis of petroleum. Prior to oxidation, many of the compounds in oil are hydrocarbons. The smaller, more volatile compounds can be analyzed by GC-MS, while larger less volatile compounds cannot. High resolution mass spectrometry techniques have been applied in the analysis of petroleum, typically using electrospray ionization (ESI) [10, 11]. Ionization, which is necessary for analysis by MS, exhibits a dependence on the molecule being analyzed. ESI works well to ionize polar compounds, typically those containing one or more heteroatoms, but does not ionize hydrocarbon PAHs unless exceptional steps are taken [12]. Intermediate ionization methods, such as atmospheric pressure chemical ionization and atmospheric pressure photoionization ionize PAHs as well as compounds containing heteroatoms, but still do not ionize saturated or mostly saturated hydrocarbons (normal alkanes, hopanes, *etc.*). This work also demonstrated that APCI can be used to effectively ionize PAHs and the resulting oxidized products for high resolution MS analysis. Therefore, APCI provides ionization for a larger range of compounds and would be useful to monitor oxidative processes (photooxidation and biodegradation) in petroleum products.

An additional limitation in this work was the lack of a chromatographic separation prior to high resolution MS analysis. Large molecules often form a number of isomers, which could not be differentiated by single-stage MS because they have the same

elemental formula and molecular mass. Plata *et al.* showed that two PAH structural isomers had an approximate two-fold difference in the apparent rate constant for photooxidation [13]. In the MS experiment performed in this work, all isomers would be accounted for in the same mass, preventing the determination of individual rate constants. For additional experiments, differentiation of isomers would be an important consideration in obtaining accurate rate constants.

### 5.2.3 Future Directions

Very little is known about the mechanisms and processes associated with photooxidation and experiments often lead to conflicting conclusions. These contradicting views arise from the highly variable experimental conditions, including different light sources, oil samples, and environmental matrices. Tightly regulated laboratory experiments, where a single variable is changed, would allow for a better understanding of the role each variable plays in photooxidation, which would be necessary for model development.

One area that might provide particularly useful additional insight is the effect of environmental sensitizer. Most research agrees that indirect photolysis via photosensitizers is occurring in oil, however, it is not clear whether the effect is only from sensitizers in the fuel or whether sensitizers found in the environment also play a role in photooxidation. This research has demonstrated that the photosensitizers in the diesel fuel were sufficient to lead to photooxidation. Sensitizers, including dissolved organic matter, nitrates, or iron could be placed into water to determine if the rate of photooxidation is increased or if new oxygenated compounds are formed [14]. If sensitizers in the water did not lead to increased photooxidation, future experiments and

models could be simplified because only the composition of the fuel would affect the photooxidation.

Another challenge in understanding photooxidation during an environmental release is that photooxidation and biodegradation are occurring simultaneously, so it is difficult to separate the result of each process. Moreover, other weathering processes including evaporation and emulsification are occurring and leading to additional confusion in the results. Laboratory experiments of photooxidation and microbial degradation could be conducted, where conditions are tightly controlled and affects from other weathering processes could be minimized. During an experiment, evaporation would be difficult to stop, however, the evaporation model developed in this work could be utilized to account for and even correct for evaporative losses. This would allow for experiments which evaluated only photooxidation or microbial degradation. Once there is an understanding of the individual compounds that are formed from each process, multiple weathering processes could be tested simultaneously. In this work, photooxidation significantly increased the rate of evaporation, demonstrating the interdependence of weathering. Previous microbial degradation studies also suggest that the sunlight and the presence of oxidized products can greatly affect the ability of microbes to breakdown the fuel also indicating an interdependence of weathering processes [15]. By understanding individual weathering process and the linkage between weathering processes, better fate and transport models can be developed. Enhanced and more accurate models will provide a better impact assessment, thus helping to guide spill response and remediation.

## REFERENCES

## REFERENCES

- [1] R.K. Jones, Proceedings; Environmental Canada Twentieth Arctic and Marine Oilspill Program Technical Seminar, 1 (1997) 43.
- [2] C. Aeppli, C.A. Carmichael, R.K. Nelson, K.L. Lemkau, W.M. Graham, M.C. Redmond, D.L. Valentine, C.M. Reddy, Environ. Sci. Technol., 46 (2012) 8799.
- [3] R. Chebbi, S.E.M. Hamam, M.K.M. Al-Kubaisi, K.M. Al-Jaja, S.A.M. Al-Shamaa, J. Chem. Eng. Jpn., 36 (2003) 1510.
- [4] D. Mackay, R.S. Matsugu, Can. J. Chem. Eng., 51 (1973) 434.
- [5] J.S. Arey, R.K. Nelson, L. Xu, C.M. Reddy, Anal. Chem., 77 (2005) 7172.
- [6] J.D. DeHaan, Kirk's Fire Investigation, Prentice Hall, Upper Saddle River, NJ, 2002.
- [7] R.J. Harper, J.R. Almirall, K.G. Furton, Talanta, 67 (2005) 313.
- [8] W. MacCrehan, S. Moore, M. Schantz, J. Chromatogr. A, 1244 (2012) 28.
- [9] National Research Council, Oil in the Sea III : Inputs, Fates, and Effects, National Academy Press, Washington, D.C., 2003.
- [10] C.A. Hughey, R.P. Rodgers, A.G. Marshall, Anal. Chem., 74 (2002) 4145.
- [11] A.G. Marshall, R.P. Rodgers, Proc. Natl. Acad. Sci. U. S. A., 105 (2008) 18090.
- [12] G.W. Lien, C.Y. Chen, C.F. Wu, Rapid Commun. Mass Spectrom., 21 (2007) 3694.
- [13] D.L. Plata, C.M. Sharpless, C.M. Reddy, Environ. Sci. Technol., 42 (2008) 2432.

[14] R.P. Schwarzenbach, P.M. Gschwend, D.M. Imboden, *Environmental Organic Chemistry*, John Wiley & Sons, Hoboken, NJ, 2003.

[15] T.K. Dutta, S. Harayama, *Environ. Sci. Technol.*, 34 (2000) 1500.